INVESTIGATION ON DEFORMATION BEHAVIOURS OF NON-FERROUS ALLOYS THROUGH CONTINUOUS FORMING EXTRUSION

Tariku Desta Besufikad

A Dissertation Submitted to the Department of Mechanical Engineering,

School of Mechanical, Chemical and Materials Engineering

Presented in Partial Fulfillment of the Requirement for the Degree of Doctor of Philosophy in Mechanical Engineering (Specialization in Manufacturing Engineering)

Office of Graduate Studies
Adama Science and Technology University

June 2023
Adama, Ethiopia

INVESTIGATION ON DEFORMATION BEHAVIOURS OF NON-FERROUS ALLOYS THROUGH CONTINUOUS FORMING EXTRUSION

Tariku Desta Besufikad

Main Supervisor: Perumalla Janaki Ramulu (Ph.D.)

Co-Supervisor: Devendra Kumar Sinha (Ph.D.)

A Dissertation Submitted to the Department of Mechanical Engineering, School of Mechanical, Chemical and Materials Engineering

Presented in Partial Fulfillment of the Requirement for the Degree of Doctor of Philosophy in Mechanical Engineering (Specialization in Manufacturing Engineering)

Office of Graduate Studies
Adama Science and Technology University

June 2023
Adama, Ethiopia

APPROVAL OF Ph.D. DISSERTATION

We hereby certify that the recommendations and suggestions made by the board of examiners are appropriately incorporated into the final version of the dissertation entitled **"Investigation on Deformation Behaviors of Non-Ferrous Alloys through Continuous Forming Extrusion"** by Mr. Tariku Desta.

______________________	______________________	______________
Major Supervisor	Signature	Date
______________________	______________________	______________
Co-supervisor	Signature	Date

We, the undersigned, members of the Board of Examiners of the dissertation open defence by Mr. Tariku Desta have read and evaluated the dissertation entitled **"Investigation on Deformation Behaviors of Non-Ferrous Alloys through Continuous Forming Extrusion"** and examined the candidate during open defence. This is, therefore, to certify that the dissertation is accepted for the partial fulfillment of requirement for the Degree of Doctor of Philosophy in Mechanical Engineering (Specialization in Manufacturing Engineering).

Chairperson	Signature	Date
Internal Examiner	Signature	Date
Prof. Swadesh Kumar Singh		**29.06.23**
External Examiner 1	Signature	Date
Dr. R. Uday Kumar		**29.06.23**
External Examiner 2	Signature	Date

Finally, approval and acceptance of the dissertation is contingent upon submission of its final copy to the Office of Postgraduate Studies (OPGS) through the candidate's Department Graduate Council (DGC) and School Graduate Committee (SGC).

______________________	______________________	______________
Department Head	Signature	Date
______________________	______________________	______________
School Dean	Signature	Date
______________________	______________________	______________
Office of Postgraduate Studies, Dean	Signature	Date

DECLARATION

I hereby declare that this Dissertation entitled "**Investigation on Deformation Behaviors of Non-Ferrous Alloys through Continuous Forming Extrusion**" is my original work. That is, it has not been submitted for the award of any academic degree, diploma or certificate in any other university. All sources of materials used for this dissertation have been duly acknowledged through appropriate citations.

______________________	______________________	______________
Name of Student	Signature	Date

RECOMMENDATION

We, the supervisors of this dissertation, hereby certify that we have read and revised the dissertation entitled "**Investigation on Deformation Behaviors of Non-Ferrous Alloys through Continuous Forming Extrusion**" prepared under our guidance by **Mr. Tariku Desta** and submitted in partial fulfillment of the requirements for the Degree of Doctor of Philosophy in Mechanical Engineering (Specialization in **Manufacturing Engineering)**. Therefore, we recommend the submission of the dissertation to the department for further review and defence.

______________________________	____________________________	__________________
Major Supervisor	Signature	Date
______________________________	____________________________	__________________
Co-supervisor	Signature	Date

ACKNOWLEDGEMENT

First of all let me praise and honor the **Almighty God** for the opportunity and capacity given to me to realize my aspiration to finish this Ph.D. research work.

I would like to express my deepest gratitude to my principal supervisor, **Dr. Perumalla Janaki Ramulu,** for his kindhearted acceptance to supervise me, trustful support, in both academic endeavor and personal life during my stay as a Ph.D. student in ASTU. His precious and kind advice helped me overcome numerous troubles and finish this dissertation. His guarantee, passion to work and prodigious learning from him empowers me to raise my academic endeavor and professional ethics competently.

I would like to express my sincere gratitude to my co-supervisor, **Dr. Devendra Kumar Sinha** for his meticulous guidance, supervision, continuous encouragement, follow-up and professional advice throughout the entire course of this research, for his insight and suggestion; he helped me to explore my capabilities and then to focus on the findings. His all-directional support empowers me to raise my academic exertion.

I would like to thank **Adama Science and Technology University (**ASTU) for giving me the chance to pursue my Ph.D. I wish also to thank ASTU Post-Graduate Office, School of Mechanical, Chemical and Materials Engineering Deans, Heads of Mechanical Engineering program, Department's staffs, all my friends and colleagues at ASTU.

The support and guidance of my Ph.D. Committee Members: Dr. Dawit Gudeta, Dr. Venkatesh Chenrayan and Dr. Sayeed Ahmed should be greatly acknowledged.

Particularly, I would also like to thank the owner and GM of Eastern Copper Manufacturing Co Pvt. Ltd, Kolkata, India for his free permission to do experimentations in his factory. I would like to thank MFM-ATTC (Harar), Ethiopian Welding Institute and Addis Ababa Science and Technology University (Addis Abeba), Ethiopia.

Finally, I also want to keep it up my special thanks for my **Families,** my wife **W/ro Getenesh Hailu** who is always there to encourage and strengthen me all the way through this challenging but rewarding work. I am full of pride with all my children (**Yafet T., Blen T. and Addis-Kidan T**.) who give me inspiration and energy by their boundless outright love along with life-long trust. Conclusively, Ato **Desta Besufikad, Emahoy Ketemash Desalegn**, my brother **Girma Desta** and my sister **Hiwot Desta** should be recognized, without their all-rounded support it is impossible to achieve my goal.

TABLE OF CONTENTS

CONTENTS **PAGE**

LIST OF TABLES

TABLE **PAGE**

LIST OF FIGURES

FIGURE **PAGE**

LIST OF ACRONYMS AND ABBREVIATIONS

3D	Three Dimensional
ACEF	Accumulative Continuous Extrusion Forming
AMS	Accumulated Mean Square
ANN	Artificial Neural Network
ANOVA	Analysis of Variance
ARBP	Accumulative Roll-Bonding Process
ASTM	American Society for Testing and Materials
CA	Cryorolling and Aging
CAD	Computer Assisted Drawing /Design
CCD	Central Composite Design
CCRD	Central Composite Rotatable Design
CDRX	Continuous Dynamic Recrystallization
CE	Conform Extrusion
CFSP	Cryogenic Friction Stir Processing
Conform	Continuous Forming
CR	Cold Rolling
CRE	Continuous Rotary Extrusion
DCAP	Dynamic Channel Angular Pressing
DIA. / Dia.	Diameter
EBSD	Electron Back Scattered Diffraction
ECAP	Equal Channel Angular Pressing
Exp.Tri.	Experimental Trial
CE–ECAP	Conform Extrusion- Equal Channel Angular Pressing
CEP	Continuous Extrusion Process
CEEP	Continuous Expansive Extrusion Process
Conform-HPTE	Conform- High Pressure Torsion/Extrusion
DT/dt	Die Temperature
ECAR	Equal-Channel Angular Rolling
EDS, EDX, or XEDS	Energy Dispersive X-ray Spectroscopy

EP	Extrusion Process
FEM (A)	Finite Element Methods (Analysis)
Fc	Friction condition
FF/ff	Friction Factor
Fig.	Figure
FT/ft	Feedstock Temperature
GA	Genetic Algorisms
HAGB	High Angle Grain Boundary
HPTE	High Pressure Torsion/Extrusion
HT	Hybrid Technique
KE	Kobo Extrusion
LAGB	Low Angle Grain Boundary
MDF	Multi Directional Forging
MPa	Mega Pascal
MSD	Mean Square Deviation
OES	Optical Emission Spectroscopy
PD/pd	Product Diameter
RCEP	Reductive Continuous Extrusion Process
RCE	Reductive Conform Extrusion
R-Conform	Repetitive-Continuous Extrusion Forming
RPM/rpm	Revolution Per Minutes
RS	Rotary Swaging
RSD	Response Surface Design
RSM	Response Surface Methodology
SPD	Sever Plastic Deformation
SSS	Sequential Sum of Square
Std Order	Standard Order
TE	Twist Extrusion
TEM	Transmission Electron Microscopy
TV-CAP	Twisted Variable Channel Angular Extrusion

UBT/M	Upper Bound Techniques/Methodologies
UDEM	Uniform–Deformation Energy Method
UFG	Ultra-Fine Grain
UKAEA	United Kingdom Atomic Energy Authority
UTS	Ultimate Tensile Strength
VDF	Variable Drive Frequency
XRD	X-ray Diffract Meter/ X-ray diffraction
XRFS	X-Ray Fluorescence Spectroscopy
YS	Yield Strength
wt.	weight
WV/wv	(Driving /Extrusion) wheel velocity (speed)

ABSTRACT

Determining the optimal input process parameters of Conform Extrusion (CE) to manufacture a non-ferrous material is critical to produce better products. This could be not only from cost perspective but also strength aspects. The main objectives of this study were to investigate the effects of CE input parameters on responses such as extrusion load, effective stress and damage, the microstructure and mechanical properties of the extrudates. The CE input variables explored in this investigation were extrusion wheel speed, feedstock temperature, die temperature, friction factors and extrusion ratio. The materials considered for this research were Aluminum (AA1100), Copper (C101) and Copper-Chromium-Zirconium (C18150) alloy. Analytical, computational and experimental methodologies were employed to explore and validate the obtained results. In the analytical investigation, Upper Bound Methodology (UBM) was applied to estimate an optimal load requirement. Deform 3D analysis tool was used for simulations and explorations of extrusion load, effective stress, and damage responses. Computational results were further analyzed and optimized through Response Surface Methodology (RSM). The same results also mathematically modeled through second order regression model and the model accuracies were also validated using ANOVA. R^2 values through RSM and Artificial Neural Network (ANN)–Genetic Algorithms (GA) compared. In the comparison, the better values were seen through ANN-GA. Experiments were performed using a commercial setup of a TBJ 350 Conform extrusion machine taking optimized input process parameters obtained from RSM and ANN-GA. Regarding optimal load obtained through UBM, it became in good agreement with computational and experimental ones. The feedstock and CE extrudes of AA1100, C101 and C18150 were tested, and characterized through microstructure and mechanical tests to observe the effects of the CE parameters. The CE input variables effects on the effective stress, damage, microstructures, tensile strength, percent of elongation, hardness, and wear characteristics of the extrudate with respect to feed-metal were investigated. It was observed that the microstructures of the extrudates were refined. Significant improvements in percent of elongation and tensile strength were obtained in all three extrudates (AA1100, C101 and C18150). Similar improvements also imparted in hardness and wear characteristics of the extrudates. Optimal CE parameters for least effective stress and damage also identified. The findings are expected to meet the requirements of industries, designers, researchers and other community working in these fields.

Keywords: *Conform Extrusion; UBM; DEFORM-3D; RSM; ANNOVA; ANN–GA; Non-ferrous metals; microstructures; mechanical properties.*

CHAPTER 1: INTRODUCTION

1.1. Background of the Study

Extrusion Process (EP) is one of the metal forming manufacturing processes which forces the feed stock to flow through a die opening with a desired shape. Generally, EP is classified as direct and indirect extrusion and most of heavy duty extrusions have been performed through the direct method. It is also classified into conventional and Sever Plastic Deformation (SPD). The Process is further sub-classified based on different factors (Bhaduri, A., 2018; Hosford and Caddell, 2011).

It is well known that a plastic deformation induced via conventional metal forming processes such as forging, rolling, extruding, drawing or stretching can considerably improve the strength of a metal or an alloy. Nevertheless, such an increase is commonly accompanied at the expense of ductility (elongation to failure) electrical conductivity and other properties in conventional ones. There are, however, other SPD techniques through which even extraordinary combinations of mutual exclusive properties such as high strength and high ductility (Jiang, K., *et al*., 2021; Wang, Y. D., *et al*., 2021; Jeong, H. T., *et al*., 2021; Huang, A. H., *et al*., 2019; Kuramoto, S., *et al*., 2019; Langdon, T. G., *et al*., 2018; Valiev, R. Z., *et al*., 2002) high strength with high conductivity (Shen, Z., *et al*., 2022; Wu, X., *et al*., 2022; Mao, Q., *et al*., 2022; Zhao, N., *et al*., 2022; Fu, *Q., et al*., 2022; Yang, H., *et al*., 2020; Zhang, P. C., *et al*., 2020; Guo, T., *et al*., 2020; Qi, Y., *et al*., 2019; Ravisankar, B., *et al*., 2019; Chembarisova, R. G., *et al*., 201; Li, B., *et al*., 2011) produced through SPD by modifying the microstructure of a metal and alloy (Jalilova, D. A., *et al*., 2022; Shan, L., *et al*., 2022; Borodin, E. N., *et al*., 2020). The combination of ultrafine grain size (UFG) and higher-density dislocations acts to enable deformation by new SPD mechanisms (Chembarisova, R. G., *et al*., 2020; Kapoor, G., *et al*., 2020; Ma, M., *et al*., 2020; Morozova, A., *et al*., 2018; Purcek, G., *et al*., 2018; Yuan, D., *et al*., 2018; Zhang, S., *et al*., 2017; HE, WX, *et al*., 2007; Vinogradov, A., *et al*., 2002).

The general yield strength difference between as-cast and as-extruded of an alloy is attributed to solid solution strengthening, precipitation hardening, and grain refinement strengthening, and working hardening effects (Xu, G. L., *et al*., 2021). Such unusual mechanical, technological and electrical behaviors are produced by the unique nanostructures generated through SPD (Mao, Q., *et al*., 2022). Such very eye-catching mechanical properties can be attained through various SPD mechanisms.

A number of SPD techniques can generate ultra-fine grain size through various processes among them Equal Channel Angular Pressing (ECAP) and Equal-Channel Angular Rolling (ECAR) (Dalan, F. C., *et al*., 2022; Snopiński, P., *et al*., 2021; Aksenov, D. A., *et al*., 2021; Abib, K., *et al*., 2020; Bourezg, Y. I., *et al*., 2020; Chembarisova, R. G. , *et al*., 2020; Guo, T., *et al*., 2020; Suresh, M., *et al*., 2019; Bagherpour, E., *et al*., 2018; Liu, Y., *et al*., 2017; Abib, K., *et al*., 2016; Shangina, D., *et al*., 2016; Abib, K., *et al*., 2015); Dynamic Channel-Angular Pressing (DCAP) (Khomskaya, I. V., *et al*., 2018); Cryorolling and Aging (Sun, X., *et al*., 2021; Li, R., *et al*., 2019; Jaseem, I., *et al*., 2018; Kao, Zhang, S., *et al*., 2017; Kao, Y. T., 2014; Li, B., *et al*., 2011); Cryogenic Friction Stir Processing (Wang, y. d., *et al*., 2021; Wang, Y., *et al*., 2019); High Pressure Torsion/Extrusion (HPTE) (Azzeddine, H., *et al*., 2022; Purcek, G., *et al*., 2020; Zhang, X., *et al*., 2020; Hernández-Escobar, D., *et al*., 2019; Edalati, K., *et al*., 2018; Purcek, G., *et al*., 2018; Shangina, D. V., *et al*., 2017; Ito, Y., & Horita, Z., 2009) KOBO extrusion (Olszówka-Myalska, A., *et al*., 2022; Ostachowski, P., *et al*., 2019; Sheik Hassan, M., *et al*., 2017; Heyduk, F., *et al*., 2015; Estrin, Y., & Vinogradov, A., 2013); Rotary Swaging (RS) (Mao, Q., *et al*., 2022; Meng, A., *et al*., 2021; Huang, A. H., *et al*., 2019; Bhaduri, A., 2018); Twist Extrusion (TE) (Borodin, E. N., *et al*., 2020, Nouri, M., *et al*., 2018; Segal, V., 2018); Twisted Variable Channel Angular Extrusion (TV-CAP) (Özbeyaz , K., *et al*., 2022); Cold Rolling (CR) (Chakraborty, J, *et al*., 2022; Xie, M., *et al*., 2021; Liao, W. *et al*., 2020; Chenna Krishna, S., *et al*., 2018); Multi Directional Forging (MDF) (Borodin, E. N., *et al*., 2020; Sousa, T. G., *et al*., 2020; Khomskaya,I. V., *et al*., 2019; Morozova, A., *et al*., 2018); Accumulative Roll-bonding process (Liu, Y., *et al*., 2022; Mungole, T., 2018; Takata, N., *et al*., 2009); hybrid technique (Wang, Y., *et al*., 2019); Conform Extrusion (Shen, Z., *et al*., 2022; Hu, P. H., *et al*., 2021; Koshmin, A. N., *et al*., 2021; Rajendran, N., 2021; Xu, G. L., *et al*., 2021; Liang, D., *et al*., 2020; Smythe, S. A., *et al*., 2020; Chen, Y., *et al*., 2019; Zinov'ev, A. V., *et al*., 2019; Hu, J., *et al*., 2017; Yuan, Y., *et al*., 2017).

Compared with the other SPD processes, the Conform process is more effective and efficient in energy and material utilization, high extrusion ratio, no pre-heating, no post-heat treatment, high homogeneity, infinite length, high dimensional accuracy, the dynamic aging, continuous profiles of extrudate and improved metallurgical and mechanical properties (Dalan, F. C., *et al*., 2022; Shen, Z., *et al*., 2022; Lu, R., *et al*., 2021; Xu, G. L., *et al*., 2021; Liang, D., *et al*., 2020; Purcek, G., *et al*., 2020; Chen, Y., *et al*., 2019; Hu, J., *et al*., 2019; Pan, H., *et al*., 2019; Zinov'ev, A. V., *et al*., 2019; Hu, J., *et al*., 2017; Yuan, Y., *et al*., 2017). As the demands of continuous profiles of products for various engineering applications are increasing day by day.

1.2. Continuous Extrusion Forming

The Continuous Extrusion Forming (CONFORM/CE) process was invented in the 1970s by Green (Green D., 1972) in the British Atomic Energy Authority (UKAEA) Springfield Laboratory, is taken as a pioneering and revolutionary in non-ferrous metal deformation. The CE process and elements are illustrated in Fig. 1. Conform extrusion wheel, shoe, coining wheel, abutment, extrusion chamber, and Conform extrusion die are the main constituent elements of a CE machine. One of the critical parts of the die set is the extrusion shoe, which encloses the groove and houses the extrusion die. It also separates tooling segments and the abutment. A revolving extrusion wheel with a circumferential groove and a coining wheel are in continuous rotation; however, all the other members are relatively stationary during operation (Bazan, D. A., *et al*., 2022).

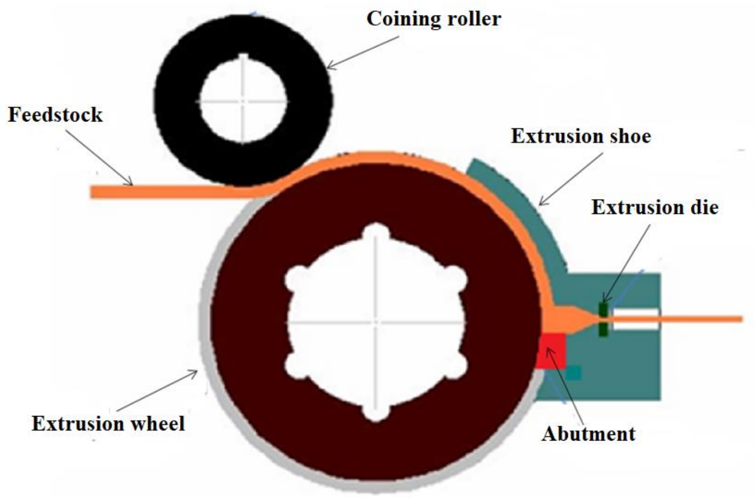

FIGURE 1. 1: SCHEMATIC DIAGRAM OF CONTINUOUS EXTRUSION

In the present scenario, CE process is becoming popularity in manufacturing industries and research community due to its specific advantages. This process can produce significantly long continuous extrudates of various sectional profiles which are hard to produce through the standard extrusion processes because of their process limitations. The CE process requires no pre- and post-heating of the feedstock (Pan, H., *et al*., 2019).

CE is also an efficient method for breaking down processing of as cast grain structure and transform into uniaxial and ultra-fine-grained one in a single pass. Because of the superiority of Continuous Extrusion and its impact on the current forming technology, evident, demands from extrusion industries have been growing rapidly since its first inception (Shen, Z., *et al*., 2022; Lu, R., *et al*., 2021; Xu, G. L., *et al*., 2021; Liang, D., *et al*., 2020; Purcek, G., *et al*., 2020; Chen, Y., *et al*., 2019; Hu, J., *et al*., 2019; Pan, H., *et al*., 2019; Zinov'ev, A. V., *et al*., 2019; Hu, J., *et al*., 2017; Yuan, Y., *et al*., 2017; Green D., 1972) .

The major CE process variables are shown in the Fig. 1.2 below.

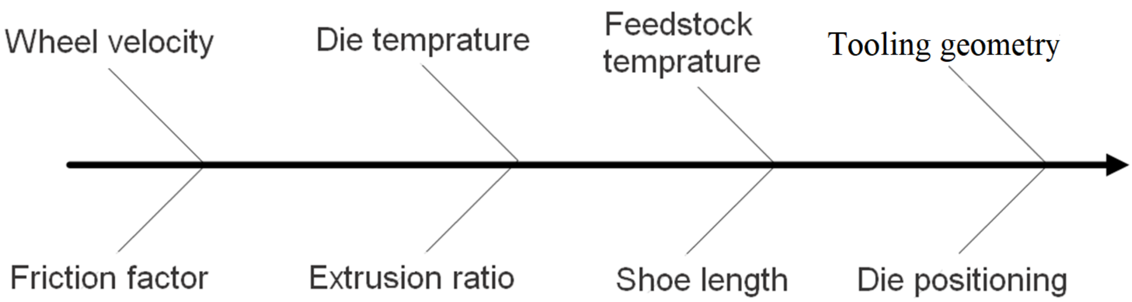

FIGURE 1. 2: PROCESS VARIABLES IN A CONTINUOUS EXTRUSION PROCESS

1.2.1. Principle of CE process

The principle of the CE process involves the frictional force exists between a circular driving extrusion wheel and the feedstock. The feedstock is pushed by means of the wheel and a coining roll to drive down into the groove of the wheel and a close-fitting shoe which encloses the wheel. Inside the shoe an abutment blocks the wheel groove to prevent the feedstock from continuing its passage around the wheel and forces the feedstock material into the extrusion chamber. The material undergoes a high plastic flow state because of the modification in the shear direction at the abutment and the frictional heat also becomes high which leads to a temperature of 500℃ or more, without any external heater. The feedstock material finally leaves the extrusion chamber through extrusion die hole of various profiles and sizes (Bazan, D. A., *et al*., 2022).

1.2.2. Types of continuous extrusion processes

Based on flow-out direction of extrudate with respect to extrusion wheel, the processes can be classified into: radial extrusion and tangential extrusion process. Both processes are shown from Fig. 1.3 to Fig. 1.5 (Katsas, S., *et al.*, 2010; Pardoe, J.A., 1984).

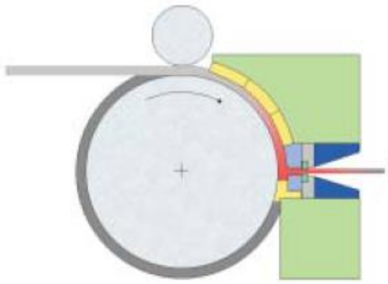

FIGURE 1. 3: RADIAL EXTRUSION

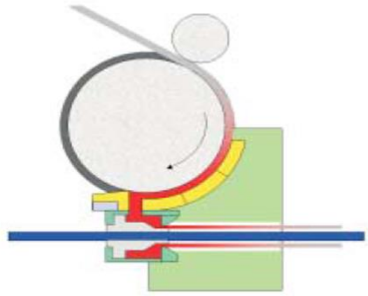

FIGURE 1. 4: TANGENTIAL EXTRUSION

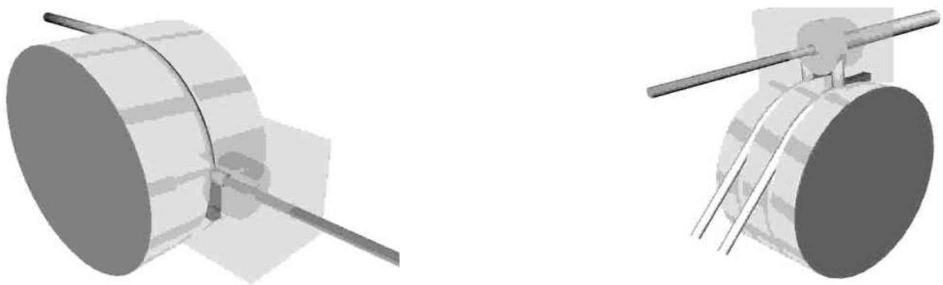

FIGURE 1. 5(a): SINGLE GROOVE RADIAL (b): TWIN GROOVE RADIAL

The flow of direction of extruded material is along radial direction to the extrusion wheel in case of radial Conform process as shown in Fig.1.3 above. In the case of tangential extrusion, the flow direction of extruded material is along tangential direction to the extrusion wheel as shown above in Fig. 1.4. In single groove radial only one feedstock feed in the groove of extrusion wheel whereas in twin groove radial, two feed-stocks feed at a time in the groove of extrusion wheel as shown in Fig. 1.5(a) and Fig. 1.5(b) respectively.

1.2.3. Analysis of the extrusion load in CE process

In extrusion process, it is an essential to know the extrusion load or ranges of loads required which causes plastic deformation and extrude the feed stock material through a die orifice. Therefore, analysis of the dominant input process parameters that can affect the magnitude of the extrusion load is an important issue in conform extrusion process. There are several methods available to analyze the extrusion loads in extrusion process such as slab method (Hu, C., *et al*., 2022; Silberschmidt, V. V., 2020; Cao, F. R., *et al*., 2014; Molaei, S. H., *et al*., 2014; Cao, F. R., *et al*., 2013; XU, M., & DAI Na-Na, Z. Y., 2012; Manninen, T., *et al*., 2006); Uniform–deformation energy method (Hwang, Y. M., & Hwang, T. F., 2002); Slip–line field theory (Silberschmidt, V. V., 2020; Bhaduri, A., 2018; Segal, V., 2018); Upper bound solutions (Silva, J. D., *et al*., 2021; Venkatesh, C., & Venkatesan, R., 2015; Cho, J. R., & Jeong, H., 2001; Kim, Y. H., *et al*., 2000; Wu, C. W., & Hsu, R. Q., 2000; Wood, P. K., 1990).

Among all, UBM is the most popular method which is based on the energy principle. The principle states that the rate of total energy associated with any kinematically admissible velocity field defines an upper bound to the actual rate of total energy required for the deformation. Hence, for a given class of kinematically admissible velocity fields, the velocity field that minimizes the rate of total energy is the lowest upper bound. Here, the kinematically admissible velocity field is used to denote a velocity field that satisfies the incompressibility requirement for a rigid-plastic material and the prescribed velocity boundary conditions. However, the velocity field may be discontinuous on a finite number of imaginary internal surfaces. The general equation for the upper bound theorem used by Hill (Hill, R. O. D. N. E. Y., 1963) for the treatment of constrained plastic deformation is denoted by Eq.1.1. The rate of total energy generally consists of three terms such that:

$$W_t = W_1 + W_2 + W_3 \tag{1.1}$$

Where *W_t: the total internal work done per unit volume per unit t time for a given stage of deformation;*

W_1: The energy (power) required to cause plastic deformation;

W_2: the power (the rate of energy) dissipated associated with internal velocity discontinuity at the velocity discontinuity surfaces;

W_3: the power at tool–workpiece interface or the rate of energy dissipation due to friction between the tool and workpiece

1.2.4. Numerical simulation for analyzing CE process

In modern scenario, there is stiff competition amongst industries to produce quality products at reduced time span and minimum cost. To solve these challenges, numerical simulation-based design developments of manufacturing processes are getting wide popularity. Using numerical and mathematical modeling along with Computer Aid Design

(CAD) system graphics, complex problems can be modeled easily. Simulation gives a clear visualization of how the stress is generated in the billet during the extrusion process. The stress values for various materials and for variation of applied forces can be obtained by merely changing the input variable values such as extrusion wheel speed, feedstock temperature, and friction condition and extrusion ratio. By simulating manufacturing processes, designers and engineers are able to: Reduce the need for costly shop floor trials and redesign of tooling and processes; Improve tool and die design to reduce production and material costs; Shorten lead time in bringing a new product to market.

1.3. Motivation for the Study

There were many extrusion process existed and proved their potentiality and impotence on various ferrous and non-ferrous metals. Even then, the necessity of continuous extrusion had been expanding in many engineering industries due to more advantageous over other processes. Table 1.1 was indicating the comparison of continuous extrusion of process with conventional process.

Table 1. 1: Comparison between conventional extruder and continuous extruder

Points	Conventional Extruder	Continuous Extruder
Feed	Billet	• Coiled rod • Molten metal • powder form
Process	• billet homogenizing needed • intermittent • tooling - big and need preheating • man power at least 6	• not needed • continuous • tooling -big and don’t need preheating • manpower only 4
Cost and productivity	• tooling cost high • power requirement - higher • maintenance cost - high • productivity -lower • product range -higher • tolerance wider	• low • much lower • Low • higher • Lower • Tolerance closer
Product	• product such as ref. tubes & very thin tubes not possible • recovery 75%	• Possible • 85%
Metallurgical properties	• strength -good in all alloys • elongation is good • surface quality good	• Better • good • better

However, analytical, computational and experimental studies on CE had been underway continuously since three decades. Some of the theoretical and numerical studies were still insufficient to analyze accurately the complicated CE process characteristics accordingly. Furthermore, studies on the simultaneous effects of major input process parameters such as wheel velocity, extrusion ratio, friction condition and feed stock temperature on responses such as load were not yet exploited well. Even though it was essential for the optimal design of continuous extrusion processes and operational costs, only few explorations on these parameters were made. In this dissertation work, Non-Ferrous metals like *Al*, *Cu*; and Copper-Zirconium-Chromium were investigated.

1.4. Problem Statement

In the modern industries, there was a huge demand for non-ferrous materials, mainly Al and *Cu* metals and their alloys, which found wide range applications in manufacturing, electrical/electronic, aerospace, automobiles, military, food, agricultural, pharmaceutical optical and other various sectors. However, it was difficult to obtain a material which had excellent mechanical, metallurgical and electrical/electronic and other properties that were of high strength, high strength-weight ratio, outstanding corrosion resistance, high wear resistance, resistance to elevated temperature and mutual exclusive properties such as high strength with high ductility, high strength with high conductivity. Additionally, a product with infinite profile length and better quality, a process with reduced tooling cost, processing cost and low scrap rate were among the challenges facing now a days. A lot of investigations were made by the researchers, scholars and industrialists to consolidate all the above requirements by a single manufacturing process from a single material at a reasonable cost. Among all severe plastic deformation (SPD) metal forming processes and conventional extrusion processes, the CE process provided product of infinite length, complex profile with better quality, better surface quality, and refined grain size, extraordinary combinations of mutual exclusive properties such as high strength and high ductility and high strength and high conductivity are some of the benefits of CE process products. Even though the process had superiority and impact over other methods, it hadn't yet well-exploited on the effects of input process parameters of the conform extrusion on optimized load requirement using optimization tools, microstructural and mechanical properties.

1.5. Objectives of the Dissertation

1.5.1. General objective:

The general objective of the dissertation work was to investigate the effects of the Conform extrusion input process parameters on non-ferrous alloys deformation behaviors and optimize the parameters for optimal responses and requirements.

1.5.2. Specific objectives:

- To determine analytically the extrusion load required for the deformation of non-ferrous alloys such as Aluminum (AA1100), Copper (C101) and Copper-Chromium-Zirconium (C18150) alloy in CE process.
- To investigate the effects of various input Conform process parameters (such as wheel velocity, extrusion ratio, feed stock temperature, friction condition and die temperature) on the load effect, effective stress-effect, and damage effects on nonferrous alloys such as *Al*, *Cu* and *Cu-Cr-Zr* through Deform-3D FE simulations technique.
- To propose the optimal values of input process parameters that can lead to optimal power consumption through RSM, ANN and GA.
- To investigate the effect of CE input process parameters on the extrudates produced through experimentation on microstructural and mechanical properties using tensile tests, hardness tests and wear tests along with microstructural analysis on pre and post deformation of *Al*, *Cu* and *Cu-Cr-Zr* alloy and validate load requirement through experimentation.

1.6. Scope of the Study

The proposed materials were for non-ferrous alloys such as Aluminum (AA1100), Copper (C101) and Copper-Zirconium-Chromium (C18150) alloy feedstock material to investigate through CE process. Additionally the methodologies suggested to explore the deformation load requirement for non-ferrous alloys are analytical, numerical and experimental methods. The theoretical modeling technique to determine the total extrusion load analytically was through Upper Bound Method. The numerical modeling of the work was proposed through DEFORM-3D finite element analysis simulation tool. The optimum values of process parameters were also investigated through RSM, ANN and GA. The experimentation of the feedstock materials investigated through continuous forming process on commercial setup followed by characterization of products pre and post deformation.

1.7. Significance of Study

The finding of the study is expected to help researchers and industrialists in the area of metal forming process especially in continuous extrusion. The optimum results of the proposed work will benefit many industries: automobile industry, aerospace industry, electrical-electronics industries where non–ferrous materials are in huge demand.

CHAPTER 2: LITERATURE REVIEW

2.1. Introduction

In extrusion process (EP), the reduction of a cross-section of billet material is achieved by forcing it to pass through a die. The process is performed under hot and cold conditions. Moreover, the hot extrusion process has a better feature to shape the product in the required shape than the cold working process (Bhaduri, A., 2018). In a single operation, getting the expected extrudate shape is the most important aspect of this process. Based on the design and shape of the die profile, different geometric profile products of solid, tubes, rods, bars, and various sections, can be manufactured (Kumari, S., *et al*., 2015).

The working principle of this process on various metals and their alloys is similar other than deformation conditions. Every material has its deformation limitation during the process, which leads to specific extrusion technology requirements with different process parameters. The process parameters include billet material conditions, workability, billet temperature, process conditions, ram speed, reduction ratio, pressure, etc., (Yadav, R. R., *et al*., 2018; Valberg, H. S., 2010). Most of these process parameters are interrelated with each other. Among all, the most significant parameter is extrusion temperature.

Due to this, analyzing the thermal and mechanical response of the billet material during the deformation is very critical. From the deformation analysis, optimization of the process is inevitable. From the reported studies on Al and Cu thermo-mechanical behavior significant during the extrusion was noted (Halmos, G. T. *et al*., 2005). A similar phenomenon is applied to various metals under different operating temperature ranges. For example, 300-600°C temperature range for Al and Mg; 600-1000°C range for Cu, Ti, Zr, Be, and U; and 1000°C for Ni and steel.

As per the deformation process, the extrusion process is classified under "compressive deformation". Also, extrusion is indicated in DIN 8582 and 8583 German standards. The variation in axial principal stress during the extrusion process is represented in Fig. 2.1 schematically. By this nature, high stains reach without fracture in the workpiece. The principal stress order as per their magnitude and impact is notified in equation 2.1.

However, the influence of mean stress (equation 2.2) on workability increases by increasing and vice versa.

$$\sigma_1 > \sigma_2 > \sigma_3 \quad (2.1)$$

$$\sigma_m = \frac{(\sigma_1 + \sigma_{12} + \sigma_3)}{3} \quad (2.2)$$

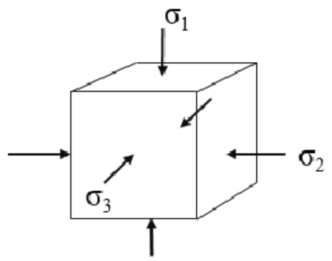

FIGURE 2. 1: VARIATION OF AXIAL STRESS FOR EXTRUSION

Extrusion is one of the continuous solid-state deformation processes which compete with roll forming, drawing, and hydroforming. The extrudates are used in automotive, manufacturing, aerospace, and construction industries, etc., (Peris, R. G., 2007).

2.2. Classifications and Comparison of Extrusion Processes

Based on the working principle and phenomenon, the extrusion process is categorized as direct (forward) extrusion, indirect (backward) extrusion, impact extrusion, and hydrostatic extrusion based on the material flow (Yadav, R. R., *et al*., 2018). Direct extrusion is the most used process among all (Valberg, H. S., 2010). Other than metal flow, the extrusion process is also classified as a hot process, cold process, and co-extrusion process. However, the equipment, operating conditions, tools, etc., are differing in different processes.

2.2.1. Extrusion process under hot condition

This process is the most successful process used in most industries; this process is carried out at $0.6T_m$ (melting temperature) of corresponding metals. During the hot extrusion process, either lubricated or non-lubricated is used. For non-ferrous metals like Aluminum alloys, a non-lubricated extrusion process is used whereas for Copper Alloys, Titanium and Steel are lubricated (Peris, R. G., 2007). During the process, due to deformation temperature, stresses, and strain rate decrease (Wagiman, A., *et al*., 2020; ASTM, B., 2005).

2.2.2. Extrusion process under cold condition

The cold extrusion process is another important process used in many industries for non-ferrous metals. At the beginning of the process, a base billet material is at ambient temperature. The most typical mechanism is punch movement with high pressure by keeping the billet partially or completely closed in a fixed die. From this process also *Al* and its alloys, *Cu* and its alloys, and steels and its alloys can be extruded. In comparison with the hot process, precision in dimensions, better surface finish, oxide layers, more productivity, and low costs are seen in the cold process (Wagiman, A., *et al*., 2020). Whereas, lubrication cost, heavy loads, less deformation, and limited shape complexity are the drawbacks (Peris, R. G., 2007).

Similar manner, other extrusion processes like impact extrusion mechanism are similar to cold extrusion and backward extrusion process. This process is highly suitable for making thin wall tubular sections that are made from non-ferrous alloy (Karamış, M. B., and Nair, 2008). In the case of the hydrostatic extrusion process, for work-piece deformation, pressure is supplied through a fluid. This process is also performed at ambient conditions like impact extrusion and used for ductile and brittle materials. The major limitations of the processes are operational maintenance and complex mechanism, by which industries were, limited their usage (Bhaduri, A., 2018; Peris, R. G., 2007). Another popular process is co-extrusion used to form an integral product of two or more metals. The core and sleeve deformation take place simultaneously at an appropriate temperature to form an interfacial bond. This has applications in multi-filamentary superconductors and ceramic composite precursors. There are many more studies that are expected to understand in a better manner about this process. Still, this process is in the development stage due to its limited usage in the industry. The most suitable materials for extrusion are *Al* and its alloys. The available *Al* alloys are 1xxx, 2xxx, 3xxx, 5xxx, 6xxx, 7xxx, and 8xxx used for extrusion. Among all *Al* alloys, 2xxx and 7xxx are high-strength aluminum alloys thus they are relatively difficult to deform (extrude) (Peris, R. G., 2007).

Similar extrusion behavior is observed in the *Mg* and its alloys. While high-density materials such as *Pb* and *Sn* are easy to extrude in all conditions. The most commonly used materials in the industry are *Pb, Al, Mg,* and *Cu.* The majority of the extrudates are wires, rods, and bars. The major applications of these extruded materials are for electrical wires, cables, pipes, tubes, connectors, etc. (Zeng, Z., *et al*., 2019, Bhaduri, A., 2018). For high melting point materials like steel, Titanium alloys, and Nickel alloys hot extrusion process is highly recommended with lubricant conditions to avoid wear in tooling. While the metal powders based on their characteristics are extruded by the cold and hot process (Peris, R. G., 2007).

The feasibility study of the recently developed materials (metal matrix composites, metal powders, inter-metallics, etc.) extrusion behavior had been investigated through experiments and numerical simulations and followed by the optimization. From the simulation results, it revealed the material behavior during the extrusion, by which the extrusion process was optimized for die design, and process parameters (Park, N., *et al*., 2021; Fang, G., *et al*., 2009; Karamış, M. B., and Nair, 2008).

The forming analysis of various metallic materials and their applications in real time is to be improved. The existing extrusion techniques have to be improved with their technology for production. The improved technology should provide a homogeneous microstructure, stronger, and light in the extruded product, and consecutively economically admissible technological solutions. This leads to new extrusion process (Continuous extrusion (e.g. Extrolling, Linex, Conform)) elaboration including the special extrusion processes (Hydrostatic extrusion, Explosive extrusion, Extrusion with liquid phase, and Isothermal extrusion) (Gronostajski, Z., *et al*., 2019).

2.3. Conform Extrusion Process

The Continuous forming extrusion also called Conform extrusion is a unique technology of continuous metal extrusion process. This process was developed by Green in the UK Atomic Energy Authority in the 1970s as an alternative recycling method for used and scrap electrical wiring of Copper and aluminum electrical conductors and was commercialized in (He, Y. L., *et al*., 2012; Etherington, C., 1974). Since then the process has been developed rapidly, both in machine design and in operating techniques since its first inception (Belyaev, S. V., *et al*., 2022; Cho, J. R., and Jeong, H., 2000) it has been established as a commercially feasible and viable extrusion technological method to particularly beneficial to processes non-ferrous metals and alloys of lower-strength materials such as aluminum, copper, magnesium and other alloys. Therefore it has become one of the most widespread, burgeoning, and environmentally friendly manufacturing technology (Yun, X., *et al*., 2016).

The CE machine has constituent elements in its complete setup (Fig 2.2 and 2.3). In the CONFORM extrusion process, an extrusion driving wheel and a pivoted CE shoe are the main components of the CE machine tooling. The driving wheel and the coining wheel are rotating at a constant speed (RPM) whereas the other CE machine toolings and components are stationary (Cho, J. R., and Jeong, H., 2000). The extrusion wheel has a single or multiple circumferential grooves along its periphery which accepts the feedstock and transfer the feedstock to the extrusion zone. This feedstock under friction grip conditions pushed into the driving wheel groove by a pressing roller and supplied in the form of a continuous feed rod. During the extrusion process, the extrusion wheel with a circular groove formed on its circumference. A driving extrusion wheel drives the feed metal to the deformation zone which is encircled by the driving wheel groove, a pivoted stationary shoe, and an abutment. The pivoted stationary shoe overlaps a sector of the extrusion wheel peripheral (circumferential) surface and also combines the other tooling. The position of the tooling concerning the groove forms a chamber (or 'mini-extrusion container') into which the feed is drawn by the frictional grip. The abutment protrudes further to the extrusion groove root to halt the rotational motion of the feed metal and develop an 'upset zone' in front of the extrusion chamber to deform the material plastically. The deforming metal flows into the extrusion chamber to be extruded through the die (Khawaja, K., *et al*., 2005).

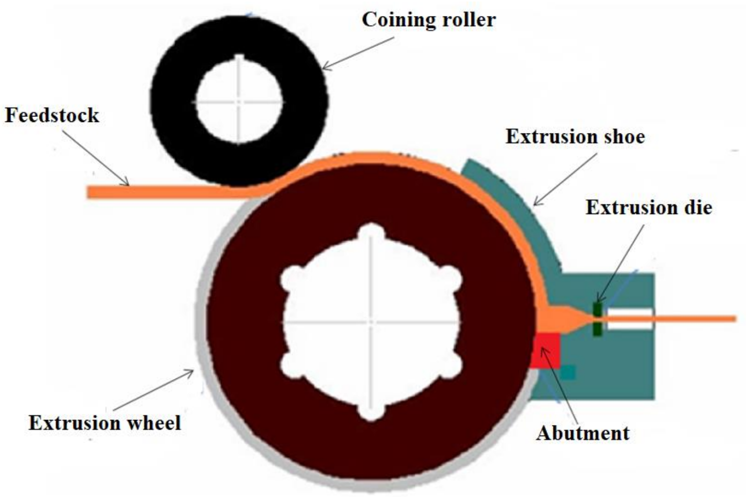

FIGURE 2. 2: CONFORM PROCESS SCHEMATIC VIEW

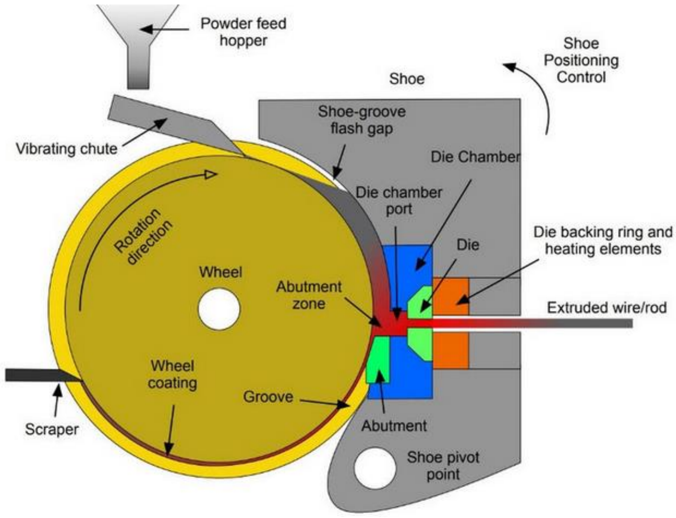

FIGURE 2. 3: CONFORM PROCESS POWDER AS A FEED (Smythe, S. A., *et al*., 2020)

A die chamber, carrying the appropriate die, is supported in a shoe. The extrusion die chamber integrates an abutment that projects into the wheel groove and stalls the material passage. This generates adequate pressure to form an extrudate. The feed metal is in the flow stress state before entering into extrusion chamber and forms a "seal" in the regions among the driving wheel, the stationary shoe, and the abutment (Khawaja, K., *et al*., 2005). The extrusion die of the CE has influenced the productivity of the extrusion process. There are different die materials available; however H13-tungsten steel; H13 and H10 are the most commonly used die materials for the CE process. They are arranged from the highest level to the lowest one in terms of productivity and service life (Yousif, A., *et al*., 2016).

The rotation of the driving wheel pushes a bar billet or scrap or powder or molten metal into the wheel grove ,extrusion chamber and die opening in which it experiences high shear deformation and compressive stresses by which the billet gets heat and extrusion takes place without any pre-heating (Zinov'ev, A. V., *et al*., 2019). Similar to shear, rolling, and conventional extrusion and the workpiece experiences a series of severe plastic deformations in CONFORM extrusion process when the feed metal is driven by the driving extrusion wheel (He, Y. L., *et al*., 2012). The extrusion die of the CE has influenced the productivity of the extrusion process. There are different die materials available; however H13-tungsten steel; H13 and H10 are the most commonly used die materials for the CE process. They are arranged from the highest level to the lowest one in terms of productivity and service life (Yousif, A., *et al*., 2016).

Within the upset length, in front of the die, the compressive stress was 1000MNm^{-2}, and temperatures were 350-450°C (within the range and above the recrystallization temperature for aluminum which is 340° to 400°C (Monteiro, W. A., 2014), and deformation zone temperature of the copper alloy was 450–600°C for copper (which is above the recrystallization temperature for copper and its alloys) (Zinov'ev, A. V., *et al*., 2019). Preheating the feedstock is not generally required.

For producing UFG or nanostructured (NS) materials, high shear deformation is imposed due to severe plastic deformation (SPD) in the metal-forming process (Faraji, G., & Torabzadeh, H., 2019). A similar shear deformation mechanism was found in the CONFORM process like ECAP (Valiev, R. Z., *et al*., 2022; Zemko, M., *et al*., 2013).

In one continuous cycle of conforming extrusion process, it combines cycle rolling, pressing, and heat treatment (Sidelnikov, S. R., *et al*., 2015). By generating a large amount of heat through friction-assisted deformation, CE reduces the occurrence of severe shear deformation. Consequently, the refinement of grain and improvement in the material property was noted (Yun, X. B., *et al*., 2013). This demonstrates the potential application of CONFORM to manufacture fine-grained metals for superplastic performances. Substantial grain refinement (~2µm) was attained from cast rods of grain size ~150µm in a single extrusion process (He, Y., *et al*., 2010).

Ultra-fine-grain structures (10-20µm) can be achieved through the CONFORM extrusion process by breaking down the course grain ones in a solo pass or multiple passes (Murashkin, M., *et al*., 2015; Cao, F. R., *et al*., 2014; Zhang, H., *et al*., 2013; Xu, C., *et al*., 2010). The material properties are achieved by SPD and rapid heating generated from material conformation (Tressia, G., *et al*., 2018). The microstructural and mechanical properties (such as hardness and strength) of the extrudates of the conform extrusion have been improved because of the effects of the process characteristics. Conform process prominently improves mechanical properties such as the hardness and ultimate tensile strength of the extrudate with little or no scarification of a percentage of elongation on certain materials. On certain metals and alloys, tensile elongation of about 200% was also achieved at 473K using the extruded sample (Mertová, K., *et al*., 2020; Lin, G. Y., *et al*., 2019; Sinha, D. K., *et al*., 2018; Song, L., *et al*., 2013; Zemko, M., *et al*., 2013; He, Y. L., *et al*., 2012; Ying, Z. H., *et al*., 2012; Valiev, R., *et al*., 2006; Valiev, R., 2004).

Continuous forming extrusion technology has many excellence and advantages over conventional extrusion and other SPD processes and product characteristics. Compared to others, the CONFORM process provides better features. Some of the conform process and product characteristics are the process involves lower capital investment, less physical space for machinery installation, lower installation and maintenance costs, as the process generates temperatures up to 500℃, pre-heating and post-mechanical treatment are not required which substantially reduces energy consumption irrespective of the feedstock materials (Ying, Z. H., *et al*., 2012). High extrusion ratio, runs without lubrication, higher production efficiency in terms of labor, energy, and raw materials, high automation as the process is characterized by computerized intelligent control, only two operators control the production line, lower energy consumption, lower production cost, low material consumption as the process scrap levels are low to less than 1%, better economic efficiency over conventional methods while manufacturing bar (on average 20%). Additionally, the extrudates also have unlimited length, various sectional shapes and profiles with a high degree of accuracy and high complexity, ultra-long seamless products, ultra-fine grain size, and higher homogeneity, and improved physical, mechanical and technological properties of the extrudate due to higher grain refinement and bulk dislocation density, higher production rates. Less scrape for aluminum and copper extrudes, presented yield up to 95% in the first pass and above correspondingly (Tressia, G., *et al*., 2018; Rajendran, N., *et al*., 2017; He, Y. L., *et al*., 2012; Khawaja, K., *et al*., 2004). The process also permits the manufacturing of solid, hollow, and cord products of continuous extrudates of diverse profiles and functions. Refined grain structured extrudates from a cast (un-deformed) billet (800–1000µm) to 50–35µm (Valiev, R. Z., *et al*., 2022; Edalati, K., *et al*., 2019; Zinov'ev, A. V., *et al*., 2019; Song, L., *et al*., 2013; He, Y. L., *et al*., 2012).

Despite its outstanding advantages the CONFORM process, the product suffers excessive heat generation, process defects, curling phenomenon, and surface separation. The numerical analyses were performed to investigate the quantity of heat generated through friction force and the imposed high strains (Cho, J. R., & Jeong, H., 2003).

Various feedstock materials have been investigated and industrialized using the conform processes. Some of the wide range of non-ferrous metals and alloys processed by CE are aluminum alloys such as pure aluminum, Al6600, Al–Mn alloys Al–Mg–Si alloy; copper alloys such as pure Cu, Cu-Mg, Cu-Mn, Brass, brazing alloys, Cu-Cr, Cu-Cr-Zr;

zinc; calcium; lead, precious metals; solders, and magnesium. Particulate materials such as Al-Cu, and Al-Zn powders, fiber-reinforced (C and SiC) aluminum alloys also CE extruded. Co-extrusion and cladding of two or more feed metals (materials) are also done to manufacture coaxial cables for cable TV and aluminum-clad with steel wire and the core metal respectively (Lu, R., *et al*., 2021; Hu, J., *et al*., 2019; Lin , G. Y., *et al*., 2019; Pan, H., *et al*., 2019; Rajendran, N., *et al*., 2017; Kumari, S., *et al*., 2015; Zhang, H., *et al*., 2013; He, Y. L., *et al*., 2012; Karamış, M. B., & Nair, 2008).

The feedstock material may be fed as coiled rods, continuously cast, molten metal (Castex) directly from melting furnaces, granules, powders materials, or clean scrap (Rajendran, N., *et al*., 2017; Cao, F. R., *et al*., 1999). The continuous forming process has been quickly stretched to enable the continuous re-forming of rod feedstock into new profiles, with solid rod feedstock dominating current commercial setups. Since the feed metal is frequently supplied as a long continuously cast coil, welding between the 'billets' is not needed. A metallic material of any morphology provided that it can be fed into a suitably sized groove, the CE process can work.

Extrudates produced by the CE are widely used in different engineering applications such as electrical/electronic engineering, vehicle engineering, construction sectors, and machine manufacturing. Electrical engineering uses the extrudates to manufacture transformers, big and middle-sized electric motors, DC electric commutators, contact wires for electric locomotive rail way, high-low voltage switch and switching devices, heat-transfer tubes, the evaporator and condenser units of refrigerators, round refrigeration multiport and air conditioners, transformer, electrical conductors, architectural and decorative sections, lightning conductor, superconductor, shaped tubes, magnet wire, heat sinks, switch gear, custom profiles electric appliance, and so on (Zinov'ev, A. V., *et al*., 2019; Cho, J. R., & Jeong, H., 2003; Kim, Y. H., *et al*., 2000).

These shapes then continue to be cooled and dried before being cut or coiled as required. There are three typical extrusion ways: single groove single wheel, twin groove single wheel, and single groove twin wheel. Based on different extrusion ways, there are different die design ways. Advanced die manufacturing can improve production efficiency and product quality.

2.3.1. Principle and mechanics of Conform extrusion process

2.3.1.1. Extrusion principle through dragging

A stationary bottom platen is equipped with a die with a hole. The top platen having a square groove is mounted over the bottom platen. The latter is made to slide toward the die. Therefore friction factor and frictional force from the three sides of the moving top platen groove drag the feed rod towards the die as shown in Fig. 2.4.

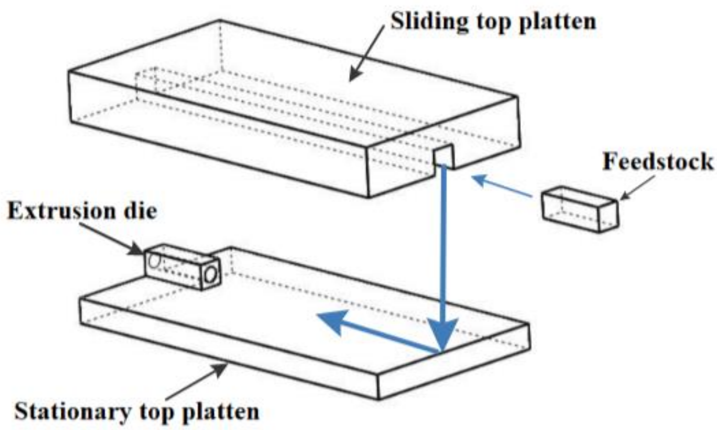

FIGURE 2. 4: SCHEMATIC EXTRUSION BY DRAG

2.3.1.2. Extrusion principle for Conform process

The basic principle of the Conform process is based on the friction factor which exists between a feedstock material (billet) and the driving wheel peripheral groove and the shoe. If the groove with three sides in a cross-section out of a rectangular developed on the sliding platen in Fig. 2.4 is replaced with a groove in a rotating extrusion wheel, the fourth side with the die on the bottom platen is also replaced by a stationary shoe fitting against the outside periphery of the wheel, then the rotation of the extrusion wheel will transport the feedstock along its periphery. If a stop in the wheel grove is put, the metal collides with the stop (abutment) from upsetting reaches to flow states and moves through a die orifice fixed to the shoe.

The Conform process works based on the principle of heating the feed-stock metal through friction. The frictional force (factor) that arises between the feedstock and the driving wheel is the main cause of the process. The total frictional force developed among the feedstock, the wheel groove, and the stationary shoe must overcome not only the power required for to cause plastic deformation but also to compensate the energy loss due to frictional resistance arising between the feedstock and the stationary toolings, especially in the die chamber; and velocity discontinuities during the extrusion process. The friction force creates a substantial amount of heat and pressure to continuously extrude the feedstock material through an extrusion die office. Figure 2.5 depicts the working principle of CE forming with all details of tools.

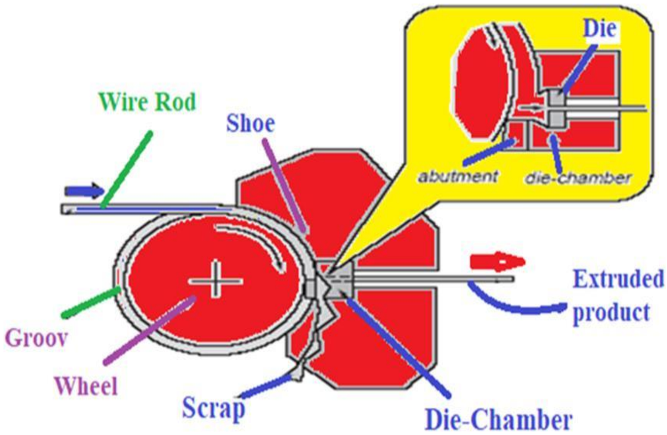

FIGURE 2. 5: SCHEMATIC REPRESENTATION OF PRINCIPLE OF CE PROCESS

The working principle (power) of CE is the frictional grip developed between the feedstock and the driving wheel. The driving wheel continuously rotates and is used as the driving force in the process. Initially, the feed metal is dragged and pushed forward in CE purely by frictional forces. In the process, the feedstock is baited and fed into the profiled circumferential groove of the extrusion wheel and the groove of a closely fitted shoe using the extrusion wheel and a coining wheel. This pushing continues until the stock continuing passage around the wheel is stopped by the fixed abutment, a unit that protrudes and fits into the wheel groove causes changes in the flow directly into the extrusion die chamber cavity leading, were upsetting as well as deformation stress of the feedstock reaches to its flow stress. The friction creates a substantial amount of heat and pressure to cause feedstock to reach a deformation temperature (plastic state), softening, allowing it to bond together, and finally extruding radially into the extrusion chamber to pass through an extrusion die orifice of desired shapes. The process permits an infinite length of extrudates to be manufactured for continuously fed blanks and welding phases of the billets are not required (Shen, Z., *et al*., 2022; Faraji, G., & Torabzadeh, H., 2019; Lu, L. P., *et al*., 2010; Wu, P. Y., *et al*., 2007; Barcellona, A., *et al*., 2000).

2.3.2. Conform extrusion process design and parameters impact

The CE process intends to extrude different products from non-ferrous metals and alloys leading to a huge industrial application (Pan, H., *et al*., 2019). The nature of the process in the current stage passed through many design modifications which increased process parameters. However, the design considerations are to be optimized on the load/force analysis, energy saving aspects, and power calculations by considering the type of materials and geometry of extruding. Cho, J. R., & Jeong, H. (2003), investigated the influences of the extrusion wheel diameter of a continuous forming process on the surface separation and the curling phenomenon numerically. For numerical experiments, AA1000 was considered as exudates by changing the wheel diameters (300, 400, and 600mm) and extrusion ratios (1.0, 2.0, 2.1, and 2.2). Based on their investigation, the surface separation increases proportionally to the wheel diameter (increases linearly) however the curling is not affected. Previous investigation has revealed that the visco-plastic behavior of alloys in the region of the abutment and extrusion die in continuous forming extrusion results in flow behavior similar to that of fluid in a pipe (Smythe, S. A., *et al*., 2020).

Kim, Y. H., *et al*. (2000) used the UBM to derive an equation for calculating the powers required in the steady-state continuous forming process. The theoretical result and possible similarity were verified using a commercial computation method DEFORM program simulations. It was also observed that the extrusion powers decreased as the extrusion ratio rose. Aluminum (Al-1100) of yield stress 60MPa was used as the feedstock material. Khawaja, K., *et al*. (2004) developed and installed a gap sensing system for continuous extrusion machinery to maintain an accurate pre-defined extrusion gap and product quality.

Ying, Z. H., *et al*. (2012) analyzed the influence of extrusion wheel velocity and flow passage length in the die cavity on the shape of aluminum sheath computationally and validated the results experimentally. Their findings showed that the length of the flow passage had influenced on uniformity of the cross-section of the sheath when the length increased the sheath tended to be uniform. Moreover, the wheel speed had negligible influences on the bending shape and cross-section upon using a larger flow passage. Sinha Sinha, D. K., *et al*. (2012) designed and fabricated a continuous extrusion machine setup using virtual computer-aided design and manufacturing concepts. The machine setup has been developed to explore the continuous extrusion process in detail for nonferrous alloys. Kubina, T., *et al*. (2015) investigated the effects of the combined process of conform and the ECAP method on the microstructural sizes of a 10mm diameter of titanium bar. They examined the effects of continuous forming extrusion set-up parameters on the resulting microstructure of Ti wire on the first pass in their pilot experiment. Based on their investigation, the die chamber temperature was the process critical parameter. They varied it from 500°C to the final one of 350°C. At the die chamber temperature of 350°C, the 1.4μm grain size which was the finest was achieved.

Zemko, M., *et al*. (2013) developed a set of CONFORM processes and ECAP methods to enhance the production efficiency of sections. They studied the effects of the die chamber temperature of the continuous forming machine and the number of repeated passes on the microstructure of CP Ti grade 2bars of a 10mm diameter. The die chamber temperature varied from the initial temperature of 500°C to the final 200°C. Based on their finding the smallest grain size was achieved at two passes at 200°C. The die chamber temperature had the strongest influence on mean grain size to be the smallest in mean grain size of 310nm.

Li, B., *et al*. (2014) investigated two kinds of forming channel shapes during conform extrusion on grain size and properties of brass rod billet. The flow characteristics of the billet were investigated based on CONFORM process. Based on their investigations, in a round-table-shaped channel, the billet flow velocity was non-uniform, and the extrudate had a circular microstructure, which made the performance and microstructure of the extrudate became uneven. However, during conform extrusion the table cone-shaped channel gave uniform grain sizes and outstanding properties over the round-table-shaped one.

Yun, X., *et al*. (2015) proposed to CONFORM extrusion and rolling technology for strip production using DEFORM-3D simulation software. They analyzed the effect of the driving wheel speed and the strip size on both processes. The hot rolling process had done by using the surplus heat of the conform process. Experimentation was carried out using the optimized results of computational simulation. Yousif, A., *et al*. (2016) considered the influence of die materials and their hardness on tool life and productivity in the productivity of copper strips using a hot CONFORM extrusion process. They considered two different grade tool steels H10 and H13 with three hardness different values of HRC40, HRC56, and HRC60. Based on their findings H13 tool steel with the highest hardness has become the best choice for extrusion die material with respect to tool life and productivity. Rahim, S. N., *et al*. (2016) predicted the speed of extrusion and temperature during the hot extrusion of 6061 aluminum alloy chips by modeling the process using Deform 3D by considering the effects of input processes parameters such as extrusion die angle, pre-heat temperature, pre-heat time, and ram speed and output responses such as flow stress and heat distribution. The investigation focused on improving the Ram speed and pre-heating temperature which involve the amount of heat generation and the amount of heat loss to the tooling and made insufficient quality bonding. The outcomes of the simulations were compared as well as confirmed successfully the results were obtained experimentally.

Yun, X., *et al*. (2017) considered the influence of feedstock preheating temperature of Al-Sr alloy upon microstructural and mechanical properties of the extrudate processes through Conform. Based on the numerical simulation result, the temperature raised after the feedstock material entered into the cavity during the process, and the temperature became maximum at the die exit. In the die cavity, the material was subjected to higher temperatures significantly above its recrystallization temperature (from 483°C to 512°C). Additionally, the maximum equivalent stress was observed in the right angle bending zone. The experimental results showed that the alloy phase morphology had changed from granular to blocky and increased grain size. The tensile strength of the alloy reduces even though its elongation increases.

Smythe, S. A., *et al*. (2020) converted titanium alloy swarf produced during forged billet machining in the aerospace sector into wire by using the Conform process. The machining process produces up to 95 % swarf. Based on their achievement, close to 100% of the waste powder was converted to the wire using conventional wiredrawing equipment, and wire samples were further cold-drawn down to 40% reduction. Therefore this process offers an eye-catching addition to the circular economy for manufacturers and more viable supply chains. Ying, Z. H. *et al*. (2021) considered the effects of extrusion wheel RPM on micro-morphology and weldment properties of 6063 Al alloy through microstructural observation, tensile test, and SEM analyses. During conform extrusion, welded joints were made at the union of two billets and were analyzed through finite element simulation. The outcome of the investigation showed that the oxide layer of the billets during conform extrusion had affected the metal welding significantly. The extent of breakage on the welded joint increased as the effective strain rate increased with increasing extrusion velocity. As the speed increased high temperature was induced in the billets which led to the formation of increased coalescence a portion of the weld seam lines disappeared slowly and the fraction of the welding interface that failed to reach metallurgical coalescence was also gradually minimized. Based on their investigation as the extrusion speed increased UTS and the percentage of elongation the weldment increased.

2.3.3. Analytical analysis of Conform extrusion process

The significance level of the CE process at the industry level has increased. Detailed CE experimental investigation on non-ferrous metals and their alloys is expensive in initial investment and processing costs. Therefore, analytical methods can help to predict the responses by minimizing extensive experiments and associated costs. Some of the literature covers the analytical studies of the CE process. Green was the first person known to formulate analytical model to predict the maximum extrusion load necessary using the upper bound energy method (UBEM) for tangential and radial continuous forming extrusion (Green D., 1972). Etherington, C. (1974) subsequently extended the model using UBEM. Tirosh, J., et al. (1979) performed an analytical as well as an experimental investigation of the continuous forming extrusion process. According to them, the load necessary for CE extruding was the frictional shear force produced by a rotating extrusion wheel against the feed metal. They also developed mathematical equations to predict the extruding force as well as the power needed to extrude an infinite length of extrudate by considering the optimal condition. The analytical expressions were validated by experimental results with an acceptable agreement. Wood, P. K. (1990) developed mathematical expressions regarding mechanics of Conform extrusion and validate the formulation with experiment. Peng, D. S., *et al*. (1992) developed equipment for experimental simulation of the process and studied the deformation behavior of metals in the process. The force of friction was taken as the driving force that causes plastic deformation and extrudes the metal through the die. During their investigation, a Moiré method was implemented to simulate the plastic flow of metal. In the plastic deformation zone powerful internal shear band exists. Thus, the existence of the internal shear band not only diminishes inhomogeneity in the plastic deformation zone but also improves the attainable level of material plastic deformation.

Kim, Y. H., *et al*. (1998) studied the responses of several CE-independent process variables on the outputs, such as material flow, temperature, and effective strain distributions through a commercial DEFORM simulation tool and FEM code. They concluded that since many parameters are governing the CE process, it is un-easy to take an optimal combination of independent process parameters. They carried out numerous computational investigations and consequently, based on their parametric findings they suggested a qualitative guide for the optimal CE process responses. Lu, J., *et al*. (1998) developed a mathematical expression for the CE process. It enabled us to estimate the temperature distribution in the temperature field and, stress, strain, and strain–rate distributions in their corresponding fields in the workpiece and machine parts. It provided useful awareness to perform an appropriate material selection for tooling, dies, and other moving parts of the CE machine and to optimize its machine design. The numerical results found from the mathematical expression were exceptionally useful to provide guidelines to control and optimize the process. The comprehensive mathematical formulations established by the researchers allow the combination of a phenomenon that may arise due to variations in the standard CE process.

Kim, Y. H., *et al*. (2000) applied the energy method to develop an analytical expression to determine the power needed to extrude in the steady-state continuous forming process. The theoretical result obtained using the UBM was to an acceptable accuracy with the simplified equivalent side extrusion one. It was also verified using a commercial computation method DEFORM program simulations. Based on their findings, the power required decreases as the product diameters decrease. The feed metal used for the investigation was Al-1100 grade aluminum with a 60MPa yield. Cho, J. R., and Jeong, H. (2000) addressed a parametric analysis of the existence of the surface defect in the continuous extrusion process. During the investigation, different input parameters: the extrusion wheel speed, the extrudate diameter, the abutment protruding length, the friction factor, and the size of the flash gap were taken. Numerical experiments were carried out and their effects were also analyzed on the surface defect existence. A DEFORM-3D tool was used for the simulation. Kim, Y. H., *et al*. (2000) addressed the 3D-FEA of the CE process addressed the parametric analysis of the curling occurrence. Additionally, the CE process characteristics are becoming closer to the actual one. They first performed the dynamic analysis of the process flow on the phenomenon and 3D-FEA of the CONFORM process to come to their conclusions.

Katajarinne, T., *et al*. (2019) performed near to realistic 3D–FEM simulations to investigate the formation of flash in the CE process of copper feed metal under different frictional factors working conditions. Wu, P. Y., *et al*. (2007) investigated the CE process for manufacturing a concave bus bar under various extrusion wheel speeds through 3D-FEM technology using DEFORM-3D software. The model employed was a constitutive equation of the rigid-visco-plastic. Under different wheel speeds, linear velocity, stress, strain, and temperature distributions in their corresponding field were investigated and the damage field was also considered. The numerical simulation results showed that when the wheel speed increased the deformation flow velocity in the die orifice increased slowly. However, slippage between the feed metal and the CE wheel was observed with a higher angular velocity of the Conform extrusion wheel. The product effective strain and the effective stress were also increased with wheel angular velocity near the die orifice and close to the abutment than that adjacent to the die orifice respectively. Stress is intense in and around neighboring regions of the flash gap. As the angular velocity of the extrusion wheel increases the product's effective strain also increases gradually. In the process due to the friction factor, deformation takes place as a result the feed metal, tools, and dies temperature increases considerably.

Chen, X., *et al*. (2010) considered the effects of different structure porthole structures on the deformation homogeneity and the flow velocity variances by modeling the continuous forming processes using rigid-plastic FEM based on DEFORM-3D to extrude copper bus-bar. The results revealed that using the stratum form of porthole without a transition plane, the deformation became the most homogeneous and the variance of flow velocity also become the minimum. Manninen, T., *et al*. (2006) investigated the CE process model developed using FEM software. Visco-plastic and thermally coupled material was taken as model one. The abacus/explicit as well as DEFORM-3D tools were used to simulate the CE process. The modeling results depict that considerable internal shearing occurs within the extrusion chamber. Changes in the tool geometry can affect the material flow and process conditions. Streamlined tool designs may facilitate the use of conventional tool steels in the extrusions of copper. Savings in tool material costs can be significant in the long run.

Yun, X., *et al*. (2011) developed a computational model using the FEM-DEFORM-3D simulation tool by taking rigid-plastic material to process copper strips through CE at a large expansion ratio. In the model, some of the structures such as mold, die, expansion chamber, as well as the shape of the billet section, were taken as rigid. The investigations considered the influences of those structures and the billet section shape as input parameters of the CE extrusion on flow velocity uniformity at the center and edges at the calibrating strap. Based on their investigations, compared with the round feedstock material, the flat one with the same cross-section has better uniformity in flow. The mean-square deviation (MSD) of velocity was the mathematical tool used to validate. Their computational model results were validated experimentally.

Cao, F. R., *et al*. (2013) developed an analytical model to predict the deformation force necessary to carry out a conform extrusion processing of Al−5%Ti−1%B alloy using the corresponding force equilibrium equations of the Slab Method. The deformation region of the process was subdivided into five zones: primary gripping, secondary gripping, expansion chamber (conical), cylindrical, and final sizing zone or extrusion die. They developed a formula to predict the deformation force at any wrapping angle in the conical expansion chamber zone. The alloy had been extruded experimentally. The resistance to deformation was measured with the thermal compression simulator Gleeble 1500. Their finding revealed that the radial force obtained by the theoretical formula was in harmony with the experimental CONFORM radial force. Li *et al.* (2013) simulated, analyzed, and established the H62 brass analysis model, based on the rigid visco-plasticity finite element method for the deformation process. The investigation considered and analyzed the billet and die temperature field, equivalent strain field, and equivalent stress field. Based on their findings as the width-thickness ratio increases, die deformation temperature, strain field, billet, and stress field increase numerically. The grain sizes of the extrudate became finer and its distribution was more uniform. As the width-thickness ratio increases, the grain size increases slowly which leads to a decrease in the mechanical properties such as UTS and the percentage of elongation of the alloy.

Yun, X., *et al*. (2016) suggested CE and rolling forming velocity of copper strips. During the investigation, the bite condition was fixed. A compatibility equation of the continuous extrusion process was also developed using the DEFORM-3D computational tool to investigate the relationship between the two processes namely the roll-forming with CE velocity of the feed metal. The computational analysis outcomes were taken to compare with that of the experimental. The compatibility equation of roll-forming and Conform process velocity was verified.

Zemko, M., *et al*. (2013) carried out FEM modeling of the CE to process titanium which is among high-strength metals and verify it experimentally using a commercial setup of a CE forming machine. The simulation work was done by modeling of CE of titanium using the FEM and DEFORM-3D tools. In the computational and experimental analyses of the CE process, the driving wheel temperature, feed metal temperature, and the velocity of the driving wheel were taken as input parameters to investigate their effect on the entire continuous extrusion forming process, especially their effects on temperature distribution and strain fields. The responses from computational methods were then compared to the experimental one obtained from the CE of titanium feed metal. The main objective was to find sufficient boundary conditions to develop a mathematical expression that fits the real-world Conform Extrusion process as near as possible and carry out optimization.

Yun, X., *et al*. (2017) investigated the consequence of feed metal pre-heating temperature on temperature state during the process, mechanical and microstructure proprieties of the extrudates through the CE processing of Al-Sr alloys. The investigation was performed computationally and experimentally. DEFORM-3D numerical tools were applied in the computational investigation to study the temperature state during the process in the computational simulation and experimental investigation. The microstructure and mechanical properties of the alloy were also considered. The computational output revealed that the feed metal temperature starts to rise once the feedstock enters the wheel-shoe cavity during the CE processing and the highest feedstock temperature was observed at the extrusion die exit. Additionally, the extreme equivalent stress happened in the right-angle bending zone. Rajendran *et al.* (2017) developed a FEM model using Deform-3D computational tool to investigate the influence of a CE driving wheel rpm on AA3003 feed metal flow conditions processed through CRE extrusion. Their investigation results showed that an increase in extrusion driving wheel rpm heated the feed metal temperature because of great shear deformation and higher friction factor, which considerably affects the alloy flow conditions at the extrusion die exit. Around one-quarter rotation of the feed stock-extrusion wheel, stable flow conditions are achieved in the Continuous extrusion process. Increasing to sufficiently high RPM of extrusion wheel speed, hot extrusion conditions are attained to cause extrusion of the feedstock through die opening in the CE process, even keeping the feed-stock at room temperature. Around one half the temperature increments is because of shearing occurring in the upset zone, the other one is owing to deformations in the extrusion zone (Valberg, H., *et al*. 2018).

Hu, J., *et al*. (2020) studied the effects of input variables and repetitive passes on the plastic deformation behavior of aluminum alloys, process efficiency, and saving aspects in terms of energy and processing cost using the Conform-HPTE process. They developed a FEM of the Conform-HPTE process to computationally study the plastic deformation performance of the alloys processed under different independent process variables. Based on their finding the Conform-HPTE process successfully generates accumulated large plastic strain after a solo extrusion pass. The CE machine provided driving power to cause shear deformation and heat the feedstock for the succeeding HPTE process. The severe gradient in shear deformation conditions could cause the formation of refined grain microstructure. Hence, this innovative method could be a promising forming technique to generate ultra-fine grain structures through SPD to continuously manufacture advanced engineering materials. Additionally, the process is advantageous from an energy and cost perspective because it has high process efficiency.

2.3.4. Effect of CE input parameters on mechanical and micro-structural behavior of extrudates

The CE-processed rods of non-ferrous materials with different process parameters on mechanical properties and microstructure studies are included in this section. In most of the studies, the mechanical properties were evaluated through tensile and hardness testing. The microstructure analysis was performed under different magnifications using a microscope, SEM, and TEM. The detailed literature is included in the coming paragraphs.

Zhang *et al.* (2008) successfully carried out the CE forming of AZ31 magnesium alloy on a modified commercial Conform deformation machine. Their investigation demonstrated a possibility of the efficient CE processing of the feed metal. The authors compared their modified CE forming method with traditional direct extrusion practice. They concluded that the former can better refine the grain structure, improve the grain structural homogeneity and alter the alignment of the basal plane. Therefore, the CE process improves the formability (ductility) of the alloy but decreases to some extent the alloy UTS. The fracture mechanism of the alloy prepared by both processes was also investigated. Based on their findings mixture of ductile and brittle to the full dimpled rupture were observed. Xu, C., *et al*. (2010) investigated a commercial aluminum alloy of Al-6061grade using hybrids ECAP-Conform manufacturing process to critically estimate the two areas where no information was then available. The first was on the extent of hardness homogeneity within the cross-sectional planes and along the lengths of extrudates rods. The second investigation was a mechanical one conducted to examine the extent of any plastic anisotropy that may exist within the extruded done using ECAP–Conform. Li, B., *et al*. (2017) studied the microstructural evolution of the brass alloy during the entire Conform deformation process. During the CE process, the alloy microstructure was considerably influenced by its formability and properties. Through observation of the microstructure evolution at different regions, the evolution rules of microstructure and properties of Conform extrusion brass alloy were investigated. Based on their findings dynamic recrystallization and hardness evolution occurred at the right-angle bending region of the in-process feed brass alloy. By this, they found that the right-angle bending region was the viable region to control the properties of the extrudate.

He, Y. L., *et al*. (2012) employed the Conform process as an SPD method to refine the grain structure of cast Mg alloys with AZ31 grade. The feedstock material used was Cast Mg-3%Al-1%Zn round bars with a grain size of ~150 microns were refined to ~1micron after the first single pass of CE. Uniaxial mechanical tests were conducted on both as-cast rods and extrudates. Based on their findings CE extrudates had considerable grain size refinement over the cast rods. Additionally up to 200% percentage of elongation was attained. CE is also one of the potential options to manufacture continuous products of Mg alloys in addition to traditional extrusion forging and rolling. Song, L., *et al.* (2013) investigated the microstructure evolution of Cu base alloy during the CE process. Their finding indicated that the CE refines the structure of Cu-Mg alloy by breaking as-cast grains. Dynamic recrystallization happened during deformation because of the relatively high deformation temperature. The process also improved the degree of homogeneity of the structure. Refined structures formed by dislocation reconstruction were obtained due to shear deformations which include broken grains and sub-grains. However, the coarse grains were refined by annealing twins. The sub-grain rotation and nucleation took place. Migration of grain boundary resulted in grain growth. TEM and EBSD techniques were used to examine the size of the grain, mis-orientation, and morphology of the feed metal at the cavity entrance and cavity export.

Purcek *et al.* (2014) studied the effect of a microstructure and subsequent aging treatment on the electrical, mechanical, and tribological behavior of Cu–Cr–Zr alloy manufactured through an equal channel angular extrusion process. Their findings indicated that the precipitates distributed within the UFG matrix considerably increase the strain hardening of the extrudates, leading to the improvement of the hardness, strength, and wear resistance properties of the product, without remarkably forfeiting the elongation to failure and electrical conductivity, in consequence of the collective effect of grain refinement and precipitation hardening. The wear behavior of the product was found to be significantly reliant on the strength and hardness of the extrudate. Kumuri *et al.* (2015) studied the effects of extrusion on a Copper rod of diameter 12.5 mm experimentally via a commercial CE setup. They conducted microstructure and mechanical investigation of the extrudates of Copper alloy pre and post-extrusion process. Based on their finding, more uniform and homogeneous grains were obtained after extrusion. Additionally, the extrudates' UTS and hardness increase after the continuous extrusion processes. Shen *et al.* (2015) investigated the effects of the accumulative continuous extrusion process (ACEP) on grain size refinement and nano-sized precipitates distribution of Al–0.2Sc–0.1Zr alloy. Using this novel manufacturing process, the contribution of nano-sized precipitates Al_3(Sc, Zr) on grain refinement of the alloys and pure aluminum processed using ACEP was investigated. The samples of the feed metal and extrudates were analyzed using EBSD and TEM. Ultrafine-grained extrudates with 0.8µm were obtained from 100µm of feed alloy through ACEP.

Devendra *et al.* (2018) carried out CE of a pure copper rod with a diameter of 12.5mm on a commercial outfit TBJ 350 to extrude the feed metal at different process parameters. Mechanical tests were conducted on the extrudates manufactured at different parameters to estimate the product yield strength and percentage of elongation. He studied aluminum rods at various extrusion CE parameters. A mathematical expression was established to estimate the extrudate mechanical properties and validated with the ANOVA technique. The UTS, hardness, and percentage of elongation of the extrudates at various wheel speeds and product diameters were assessed by using standard tests. Mathematical expressions were established to estimate the UTS and hardness of the extrudates using the RSM. A 95% confidence level was achieved for the mathematical expression.

Zhang *et al.* (2015) studied the horizontal continuous casting and subsequent CE process effect on the microstructure and mechanical properties of Al−0.70Fe−0.24Cu alloy. The experimental finding revealed that the alloy's microstructural and mechanical (Comprehensive) properties improved. Based on their investigation, the main contributors to the property enhancements were strain-induced precipitation, crystal orientation transformation, and extrudate grain refinement due to post-treatment and CE forming methods. Su *et al.* (2016) studied the influence of the accumulative continuous extrusion (ACEF) forming process and the number of passes on Al base alloy grain refinement. The material investigated during ACCE was Al-Er alloy. As the passes of ACEF passes increased to four, extraordinary efficiency in reducing grain sizes of the alloy from 26.01µm to 1.3µm. In addition, fine grains were acquired due to grain growth which is clogged as a result of embarrassing boundary flows. Ji *et al.* (2016) conducted experimentation to explore the influence of horizontal continuous casting, Conform process, and aging treatment on Microstructures and mechanical properties of Al-Mg–SI alloy. During the investigation, horizontal continuous casting, subsequent Conform extrusion, and continuous in-line solution were carried out. Based on their finding, the product's mechanical properties improved with little sacrifice in electrical conductivity. Additionally, solution-treated extrudate grain sizes were refined. Generally, they concluded that a continuous forming process can applicably refine product grain sizes to enhance the product's mechanical properties.

Zhao *et al.* (2016) conducted numerical simulation and experimental analysis of AA6063 aluminum alloy via Deform and the continuous extrusion machine LLJ350 with double billets respectively to evaluate the metal flow and welding process during the CE of the feed metal. The microstructures of the weldment were examined through OM and SEM. Mechanical properties (UTS) of the extrudates were tested using a tensile testing machine. The finding showed that both the structure and properties of the weldment were affected by the process. The weldment on the extrudates exhibited the oxides on the billet surface participating in the metal flow and affecting the microstructure and mechanical properties of the weldment. The extrudate weldment exhibited the bud morphological characteristics on the cross-section area of the product. Based on the experimental result regarding the quality of the weldment, superior quality was obtained on the bottom portion compared to the lower one. Therefore it is found that through the CE process with double billet entries, the alloy can be extrude-welded but the process affects slightly UTS but significantly does percentages of elongation.

Tressia *et al.* (2017) studied the influence of the accumulation chamber geometry and the product diameter (extrusion ratio) manufactured using the Continuous forming extrusion process. Two types of extrudates were produced based on the geometry and size of the product such as a smaller rectangular cross-sectional area and another with a larger round cross-sectional area. For the latter, two types of accumulation chambers were used, one being of a larger size, resulting in a higher accumulation of feedstock before Conform extrusion through the extrusion die. Measurements of temperature were carried out at the extrusion die exit. Mechanical tests such as UTS, yield strength, and percentage of elongation tests were also done on the extrudates. Grain size analysis in the accumulation chamber and on the extrudates was carried out. The investigation revealed that an increase in the extrusion ratio increases the in-process metal and product temperatures and therefore the grain size of the final product growths.

Sheng *et al.* (2017) examined the microstructure evolution of Al−Sr master alloy (Al_4Sr) during the continuous forming extrusion process. The evolution of the alloy was examined through X-ray Diffract Meter (XRD), SEM, and TEM. The examination output showed that the particle size and morphology of the alloy were changed meaningfully through the Conform extrusion process. Al_4Sr particles are not only smashed into minor blocks in the upsetting zone but crushed deeply in the adhesion zone too. Piles of dislocations scrambled up in the right-angle bending zone. Al_4Sr particles develop in the extending zone. Finally, Al_4Sr particles in extrudates were around 28μm in length. Al_2Sr particles precipitated during the Conform extrusion process. Based on their finding compared with the extrudates through the horizontal extrusion method, better allocated and more evenly distributed Al_4Sr particles were obtained. Hu *et al.* (2017) examined the effects of repetitive CE and subsequent aging treatment on the formability and mechanical properties of an Al-based (Al-Mg-Si) alloy. Based on their investigation, the number of continuous extrusion forming passes affected both ductility and UTS of the alloy (improved the property if passes increased). The main factor for such property enhancements was structural homogeneity, superimposed solid solution, as well as dislocation density, scrambled up. Li *et al.* (2017) investigated the microstructure evolution of a two-phase H62 brass material during Conform Extrusion. The grains of the whole regions of the alloy were examined using OM and TEM. After CE forming process, the grain of the extrudate became sophisticated. The finding revealed that result flatter microstructures were obtained in the groove rolling region upon comparing the raw feed alloy. Yuan *et al.* (2017) studied the microstructure evolution and mechanical properties of a Cu-Cr alloy during the CE process. The structure of the in-process feedstock was analyzed using OM and TEM. The hardness and conductivity properties were also studied in different regions of the process. The investigation result revealed that the maximum hardness of value148 HB was obtained in the right-angle bending region, then reduced in the encompassing extrusion zone and in adhesion zone sub-grains too.

Tressia *et al.* (2018) examined the effect of the RPM of the driving extrusion wheel on the microstructural homogeneity of low oxygen copper (ASTM C10200) through the CRE process experimentally. Based on the experimental result, RPM increment did not contribute to microstructural and UTS properties improvements on the alloy microstructural homogeneity, tensile strength, and average size of the grain. Mitka *et al.* (2018) also investigated the effects of the Continuous Rotary Extrusion (CRE) of AZ81 magnesium alloy to enhance the characteristics of the alloys. During the CRE, the driving wheel velocity was controlled. The die temperature was also recorded. The microstructure analysis and mechanical testing of extrudates had been taken to select the effective process variables to obtain rods from AZ81 magnesium alloys in the CRE process.

Zinov *et al.* (2019) considered microstructural evolution during the CE process and examined the influence of input process variables on the mechanical properties of M1-grade copper rods by using a Conform 350 industrial machine. The investigation considered the deformation zones during conform extrusion to get information on microstructure evolution as well as extrudate mechanical properties. Investigation of the material flow in the zone showed that structural transformation features were reserved for all specimens. Grain size refinement was achieved as a result of the process from a large grain size of a cast billet feedstock with 80–1000 µm reduced to extrudate fine grain size of 50–35µm. regarding the effects of CE input parameters on extrudate; Based on their findings optimum hardness levels from quantitative data were achieved on the products extruded at a rate of 6m/min rather than extruded at a lower rate.

Mosleh *et al.* (2018) proved that valuable information regarding the metal extrusion process can be obtained through modeling to predict the flow behavior of feedstock metals subjected to sever plastic deformation. Through this information manufacturing time cost will be reduced by selecting optimal parametric combinations of process parameters.

Hu *et al.* (2019) explored the effects of repetitive Conform extrusion (R-Conform) and subsequent heat treatment (tempering) on the mechanical properties of Al-Mg-Si alloys with Nano-scale precipitates. During this noble process, the relationship between microstructure evolution and the mechanical properties of the extrudate was studied. The investigation result showed that the product microstructure became homogeneous and sophisticated and therefore the mechanical property of the extrudate improved by the R-Conform process.

Koshmin *et al.* (2021) made a thorough research on the features of physical and mechanical properties arising in the deformation zone of the Cu-ETP feedstock during the CE forming process. The feed metal was of rectangular Cu-ETP buses of 10×60mm in size. The power parameter (torque and force) values necessary to extrude the feed metal were obtained through the FEA simulation tool. Based on the computational result, the extrusion torque and force values were increased until the free space of the extrusion chamber was filled with the feedstock, and reached maxima of 12.26kN m and 1.54MN, respectively. Additionally from the stress-strain state analysis of feedstock in the deformation zone, the equivalent strain distribution field, and strain rate intensity were found. The graph of the feedstock temperature change with time during the CE forming process was plotted. Based on the computational result in the region of contact between the workpiece and the abutment, maximum equivalent strain and compressive stresses were noticed. Based on simulation modeling and microstructural evolution investigations, substantial grain refining from the cast structure occurred at the entrance to the secondary deformation zone and in the abutment region. In the latter region, the highest level of compressive stresses was observed. When the work leaves the abutment region, where deformation-induced heating arises, a decrease in the hardness of the workpiece was observed from 93 to 67HV. In the die region where the oriented crystal structure formed, the grain size increased from 25 to 30µm due to the continuing recrystallization process till the extrudate reached a cooling medium and consequently a slight decrease in the extrudate hardness from 79 to 7HV.

Yang *et al.* (2022) investigated the influence of ACEF process passes on the mechanical properties of 5087 alloy. The strengthening mechanisms induced by microstructural evolution in a rheo-extruded 5087 alloy processed through ACEF processes were also investigated. The microstructures of the extrudates subjected to ACEF with various passes were characterized using EBSD and TEM. The investigation findings proved that there was a noteworthy grain refinement effect on the extrudates after 3 passes of ACEF, as a result, the average grain size decreased from 45.6µm to 2.5µm. The mechanical properties of the extrudates also improved. From microstructure evolution and EBSD and TEM characterizations, dislocation walls were generated during the ACEF process which stimulated the low-angle grain boundaries (LAGBs) formation. Additionally, the accumulative strains enhanced the transformation of LAGBs to high-angle grain boundaries (HAGBs). High dislocation pile-up enhanced the CDRX driving force, and nano-sized $Al_6(Mn, Fe)$ phases at the grain boundaries of the extrudate prevented the growth of grains due to the pinning effect. As a result, the yield strength of the ACE extrudate improved.

2.4. Optimization of CE Process Parameters through Response Surface Method, Artificial Neural Network and Genetic Algorism

At elevated temperature, flow stress, strain rate and feedstock temperature relationship is usually described using the Arrhenius constitutive model (Niu, X., *et al*., 2019). One of the most commonly and well-implemented optimization methods is a Response Surface Methodology (RSM). They applied RMS to determine the best conditions for an optimal response. It is an extensively applied mathematical as well as statistical method to model and analyze any process in which the output (response) is influenced by various input-independent parameters. The method is usually applied to optimize factors, together with other interactive parameters. The shortcomings of RSM are its requirement in screening appropriate ranges of the running parameters and the optimization response being restricted to certain scales and operating systems. The objective of RSM is to optimize the response. In other words, Through RSM, a theoretical model delivering information about the relationship between controllable variables (factors) and the response of interest can be obtained empirically (Chan, C. H., *et al*., 2017).

FIGURE 2. 6: HIGHLIGHT OF RSM (Manojkumar, N., *et al.*, 2022)

An experiment in any process can be designed, optimized and analyzed using RSM (Baş, D., *& and Boyacı,* 2007). Figure 2.6 shows the highlight of RSM. RSM is a useful statistical tool and contains optimization techniques for the settings of factorial variables, such that the dependent variable reaches a desired optimal value. Factorial techniques and

ANOVA is used to model the independent parameter in effect. Basri, M., *et al*. (2007) also did assessment on the estimation capabilities of RSM with ANN.

Jagota, V., & Sharma, R. K. (2020) investigated the influence of microstructure obtained by varying heat treatment parameters on sliding wear of H13 hot die steel. During the investigation they use optimization tools of RSM and ANN with 1-1-1 ANN topology implies single input, single hidden and one output layer .They found that ANN demonstrates a better technique than RSM to predict sliding wear of H13 hot die steel with more accuracy Since ANN tool had a higher correlation coefficient R2 values.

RSM is designed to allow an experimenter to estimate interactions, therefore giving them knowledge of the response surface shapes and plots from the investigation. This technique is often used when simple linear and interaction models are not adequate, e.g., experimentation far from the region of optimum conditions. Here, the experimenter can expect curvature to be more prevalent and need a mathematical model, which can represent the curvature. The simplest of such a model has the quadratic form in equation 2.3:

$$Y = \beta_0 + \beta_1 X_1 + \beta_2 X_2 + \beta_{12} X_1 X_2 + \beta_{11} X_{12} + \beta_{22} X_{22} \quad \ldots\ldots\ldots\ldots\ldots\ldots\ldots\ldots\ldots 2.3$$

The equation contains linear terms for all variables, squared terms for all variables, and interaction of input parameters. The two most common designs generally used in RSM modeling are central composite rotatable designs (CCRD) and Box–Behnken designs. In these designs, the independent variables are set at three or five distinct levels, but not all combinations of these values appear in the design (Hanrahan, G., & Lu, K., 2006).

CCDs contain embedded factorial or fractional factorial design with center points that are augmented with a group of axial (star) points that allow estimation of curvature (Fig. 2.7). A CCD contains cube points at each corner of a unit cube that is the product of the intervals [−1, 1], star points along the axes at or outside the cube, and center points at the origin. Points *A*, *B*, *C*, and *D* are the points of the initial factorial design with points *E*, *F*, *G*, and *H* being the star points at the central 0.

Hanrahan & Lu (2006) stated that A CCD always holds twice as many star points as factors in the design. The star points symbolize new low and high extreme values for each variable in the design. RSM comprises much more than model fittings and analysis of them. Indeed, RSM is generally understood and become the core of industrial experimentation.

For instance, Kim *et al.* (1998) studied the influences of several input CE process variables on the process responses such as the flow of the feed metal, temperature distributions, defect existence, and effective strain using DEFORM computational tool. A qualitative guideline was proposed for the optimal input process variable design. The first suggestion was on the extrusion wheel velocity which was not made remarkable changes in metal flow until it reaches a certain high value. Third, the length of the lower straight part of the die and its effect on the flow direction of the extrudate were explored while the product is flowing out of the die orifice. Based on their findings inherent flow of the extrudates can be corrected by lengthening the lower straight unit of the extrusion dies. Finally, by increasing the feed metal width, manufacturing extrudates of larger cross-sectional area and desired quality are possible.

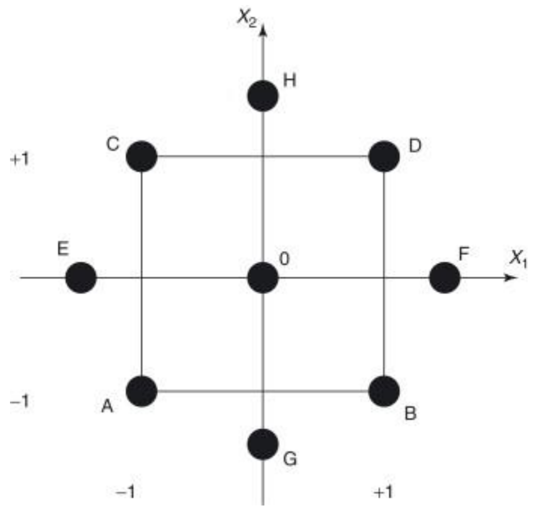

FIGURE 2. 7: CCD WITH A FULL FACTORIAL TWO-LEVEL STAR DESIGN

Optimizations of the CE process responses of interest have significant roles to determine an appropriate combination of independent parameters and levels to process a feedstock material. As per the literature very limited CE process optimization studies were carried out. Various optimization techniques have been applied by scholars. As per the literature very limited CE process optimization studies were carried out. However various optimization techniques have been applied by scholars to determine the response. RSM, ANN, and GA are the areas of focus to be applied to optimize the responses in this study.

The mechanical, microstructural, tribological and other properties of non-ferrous alloys such as Aluminium, Copper, etc., and their alloys like AA1100, C101, and C18150 can be improved through SPD techniques like Conform extrusion (Fu, *Q., et al.*, 2022;

Mao, Q., *et al*., 2022; Shen, Z., *et al*., 2022; Wang, y. d., *et al*., 2021; Xu, G. L., *et al*., 2021; Borodin, E. N., *et al*., 2020; Mertová, K., *et al*., 2020; Faraji, G., & Torabzadeh, H. 2019; Kuramoto, S., *et al*., 2019; Lin , G. Y., *et al*., 2019; Langdon, T. G., *et al*., 2018; Sinha, D. K., *et al*., 2018; Tressia, G., *et al*., 2018; Yadav, R. R., *et al*., 2018; Sheik Hassan, M., *et al*., 2017; He, Y., *et al*., 2010; Valiev, R., *et al*., 2006). These materials have very distinctive behaviors that make them important for different purposes. Aluminium of AA1100 grade and its alloys are known for their outstanding corrosion resistance, high conductivity, high formability and super reflective appearance (Sidelnikov, S. R., *et al*., 2015; Monteiro, W. A., 2014; Fang, G., *et al*., 2009; ASTM, B., 2005; Halmos, G. T. *et al*., 2005). Therefore, AA1100 grade can be used for chemical apparatus, welding transformers, power electrical grid, solid and pop rivets, tanks of railroad car, lighting industry for reflectors, radiator fins, different name plaque, cookery utensils, plumbing, and sheet metals (Zeng, Z., *et al*., 2019; Kubina, T., *et al*., 2015; Monteiro, W. A., 2014; Ying, Z. H., *et al*., 2012; Davis, J. R., 1993). In-case of pure copper of C101 grade, it has high thermal and electrical conductivity (Yang, H., *et al*., 2020; Yun, X., *et al*., 2016; Kumari, S., *et al*., 2015; Chen, X., *et al*., 2010) and used for different applications such as general engineering, cables, electrical conductors, contacts, terminals, busbars, motor and transformer components, automotive and industrial radiators and domestic appliances (Monteiro, W. A., 2015; Davis, J. R., 2001). There are numerous Cu-based alloys in which Cu-Cr is the one extensively used for different applications due to their good strength, good conductivity in electrical and thermal, super age hardenability, and corrosion resistance properties (Jalilova, D. A., *et al*., 2022; Mao, Q., *et al*., 2022; Shan, L., *et al*., 2022; Aksenov, D. A., *et al*., 2021; Guo, T., *et al*., 2020; Zhang, P. C., *et al*., 2020; Li, B., *et al*., 2011). However, the binary alloy of Cu-Cr displays poor softening resistance at higher temperatures (Jalilova, D. A., *et al*., 2022; Shan, L., *et al*., 2022; Ma, M., *et al*., 2020; Shangina, D., *et al*., 2016; Li, B., *et al*., 2011). The properties of Cu-Cr like softening resistance at elevated temperatures, mechanical, and other properties improvement has seen by adding Zr element to the binary alloy (Wang, Y. D., *et al*., 2021; Huang, A. H., *et al*., 2019; Shangina, D. V., *et al*., 2017). Further improvement can be also obtained through SPD. Cu-Cr-Zr alloy has been explored and enhanced its overall properties (Dalan, F. C., *et al*., 2022; Borodin, E. N., *et al*., 2020; Bourezg, Y. I., *et al*., 2020; Chembarisova, R. G. , *et al*., 2020; Kapoor, G., *et al*., 2020; Li, R., *et al*., 2019; Khomskaya, I. V., *et al*., 2018; Purcek, G., *et al*., 2018; Morozova, A., *et al*., 2018; Zhang, S., *et al*., 2017; Abib, K., *et al*., 2015; Vinogradov, A., *et al*., 2002). Hence, C18150 grade of Cu-Cr-Zr alloy is an upgraded version of Cu-Cr alloy and adapted in many new application eras.

2.5. Research Gap Analysis

Several studies have addressed different engineering materials to identify the various input process parameters of CE; however, a limited number of research papers addressed the exploration of the effects of the process parameters (factors) on the deformation behavior of Non-Ferrous feedstock metals and their alloys. Most of the studies observed the CE process parameters on various non-ferrous metals and their alloys such as Aluminum, Copper, Magnesium, etc. However, the comprehensive and combination effects of the CE process parameters such as driving wheel speed, feedstock temperature, die temperature, extrusion ratio and friction factor on AA1100, C101, and Copper-Zirconium-Chromium (C18150) alloys not fully notified computationally in-terms of optimal total load requirements, effective stress induced, and the damage of feedstock due to the process. Moreover, the optimization of the CE input process parameters on mechanical and technological properties of AA1100, C101 and C18150 alloys through RSM, and ANN-GA was not reported in depth. Hence, the motive behind this dissertation is to investigate the deformation behavior of non-ferrous alloys such as AA1100, C101 and C18150 alloys in a continuous forming process. Additionally, the process parameters' influences on mechanical and microstructural properties of non-ferrous metals and alloys also need to be investigated. As a case study of exploration, Aluminum, Copper, and Copper-Zirconium-Chromium are selected.

CHAPTER 3: MATERIALS AND METHODOLOGIES

3.1. Introduction

In this chapter, the effects of input process parameters on the deformation behaviors of Aluminum (AA1100), Copper (C101), and Copper-Zirconium-Chromium alloy (C18150) were investigated through different techniques. Analytical, computational, and experimental investigation methods were applied in this research to analysis, predict and validate different response parameters. The principles, assumptions, standards, techniques, tools, and machines applied for the investigations, characterizations, and testing of the feed metals and extrudates presented in detail.

The theoretical analysis of load requirement for the Conform deformation process was done through Upper Bound Method (UBM) technique. The Designs of Experiment (DOE) techniques were used for designing the numerical experiments. The numerical modelings of deformation behavior of the feed metals were done through the FEM simulation tool DEFORM-3D analysis software. The optimizations of process parameters were done using RSM, ANN, and GA approaches. Experimental investigations on the behavior of the feedstock materials were also performed by extruding them through a commercially available continuous extrusion setup of the TBJ350 model. The experiments were conducted by optimized parameters obtained through the DEFORM 3D simulation, RSM, ANN, and GA.

The size of the Aluminium feed metal used for the investigation was 9.5mm in diameter. The feedstock was then extruded to product diameters of 6mm, 7mm, and 8mm. The same method was followed for Copper alloy (C101) feedstock. The feedstock material used for the investigation was 12.5mm in diameter. It was extruded to product diameter of 6mm, 7mm, and 8mm at 4, 6, and 8RPM. Also, continued for the third material Cu-Cr-Zr alloy of C18150 grade rod. The feedstock of the alloy rod was of 12.5mm diameter. The extrusion of feed metal was carried out at a driving wheel velocity of optimized 8RPM to extrude 10mm and 8mm diameter rods. All the feedstocks and Conform extrudates taken for the investigations were circular rods.

Extrudates of feed materials were manufactured at various optimized input parameters computationally and experimentally. The validations of the deformation load requirements were carried out numerically and experimentally. The feedstock and Conform extrudates were collected for testing and characterization without any further heat treatment and artificial aging. The feedstock and extrudates were tested and characterized mechanically and micro-structurally pre and post-deformation through standard procedures. The mechanical tests encompassed tensile, hardness, and wear properties and the microstructural investigation covered metallographic tests to explore the effect of the input processes parameters on the properties. The feed materials and extrudates were tested and characterized in terms of microstructure, hardness, tensile testing, and wear test.

3.2. Feedstock Materials

For the investigation, three materials namely: Aluminum (AA1100), Copper (C101), and Copper-Zirconium-Chromium alloy (C18150) were taken to explore the effects of the CE input process parameters on the material deformation behaviors. The responses considered were deformation load (energy) requirements, effective stress, and others.

3.2.1. Chemical analysis

The chemical analysis (characterization) is one of the non-destructive testing methods to detect elements in place. The analyses were carried out on the feedstock metals to identify the chemical components and their weightage percentages in them. The analysis provided valuable information about the actual chemical constituents to verify whether the material fulfilled the required composition and conditions. The analyses were done via an optical emission system that decides the elemental composition of the alloy. The technique used to detect an alloy composition is called Positive Material Identification (PMI). PMI can determine quantitative and qualitative elemental composition. Even though many different techniques were in the PMI industry, the most commonly used methods to determine the chemical compositions of constituents in the feed metal or alloy were X-ray fluorescence spectroscopy (XRF) and optical emission spectroscopies (OES). XRF is non-destructive; however, OES is more sensitive than XRF to lighter elements (Pavia, D. L., *et al*., 2014). In this analysis, the type and the ratio of atoms in the alloys of the chemical substances were analyzed using Bruker Q2 ION OES metal analyzer.

3.2.1.1. Aluminum alloy (AA1100)

The first feedstock taken for analysis was an aluminum alloy with AA1100 grade. The chemical composition of the feedstock material sample with a 9.5mm diameter was tested using Bruker Q2 ION OES metal analyzer for chemical analysis. From the analyzer, the composition of the AA1100 alloy with its weight percentage is shown in Table 3.1.

Table 3. 1: Aluminum alloy (AA1100) grade chemical composition in wt.%

Al	Cu	Mn	Si, Fe	Be	Zn	Other elements
99.50	0.15	0.05	0.2	0.001	0.09	NA

3.2.1.2. Copper alloy of C101 grade

The second feed metal taken for the Conform deformation process investigation was a pure Copper metal with C101 grade. The chemical composition of the feedstock material with a diameter of 12.5mm was used for the investigation and was analyzed using the OES analytical tool. From the OES system, the chemical composition it with their weight percentage is given in Table 3.2.

Table 3. 2: Copper alloy of C101 grade chemical composition in wt.%

Element	O_2, Fe, Pb, Zn, P, Ag, As, Sb, Te	The remaining
C101 alloy	0.01%	99.99%

3.2.1.3. Copper-Zirconium-Chromium alloy of C18150 grade alloy

The chemical composition of a C18150 grade alloy sample was tested using the Bruker Q2 ION analyzer for the constituents' analysis. The composition is shown in Table 3.3. From the OES system, Cr and Zr were identified with the weight percentage of 0.52% and 0.90% respectively and the remaining was Cu.

Table 3. 3: C18150 grade alloy chemical composition in wt. %

Cr	Si	Zr	Cu
0.52	0.01	0.90	98.57

3.3. Analytical Investigation on the Deformation Load in CE Process

Basic principles and assumptions were taken into considerations from plasticity theory to solve load requirement issues. The development of a consistent mathematical model was depending on the selection of the suitable constitutive equations (Wood, P. K., 1990). The equations were obtained by considering the flow stress of the feed metal related to a certain stage in the deformation zone. The flow stress was estimated from a kinematically admissible velocity field. The field was also estimated using the level of strain, strain rate, temperature and feed metal property under consideration. In addition to the summation of the constitutive equations into a single mathematical expression to describe the rate of internal work of deformation (work done), derived using the minimum upper bound (or energy) theorem was used (Hill, R. O. D. N. E. Y., 1963).

In this investigation, the theoretical analysis of extrusion load requirement to extrude the feed metal through the Conform deformation process was done through Upper Bound Method (UBM) technique for Aluminum (AA1100), Copper (C101), and Copper-Zirconium-Chromium alloy (C18150) feed metals. In the analysis, the theory of plasticity and necessary assumptions were made to estimate the power / load requirement to CE extrude the feed metal using UBM.

3.3.1. Basic concepts of the theory of plasticity for CE extrusion

3.3.1.1. Effective stress and strain expressions

Using the invariant functions, determining the complex state of stress or strain in terms of mathematical expressions to flow curve concept is inevitable. The flow curve is determined through different experimental methods for observing the deformation phenomenon by which stress and strain relationship described (Wood, P. K., 1990).

The effective stress can be estimated from the uniaxial testing result of tensile or compression test. It can also be expressed in Eq.3.1 as a uniaxial stress system (Wood, P. K., 1990; Bridgman, P. W., *et al*., 2013; Darvell, B. W., *et al*., 1900).

$$\sigma_{eff} = \sigma_{ut} \quad \text{…………} \quad (3.1)$$

Where σ_{eff}: effective stress (MPa)

σ_{ut}: the uniaxial result of tensile or compression test (MPa)

The components of true strain (three normal strain components) can be expressed in the fundamental principle of metal forming (i.e volume consistency) in Eq.3.2,

$$\varepsilon_L + \varepsilon_R + \varepsilon_C = 0 \quad \text{…………} \quad (3.2)$$

Where ε_L: longitudinal strain; ε_C: compressive strain; ε_R: radial strain

Equation 3.3 explains the relation for effective strain to the uniaxial compression test

$$\varepsilon_L = \varepsilon_L = 2\varepsilon_C = 2\ln\left(\frac{d_f}{d_i}\right) \quad \text{…………} \quad (3.3)$$

Where d_f: extrudate diameter (mm); d_i: feed metal diameter (mm)

3.3.1.2. Friction model

The friction factors between feed rod and extrusion driving wheel, feed rod and other continuous forming extrusion toolings can be determined with the conditions and relations explained below (Wu, P. Y., *et al.*, 2007, Tirosh, J., *et al.*, 1979, Wood, P. K., 1990).

The friction conditions occur between the tooling and the feedstock in a deformation process where feedstock deforms plastically. For which, Coulomb friction and the constant friction factor are mostly used in the theory of plasticity. The Coulomb friction decides the tangential shear stress as expressed with consideration of pressure in Eq. 3.4.

$$\tau = \mu P \qquad (3.4)$$

Where τ: tangential shear stress; μ: coefficient of friction; P: normal stress

Whereas**,** the friction factor (usually assumed to be constant for a given set of conditions), explains with constant shear yield stress of the feed metal being deformed irrespective of pressure and shear yield stress as expressed in Eq.3.6.

$$\tau = m\kappa \qquad (3.5)$$

Where m: the friction factor, k: maximum shear stress (MPa)

The friction factor was supposed to be constant for a given set of conditions. The value of the friction coefficient taken was small (typically < 0.1 for the wire drawing and upto 0.3 for CE forming process), however, the friction factor can hold a value in the range 0 to 1. Noting, that in the absence of friction, m is approximated to be zero (m = 0). For complete sticking between the tools and feed material, m = 1.

The feed metals considered were Aluminum (AA1100), Copper (C101), and Copper-Zirconium-Chromium alloy (C18150). Al and Cu feedstock have a tendency to stick to tooling due to the mechanical and thermal stresses developed in the deformation zone. Consequently, the feedstock favorably shears internally at a small distance from the interface of feedstock and tooling. Therefore it is reasonable to assume that m=1 which holds true for the entire deformation zone (Wu, P. Y., *et al*., 2007; Tirosh, J., *et al*., 1979). In other words, the maximum shear stress *k* a metal can withstand according to the Von-Mises yield criterion is the combination of equations (3.5) and (3.6) as follows,

$$\tau = \frac{\sigma_{eff}}{\sqrt{3}} \quad \text{...} \quad (3.6)$$

Noting that τ= κ since m = 1

$$\kappa = \frac{\sigma_{eff}}{\sqrt{3}} \quad \text{...} \quad (3.7)$$

Although, the friction factor has been assumed equal to unity, comparisons between experimental and theoretical data for the condition is 0 < m < 1.

3.3.2. Basic assumptions for the theoretical investigation

The following assumptions/considerations were made for the analytical investigation of the CE process:

- Material is incompressible and von-Mises rigid visco-plastic,
- Elastic strain was negligible,
- The existence of yield criteria and the hypothesis that there exists flow relationship between strain increment and stress,
- The friction factor between the wheel and feed was assumed to be independent of slip,
- Development and adaptation of formulas to determine power requirements for the whole CE using UBM/ Energy Method,
- Derivation of the minimum upper bound at a dead zone angle where work done is minimum,
- Constant temperature is assumed during the deformation in each zone.

For the boundary value problems, velocity field needs to be a kinematically permissible, must satisfy the incompressibility (geometric self-consistency) and the velocity boundary conditions in plasticity and be continuous except at particular surfaces where velocity slips was permitted. An appropriately built admissible velocity field is considered vital to ensure the accuracy of the final solution. The UBM is an extremum principle to analyze plastic deformation for the boundary value problems which states that among all kinematically admissible velocity fields; the actual velocity field minimizes the expression. Thus, the geometrical configuration of the material during plastic deformation must be known. In the CE process, the geometrical configuration of the feedmetal is confined by the die surface. If the function represents the feed geometry in the deformation zone, then, according to condition of incompressibility.

The velocity vector field was also expressed using any appropriate coordinate system including Cartesian coordinates to represents the velocity of the flow metal at a point in space (zone under consideration) (x, y, z) at the instant in time t. The distribution of flow velocities was defined by the vector function $\vec{V}$ (x, y, z, t). $\vec{V}$ (x, y, z, t) velocity field was expressed mathematically in Eq. 3.8.

$$\vec{V} = \vec{V}(x, y, z, t) \qquad (3.8)$$

Where $\vec{V}$: velocity vector field; x, y, z: the coordinates of a point in space;

t: the instant in time

Velocity vector field can be described in-terms of three components or functions *u* (x, y, z, t), v(x, y, z, t) and *w*(x, y, z, t) one in each direction, i.e, *u*, *v* and *w*; in x, y and z directions respectively were needed and it was put as follows in Eq. 3.9:

$$\vec{V} = u\vec{i} + v\vec{j} + w\vec{k} \qquad (3.9)$$

The velocity vector field can be expressed in Eq. 3.10 using components of velocity vector field and their corresponding x, y, and z directions as follows:

$$\vec{V} = u(x, y, z, t)\vec{i} + v(x, y, z, t)\vec{j} + w(x, y, z, t)\vec{k} \qquad (3.10)$$

Where u, v and z: components of velocity vector field in x, y, and z direction respectively;

i, j, and k: unit vector in x, y, and z direction respectively

- ***Steady flow condition***

For most flows the field varies in time, but in some special cases the flow was modeled by assuming the velocity field does not change in time, such a case known to be a steady flow expressed mathematically in Eq. 3.11. The flow of a metal is said to be steady if V does not vary with time.

$$\frac{\Delta V}{\Delta t} = 0 \rightarrow \text{(steady flow)} \qquad (3.11)$$

Where ΔV : constant velocity field

For steady flows the velocity field is independent of time and also expresses in Eq. 3.12,

$$\vec{v}(x,y,z,t) = v_x(x,y,z,t)\hat{i} + v_y(x,y,z,t)\hat{j} + v_z(x,y,z,t)\hat{k} \quad \text{(Steady flow)……..} \quad (3.12)$$

- ***Incompressible flow condition***

If the metal under consideration is incompressible the divergence of V is zero. Thus, it can be expressed seen in Eq.3 13

$$\nabla V = 0 \quad \text{…………………………………………………………………} \quad (3.13)$$

Where **∇***V: the divergence of the volume of the metal*

3.3.3. Governing equations and boundary conditions

The design of a reliable mathematical model is governed by the selection of the proper constitutive equations. The equations are obtained by considering the flow stress of the feedstock material, corresponding to a particular stage in the deformation zone. The flow stress is determined from strain, strain rate, feedstock and tooling temperature, and the feedstock under investigation. Additionally, the summation of the constitutive equations into a single mathematical expression to describe the rate of internal work-done derived using the UBM (Kim, Y. H., *et al*., 1998; Wood, P. K., 1990).

In metal forming, principal equations and boundary conditions are necessary to determine the rate of internal energy of deformation. Therefore both constrictive equations and boundary conditions are stated below.

The governing equations for dedicative continuous forming process consist of five basic equations and criterion (conditions) (Kim, Y. H., *et al*., 1998) such as

i. Equilibrium Equations

$$\sigma_{ij,j} = 0 \quad In \quad \Omega \quad \text{……………………………………………………} \quad (3.14)$$

Where σ_{ij}*: deviatoric stress tensor*

ii. Velocity Strain-Rate Relations

$$\dot{\varepsilon}_{ij} = \frac{(u_{i,j} + u_{j,i})}{2} \quad \text{…………………………………………………} \quad (3.15)$$

where $\dot{\varepsilon}_{ij}$ *is strain rate*; u_i*: component of the velocity vector*

iii. Constitutive Equations

The constrictive equation can be given written as (Giuliano, G., 2011):

$$\dot{\varepsilon} = k\sigma^{n} \quad \ldots\ldots\ldots\ldots\ldots\ldots\ldots\ldots\ldots\ldots\ldots\ldots\ldots\ldots\ldots\ldots \text{(3.16)}$$

Where $\dot{\varepsilon}$: Strain rate; k: strength coefficient (MPa); σ: the applied stress (MPa); n: strain hardening coefficient is equal to 1/m

Strain rate, at which feed stocks deform at elevated temperature, as defined in Eq. (3.16) can also be rewritten with temperature dependent form (Wood, P. K., 1990) as follows:

$$\bar{\sigma} = A(1 - BT_H)\bar{\varepsilon}^{n}\,\dot{\bar{\varepsilon}}^{m} \quad \ldots\ldots\ldots\ldots\ldots\ldots\ldots\ldots\ldots\ldots\ldots\ldots\ldots \text{(3.17)}$$

Where, $\bar{\sigma}$: effective stress (MPa) ; $\bar{\varepsilon}$: Effective strain ; A and B are constants; $\dot{\bar{\varepsilon}}$: Effective strain rate; n: strain hardening coefficient is equal to 1/ m; m: strain rate sensitivity index; T_H: homologous temperature

This is the commonly used the constitutive equation to define elevated temperature deformation. The constrictive equation can also be re-written as (Kim, Y. H., *et al*., 1998).

$$\dot{\varepsilon}_{ij} = \left(\frac{3\dot{\bar{\varepsilon}}}{2}\right)\sigma_{ij}' \quad \ldots\ldots\ldots\ldots\ldots\ldots\ldots\ldots\ldots\ldots\ldots\ldots\ldots\ldots\ldots \text{(3.18)}$$

iv. Yield Criterion,

$$\bar{\sigma} = \sqrt{\frac{3}{2}}(\sigma'_{ij}\sigma'_{ji})^{\frac{1}{2}} \quad \ldots\ldots\ldots\ldots\ldots\ldots\ldots\ldots\ldots\ldots\ldots\ldots\ldots \text{(3.19)}$$

Where $\bar{\sigma}$: effective stress (MPa)

v. The full velocity field for the flow of the material in the deformation zone is obtained by incompressibility or volume consistency conditions

$$\dot{\varepsilon}_{kk} = 0 \quad \ldots\ldots\ldots\ldots\ldots\ldots\ldots\ldots\ldots\ldots\ldots\ldots\ldots\ldots\ldots\ldots\ldots \text{(3.20)}$$

Eq. 3.20 can be rewritten as

$$\dot{\varepsilon}_{xx} + \dot{\varepsilon}_{yy} + \dot{\varepsilon}_{zz} = 0 \quad \ldots\ldots\ldots\ldots\ldots\ldots\ldots\ldots\ldots\ldots\ldots\ldots\ldots \text{(3.21)}$$

Where $\dot{\varepsilon}_{xx}, \dot{\varepsilon}_{yy}, \dot{\varepsilon}_{zz}$ *: strain rate in the principal directions*

- **Boundary (velocity and traction) conditions** are:

$$u_i = \tilde{u}_i \quad \text{on} \quad \partial\Omega_D \quad \text{……………………………………..…. (3.22)}$$

$$\sigma_{ij} n_j = t_i \quad \text{on} \quad \partial\Omega_N \quad \text{…………………………..……..……... (3.23)}$$

Where u_i: component of the velocity vector; n_j: component of outward unit normal vector to the boundary; t_i: the applied external frictional traction

In particular, along the feedstock–tooling interface, essential and natural boundary conditions were mixed; no penetration into tool (rigid visco-plastic condition) and applied frictional force were taken.

3.3.4. Upper bound theorem for Continuous Extrusion (CE) process

The upper-bound method (UBM) is based on the energy principle. It is also known as the upper-bound theorem. It states that the rate of total energy associated with any kinematically admissible velocity field defines an upper bound to the actual rate of total energy required for the deformation. Kinematically admissible velocity field assumption is a significant step in analyzing metal forming processes by the upper bound method (UBM) (Haghighat, H., & Amjadian, P., 2013).

The actual rate of total energy mathematically expressed Hill (Hill, R. O. D. N. E. Y., 1963) in Eq.3.24. Hence, for a given class of kinematically admissible velocity fields, the velocity field that minimizes the rate of total energy is the lowest upper bound, and therefore is nearest the actual solution. Therefore, the kinematically admissible velocity field is used to denote a velocity field that satisfies the incompressibility requirement for a rigid-plastic material and the prescribed velocity boundary conditions. However, the velocity field may be discontinuous on a finite number of imaginary internal surfaces.

Detail illustrations of continues extrusion deformation zones are illustrated in Fig.3.1. From Fig. 3.1, there are three feed deformation zones due to internal work done per unit volume per unit time for a given stage of deformation (P_a). Whereas work of deformation zones represented as $W_{\mathbf{t\ (1\text{-}2a)}}$ – work of deformation for stages 1 to 2a; Wt $_{\mathbf{(2b\text{-}3)}}$ – work of deformation for stages 2b to 3; Wt $_{\mathbf{(3\text{-}5)}}$ – work of deformation for stages 3 to 5.

The equation of the rate of total energy used to determine to power requirement through UBM is also expressed in Eq.3.24

$$\dot{E}_r = \int_V \bar{\varepsilon}\bar{\sigma} dV + \int_{SD} k|\Delta v_t| dS + \int_{SV} mk|\Delta v_t| dS \ldots\ldots\ldots\ldots\ldots\ldots\ldots\ldots\ldots\ldots\ldots\ldots \text{(3.24)}$$

Where *Δv_t: the magnitude of velocity discontinuity tangent to the velocity discontinuity surfaces; ΔV_s: the magnitude of sliding velocity on the contact surface S_F; m: friction factor*

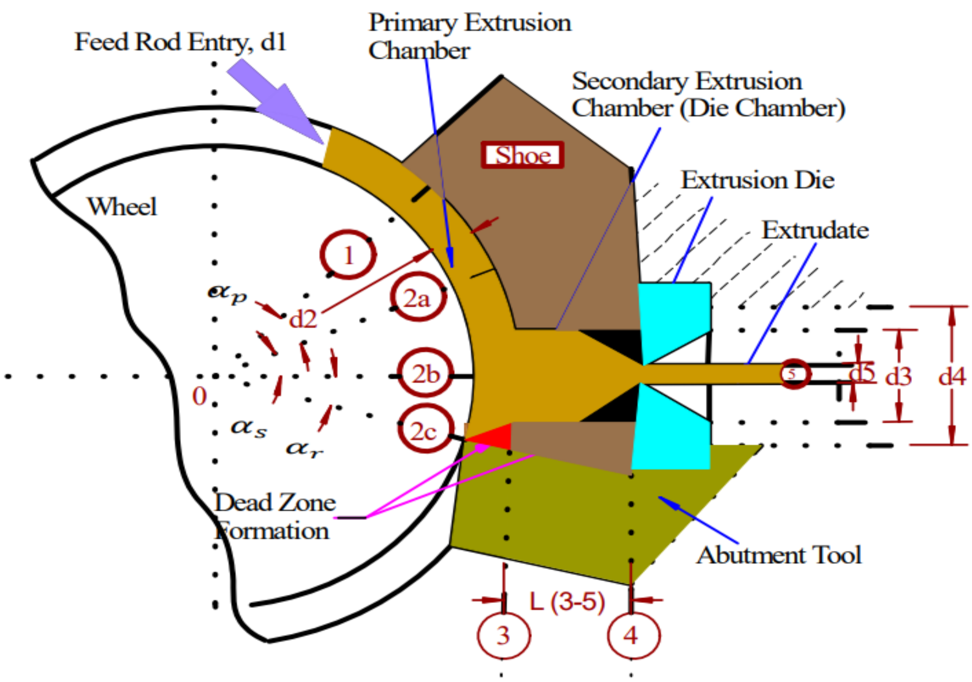

Where α_p *=Primary Grip length;* α_s *= Secondary Grip length, and* αr *= L* **(2b-2c)**

FIGURE 3. 1: THE GEOMETRY OF THE DEFORMATION ZONES DIAGRAM

(Wood, P. K., 1990)

3.3.4.1. Velocity field in the deformation zone

In metal forming process analysis, assuming a velocity field that is admissible kinematically is a significant step (Farokhpey, A., & Parsa, M. H., 2022). Therefore, the first step in the upper bound is to choose an admissible field for the material undergoing plastic deformation. The velocity field that derived from the incompressibility condition and boundary conditions is kinematically admissible velocity field.

The Velocity components in the radial direction within the deformation zone can be obtained by assuming volume flow balance. The volume flow of the material across S1 surface at the point (r_o, y, z) in the radial direction is

$$\Delta\alpha = -V_0 COS(\gamma) br_0 dy \text{ .... } (3.25)$$

The volume of material in the radial direction at the point (r, Θ, z) in the deformation zone is

$$\Delta\alpha = U_r brdy \text{ .... } (3.26)$$

From (3.25) and (3.26)

$$U_r = -V \frac{ro}{r} \cos\gamma \frac{d\gamma}{d\theta} \text{ .... } (3.27)$$

The internal power dissipation in the extrusion die chamber can be calculated with Fig 3.2. Using Fig 3.2 the extrusion die chamber zone can be further subdivide into five sub regions taking the velocity discontinuity lines as a boundary.

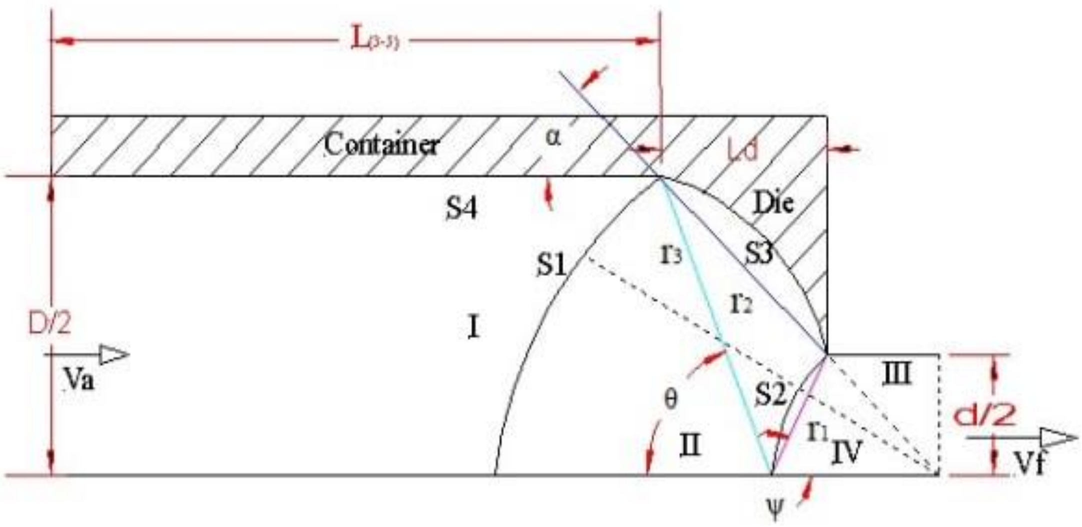

FIGURE 3. 2: TOTAL WORK DONE IN THE EXTRUSION DIE CHAMBER

Regarding the relationship between the angular positions, on the surfaces S1 and S2 and the angular positions in the deformation zone and assuming proportional distances from the midline deformation is given by

$$\frac{\sin\gamma}{\sin\alpha} = \frac{\sin\theta}{\sin\psi} \quad \ldots\ldots\ldots\ldots\ldots\ldots\ldots\ldots\ldots\ldots\ldots\ldots (3.28)$$

Where ψ: angular position of a point on the die profile

Differentiating Eq (3.28)

$$\cos\gamma \frac{dy}{d\theta} = \sin\alpha \frac{\cos\theta}{\sin\psi} \quad \ldots\ldots\ldots\ldots\ldots\ldots\ldots\ldots\ldots\ldots (3.29)$$

From Eq. (3.26) – Eq. (3.29)

$$U_r = -V_O \frac{r_o \sin\alpha}{r\sin\psi}\cos\theta \quad \ldots\ldots\ldots\ldots\ldots\ldots\ldots\ldots\ldots\ldots (3.30)$$

The strain rates' components in the cylindrical co-ordinates are defined as:

$$\dot{\varepsilon}_{rr} = \frac{\Delta U_r}{\Delta r}, \dot{\varepsilon}_{\theta\theta} = \frac{1}{r}\frac{\Delta U_\theta}{\Delta \theta}, \dot{\varepsilon}_{rr} + \frac{U_r}{r}, \dot{\varepsilon}_{zz} = \frac{\Delta U_z}{\Delta z},$$

$$\dot{\varepsilon}_{r\theta} = \frac{1}{2}\left(\frac{\Delta U_\theta}{\Delta r} + \frac{1}{r}\frac{\Delta U_r}{\Delta \theta} + \frac{U_\theta}{r}\right) \quad \ldots\ldots\ldots\ldots\ldots\ldots\ldots\ldots (3.31)$$

$$\dot{\varepsilon}_{\theta z} = \frac{1}{2}\left(\frac{\Delta U_\theta}{\Delta z} + \frac{1}{r}\frac{\Delta U_z}{\Delta r}\right) \quad \ldots\ldots\ldots\ldots\ldots\ldots\ldots\ldots\ldots (3.32)$$

$$\dot{\varepsilon}_{zr} = \frac{1}{2}\left(\frac{\Delta U_r}{\Delta z} + \frac{1}{r}\frac{\Delta U_z}{\Delta r}\right) \quad \ldots\ldots\ldots\ldots\ldots\ldots\ldots\ldots (3.33)$$

Assuming the plain strain extrusion (u, U2 =0), the full velocity field is obtained by placing U_r from equation (3.27), and (3.30) solving for U_Θ and applying appropriate boundary conditions are

U_Θ at $\Theta = 0$

$U_{\Theta/\Theta} = 0$ …………………………………………………………… (3.34)

Additionally for die surface

$$\left(\frac{U_\theta}{U_r}\right)_{\theta=\psi} = r\frac{\Delta\psi}{\Delta r} \quad \ldots\ldots\ldots\ldots\ldots\ldots\ldots\ldots\ldots\ldots\ldots (3.35)$$

The velocity components are given as:

$$U_r = -V_O \frac{r_o \sin\alpha}{r \sin\psi} \cos\theta \quad \text{..} \quad (3.36)$$

$$U_\theta = -V_O r_o \frac{\sin\alpha \Delta\psi}{\sin\psi \Delta r} \cos\psi \sin\theta \quad , U_z \text{..} (3.37)$$

Based on derived velocity field, the strain rate field for the deformation zone can be obtained from eq. (3.37)

$$\varepsilon_{rr} = -\varepsilon_{\theta\theta} = Vo \frac{r_0 \sin\alpha}{r^2 \sin\psi} \left(1 + r\frac{\Delta\psi}{\Delta r}\cos\psi\right)\cos\theta \quad \text{...........................} (3.38)$$

$$\varepsilon_{r\theta} = \frac{1}{2} Vo \frac{r_0 \sin\alpha}{r^2 \sin\psi} \left[1 - r^2 \cot\psi \frac{\Delta^2\psi}{\Delta r^2} + r^2(1+\cot^2\psi)(\frac{\Delta\psi^2}{\Delta r}) + \cot^2\psi(\frac{\Delta\psi}{\Delta r})^2 + r\cot\psi\frac{\Delta\psi}{\Delta r}\right]\sin\theta \ldots$$

$$\text{...} \quad (3.39)$$

$$\therefore \dot{\varepsilon}_{zz} = \dot{\varepsilon}_{\theta z} = \dot{\varepsilon}_{zr} = 0 \quad \text{..} \quad (3.40)$$

With the developed strain rate field and the velocity field, the UBM can be implemented.

3.3.4.2. Feed metal temperature (T)

In general, the feedstock temperature of in the deformation zone depends on certain conditions such as the tooling chamber and feedstock initial temperature, plastic deformation related heat generation, friction caused heat generation especially between feedstock and tooling such as the interface feedstock and extrusion wheel or extrusion container or die chamber and, heat transfer cases between the deforming feed metal and the toolings and the surroundings. When a metal is deformed especially in plastic form, the majority of the internal deformation work reveals itself as heat form. For a heavily deformed metal, between 90 and 99% of the work done is changed into heat (Myshkin, N. K., et al., 2005; Prasad, Y. V. et al., 2015). Therefore, the significant amount of heat generated due to the plastic deformation per unit volume. In other words, the feedstock temperature increases because of plastic deformation caused by the work done, the density and specific heat capacity of the feed metal. The constant β_1 is the fraction of deformation work which is converted into heat and the value β_1= 95% has been assumed. Therefore the temperature (T) at any stage can be determined with (Wood, P. K., 1990) Eq.3.41:

$$\delta T_i = \frac{\beta_1 w_t}{\rho_f C_f J} \quad \ldots\ldots\ldots\ldots\ldots\ldots\ldots\ldots\ldots\ldots\ldots\ldots\ldots\ldots\ldots \text{(3.41)}$$

Where *δT : the change in temperature due to plastic deformation; β_1: the fraction of deformation work converted into heat; Wt; workdone in the deformation zone; ρ: the density of the feed metal; C_f: specific heat capacity of the feed metal; J: the mechanical equivalent of heat*

3.3.4.3. The power requirement (P)

Using force equilibrium, the power can be calculated using

$$Power(P) = \frac{p_t H 2\pi R n}{60}(w) \quad \ldots\ldots\ldots\ldots\ldots\ldots\ldots\ldots\ldots\ldots\ldots\ldots \text{(3.42)}$$

Where pt: tangential force, R: driving wheel radius and n: revolutions per minutes

3.3.4.4. Minimum feed metal length for Continuous forming extrusion

Based on Kim's recommendation (Kim, Y. H., *et al.*, 2000), the minimum feedstock length L and the power (P) required for a successful single pass of the RCE process using Tresca yield criterion σ_{ext} = q + Y . The equilibrium requires the relationship shown in Eq. 3.58. Consequently, the minimum feed metal length L is calculated using:

$$L = \frac{\sigma_{ext} H}{k(m_2 - m_1)} \ldots\ldots\ldots\ldots\ldots\ldots\ldots\ldots\ldots\ldots\ldots\ldots\ldots\ldots\ldots \text{(3.43)}$$

Where m_1 and m_2 : friction factors and coefficients respectively , H: die chamber diameter, Y denotes the yield stress. k = 1.73Y,

3.4. Modelling and Simulation of a CE Process

Modeling and simulation of a CE process were done for each feed stock material based on experimental plan developed to investigate the input process variable effects on responses selected. The modeling of RCE process was carried out using AUTO-CAD engineering tools for all feedstock materials such AA1100, Cu101 and C18150 alloy. Different process parameters and methods were taken to model and simulate the RCE process. The 3D model elements of the RCE setup such as feedstock, extrusion wheel, shoe, and abutment was done as per the actual machine dimensions, a commercial setup of

TBJ 350 Conform Extrusion machine, through AUTO-CAD. The assembled model of CE process is shown in Fig. 3.3.

Certain constituent elements of the RCE machine such as extrusion wheel, coining wheel, extrusion shoe and abutment, were suggested as the rigid ones. Additionally extrusion wheel and coining wheel were taken as rotating members to simplify and reduce the simulation running time; however, other machine units were considered stationary during the process. Nevertheless, regarding the high temperature and the long exposure time between the feedstock and the tooling during Conform extrusion, the materials constants of the rigid members were specified.

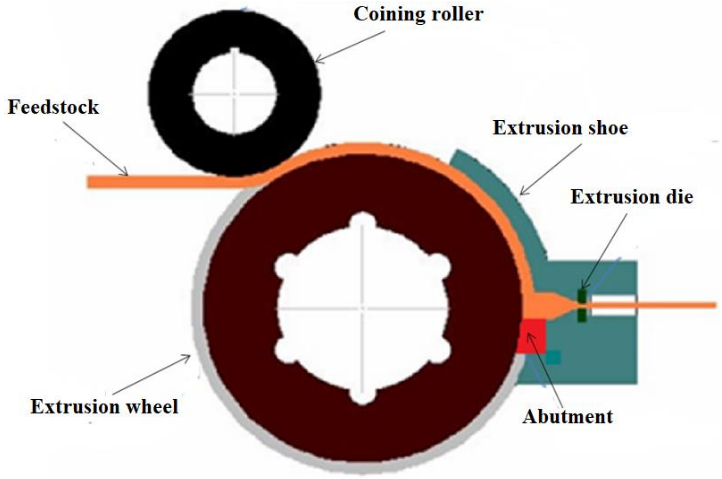

FIGURE 3. 3: A CAD MODELED ELEMENTS WITH ASSEMBLY OF CE

For the analysis of flow formulation FEA was selected since severe plastic deformations takes place on the feedstock material during Conform extrusion (Davis, J. R., 2001). FEA tool was used to build predictive computational models of CE set-up. It began with a CAD model that represented the RCE tools and simulated with different process parameters. The feed material model was taken as visco-plastic one. The model was then imported into FEM based DEFORM-3D simulation tool and developed as Deform-3D modeling to simulate and investigate through a computational RCE process setup shown in Fig 3.4

The solution accuracy of FEA is based on the type and size of the mesh. For the best selection of mesh, local adaptive mesh refinement technique was selected as the error was evaluated only over some subset of the entire model space. These equations approximately represent the governing equation of interest via a set of polynomial functions defined over each element. Tetrahedral mesh elements were chosen for each feedstocks and CE tooling. The finite element mesh was used to subdivide the CAD model into smaller domains called elements, over which a set of equations are solved. As these elements are selected in a finer range, the mesh is refined; the computed solution will approach the accurate solution. The details of mesh elements are shown in the corresponding feed metals summary tables.

The “sparse” was used as the solver, and the “direct iteration” was used as the iterative method. Each step was set to 0.05seconds, and the maximum polygon length of sub stepping was 0.5, and during the CE processing, the temperature of the deformed body (Cu101) varies (about 25 to 800℃); that of the deformed body (AA1100) varies (about 25 to 1000℃), and that of the deformed body (C18150) varies (about 25 to 1200℃). Other processing conditions for each material are stated in their perspective modeling and simulation sub-sections. With the data fed, the tool enables the prediction of total load needed, effective stress induced, effective strain experienced and damage of the extrudate with very high levels of accuracy.

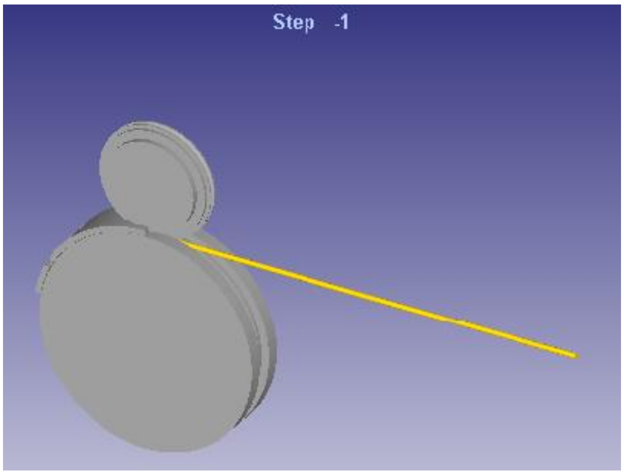

FIGURE 3. 4: DEFORM-3D MODELING OF THE COMPLETE CE PROCESS SETUP

3.4.1. Numerical modeling and simulation of feedstock materials

The numerical simulations of RCE process were performed at various wheel speeds, the diameters of the product, and temperatures of feedstock, die temperature, and friction factors. All experiments were designed through Minitab tool and performed numerically through finite element simulation tool DEFORM-3D. The feed raw material used was of 9.5mm diameter of pure aluminum and 12.5mm in diameter for C101 metal and C18150 grade alloy. In the investigation, the process parameters influence on total load, effective stress, and damage were studied under different RCE input process parameters. The total load encompasses extrusion wheel load and load on the extrusion shoe. The input process parameters taken for the study were wheel velocity, extrusion ratio, friction factor, feedstock temperature, and die temperature. The wheel diameter of 350 mm and die length of 10 mm (Table 3.18) had been considered since the actual experimentation machine had similar dimensions for all feedmetals. The interface friction coefficient of 0.95 has been considered between the wheel and feedstock material (Kim, Y. H., *et al.*, 1998).

3.4.1.1. AA1100 grade aluminum alloy feedstock

The detailed simulation process parameters and meshing element taken for computational investigations are shown in Table 3.4 and Table 3.5 respectively. The product diameters of 6mm, 7mm, and 8 mm out of that of 9.5mm in diameter AA1100 grade feedstock were taken for computational analysis.

Table 3. 4: Simulation parameters for AA1100 feed metal

S. No.	**Geometry data**		
	Parameters	**Units**	**Details**
1	Driving wheel diameter, *D*	mm	350
2	Die diameter, *d*	mm	6,7,8
3	Flash-gap size, *G*	mm	1
4	Die length, *L*	mm	10
Simulation data			
1	Wheel velocity	RPM	2, 6, 10
2	Initial temperature	℃	20
3	Environment temperature	℃	20
4	Die temperature	℃	400, 450, 500
5	Feed metal temperature	℃	100, 300, 600
Feedstock material data			
	Material	--	AA1100
1	Yield stress	MPa	20.9
2	Tensile strength	MPa	89.2
3	Strain rate sensitivity	--	0.22
4	Specific heat capacity	J/g-°C	0.904
5	Thermal conductivity	W/m-K	222
6	Poisson ratio	--	0.33
7	Convection coefficient	N/s°Cmm	0.02
8	Emissivity		0.050
9	Boltzmann constant	N/s℃mm^4	5.669×10^{-11}
10	Interface heat transfer coefficient	N/s℃mm	30
11	Interface condition	0.95 for feed metal and extrusion driving wheel (Zhao, Y., et al., 2013)	
		0.3 for shoe / abutment and feed metal (Kim, Y. H., et al., 1998)	
		0.1 for die and feed rod (Katajarinne, T., *et al.*, 2006)	

Table 3. 5: Summary of mesh elements for AA1100 simulation

S. No.	Objects	Mesh-elements
1	Workpiece	72,580
2	Extrusion wheel	157,019
3	Extrusion shoe	26,757
4	Coining wheel	75,902
5	Abutment	75,380
6	Die	46,132

3.4.1.2. C101 grade copper feedstock

The detailed input parameters and meshing details of the RCE components taken for the simulation of C101 grade copper feedstock are stated in Table 3.6 and Table 3.7 respectively. The product diameter of 6mm, 7mm, and 8mm out of that of 12.5mm C101 feedstock were taken for computational analysis.

Table 3. 6: Simulation parameters for C101 feedstock

S. No.	Geometry data		
	Parameters	**Units**	**Details**
1	Wheel diameter, *D*	mm	350
2	Die diameter, *d*	mm	6,7,8
3	Flash-gap size, *G*	mm	1
4	Die length, *L*	mm	10
Simulation data			
1	Driving wheel velocity, *N*	RPM	4,8,12
2	Initial temperature	℃	20
3	Environment temperature	℃	20
4	Die temperature	℃	400-600
5	Feed metal temperature	℃	500-850
Feed metal data			
	Material	--	C101
1	Yield strength	MPa	138
2	Tensile strength	MPa	207
3	Young modules	GPa	117
4	Shear modules	GPa	43
5	Melting point	℃	1083
6	Strain rate sensitivity	--	0.22
7	Poisson ratio	--	0.34
8	Specific heat capacity	J/g℃	0.385
9	Thermal conductivity	W/m-K	391.1
10	Electrical resistivity	Ωm	0.0171x10-6
11	Convection coefficient	N/s˚Cmm	0.02
12	Emissivity		0.3
13	Boltzmann constant	N/s°Cmm^4	5.669 × 10−11
	Interface heat transfer coefficient	N/s°Cmm	30
14	Interface condition	0.95 for feed stock and extrusion wheel	
		0.3 for shoe and feed metal	
		0.3 for abutment and feed metal	
		0.1 for extrusion die and feed rod	

Table 3. 7: Summary of mesh elements

S. No.	Objects	Mesh-elements
1	Workpiece	72,580
2	Extrusion wheel	157,019
3	Extrusion shoe	26,757
4	Coining wheel	75,902
5	Abutment	75,380
6	Die	46,132

3.4.1.3. C18150 alloy feedstock

The detailed input parameters and meshing details used for computational analysis of C18150 feed alloy are shown in Table 3.8 and Table 3.9 respectively. The product diameter of 8mm was taken for computational analysis from a feedstock of 12.5mm.

Table 3. 8: Simulation parameters for C18150 alloy feedstock

S. No.	Geometry data		
	Parameters	**Units**	**Details**
1	Wheel diameter, *D*	mm	350
2	Die diameter, *d*	mm	8
3	Flash-gap size, *G*	mm	1
4	Die length, *L*	mm	10
Simulation data			
1	Wheel velocity, *N*	RPM	4, 8, 12
2	Initial temperature	°C	20
3	Environment temperature	°C	20
Feedstock material data			
	Material	--	**C18150**
1	Yield strength	MPa	432.01
2	Tensile strength	MPa	452.03
3	Strain rate sensitivity	--	0.5*
4	Heat capacity	$N/mm^2°C$	2.3
5	Conductivity	IACS	75.3 %
6	Convection coefficient	N/s°Cmm	0.02
7	Emissivity		0.3
8	Boltzmann constant	$N/s°Cmm^4$	$5.669 \times 10-11$
9	Interface heat transfer coefficient	N/s°Cmm	30
10	Interface condition	0.95 for feed stock and driving wheel	
		0.3 for Shoe and feed metal	
		0.3 for abutment and feed metal	
		0.1 for feed rod and extrusion die	

Table 3. 9: Summary of mesh elements of CE elements for C18150 alloy

S. No.	Objects	Mesh-elements
1	Workpiece	71,719
2	Extrusion wheel	148,537
3	Extrusion shoe	24,885
4	Coining wheel	65,307
5	Abutment	76,391
6	Die	45,589

3.5. Experimental Design and Optimization Setup

The five independent factors with a three-level factorial design were chosen for determining and modeling output characteristics of the RCE process. All the input factors considered were wheel velocity, product diameter; frictional factor, feedstock temperature, and die temperature. All the input variables at three levels were also considered. The input values of the independent variables were taken between ranges. Uniform variation in the values of variables was made as per the principles of the design of the experiment (DOE). The experimental design was carried out through the Minitab tool. Detailed experiments were generated as per the design of the experiment for the factors and levels based on the Central Composite Rotatable Design (CCRD) method or Box Behnken Method

The mathematical modeling also developed through RSM to investigate the responses. Using the p-values of the response values of the input parameters second order regression equation mathematical models were developed. The least value of the significance level of the factor was checked against their P-value. The significance of the mathematical model developed was tested through ANOVA. RSM, GA using ANN also used for finding out the minimum value of responses at the optimum combination value of input process variables taken for analysis.

3.5.1. Experimental design parameters setup for AA1100 feed material

The five independent factors with a three-level full factorial design were chosen to obtain and model AA1100 alloy output characteristics through the RCE process. The input values of the independent variables at three levels are shown in Table 3.10.

Table 3. 10: Independent process variables

Factors	Levels		
	−1	0	1
Speed of extrusion wheel (*RPM*)	2	6	10
Product diameter (*mm*)	6	7	8
Frictional conditions	0.6	0.8	1.0
Feedstock temperature (℃)	100	300	500
Die temperature (℃)	400	450	500

A total of 32 experiments were generated as per the design of the experiment for five factors and three levels using the Central Composite Rotatable Design (CCRD) method. The entire detailed experimental plans are also shown in Table 3.11.

3.5.2. Experimental design for AA1100 feedstock

The independent variables such as extrudate diameter and extrusion wheel velocity and their levels used to carry out the experiments are shown in Table 3.12. A total of 13 experiments were planned on two factors and three levels using CCRD of RSM. The plans performed using DEFORM-3D tool. The feedstock materials with a diameter of 9.5mm were extruded to diameters of 6mm, 7mm, and 8mm computationally. The extrusion (deformation) of the feed metal was carried out at the various driving wheel speeds of 4, 6, and 8rpm.

Table 3. 11: Details of experiments listed as per CCRD

Run	**Block**	**Velocity of wheel (RPM)**		**Diameter of product (mm)**		**Friction factor**		**Feedstock temperature (℃)**		**Die temperature (℃)**	
		Coded	Actual	Coded	Actual	Coded	Actual	Coded	Actual	Coded	Actual
1	1	-1	2	1	8	1	1.0	1	500	-1	400
2	1	1	10	1	8	-1	0.6	1	500	-1	400
3	1	0	6	0	7	0	0.8	0	300	0	450
4	1	0	6	0	7	0	0.8	0	300	0	450
5	1	-1	2	-1	6	-1	0.6	-1	100	1	500
6	1	-1	2	-1	6	1	1.0	-1	100	-1	400
7	1	-1	2	1	8	1	1.0	-1	100	1	500
8	1	0	6	0	7	0	0.8	-2	100	0	450
9	1	0	6	2	9	0	0.8	0	300	0	450
10	1	1	10	1	8	1	1.0	-1	100	-1	400
11	1	0	6	0	7	0	0.8	0	300	2	550
12	1	0	6	0	7	0	0.8	0	300	0	450
13	1	0	6	0	7	0	0.8	0	300	-2	350
14	1	0	6	0	7	0	0.8	0	300	0	450
15	1	-1	2	1	8	-1	0.6	-1	100	-1	400
16	1	1	10	-1	6	-1	0.6	-1	100	-1	400
17	1	-1	2	1	8	-1	0.6	1	500	1	500
18	1	0	6	0	7	0	0.8	0	300	0	450
19	1	−1	2	−1	6	-1	0.6	1	500	−1	400
20	1	2	14	0	7	0	0.8	0	300	0	450
21	1	0	6	−2	5	0	0.8	0	300	0	450
22	1	1	10	1	8	1	1.0	1	500	1	500
23	1	1	10	−1	6	-1	0.6	1	500	1	500
24	1	0	6	0	7	2	1.2	0	300	0	450
25	1	0	6	0	7	-2	0.4	0	300	0	450
26	1	-2	-2	0	7	0	0.8	0	300	0	450
27	1	0	6	0	7	0	0.8	0	300	0	450
28	1	1	10	1	8	-1	0.6	-1	100	1	500
29	1	1	10	-1	6	1	1.0	1	500	-1	400
30	1	0	6	0	7	0	0.8	2	700	0	450
31	1	1	10	-1	6	1	1.0	-1	100	1	500
32	1	-1	2	-1	6	1	1.0	1	500	1	500

The 13 experiments in Table 3.13 were carried out to investigate the effects of the process parameters on the metallurgical as well as mechanical properties of the metal pre and post-extrusion processes. The mathematical modeling also developed through RSM to investigate the extrudate yield strength and percentage of elongation. The significance of the mathematical model developed was tested through ANOVA.

Table 3. 12: Input parameters and their levels

	Levels of factor		
Factors	-1	0	1
Driving wheel rpm	4	7	10
Extrudate diameter (mm)	6	7	8

Table 3. 13: Experiments to the analysis of extrudate yield strength

Experiment No.	**Driving wheel speed (RPM)**		**Extrudate diameter (mm)**	
	Coded values	**Actual Values**	**Coded values**	**Actual Values**
1	-2	1	0	7
2	1	10	1	8
3	-1	4	1	8
4	0	7	0	7
5	0	7	-2	5
6	0	7	0	7
7	2	13	0	7
8	-1	4	-1	6
9	0	7	0	7
10	1	10	-1	6
11	0	7	2	9
12	0	7	0	7
13	0	7	0	7

3.5.3. Experimental design for Copper feed of C101 grade

Independent process variables used for numerical modeling and optimization of CE process parameters for C101 Copper alloy are shown in Table 3.14,

Table 3. 14: Independent process variables for C101 Copper feed

Factors	Levels		
	−1	0	1
Speed of extrusion wheel (*RPM*)	4	8	12
Product diameter (*mm*)	6	6	6
Frictional conditions	0.85	0.925	1.0
Feedstock temperature (℃)	500	675	850
Die temperature (℃)	400	500	600

The four independent factors at three-level full factorial design were chosen to find and model output characteristics of the process. The factors investigated were driving velocity, frictional factor, feedstock temperature, and die temperature. A total of 31 experiments, shown in Table 3.15, were generated for four factors at three levels using CCRD by taking a product diameter of 6mm.

RSM was used for finding out the minimum value of extrusion load at the optimum value of corresponding input variables such as wheel driving speed, diameter of extrudate, friction factor, feedstock temperature, and die temperature. Based on analysis of variance (ANOVA) table, the least value of the significance level of the factor was indicated by P - the value to develop the mathematical model.

Table 3. 15: Details of experiments as per CCRD for C101 Copper feed

Std. order	Run order	Wheel velocity (RPM)	Feedstock temperature (℃)	Die temperature (℃)	Friction factor
29	1	8	675	500	0.925
3	2	4	850	400	0.850
5	3	4	500	600	0.850
25	4	8	675	500	0.925
30	5	8	675	500	0.925
12	6	12	850	400	1.000
26	7	8	675	500	0.925
15	8	4	850	600	1.000
18	9	16	675	500	0.925
16	10	12	850	600	1.000
21	11	8	675	300	0.925
1	12	4	500	400	0.850
17	13	0	675	500	0.925
24	14	8	675	500	1.075
7	15	4	850	600	0.850
6	16	12	500	600	0.850
2	17	12	500	400	0.850
11	18	4	850	400	1.000
14	19	12	500	600	1.000
28	20	8	675	500	0.925
20	21	8	1025	500	0.925
13	22	4	500	600	1.000
27	23	8	675	500	0.925
4	24	12	850	400	0.850
10	25	12	500	400	1.000
31	26	8	675	500	0.925
9	27	4	500	400	1.000
8	28	12	850	600	0.850
19	29	8	325	500	0.925
22	30	8	675	700	0.925
23	31	8	675	500	0.775

3.5.4. Experimental design for Copper-Zirconium-Chromium (C18150)

Computational investigations, numerical modeling and optimization of the CE input process parameters to extrude a C18150 alloy were performed. The four independent variables: wheel velocity, frictional factor, feedstock temperature, and die temperature were chosen to investigate response characteristics. Table 3.16 below shows the parameters with the levels taking a product diameter of 8mm were used the analysis.

Table 3. 16: Experimental parameters and levels for C18150 alloy

Factors	Level		
	-1	0	1
Wheel Velocity (RPM)	4	8	12
Product diameter (mm)	8	8	8
Feedstock temperature (^oC)	500	600	700
Die Temperature (^oC)	400	500	600
Friction condition	0.85	0.90	0.95

A total of 27 experiments were generated as per DOE for the factors based on the Box Behnken Design method. Those 27 computational experiments shown in Table 3.17 were carried out to investigate output characteristics for C18150 feedstock material with 8mm product diameter through CE process.

Table 3. 17: Box Behnken Design for product diameter of 8mm C18150 alloy

S. No	Wheel Velocity (RPM)	Feedstock temperature	Die Temperature	Friction Factor
1	4	600	500	0.95
2	8	600	500	0.90
3	12	600	600	0.90
4	8	600	400	0.85
5	8	500	500	0.95
6	12	600	500	0.85
7	12	600	400	0.90
8	8	600	500	0.90
9	8	700	600	0.90
10	8	700	400	0.90
11	4	500	500	0.90
12	12	500	500	0.90
13	12	600	500	0.95
14	4	600	400	0.90
15	8	600	400	0.95
16	12	700	500	0.90
17	8	500	500	0.85
18	8	600	600	0.85
19	4	700	500	0.90
20	4	600	600	0.90
21	8	600	600	0.95
22	8	600	500	0.90
23	8	700	500	0.95
24	8	700	500	0.85
25	8	500	600	0.90
26	4	600	500	0.85
27	8	500	400	0.90

Based on analysis of variance table, the significance level of the input factors were checked with the least P value. RSM and ANN-GA were used to determine the minimum value of output characteristics at the optimum combination of input variables.

3.6. Mathematical Modelling and Optimization of Variables using RSM, ANN-GA

All the designed experiments were carried out numerically using Finite Element simulation tool DEFORM-3D. The response characteristics of Conform extrusion of AA1100, C101, and C18150 grade alloys were collected based on the designed experimental setups. The responses considered in these investigations were total extrusion load, the effective stress and damage induced in the raw material and extrudate. The relation between the input process parameters and the dependent ones was developed using a general mathematical expression of second-order polynomial equation of the regression model, (Eq. 3.60). The number of terms in the model was based on the number of independent parameters considered. The optimum values of Conform extrusion response characteristics of AA1100, C101, and C18150 grade alloys were determined using Response Surface Methodology (RSM). Through RSM, a mathematical modelling was developed to optimize the response characteristics. The model was presented as follows in eq. 3.44

$$Y = \beta_0 + \sum_{i=1}^{n} \beta_i x_i + \sum_{i=1}^{n} \beta_{ii} x^2{}_i + \sum_{i<j}^{n} \sum \beta_{ij} x_i x_j + \varepsilon \quad \ldots\ldots\ldots\ldots\ldots\ldots\ldots\ldots \text{(3.44)}$$

Where, Y: the response variable; β_0: Constant or the grand average of the response variables; x_i: the coded value of the input parameters of the i_{th} CE parameters for the u_{th} experiments; β_i, β_{ii}, β_{ij}: the coefficients of the linear effect, the quadratic effect, and the interaction effect for ith factor of the regression model respectively; ε: random-error

From summarized results of responses, ANOVA and significant test values of independent factors affecting dependent parameter were taken for determination based on their P-value. If P-value of any treatment fell below 0.05, then the treatment had significant influence on the dependent variable. The statistical significance of the mathematical model was verified through analysis of variance (ANOVA). The value of correlation coefficient (R^2) and adjusted R^2 were also considered and should be found to be just above the standards which indicate that the data are well correlated with the regression mathematical model developed. Second-order regression model was used for RSM mathematical modeling of process variables. In addition to RSM, ANN-GA also applied to accurately predict the best output process characteristics of the Conform extrusion.

3.7. Experimentation

The details of a distinctive experimental set-up and procedures are given under the corresponding feedstock material load optimization section. The main input parameters taken for consideration were the extrusion wheel speed, product size, tool (die) temperature, and friction factor and feedstock temperature. The product diameters taken for these investigations were from 6 to 10mm in diameter depending on the type of feed material extruded taking the driving wheel velocity of a commercial setup of TBJ 350 machine. The parameters collected directly from the machine were current and voltage to determine the power the CE process consumed during the process.

3.7.1. Experimental test data layout

The detailed values of the corresponding input variables for machine setup for experimentation were taken from the optimized results of the corresponding materials through RSM, ANN-GA. The feedstock materials were extruded using a commercially available continuous extrusion set up using the input parameters for the optimized load. For the investigation, TBJ350 Continuous forming extrusion machine shown in Fig. 3.5 was used. The machine was run with a powerful a variable drive frequency motor coupled with a reduction gearbox used to run the extrusion wheel and AC motor to run the hydraulic system that control the extrusion shoe movement. The specifications of TBJ350 continuous forming extrusion machine are shown in Table 3.18

FIGURE 3. 5: A COMMERCIAL CE SETUP OF THE TBJ350 MACHINE

Table 3. 18: Specification of the TBJ350 commercial setup

S. No.	Parameters	Values	Applications
1	Extrusion wheel speed	4-12.5rpm	Pure copper / copper alloy and Aluminum /Aluminum alloy
2	Feedstock Diameter	12.5mm	
3	Extrusion wheel Diameter	350 mm	
4	Motor Power	180kW	
5	Power kw:	DC180AC180	
6	Bed Length	5m	

Prior to the final experimentations, pilot experimentations with the extreme parameters set-up were also performed for Al1100, C101 and C18150 materials to consider the deformation behavior of the feedstock materials and fix input parameter range setting.

3.8. Microstructural Analysis

All the samples taken for the investigation had circular shapes of the feed metal and extrudates. The microstructure analyses of the samples were carried out using Light Optical Microscopy (LOM). The samples for microstructure analysis and hardness were prepared from the feed metal and the extrudates manufactured at different combinations of input process parameters. The microstructure test samples of feed metals and extrudates were prepared. The standard procedures followed for the analysis were cut-off, mounting (optional), grinding and polishing, etching, and evaluation using the microscope. The sample faces were ground with emery papers with grain sizes from P240 → P320 → P600 → P1200. The samples were then polished on velvet using a diamond abrasive emulsion, Brasso, and kerosene. The samples' surfaces were etched chemically with appropriate etchant and dipped within a certain period depending on the alloy compositions to expose grain boundaries. The same samples were used for micro-structure and hardness tests. Magnifications of 50×, 100× and 200× were used for all AA1100 and C101 samples; however, the microstructures of C18150 samples were captured at 100x, 200x, and 400x magnifications.PL-Ink captures and Axiovision Rel 4.8 software were used to take the images under a microscope.

Grain size measurement and its comparison pre and post-extrusion were performed by taking standard length at different places in the image and the equations applied for estimation are given as shown in Eq.3.45 (Struers, V. V. C. L., & Yang, D., 2019; Higginson, V. V. C. L., *et al*., 2003).

$$d = \frac{(L_{ave})}{M} \quad \ldots\ldots\ldots\ldots\ldots\ldots\ldots\ldots\ldots\ldots\ldots\ldots\ldots\ldots\ldots\ldots \quad (3.45)$$

Where d: grain diameter; L: average grain length; M: magnification

The grain shape factor is constant for every material (eq. 3.46). Therefore its value can be neglected for comparison pre and post-extrusion.

$$L(ave) = \frac{1}{N}\sum\frac{L}{n_i} \qquad (3.46)$$

Where N: number of data; L: real visible and measured test length; n_i: number of intercepts

3.8.1. AA1100 samples

The microstructure analysis of the aluminum alloy was performed using LOM that is shown in Fig. 3.9. The microstructure analysis samples with samples of feed metal 9.5mm and extrudates 8mm and 7mm are shown in Fig. 3.6. .All the standard procedures of microstructural analysis stated in section 3.8 were followed for AA1100 investigation. The surfaces of the aluminum samples were etched chemically with Keller's reagent.

(a) **(b)** **(c)**

FIGURE 3. 6: AA1100 MICROSTRUCTURE AND HARDNESS TESTING SAMPLES

Finally, the polished and scratch-free samples were mounted on the slide and placed under the microscope with magnifications of 50×, 100×, and 200×, as stated in section 3.8, to obtain the microstructures of the prepared samples. PL-Ink capture and Axiovision Rel 4.8 software were used for obtaining the images under the microscope. The same samples of AA1100 metals shown in Fig 3.6 were also used for hardness testing.

3.8.2. Pure Copper samples

The microstructure analyses of C101 Copper samples were carried out using Light Optical Microscopy (LOM) shown in Fig.3.9. The microstructure test samples were prepared from the feed metal as well as the extrudates of various sizes manufactured at various Conform extrusion input process parameters are shown in Fig. 3.7. During the investigation, the standard procedures, stated in section 3.8, were followed. Velvet cloth, Brasso, and Kerosene were used while polishing the prepared samples. After polishing, the samples were etched using Ferric chloride in a suspension of hydrofluoric acid and water.

FIGURE 3. 7: MICROSTRUCTURAL AND HARDNESS TEST SAMPLES OF C101

Finally, the polished scratch-free samples are mounted on the slide and placed under the microscope with different magnifications of 50×, 100×, and 200×, as stated in section 3.8, to obtain the microstructures of the prepared samples. PL-Ink capture and Axiovision Rel 4.8 software were used for obtaining the images under the microscope. The sample with 12.5mm was the feed rod and 8mm and 6mm were the extrudates. The same samples of C101 metals shown in Fig 3.7 were used for hardness testing too.

3.8.3. C18150 alloy

The standard procedure stated in 3.8 was followed. The C18150 test sample faces were grounded with emery papers (cloths) having the following grades in sequence P240 → P320 → P600 → P1200. The specimens were then polished using velvet with a diamond abrasive emulsion. The sample faces were etched chemically with Copper No. 1 etchant (a solution of nitric acid with distilled water) and the samples were dipped for a period of 30-60sec to expose grain boundaries. For three C18150 rods of 8mm, 10mm, and 12.5mm diameters, the microstructure was observed with an Olympus GX71 optical microscope shown in Fig. 3.9. Their microstructures were captured at 100×, 200×, and 400× magnifications. For microstructure and hardness testing, mounted C18150 specimens are shown in Fig. 3.8.

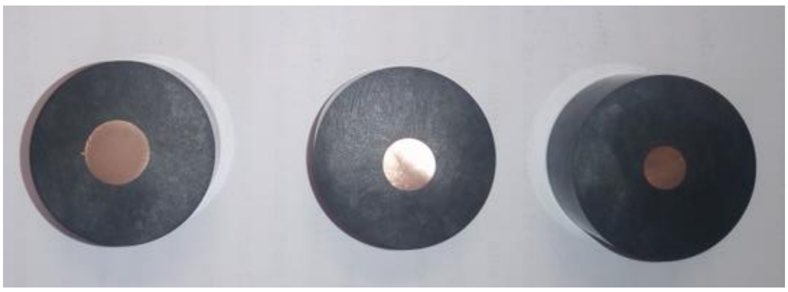

FIGURE 3. 8: C18150 MICROSTRUCTURE AND HARDNESS SPECIMENS

3.9. Hardness Testing of AA1100, C101 and C18150

AA1100 samples of diameters of 9.5mm feed metal and extrudates of that of 8mm and 7mm; Samples of 12.5mm diameter feedstock, 6, 7, and 8mm in diameters of C101; and 8mm, and 10mm diameters of Conform extruded C18150 alloy rods were polished using different grades of sandpapers to make their surfaces dents free before hardness testing. Micro-Vickers hardness (Fig. 3.10) testing machine was used. A 0.1kgf load was applied with a dwell time of 10sec for hardness measurements. The hardness was measured from the center to the surface for each rod as per ASTM E384. An average hardness value was taken for analysis after three trials. Figure 3.11 shows the schematic representation of the locations of hardness indentation on the rods along the radial line during hardness measurement.

FIGURE 3. 9: OLYMPUS GX71 MODEL OPTICAL MICROSCOPE

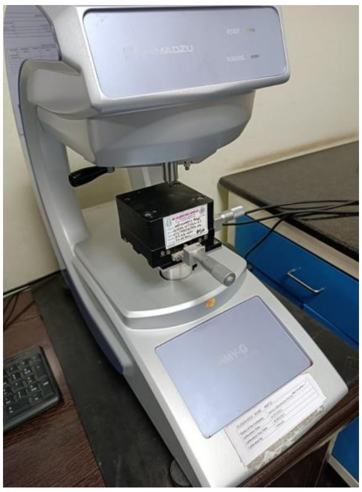

FIGURE 3. 10: HARDNESS TESTING MACHINE

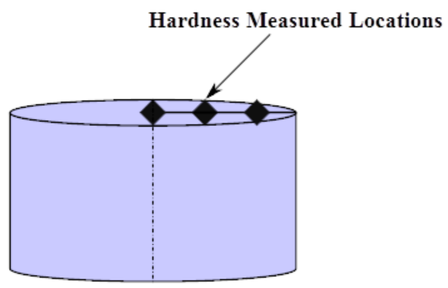

FIGURE 3. 11: SCHEMATIC REPRESENTATION OF THE HARDNESS MEASUREMENT

3.10. Investigations on the Mechanical Properties

Tensile testing carried out to investigate the CE input variables influence on the mechanical behavior of CE extrudate of Al1100, C101, and C18150 alloys. Standard test samples were prepared and testing also conducted based on ASTM standards which included placing the sample with a well-defined shape between two grips (clamps) and loading the sample with a well-defined magnitude along the axis in tension normally to fail. The resultant load and accompanied displacement were recorded to determine mechanical properties.

3.10.1. Tensile testing of AA1100

The AA1100 tensile test samples of feed and extrudates were prepared according to the ASTM-B557 standard with a gauge length of 15.6mm, 4.5mm gauge diameter, and a total length of 30mm as shown in Fig. 3.12. The tensile test was performed on an Instron machine a strain rate of 1mm per minute shown in Fig. 3.13. The strength and percentage of elongation data were collected. All specimens were tested until they fail. Three repetitive tests were conducted to take the average value of yield strength and percentage of elongation.

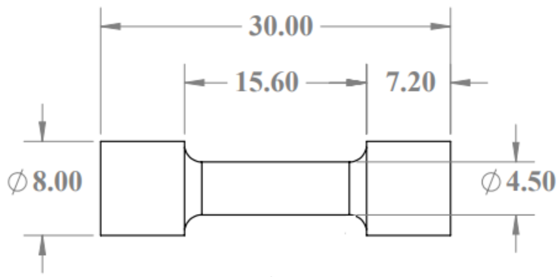

FIGURE 3. 12: ALUMINUM TENSILE TEST SAMPLE

3.10.2. Tensile testing of Copper (C101)

FIGURE 3. 13: INSTRON UNIVERSAL TESTER

The testing was then carried out using the Instron machine with a strain rate of 1mm per minute (Fig. 3.13). Test results of UTS samples were recorded after the test. The tensile testing performed according to ASTM E8M testing standards. Therefore, the test specimens of the feed metal and extrudate were machined to size as per the standard and shown in Fig. 3.14. The specimens' gauge lengths and gauge diameters were 22.5mm and 4.5mm respectively.

FIGURE 3. 14: TENSILE TEST SAMPLE OF A C101 ROD

3.10.3. Tensile testing of Cu-Cr-Zr (C18150)

The mechanical properties of C18150 rods of 12.5mm feedstock, 10mm, and 8mm extrudates were tested using an MCS/UTE 20T tensile testing machine (Fig. 3.15) according to ASTM-E8M. The tests were conducted at a nominal cross-head speed of 2mm/min with the machine at room temperature. For each set, the tests were repeated twice for reproducibility.

FIGURE 3. 15: MCS/UTE 20T TENSILE TESTING MACHINE

Slippage (failure from grip) during testing did not observe. Outer surface machined and as-extrudate specimen samples are shown in Fig. 3.16. The mechanical properties of the specimen responses such as strength (both tensile and yield), and total elongation were recorded by conducting repeated trials as per the standard procedure.

a) as-extrude **b) machined**

FIGURE 3. 16: TENSILE TESTING SPECIMENS

3.11. Wear Testing of Feedstock and Extrudates

The tribology testing method applied in the investigation was a dry-friction type. It is a sliding motion between the test pin (test sample) and a disk in a dry friction case at ambient room temperature. A Micro Pin on Disc TRIBOMETER (TR-20Micro) machine shown in Fig. 3.17 was used to investigate the effects of CEP process parameters on the wear characteristics of the extrudates of AA1100 and C101 materials. The characteristics investigated were wear rate, coefficient of friction (CoF), and coefficient of wear rate.

FIGURE 3. 17: MICRO PIN ON DISC TRIBOMETER (TR-20MICRO) MACHINE

The machine had a horizontal rotating disc and a pin with calibrated dead-weight load. In the testing, the tip of the pin was in the form of a non-rotating cylinder. The friction force and pin vertical movement (displacement) was automatically measured in the machine with a load cell and a linear variable differential transformer (LVDT) respectively.

3.11.1. AA1100 alloy and C101 alloy

The test specimens (pins) were manufactured from AA1100 and C101 CEP extrudates. The experimental setups and conditions for wear test of Al1100 and C101 metals presented in Table 3.19.

Table 3. 19: Sliding wear test parameters and experimental conditions

Parameters (conditions)	**Al1100**	**C101**	**C18150**
Temperature (°C)	12	12	12
Relative humidity (%)	58	58	58
Applied normal load (N)	10	20	20,30,40
Sample pin diameter in (mm)	6	6	8,10,12.5
Sample pin length in (mm)	12	12	12
Sliding Speed (m/s)/RPM	0.5 / 318	0.5 /318	0.5/318
Sliding distance (m)	500	500	500,600,700
Wear track diameter(mm)	30	30	30
The density of material (g/cm^3)	2.72	8.92	8.89

The testing environment was ambient and almost the same for each. For all Al1100 and C101 experiments, the normal load on the pin was the same for each metal category and was set to 10N and 20N respectively. Before and after each experiment, all specimens and the disc were cleaned using acetone and air-dried.

The wear test specimens preparation and tests were performed based on the ASTM G99 wear test pin on disc (Designation: G 99-95a (Reapproved 2000)) standard. The diameter of the typical disk track used for the investigation was 30mm and the disc also had a thickness of 10mm.

The test samples were prepared based on the testing machine's recommended sizes for the test diameter and length. Each test specimen's dimensions were 6mm in diameter and 12 mm in length for both AA1100 and C101 CE extrudates. The wear test specimens were machined to size using an engine lathe of Pinächo SP/180 Lathe machine. Wear test Specimens of Cu101 and AA1100 are shown in Fig 3.18 and Fig 3.19.

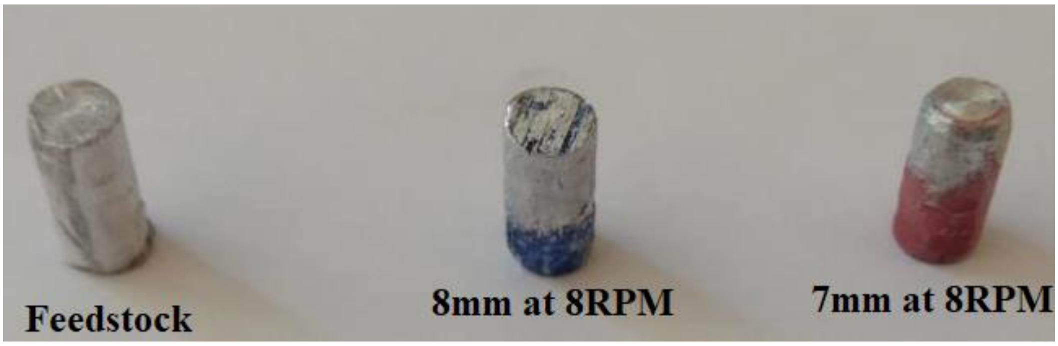

FIGURE 3. 18: AA1100 SAMPLES FOR WEAR TEST

FIGURE 3. 19: C101 EXTRUDATE SAMPLES FOR WEAR TEST

The sliding wear behavior of the Al1100 aluminum sample was studied as a function of extrusion wheel speed of 6, 8, and 10RPM using a pin-on-disk test system. The sliding wear behavior of the C101 copper sample was studied as a function of extrusion wheel speed of 6, 7, and 8mm using a pin-on-disk test system.

3.11.2. C18150 grade alloy

Dry sliding wear tests were performed on a pin-on-disc type machine of model Ducom TR-201 apparatus shown in Fig. 3.20 and a specimen holding system in Fig. 3.21. The test specimen dimensions were made as per ASTM G99 and tested. Wear tests were performed by varying the speeds (500, 600, and 700rpm) and loads (20, 30, and 40kN) on the three sample rods (12.5mm, 10mm, and 8mm) under normal atmospheric conditions. Load, speed (RPM), and diameter of the rods were the input process parameters considered for analysis based on the standard testing periods. The parameters were arranged as per the L9 orthogonal array of Taguchi design shown in Table 3.20 to minimize the number of experiments. The response variable considered is the specific wear rate.

FIGURE 3. 19: PIN-ON DISK TESTING SETUP FOR C18150 ALLOY

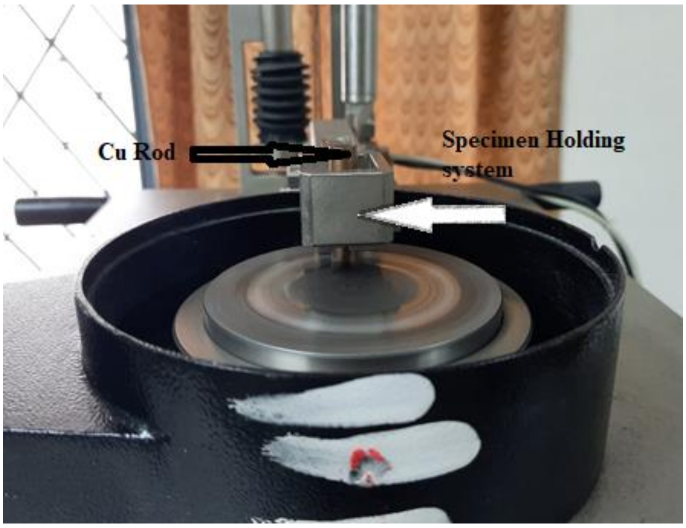

FIGURE 3. 20: SPECIMEN FIXING ON PIN-ON DISK TESTING MACHINE

Table 3. 20: Levels of wear test performance parameters

Process parameter	Level 1	Level 2	Level 3
Load (kN)	20	30	40
Speed (RPM)	500	600	700
Rod Diameter (mm)	8	10	12.5

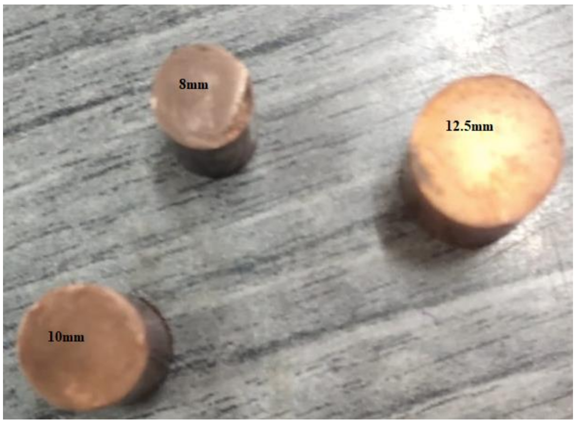

FIGURE 3. 21: C18150 ALLOY WEAR TEST SAMPLES BEFORE TESTING

The wear test samples having the dimensions of 8mm, 10mm, and 12.5mm diameter is shown in Fig. 3.22. EN31 steel was used for the test disk material. The worn-out samples, the pin, and the disk faces were cleaned properly with acetone and weighed in the balance after every test. Coefficients of frictions were continuously measured with an electric sensor attached to the machine and appropriately recorded.

CHAPTER 4: RESULTS AND DISCUSSION

4.1. Introduction

This chapter deals with the results and discussion on analytical, computational, optimization, experimental, characterization and testing of CE extruded of Al (AA1100), Cu (C101) and Cu-Cr-Zr (C18150) alloys. In the CE setup, the optimal combination of parameters such as extrusion ratio, extrusion wheel velocity, feedstock temperature, die temperature and friction factor were considered to determine responses. The effect of CE input processes parameters on responses such as extrusion load requirement, effective stress, damage, microstructure, mechanical and wear properties of Al (AA1100), Cu (C101) and Cu-Cr-Zr (C18150) alloys were investigated. Continuous extrusion setup was used to carry out experiments for AA1100, C101 and C18150 alloys in this sub-chapter. An experimental validation of the experimental results were performed on Aluminum (AA1100) and Copper (C101) and Copper-Chromium-Zirconium (C18150) alloys and found in good agreement with RCE simulation, and theoretical results. The results obtained would be required to be validated to ensure the correctness of the theory, computational (simulations), and practice (experiments). Material characterization of the product samples such as microstructure analysis, tensile test and hardness test before and after deformation has been carried out for the test samples to predict the material properties of the feedstock. The characterization and testing were made for all samples of pre and post deformation processes.

4.2. The Optimized CE Extrusion Load (Analytical Investigation)

The theoretical investigation was carried out through UBM to determine the extrusion load necessary for CE. During the analytical investigation, assumptions, governing equations and boundary conditions stated in section 3.3 were applied to determine the optimal response that is the optimized load and the summery of the analysis is tabulated in Table 4.1. In this investigation, the punch load was investigated using UBM. All loads obtained through computational and experimental methods are also incorporated in the table.

The rate of total energy was expressed taking work of deformation at different deformation stages and shown in Eq.3. 14. Hill (1963) developed the generalized expression which consists of three terms for total deformation energy using UBM Eq.1.1.

Avitzur and Tyne (1982) also developed a generalized expression for the total work-done per unit volume and time in the geometrically self-consistency region using of UBT from Eq. (1.1) for the conventional direct extrusion process. Wood also proposed a similar expression of Eq. 1.1 for conform extrusion (Wood, P. K., 1990) as follows,

$$P = W_T = W_{t(1-2a)} + W_{t(2b-3)} + W_{t(3-5)} \quad (4.1)$$

To perform complete analysis, the deformation zone of the Conform extrusion process was sectioned into definable stages of deformation which was plastic in-between feedstock entry and die-exit planes. Mingdian and Baoyun (1993) segmented the Continuous forming process into five sub-sections for the power investigation: (1) biting, (2) upsetting, (3) filing, (4) extruding, and (5) flashing, as described in Fig.4.1. However, once the process starts it immediately becomes in the steady-state process, the powers requirement for the biting (1) and upsetting regions (2) and is relatively smaller than those for the other regions so that the effects of these two sub-regions can be neglected without a significant loss of accuracy (Kim, Y. H., *et al.*, 2000; Kim, Y. H., *et al.*, 1998). Additionally in this investigation, the velocity discontinuity and power loss due to frictional loss in the biting and upsetting section neglected. Additionally once the traditional extrusion could be made continuous process, the problems connected with sealing of the high pressure fluid would be absent (Lengyel, B., *et al.*, 1977; Green D., 1972).

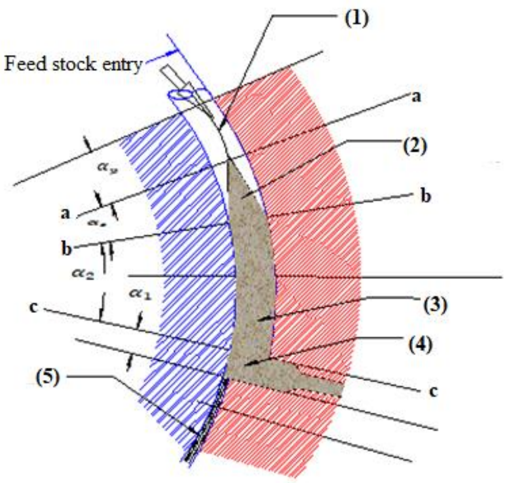

FIGURE 4. 1: DEFINITION OF THE FIVE SUB-REGIONS FOR CALCULATING THE DRIVING POWER

Therefore, for the CE processes without a flash gap (this similarity holds true for the process with a relatively small flash gap), similarity for it was made to the side extrusion shown in Fig. 4.1, where the driving wheel was assumed to a rigid punch and a frictionless side plate. Then, the resistance force was due to the friction at the shoe, the abutment , the die and the velocity discontinuities in the regions (I) and (II) were neglected without significant influence (Kim, Y. H., *et al*., 2000). The continuous process was illustrated in detail regarding the deformation zones in Fig.4.2.

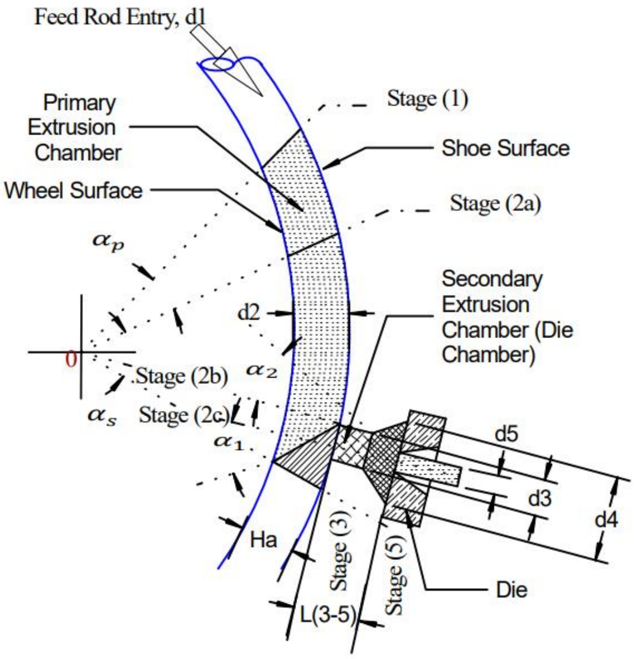

FIGURE 4. 2: REPRESENATION OF DIFFERENT STAGES IN CE (Wood, P. K. 1990)

Where:- *d1: feed stock diameter; d2: diameter of feed metal in the stage 2b; d3:extrusion die chamber; d4: dead zone angle chamber; d5: extrudate diameter;* $a_{1:}$ *angle of dead zone at stages 2b to 3;* a_2 *angle of dead zone at stages 2b to 3; L(3-5)= extrusion chamber length*

I. Work of Deformation for stages 1 to 2a

In this primary deformation stage, the feedstock materials dragged and bent along the grooves of the extrusion wheel groove. The driving wheel was assumed to a rigid punch and a frictionless side plate. In this section both power loss due to friction and power loss due to velocity discontinuity or redundant work were neglected with no significant influence on the total power requirements (Silva, J. D., *et al*., 2021; Silberschmidt, V. V., 2020; Molaei, S. H., *et al*., 2014; Hwang, Y. M., & Hwang, T. F., 2002; Kim, Y. H., *et al*., 2000; Wu, C. W., & Hsu, R. Q., 2000; Wood, P. K., 1990). To cause lateral yielding of the feedstock material in the primary deformation zone small load was sufficed to generate homogeneous deformation in this section. Therefore, the mathematical expression in Eq. 3. 25 can be rewritten for Primary Deformation Zone as follows:

$$W_{t(1-2a)} = \int_{1}^{2a} \bar{\sigma}_{(1-2a)} \delta\varepsilon \ \ldots\ldots\ldots\ldots\ldots\ldots\ldots\ldots\ldots\ldots\ldots\ldots\ldots\ldots\ldots\ldots \text{(4.2)}$$

$$\text{But } \bar{\sigma} = A(1 - BT_H)\varepsilon^n \dot{\varepsilon}^n \ \delta\varepsilon \ , \ T_H = \frac{T}{T_m} \ and \ \dot{\varepsilon}^m \cong 1 \ \ldots\ldots\ldots. \text{(4.3)}$$

Where:- $\bar{\sigma}$: Effective stress; A and B: constants; n: the strain hardening index which is assumed to be a constant for the range of strain; m: the strain rate sensitivity index which is a function of homologous temperature in the range of strain rates 1-40/s; T_m: is the feed metal melting temperature; T_H: homologous temperature; T: feed metal temperature in the primary or secondary gripping zone in the extrusion chamber-die zone

After substituting Eq. 4.2 in Eq. 4.3, the rate of energy dissipation in the griping zone can be estimated using Eq. 4.5.

$$W_{t(1-2a)} = \int_{1}^{2a} A(1 - BT_H)\varepsilon^n \dot{\varepsilon}^m \ \delta\varepsilon = \int_{1}^{2a} A(1 - BT / T_m)\varepsilon^n \delta\varepsilon \ \ldots\ldots\ldots\ldots\ldots\ldots \text{(4.4)}$$

$$W_{t(1-2a)} = A(1 - \frac{BT}{T_m}) \frac{\varepsilon_{1-2a}^{n+1}}{n+1} \ \ldots\ldots\ldots\ldots\ldots\ldots\ldots\ldots\ldots\ldots\ldots\ldots\ldots\ldots\ldots \text{(4.5)}$$

II. Work of deformation for stages 2b to 3

The secondary deformation zone that requires all the expressions was modified to generate upsetting and push forward the feedstock material to the abutment die chamber. A good modification of the upper bound expression after equation (Eq. 3.25) also proposed as follows (Silva, J. D., *et al.*, 2021; Silberschmidt, V. V., 2020; Molaei, S. H., *et al.*, 2014; Cao, F. R., *et al*., 2013; Hwang, Y. M., & Hwang, T. F., 2002; Kim, Y. H., *et al.*, 2000; Wu, C. W., & Hsu, R. Q., 2000; Wood, P. K., 1990).

$$W_{t(2b-3)} = \int_{2B}^{3} \bar{\sigma}_{(2b-3)} \delta\varepsilon + 2\kappa_{(2b-3)} \left[1.25 + \left(\frac{\alpha_1}{\sin^2(\alpha_1)} \right) - \cot(\alpha_1) \right] + 2\kappa_{(2b-3)} \cot(\alpha_1)\varepsilon_c \ldots$$

(4.6)

$$\text{But } \bar{\sigma} = A(1 - BT_H)\varepsilon^n \varepsilon^{\cdot m}, \ T_H = \frac{T}{T_m}, \ and \ \varepsilon^{\cdot m} = \frac{2\dot{V}_{2b} \ \varepsilon_{(2b-3)} \tan(\alpha_1)}{d_4}$$

$$\alpha_1 = \tan^{-1}(L_{(2b-2c)} - \frac{\frac{d_3}{2}}{H})$$

Where a_1: angle of dead zone at the face abutment tool in the deformation stages 2b to 3 (in degree); d_4: Die face exposed diameter (mm); H: abutment penetration into the extrusion wheel groove setting (mm)

It (α1) was determined by iteration for minimum upper bound. This dead zone is calculated using the α1 expression above. Moreover it is has a small effect on minimum UB.

$$W_{t(2b-3)} = \int_{2B}^{3} A(1-BT_H)\varepsilon^n \dot{\varepsilon}^m \delta\varepsilon + 2\kappa_{(2b-3)}\left[1.25 + \left(\frac{\alpha_1}{\sin^2(\alpha_1)}\right) - \cot(\alpha_1)\right] + 2\kappa_{(2b-3)}\cot(\alpha_1)\varepsilon_c \quad .. (4.7)$$

$$W_{t(2b-3)} = \int_{2B}^{3} (A(1-BT_H)\varepsilon^n 2\dot{V}_{2b}\,\varepsilon_{(2b-3)}\frac{\tan(\alpha_1)}{d_4})\delta\varepsilon + 2\kappa_{(2b-3)}\left[1.25 + \left(\frac{\alpha_1}{\sin^2(\alpha_1)}\right) - \cot(\alpha_1)\right] + 2\kappa_{(2b-3)}\cot(\alpha_1)\varepsilon_c \quad .. (4.8)$$

$$W_{t(2b-3)} = 2A\dot{V}_{2b}(\frac{\tan(\alpha_1)}{d_4})(1-B\frac{T}{T_m})\int_{2B}^{3} \varepsilon^n{}_{2b-3}\varepsilon_{(2b-3)}\delta\varepsilon + 2\kappa_{(2b-3)}\left[1.25 + \left(\frac{\alpha_1}{\sin^2(\alpha_1)}\right) - \cot(\alpha_1)\right] + 2\kappa_{(2b-3)}\cot(\alpha_1)\varepsilon_c$$

………………………………………………………. (4.9)

$$W_{t(2b-3)} = 2A\dot{V}_{2b}(\frac{\tan(\alpha_1)}{d_4})(1-B\frac{T}{T_m})\frac{\varepsilon^{n+1}_{(2b-3)}}{n+1} + 2\kappa_{(2b-3)}\left[1.25 + \left(\frac{\alpha_1}{\sin^2(\alpha_1)}\right) - \cot(\alpha_1)\right] + 2\kappa_{(2b-3)}\cot(\alpha_1)\varepsilon_c$$

…………………………………………………………………………………………. (4.10)

Where $\dot{V}_{2b}$: velocity at the secondary extrusion chamber

III. Work of deformation for stages 3 to 5

In order to decide the load at the extrusion die chamber using the optimal dead zone angle (25-70°) (Green D., 1970) and 45° was taken by Cao, *et al.*, (2013). The expression of Eq. 3.25 describing the power consumed due to the friction at the feedstock and extrusion chamber wall and die interface is neglected, i.e. m = 0.

$$W_{t(3-5)} = \int_{3}^{5} \sigma_{m(3-5)} f(\alpha_2)\varepsilon_{(3-5)} + 2\kappa_{m(3-5)}\left[\left(\frac{\alpha_2}{\sin^2(\alpha_2)}\right) - \cot(\alpha_2)\right] + \kappa_{m(3-5)}\cot(\alpha_2)\varepsilon_{(3-5)} + 2\tau_{m(3-5)}\left[(\frac{2L_{(3-5)}}{d_3}) - (1-\frac{d_5}{d_3})\cot(\alpha_2)\right]$$

……………………………………………………………………………………….………. (4.11)

Where:- $\sigma_{m(3-5)}$: average effective stress in the extrusion die chamber; f(a2): the average effective strain; L(3-5) = extrusion die chamber length = 14 mm (Directly from the machine); d3: Extrusion chamber entry diameter = 13 mm; d5: extrudate diameter (determined based on the analysis for each feedstock material product diameter)

But,

$$\bar{\sigma} = A(1-BT_H)\varepsilon^n \dot{\varepsilon}^m, \quad T_H = \frac{T}{T_m}, \; f(\alpha_2) = 1 + \frac{\alpha_2}{16} + \frac{5\alpha_2^{\,2}}{36} + \frac{2\alpha_2^{\,3}}{19}, \; and \;\; \dot{\varepsilon}^m = \frac{2\dot{V}_3\,\delta_{(3-5)}\tan(\alpha_2)}{d_4} \ldots\ldots$$

………………………………………………………………………………… (4.12)

$$W_{t(3-5)} = \int_3^5 A(1-BT_H)\varepsilon^n\,\dot{\varepsilon}^m(1 + \frac{\alpha_2}{16} + \frac{5\alpha_2^{\,2}}{36} + \frac{2\alpha_2^{\,3}}{19})\delta\varepsilon +$$

$$2\kappa_{(3-5)}\left[1.25 + \left(\frac{\alpha_2}{\sin^2(\alpha_2)}\right) - \cot(\alpha_2)\right] + 2\kappa_{(3-5)}\cot(\alpha_2)\varepsilon_c + 2\tau_{(3-5)}\left[(\frac{2L_{(3-5)}}{d_3}) - (1 - \frac{d_5}{d_3})\cot(\alpha_2)\right]$$

…………………… ……………………………………………………………….. (4.13)

When Eq.4.12 substituted in Eq.4.13:

$$W_{t(2b-3)} = 6A\dot{V}_3\,d_3^2\tan(\frac{(\alpha_1)}{(d_3^3 - d_5^3)})(1 + \frac{\alpha}{16} + \frac{5\alpha^2}{36} + \frac{2\alpha^3}{19})(1 - B\frac{T}{T_m})\int_3^5 \varepsilon\varepsilon^n\delta\varepsilon + \ldots$$

$$2\kappa_{(3-5)}\left[1.25 + \left(\frac{\alpha_1}{\sin^2(\alpha_1)}\right) - \cot(\alpha_1)\right] + 2\kappa_{(3-5)}\cot(\alpha_1)\varepsilon_c + 2\tau_{(3-5)}\left[(\frac{2L_{(3-5)}}{d_3}) - (1 - \frac{d_5}{d_3})\cot(\alpha_2)\right]$$

……………………………………………………………………………………(4.14)

$$W_{t(2b-3)} = 6A\dot{V}_3\,d_3^2\tan(\frac{(\alpha_1)}{(d_3^2 - d_5^2)})(1 + \frac{\alpha}{16} + \frac{5\alpha^2}{36} + \frac{2\alpha^3}{19})(1 - B\frac{T}{T_m})\int_3^5 \varepsilon\varepsilon^n\delta\varepsilon + 2\kappa_{(3-5)}\left[1.25 + \left(\frac{\alpha_1}{\sin^2(\alpha_1)}\right) - \cot(\alpha_1)\right] +$$

$$2\kappa_{(3-5)}\cot(\alpha_1)\varepsilon_c + 2\tau_{(3-5)}\left[(\frac{2L_{(3-5)}}{d_3}) - (1 - \frac{d_5}{d_3})\cot(\alpha_2)\right]$$

……………………………………………………………………………………… (4.15)

Where:- ***f*** *: friction factor in the extrusion chamber;* $\sigma_{(3-5)}$ *: Effective stress in the extrusion container-die chamber; L* $_{(3\text{-}5)}$*: Length of extrusion container-die chamber; d*$_{3}$*: diameter of extrudate; a*$_{2}$*: angle of dead zone at stages 3 to 5 (deg)*

According to Sheppard the angle of dead zone at stages 3 to 5 (*a*$_2$*):* is determined using (Sheppard, T., 1981).

$\alpha_2 = A + BLN(\varepsilon)$. *Where, A=54.1 and B=3.45.*

$$W_{t(2b-3)} = 6A\dot{V}_3\,d_3^2\tan(\frac{(\alpha_1)}{(d_3^3 - d_5^3)})(1 + \frac{\alpha}{16} + \frac{5\alpha^2}{36} + \frac{2\alpha^3}{19})(1 - B\frac{T}{T_m})\frac{\varepsilon_{(3-5)}^{n+1}}{n+1} +$$

$$2\kappa_{(3-5)}\left[1.25 + \left(\frac{\alpha_1}{\sin^2(\alpha_1)}\right) - \cot(\alpha_1)\right] + 2\kappa_{(3-5)}\cot(\alpha_1)\varepsilon_c + 2\tau_{(3-5)}\left[(\frac{2L_{(3-5)}}{d_3}) - (1 - \frac{d_5}{d_3})\cot(\alpha_2)\right] \ldots$$

……………………………………………………………………………...… (4.16)

$$W_{t(2b-3)} = 6A\dot{V}_3 \, d_3^2 \tan(\frac{(\alpha_1)}{(d_3^3 - d_5^3)})(1+\frac{\alpha}{16}+\frac{5\alpha^2}{36}+\frac{2\alpha^3}{19})(1-B\frac{T}{T_m})\int_3^5 \varepsilon\varepsilon^n \delta\varepsilon + \ldots$$

$$2\kappa_{(3-5)}\left[1.25+\left(\frac{\alpha_1}{\sin^2(\alpha_1)}\right)-\cot(\alpha_1)\right]+2\kappa_{(3-5)}\cot(\alpha_1)\varepsilon_c+2\tau_{(3-5)}\left[(\frac{2L_{(3-5)}}{d_3})-(1-\frac{d_5}{d_3})\cot(\alpha_2)\right]$$

……………………………………………………………………………… (4.17)

$$W_{t(2b-3)} = 6A\dot{V}_3 \, d_3^2 \tan(\frac{(\alpha_1)}{(d_3^3 - d_5^3)})(1+\frac{\alpha}{16}+\frac{5\alpha^2}{36}+\frac{2\alpha^3}{19})(1-B\frac{T}{T_m})\frac{\varepsilon_{(3-5)}^{n+1}}{n+1} + \ldots$$

$$2\kappa_{(3-5)}\left[1.25+\left(\frac{\alpha_1}{\sin^2(\alpha_1)}\right)-\cot(\alpha_1)\right]+2\kappa_{(3-5)}\cot(\alpha_1)\varepsilon_c+2\tau_{(3-5)}\left[(\frac{2L_{(3-5)}}{d_3})-(1-\frac{d_5}{d_3})\cot(\alpha_2)\right]$$

……………………………………………………………………………………… (4.18)

Where $\dot{V}_3$*: feed stock exit velocity*

Therefore Eq.3.14 can be rewritten in a detailed manner as follows:

$$W_T = A(1-\frac{BT}{T_m})\frac{\varepsilon_{1-2a}^{n+1}}{n+1}$$

$$+\left[2A\dot{V}_{2b}(\frac{\tan(\alpha_1)}{d_4})(1-B\frac{T}{T_m})\frac{\varepsilon_{(2b-3)}^{n+1}}{n+1}+2\kappa_{(2b-3)}\left[1.25+\left(\frac{\alpha_1}{\sin^2(\alpha_1)}\right)-\cot(\alpha_1)\right]+2\kappa_{(2b-3)}\cot(\alpha_1)\varepsilon_c\right] \ldots$$

$$+\left[\begin{array}{l} 6A\dot{V}_3 \, d_3^2 \tan(\frac{(\alpha_1)}{(d_3^3 - d_5^3)})(1+\frac{\alpha}{16}+\frac{5\alpha^2}{36}+\frac{2\alpha^3}{19})(1-B\frac{T}{T_m})\frac{\varepsilon_{(3-5)}^{n+1}}{n+1} + \\ 2\kappa_{(3-5)}\left[1.25+\left(\frac{\alpha_1}{\sin^2(\alpha_1)}\right)-\cot(\alpha_1)\right]+2\kappa_{(3-5)}\cot(\alpha_1)\varepsilon_c+2\tau_{(3-5)}\left[(\frac{2L_{(3-5)}}{d_3})-(1-\frac{d_5}{d_3})\cot(\alpha_2)\right]\end{array}\right]$$

………………………………………………………………………………………… (4.19)

Based on the formulated mathematical expressions for extrusion load with sufficient boundary conditions and assumptions, the theoretical results were calculated through UB Analysis for each material under different working conditions (process parameters) was summarized and tabulated in Table 4.1.

The theoretical analysis undertook a constant temperature rise across the plane in the transverse direction a derivative from the UBM equations in subsection 4.3. A more complex theoretical analysis was essential in order to define the relationship between the feedstock, friction factor, tool temperatures, feed metal temperatures and peripheral and surface temperature of conform extrusion tooling temperature and it was not within the scope of current investigation.

Table 4. 1: Theoretical power requirement for feedstock materials

AA1100 (*Feedstock Diameter=9.5mm)*	
Parameters	**Theoretical power (kW)**
Extrudate diameter=6mm,RPM of Extrusion wheel=8, Extrusion ratio=2.5	15.6
Extrudate diameter=7mm,RPM Extrusion wheel=8, Extrusion ratio=1.84	14.85
Extrudate diameter=8mm,RPM Extrusion wheel=8, Extrusion ratio=1.41	14.05
C101 *(Feedstock Diameter=12.5mm)*	
Extrudate diameter=6mm,RPM Extrusion wheel=8, Extrusion ratio=4.34	49.89
Extrudate diameter=7mm,RPM Extrusion wheel=8, Extrusion ratio=3.18	48.21
C18150 *(Feedstock Diameter=12.5mm)*	
Product diameter=6mm, RPM Extrusion wheel=8, Extrusion ratio=4.34	78.8
Product diameter=8 mm, RPM Extrusion wheel=8, Extrusion ratio=2.44	76.03
Extrudate diameter=10 mm, RPM Extrusion wheel=8, Extrusion ratio=1.56	73.66

However, the variation of CE input process parameters such as extrusion driving speed, friction factors and product diameter on feed stock temperature were investigated during computational analysis suing a finite element analysis tool-Deform 3D for comparative purposes.

4.3. Mathematical Modeling and Optimization

Mathematical modeling and optimizations were carried out based on the experimental plans developed for the proposed materials. A regression model was developed for each response as an equation with optimized combination of various process parameters to extrude a C101 alloy. If the p values in the Tables for the input variables were < 0.05 (i.e., greater than 95% confidence level) the linear and quadratic effect of the input variables were taken to develop the regression model. The significance test of the variables was performed using the data presented in their corresponding tables. The values of R^2, as well as adjusted R^2 should be above the standard. Details of the computational investigation process presented below.

4.3.1. Mathematical modeling and optimization for Aluminum (AA1100)

Mathematical modeling and optimizations were carried out based on the experimental plans developed for the AA1100 feedstock materials. Different responses were considered during the investigation.

4.3.1.1. Extrusion load modeling and optimization

In total, 32 numerical simulations were carried out as per the experiments generated using CCRD method (Table 3.11) for AA1100 feedmetal. Simulation pre-process conditions were performed as per Table 3.4 and Table 3.5 in Chapter III. The details of independent process variables are shown in Table 3.10.All the designed experiments were performed numerically through Finite Element simulation tool DEFORM-3D. The variables taken for numerical study were driving wheel speed, diameter of extrudate, feed metal temperature, die temperature and friction factor. The effects of the input variables of CE process were investigated on extrusion load. The total power requirement of extrusion system set-up during extrusion of raw material from its entry into grooved portion of extrusion wheel up to the final deformation through die exit are shown in Table 4.2.The simulation results of the extrusion load were generated along the principal directions. The resultants of the loads were calculated and presented in 4.2. Figure 4.3 shows a load prediction of AA 1100 feedstock material along the y-direction based on given input variable arrangements. The feed raw material used was of 9.5mm diameter of pure aluminum.

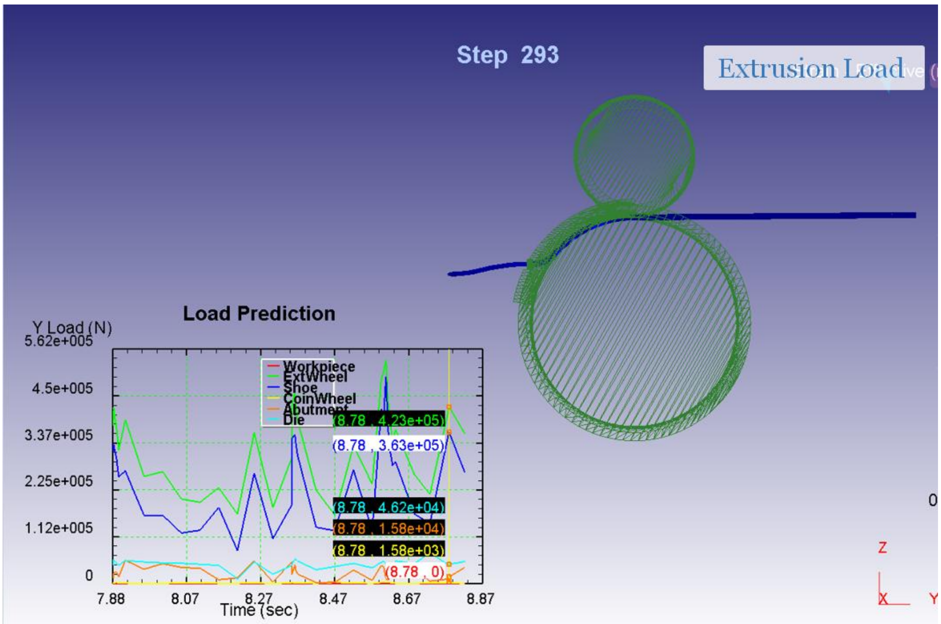

FIGURE 4. 3: Y-LOAD DISTRIBUTION FOR 9.5MM AA1100 FEEDSTOCK

Numerical simulations were carried out using DEFORM-3D computational tool. The resultants of the loads were calculated and presented in 4.2. RSM was used for modeling and optimization of output characteristic i.e., the force required for extrusion of the raw material using the five independent variables at three levels.

Consequently, if *P*-value of any treatment fell below 0.05, then the treatment or effect had significant influence on the dependent variable i.e., extrusion load. The significance of factors affecting dependent parameter was seen from Table 4.3. The value of correlation coefficient (R^2) and adjusted R^2 were found to be 91.49% and 86.07%, respectively, which indicated that the data were well correlated with the regression mathematical model developed.

Table 4. 2: Experimental plan and result based on CCRD for AA1100

Trial	CE input process variables and response					
	Wheel velocity (RPM)	**Product diameter (mm)**	**Friction condition**	**Feedstock temperature (℃)**	**Die temperature (℃)**	**Total load (kN)**
1	2	8	1.0	500	400	89.60
2	10	8	0.6	500	400	108.30
3	6	7	0.8	300	450	102.79
4	6	7	0.8	300	450	102.79
5	2	6	0.6	100	500	113.93
6	2	6	1.0	100	400	158.70
7	2	8	1.0	100	500	91.49
8	6	7	0.8	100	450	110.96
9	6	9	0.8	300	450	63.54
10	10	8	1.0	100	400	113.60
11	6	7	0.8	300	550	89.80
12	6	7	0.8	300	450	102.79
13	6	7	0.8	300	350	102.53
14	6	7	0.8	300	450	102.79
15	2	8	0.6	100	400	85.20
16	10	6	0.6	100	400	144.27
17	2	8	0.6	500	500	89.20
18	6	7	0.8	300	450	102.79
19	2	6	0.6	500	400	182.11
20	14	7	0.8	300	450	102.53
21	6	5	0.8	300	450	188.59
22	10	8	1.0	500	500	113.60
23	10	6	0.6	500	500	154.70
24	6	7	1.2	300	450	110.41
25	6	7	0.4	300	450	89.93
26	2	7	0.8	300	450	91.93
27	6	7	0.8	300	450	102.79
28	10	8	0.6	100	500	108.30
29	10	6	1.0	500	400	228.30
30	6	7	0.8	700	450	111.95
31	10	6	1.0	100	500	92.70
32	2	6	1.0	500	500	165.40

A regression model was developed to obtain an optimized total load to extrude AA1100 alloy. It was observed from Table 4.4 that the main effect, quadratic effect of X_2, interaction effect of X_2 and X_4, interaction effect of X_2 and X_5 were significant terms and taken to develop the regression model. The other terms that did not have much effect on extrusion load were neglected since their *p*-values were greater than least value of significance level. Therefore, the extrusion load was very much dependent on extrusion ratio during the extrusion process. Additionally, the feedstock temperature and die temperature also affected the extrusion load If die and feedstock temperature was increased, then shear resistance of material reducing thereby decreasing the load requirement during extrusion process. The mathematical expression (equation) model developed using Table 4.4 to determine optimal total load necessary to extrude AA1100 is shown in Eq. 4.20.

Table 4. 3: Test of significance for extrusion load for AA1100

Terms	Coefficients	Standard error coefficient	t-value	P-value
Constant	1469.76	479.113	3.068	0.011
wv	−1.98	13.399	−0.148	0.885
pd	−250.04	62.482	−4.002	0.002
fc	152.18	281.769	0.54	0.6
ft	0.3	0.268	1.138	0.279
dt	−2.12	1.358	−1.559	0.147
wv*wv	0.14	0.199	0.726	0.483
pd*pd	9.53	3.191	2.985	0.012
fc*fc	76.3	79.785	0.956	0.359
ft*ft	0	0	1.84	0.093
dt*dt	0	0.001	0.643	0.534
wv*pd	1.38	1.08	1.28	0.227
wv*fc	−0.17	5.401	−0.031	0.976
wv*ft	0.01	0.005	0.999	0.339
wv*dt	−0.02	0.022	−1.006	0.336
pd*fc	−10.25	21.606	−0.474	0.644
pd*ft	−0.07	0.022	−3.165	0.009
pd*dt	0.24	0.086	2.785	0.018
fc*ft	0.09	0.108	0.836	0.421
fc*dt	−0.46	0.432	−1.06	0.312
ft*dt	0	0	0.144	0.888

wv-wheel velocity(X_1); pd-product diameter(X_2); ft-feedstock temperature(X_3); fc-friction factor (X_4); dt-die temperature.(X_5)

Using the value of coefficients shown in Table 4.4, the model equation can be written as follows:

$$Load\ (P) = 1469.76 - 250.04\ X_2 + 9.53X_2^2 - 0.07X_2X_3 + 0.24X_2X_4 \ldots\ldots \quad (4.20)$$

Test values of analysis of variance for extrusion load are shown in Table 4.5. It was observed from Table 4.5 that *F*-value (Fishers test value) for linear and quadratic effect of diameter of product, interaction effect of product diameter and feedstock temperature and interaction effect of product diameter and die temperature were very high which signified that the developed mathematical model was significant statistically.

Additionally the values of R^2, as well as adjusted R^2, are 91.49% and 86.03% respectively. The results imply that the multivariate model delivered a comprehensive relationship between the input and response parameters. Hence, the model was found to be statistically highly significant as well as adequate.

Table 4. 4: Variance analysis of extrusion load for AA1100 feedstock

Source	DOF	SS	MSS	F-value	P-value
Regression	20	35346.4	1766.32	5.92	0.002
Linear	5	24759	1184.39	3.96	0.027
wv	1	498.1	6.51	0.02	0.885
pd	1	19890.4	4784.32	16.01	0.002
fc	1	489.1	86.15	0.29	0.6
ft	1	2109.4	386.61	1.29	0.279
dt	1	1771.9	725.91	2.43	0.147
Square	5	3570.6	714.12	2.39	0.106
wv*wv	1	26.1	156.48	0.53	0.483
pd*pd	1	2282.4	2661.73	8.91	0.012
fc*fc	1	176.3	273.24	0.91	0.359
ft*ft	1	960.5	1011.87	3.39	0.093
dt*dt	1	123.4	123.37	0.41	0.534
Interaction	10	7016.8	701.68	2.35	0.089
wv*pd	1	489.3	489.29	1.64	0.227
wv*fc	1	0.3	0.28	0	0.976
wv*ft	1	296.9	296.91	1	0.339
wv*dt	1	302.6	302.59	1.01	0.336
pd*fc	1	66.2	66.24	0.23	0.644
pd*ft	1	2992.1	2992.09	10.01	0.009
pd*dt	1	2317	2316.98	6.76	0.018
fc*ft	1	208.8	208.8	0.7	0.421
fc*dt	1	335.4	335.44	1.12	0.312
ft*dt	1	6.2	6.18	0.02	0.888
Residual error	11	3286.4	298.76		
Lack-of-fit	6	3286.4	546.73		
Pure error	5	0	0		
Total	31	38632.7			

DOF-degree of freedom; SS-Sum of Square; MSS mean sum of square

The plot of residuals for extrusion force is shown in Fig. 4.4. It was observed from the plot that all residuals were uniformly and normally located along the straight line and hence it satisfied the condition of model adequacy. It was also observed from Fig. 4.4 that all the data were very close to the straight-line. The data which fell away from the straight-line were said to be significant effects. The outliers were discarded from the rest of the data.

Figure 4.5 and 4.5 show the surface plot and optimization plot, respectively, of parametric combination of input parameters affecting the extrusion load. It is observed from the Fig. 4.5 that the load required for extrusion of material is highest in dark green zone and is lowest in light green zone. So, it can be concluded that the load required for extrusion is lower 100kN if the diameter of product is greater than 7mm, wheel speed is around 6rpm, friction condition is 0.8, and feedstock temperature is 300°C and die temperature is 450°C.

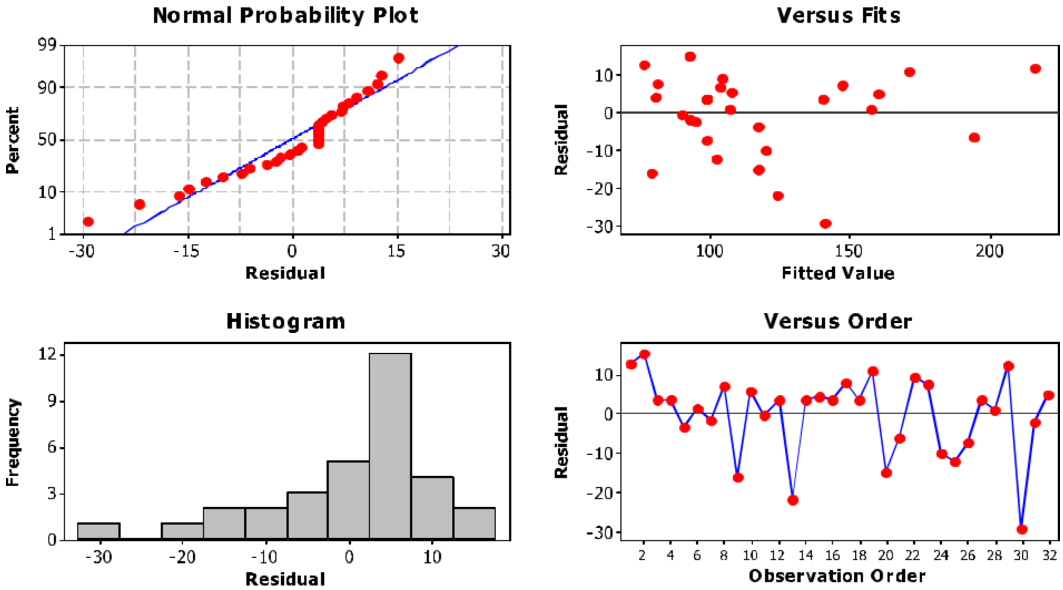

FIGURE 4. 4: RESIDUAL PLOTS FOR LOAD REQUIRED

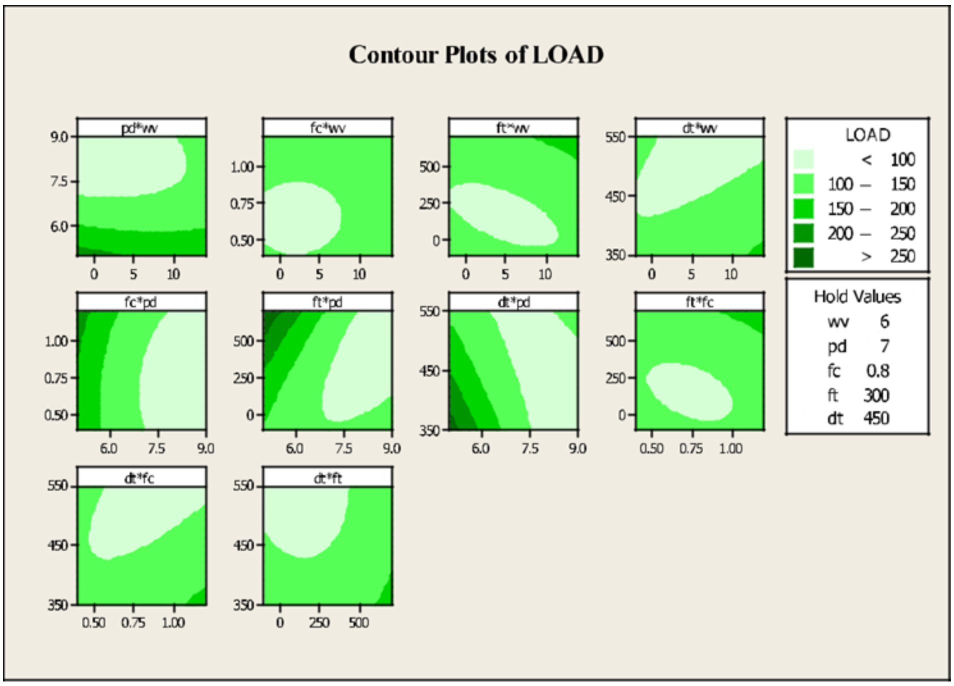

FIGURE 4. 5: CONTOUR PLOTS FOR LOAD REQUIRED

It is observed from Fig. 4.6 that load of 140kN is required if the wheel velocity, product temperature, frictional factor, feedstock temperature and die temperature are

13RPM, 5mm, 0.95, 650℃ and 550℃, respectively. The optimum value of load (140kN) has been obtained with composite desirability of 1.0 using RSM

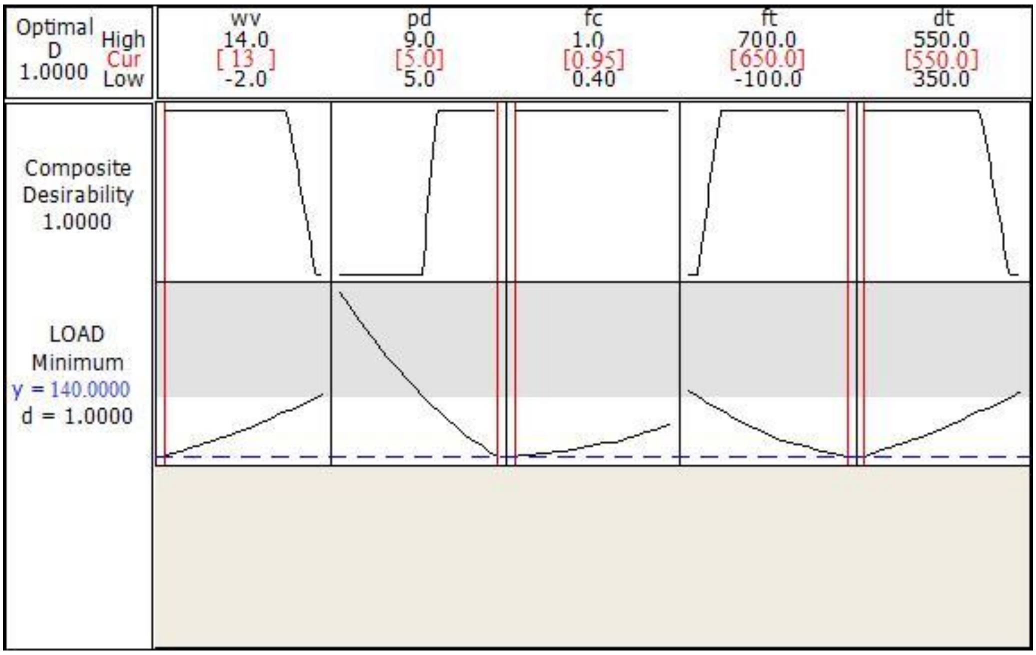

FIGURE 4. 6: OPTIMIZATION PLOT FOR LOAD REQUIRED

I. Numerical data optimization through ANN model

The most commonly used configuration in case of ANN is Feed Forward Neural Network (FFNN). A predictive model with five input variables of the CE process i.e., wheel velocity, product diameter, frictional factors, and feedstock temperature and die temperature; and the output responses of the CE process such as load required were taken in Multi-Layer Perception (MLP). The weight in every input has been normalized in a domain of (0.1–0.9) for assurance of regular attention within the process of training. There are rigid rules for selection of neuron in hidden layer; the best way is to apply trial and error method taking a proposed number of nodes in the hidden layer to be less than or upto 2 times the number of input nodes. A network consists of five input nodes representing the input process variables of the CE process, six neurons for the hidden layer and one output node for the output response parameters of the CE process at the end of training process (topology 5-6-1). The MATLAB program was used to perform ANN-based modeling investigations.

In this study; therefore, 30 data sets were generated by multiplying hidden layer nodes and the input variable nodes for the ANN setup. Twenty-Four data sets (from run no.1 to 24 as specified in Table 4.2) have been exploited as the training data sets, whereas rest 6 data sets (from run no. 25–30 as specified in the Table) have been utilized for testing the efficiency of the neural network. During the supervised training process, the associated learning error rate (mean-squared error) is minimized by increasing the number of training epochs (cycles).However, an optimal number of training epochs need to be determined in order to avoid any possible overtraining of the network. Figure 4.7 shows the training and test epoch cycles versus the calculated mean squared error of the supervised training and the comparison of input benchmark data and corresponding ANN predictions for the training process. It can be observed from Fig. 4.7 that a total number of 434 epochs have been the optimum number of training cycles for the present ANN structure and the corresponding MSE (relative error between the network output and target value) has been found to be 6.69. The convergence of Mean-Squared Error during supervised training process is found to be 6.69 at 434 epochs.

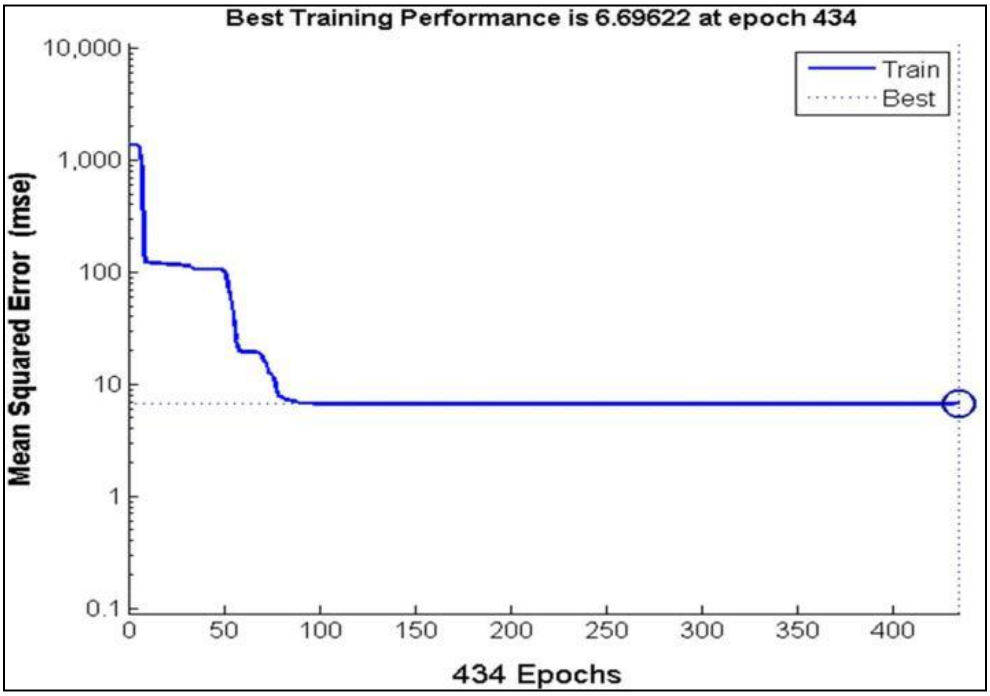

FIGURE 4. 7: TRAINING EPOCH CYCLES VERSUS CALCULATED MEAN SQUARE ERROR OF THE SUPERVISED TRAINING FOR THE DESIGNED ANN

Figure 4.8 shows the coefficient of correlation between the experimental and predicted data using ANN. The data are very closely spaced and distributed normally along the straight line which signifies that experimental and predicted data are highly correlated.

Further, the fitness of the neural network prediction has been analyzed by calculating the coefficient of R^2 using the experimental and predicted data. The R^2 (entire data including training and testing data) has been found to be 0.972 indicating that the used network is significant and the obtained data is more accurate. This has been further confirmed from Fig. 4.8 which shows that the predictions have been concentrated near the diagonal line on the graph without much scattering.

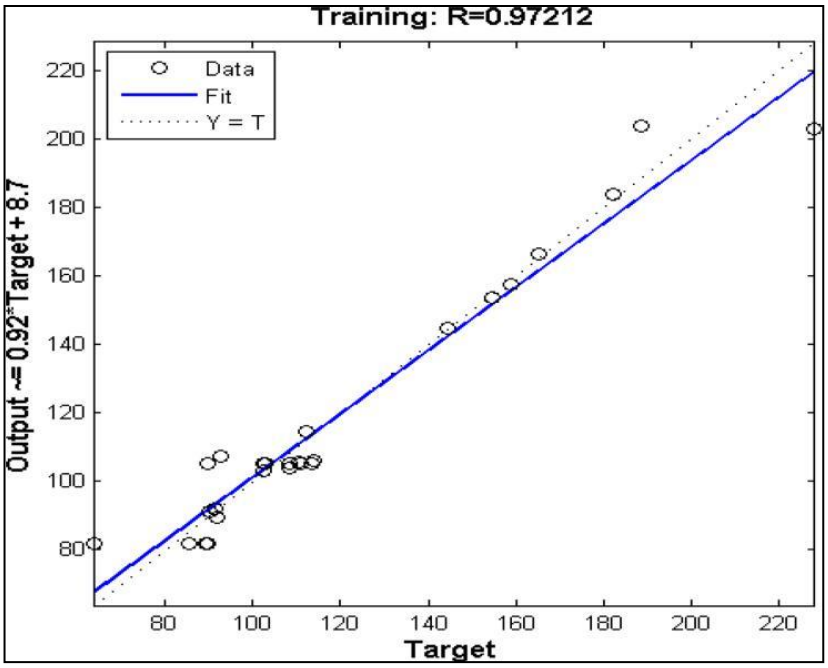

FIGURE 4. 8: CORRELATION CHART FOR EXPERIMENTAL AND PREDICTED LOAD REQUIRED FOR CE

II. GA-based optimization using ANN model

To facilitate a solution for an optimization problem (regression equation), GA creates an initial population of randomly generated individuals called chromosomes, generally represented as strings of binary digits. At each step, the GA selects the individuals at random, from current population, to be parents and uses them to produce the offspring for the next generation. Crossover operator combines two parents to form children for upcoming generations. However, mutation rules are concerned with introducing new diversities among individual parents producing children. Point mutations are the most commonly occurring mutations, which are used to avoid any convergence to local maxima. This iterative process continues until a satisfactory solution according to the need of fitness function has been achieved. The MATLAB has been used to perform GA-based modeling studies.

To facilitate an optimum solution, GA has been employed on the newly generated population (data sets) of independent variables. The CCD- and ANN-based regression models have been executed as the fitness functions by GA for minimum load required in CE process. All the five parameters of the model have been represented in terms of chromosomes for GA-based optimization technique with the following constraints:

2 ≤ Wheel velocity ≤ 10; 6 ≤ Product diameter ≤ 8; 0.6 ≤ Friction condition ≤ 1.0;

100 ≤ Feedstock temperature ≤ 500;   400 ≤ Die temperature ≤ 500.

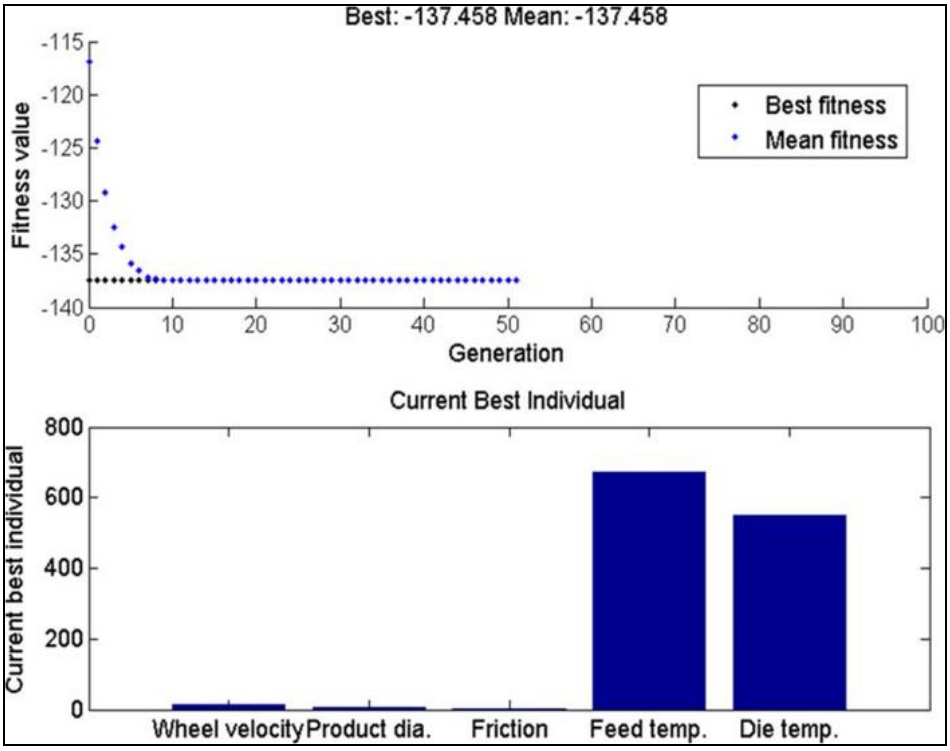

FIGURE 4. 9: GA GENERATED FITNESS AND PREDICTED PARAMETERS

The GA parameters in the MATLAB software for the optimization of load required in CE of Aluminum feedstock have been set as follows: double vector; original population size:100; cross over probability:0.8; elite count:20; crossover function: @crossover single point; migration direction: forward; selection function: @selection Roulette; mutation function: @mutation Gaussian; total generations:100. Best fitness plot Fig. 4.9 showing the progressive performance (for load required) of GA over generations till the achievement of optimum solution (upper plot). Variables (in lower plot) showing the level of wheel velocity, product diameter, friction condition, feedstock temperature and die temperature. Figure 4.9 below shows five random trials generated by GA with their model generated predicted values.

It can be observed from the plot that the convergence occurred at the value of 137.4kN. The optimized values of independent process parameters for minimum value of load of extrusion obtained are 13RPM as wheel velocity, 5mm as product diameter, and 0.95 as friction condition, 650℃ as feedstock temperature and 550℃ as die temperature. The validation of the optimal solutions has been carried out by independent experiments using the same conditions. The numerical validation of the ANN-GA results has been carried out by carrying out numerical experiment at the optimum value of input process variables. Therefore, numerical simulation has been carried out at the input value of process parameters for wheel speed 13RPM, diameter of product 5mm, friction condition between feedstock and grooved wheel as 0.95, 650℃ as feedstock temperature and 550℃ as die temperature. The extrusion load corresponding to these optimum process variables was found to be 136.4kN which is very close to the value of 137.4kN obtained through GA using ANN.

4.3.2. Computational analysis of Cu101 alloy

A total of 31 numerical simulations were developed as per the experiments generated using CCRD method. Simulation preprocess conditions were performed as per Table 3.6 and Table 3.7 in Chapter III. The details of independent process variables and levels were also shown in Table 3.14 Table 3.15 respectively. The input variables taken during study were driving wheel speed, diameter of extrudate, feedstock temperature, die temperature and friction factor of the CE process. All the designed experiments were performed numerically through Finite Element simulation tool DEFORM-3D. The effects of the input variables on the extrusion load, effective stress, and damage were investigated and tabulated in Table 4.5. The computational analyses were performed to produce a 6mm diameter extrudate out of a 12.5mm in diameter C101 feedstock metal.

4.3.2.1. Computational analysis of total load for Cu101 alloy

All the designed experiments were performed numerically through DEFORM-3D simulation tool. The summery of the effects of the CE independent parameters on the extrusion load was investigated and tabulated in Table 4.5.

Table 4. 5: Details of experiments as per CCRD and responses for C101 Copper alloy

Run order	x_1	x_2	x_3	x_4	**Total load**	**Effective stress**	**Effective strain**	**Damage during the CE**
1	8	675	500	0.925	882.9	1460	38.1	9.09
2	4	850	400	0.850	882.3	1480	42.1	10.6
3	4	500	600	0.850	882.3	1480	42.1	10.6
4	8	675	500	0.925	963.15	1550	28	819
5	8	675	500	0.925	743.33	1430	38.1	3.14
6	12	850	400	1.000	932.02	1550	39.8	14.5
7	8	675	500	0.925	876.24	1430	12.8	3.49
8	4	850	600	1.000	835.42	1450	31	20.9
9	16	675	500	0.925	969.43	1470	25.7	19.8
10	12	850	600	1.000	729.18	1300	12.6	3.56
11	8	675	300	0.925	876.44	1430	12.8	3.84
12	4	500	400	0.850	882.3	1480	42.1	8.6
13	0	675	500	0.925	0	0	0	0
14	8	675	500	1.075	824.46	1570	60.6	71.5
15	4	850	600	0.850	566.94	1300	10.5	3.3
16	12	500	600	0.850	513	1400	40.2	25.2
17	12	500	400	0.850	703.22	1400	40.2	25.2
18	4	850	400	1.000	802.01	1300	19.5	3.65
19	12	500	600	1.000	588.26	1280	14.5	4.57
20	8	675	500	0.925	755.92	1360	28.1	3.22
21	8	1025	500	0.925	755.92	1360	28.1	3.22
22	4	500	600	1.000	587.59	1230	14.6	3.01
23	8	675	500	0.925	770.39	1460	38.1	9.09
24	12	850	400	0.850	702.42	1370	11.5	3.51
25	12	500	400	1.000	743.75	1550	12.6	3.87
26	8	675	500	0.925	882.92	1460	38.1	9.09
27	4	500	400	1.000	860.43	1450	41	22
28	12	850	600	0.850	995.23	1580	40.2	25.2
29	8	325	500	0.925	1064.6	1460	38.1	9.09
30	8	675	700	0.925	943.04	1550	35.8	30.4
31	8	675	500	0.775	701.86	1280	11.8	3.26

Wheel Velocity(x_1), Feedstock Temperature(x_2), Die Temperature(x_3), Friction Factor(x_4)

A regression model was developed to obtain an optimized equation with combination of various input process parameters for extrusion load as a response to extrude a C101 alloy. If the p-values in the Table 4.6 for the input variables were < 0.05 (i.e., greater than 95% confidence level) the linear and quadratic effect of the parameters were taken to develop the regression model. The significance test of the variables was performed using the data presented in Table 4.6 and Table 4.7. The values of R^2 as well as adjusted R^2 are 94.63% and 89.93% respectively. The outcomes suggested that the multivariate model brings a strong relationship between the input and response parameters.

Table 4. 6: Test of significance for extrusion load for C101

Term	Coefficients (Coef)	Standard error coefficient	T - value	P - value
Constant	855.129	21.03	40.664	0.000
Wheel Velocity	103.562	11.36	9.119	0.000
Feedstock Temperature	-7.688	11.36	-0.677	0.508
Die Temperature	-16.271	11.36	-1.433	0.171
Friction Factor	4.021	11.36	0.354	0.728
Wheel Velocity*Wheel Velocity	-126.100	10.40	-12.120	0.000
Feedstock Temperature*Feedstock Temperature	22.838	10.40	2.195	0.043
Die Temperature*Die Temperature	22.588	10.40	2.171	0.045
Friction Factor*Friction Factor	-13.787	10.40	-1.325	0.204
Wheel Velocity*Feedstock Temperature	42.969	13.91	3.089	0.007
Wheel Velocity*Die Temperature	36.844	13.91	2.649	0.018
Wheel Velocity*Friction Factor	6.156	13.91	0.443	0.664
Feedstock Temperature* Die Temperature	9.531	13.91	0.685	0.503
Feedstock Temperature*Friction Factor	27.969	13.91	2.011	0.062
Die Temperature*Friction Factor	-32.406	13.91	-2.330	0.033

The actual mathematical model expression for the total load

$$Y = 855.129 + 103.562x_1 - 126.1x_1^2 + 22.838x_2^2 + 22.588x_3^2 + 42.969x_1x_2 + 36.844x_1x_3 - 32.406x_3x_4 \quad \ldots\ldots (4.21)$$

Table 4. 7: Analysis of variance for total load to extrude C101 alloy

Source	DOF	SS	MSS	F	P
Regression	14	873113	62365	20.15	0.000
Linear	4	265565	66391	21.45	0.000
Wheel Velocity	1	257405	257405	83.15	0.000
Feedstock Temperature	1	1418	1418	0.46	0.508
Die Temperature	1	6354	6354	2.05	0.171
Friction Condition	1	388	388	0.13	0.728
Square	4	524910	131227	42.39	0.000
Wheel Velocity*Wheel Velocity	1	488620	454706	146.89	0.000
Feedstock Temperature *Feedstock Temperature	1	14118	14914	4.82	0.043
Die Temperature* Die Temperature	1	16735	14590	4.71	0.045
Friction Factor*Friction Factor	1	5436	5436	1.76	0.204
Interaction	6	82639	13773	4.45	0.008
Wheel Velocity* Feedstock Temperature	1	29541	29541	9.54	0.007
Wheel Velocity*Die Temperature	1	21719	21719	7.02	0.018
Wheel Velocity* Friction Factor	1	606	606	0.20	0.664
Feedstock Temperature*Die Temperature	1	1454	1454	0.47	0.503
Feedstock Temperature*Friction Factor	1	12516	12516	4.04	0.062
Die Temperature*Friction Factor	1	16803	16803	5.43	0.033
Residual Error	16	49,529	3,096		
Lack-of-fit	10	49,522	4,952	3964.77	0.000
Pure Error	6	7	1		
Total	30	922,643			

The plot of residuals for dependent parameter i.e., extrusion force is shown in Fig. 4.10. It can be seen from the plot that all residuals are uniformly and normally distributed along the straight line and hence the plot satisfies the condition of model adequacy. It can also be observed from Fig. 4.10 that almost all the data are very close to the straight-line. The data which fall away from the straight-line are said to be significant effects. The outliers are always discarded from the rest of the data.

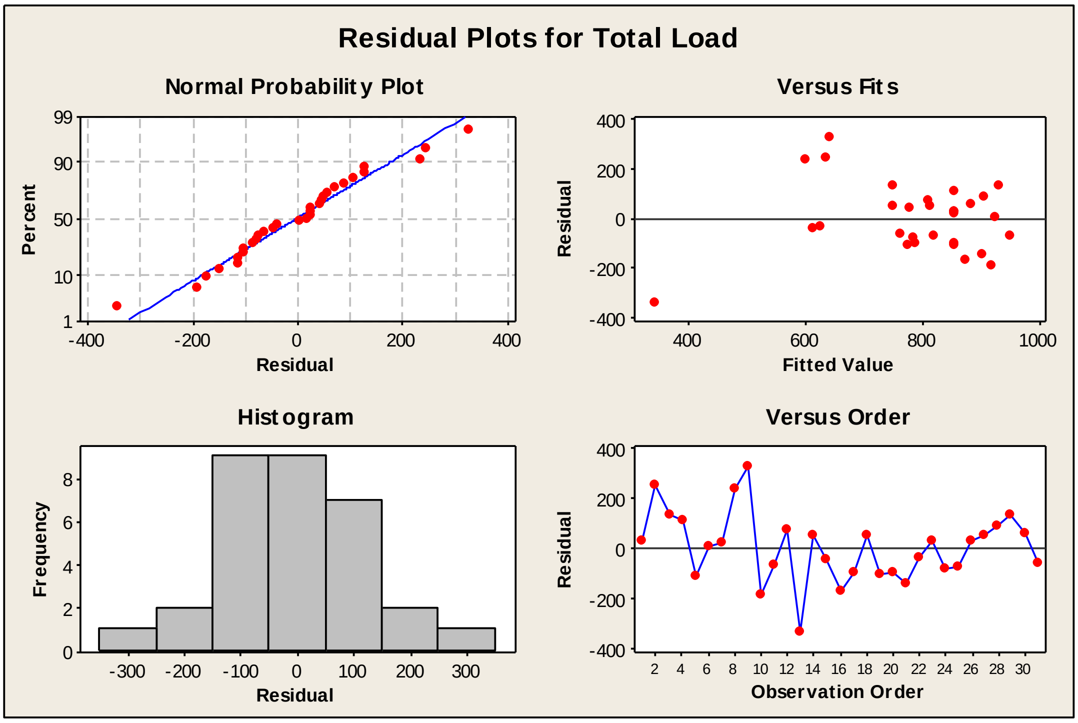

FIGURE 4. 10: RESIDUAL PLOTS FOR EXTRUSION LOAD

From Fig. 4.11 to Fig. 4.16 show the interaction or parametric combination effects of input process variables on the load required for the CE extrusion of C101 feedstock material. Figure 4.17 to Fig. 4.21 show the surface plots for parametric combination of input process variables affecting the sub-total load required for the extrusion of C101 feed metal. Optimization plot for parametric combination of input process variables affecting the total load required for the extrusion of C101 metal is shown in Fig. 4.22.

It can be observed the effect of driving wheel speed and feedstock temperature on total load from Fig. 4.11. The load required for extrusion of the material is highest in dark green zone and lowest in light green zone. So, less than 200kN extrusion load is required if the wheel speed is very low and feedstock temperature is above 600°C keeping friction factor at 0.925 and die temperature is 500°C.

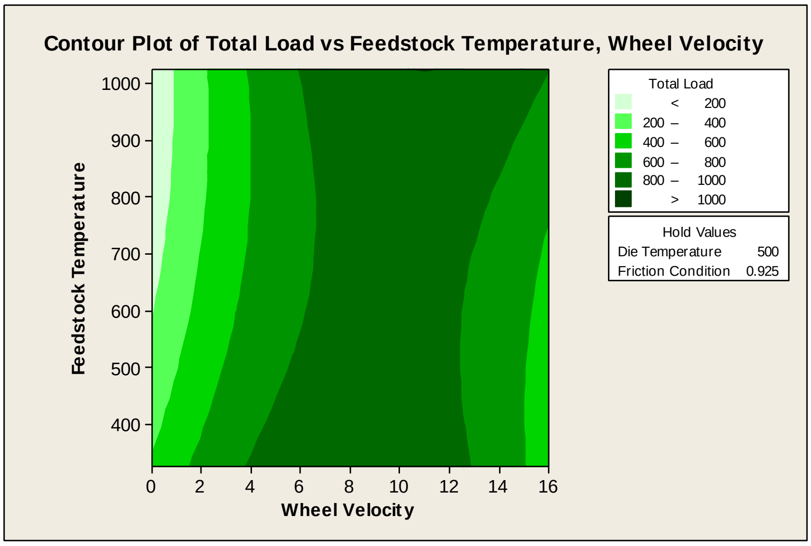

FIGURE 4. 11: EFFECT OF WV AND FT ON EXTRUSION LOAD

It can also be observed the effect of wheel velocity and die temperature on deformation load required for extrusion of the feedmetal in the Fig. 4.12. It is highest in dark green zone and is lowest in light green zone. So, it can be concluded from the figure that lower than 200kN load required for Conform extrusion, if the wheel velocity is very low and die temperature is high just above 480°C by taking holding values of feedstock temperature at 675°C and friction factor 0.925.

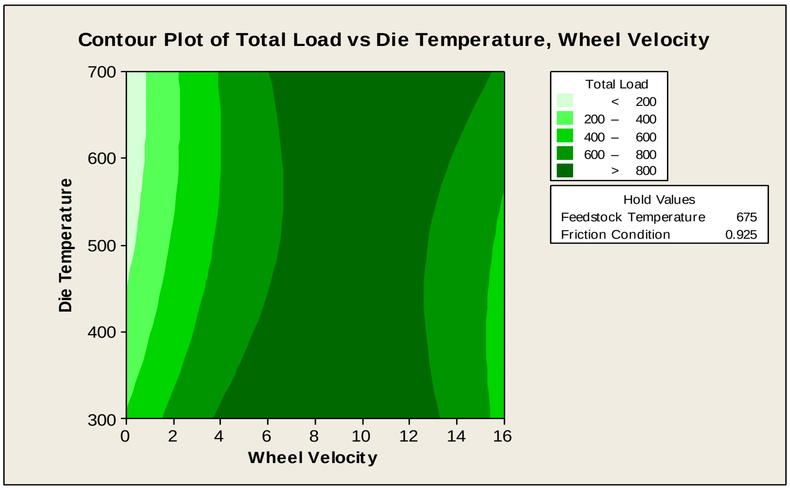

FIGURE 4. 12: EFFECT OF WV AND DT ON EXTRUSION LOAD

It can be perceived from Fig. 4.13 that extrusion load is affected by wheel velocity and friction factor. It is highest in dark green zone and lowest in light green zone. So, it can be concluded that the least load required for extrusion is lower than 200kN if the wheel velocity is very low along the whole friction factor range by taking holding values of feedstock temperature at 675°C and die temperature at 500°C.

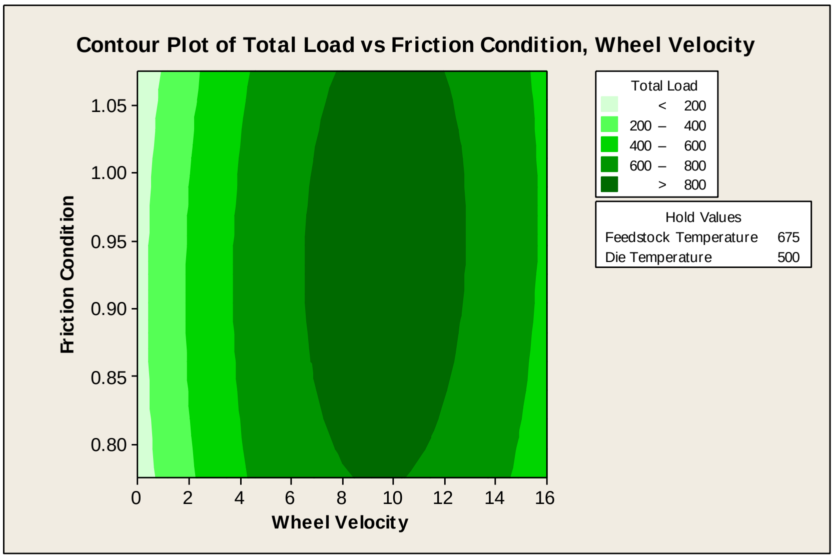

FIGURE 4. 13: EFFECT OF WV AND FF ON DEFORMATION LOAD

It can also be perceived from Fig. 4.14 that total load required for extrusion of the material was effected by feedstock temperature and die temperature. The load is highest in dark green zone and is lowest in light green zone. So, it can be concluded that the least load that is lower than 900kN required for extrusion of a C101 alloy if the feedstock temperature is between 450-900°C and die temperature at in between 400-680°C, holding wheel velocity at 8rpm and friction factor 0.925.

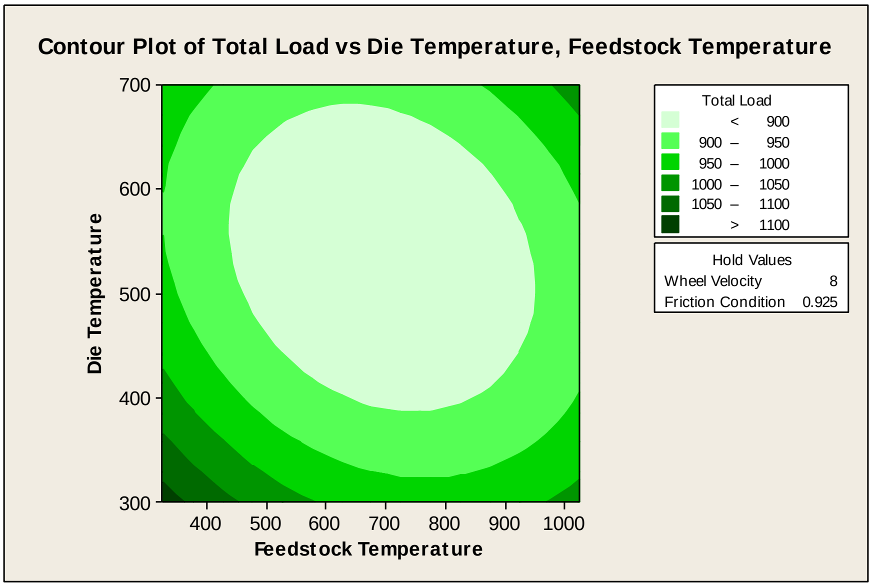

FIGURE 4. 14: EFFECT OF DT AND FT ON EXTRUSION LOAD

It can also be perceived from Fig. 4.15 the influence of feedstock temperature and friction factor on total load. It is highest in dark green zone and is lowest in dark blue zone. So, it can be concluded from the figure that the least load required for extrusion is lower than 750kN if the feedstock temperature is either very low or very high and inversely so for friction factor taking holding value of wheel velocity at 8rpm and die temperature at 500°C.

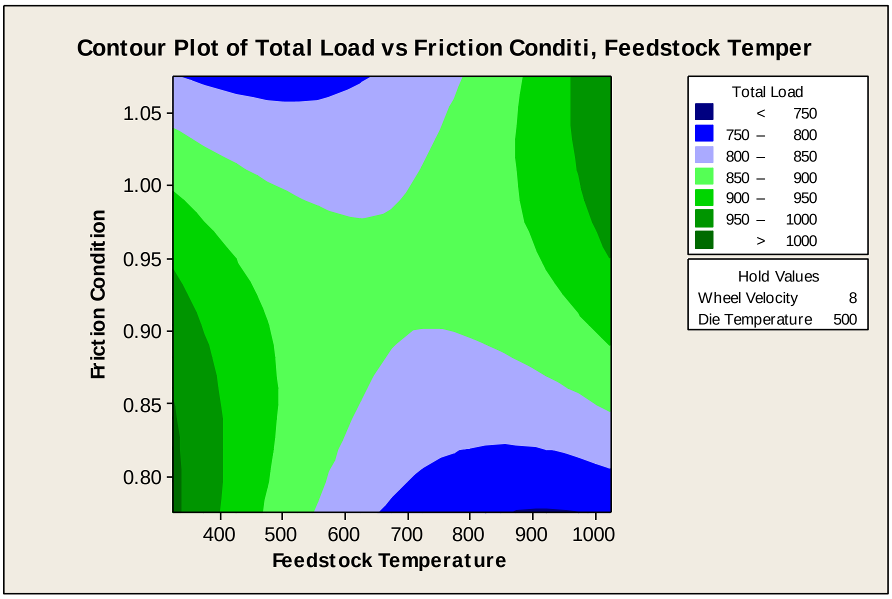

FIGURE 4. 15: EFFECT OF FF AND FT ON DEFORMATION LOAD

It can be observed from Fig. 4.16 the effect of die temperature and friction factor on total load that load required for extrusion of the material is highest in dark green zone and is lowest in dark blue zone. So, it can be concluded from the Fig. 4.16 that the load required for extrusion is less than 750kN if the die temperature and friction factor is very high, holding values of wheel velocity at 8rpm and feedstock temperature at 675°C.

The gridded surface plot is a representation of the surface plot in a 3-D space. The plot defining optimum input parametric conditions reaching minima from the best-fitted model with a map of contour lines follows a direction of movement along the path of minimum response from a reference point.

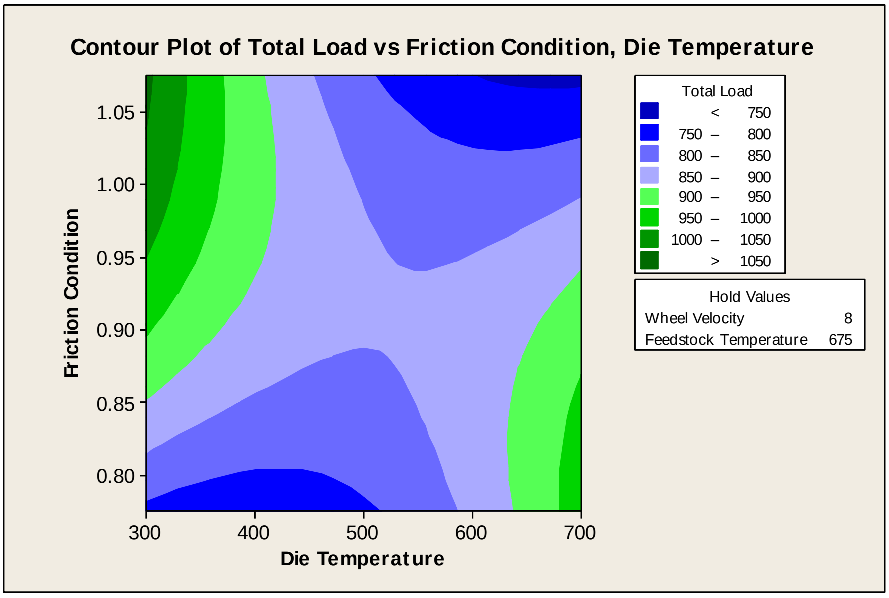

FIGURE 4. 16: EFFECT OF DT AND FF ON TOTAL LOAD

Using a smooth surface 3D surface plot (Fig. 4.17) generated for total load to examine the relationship between the total load (Z) and two predictor variables such as wheel speed and feedstock temperature by viewing a 3D surface of the projected response. The figure has a saddle shape. Therefore it has a point in the domain of function where it neither attains a maximum value nor attains a minimum value. However on either side of the saddle (either too low extrusion velocity or high wheel velocity) the total load can be lower.

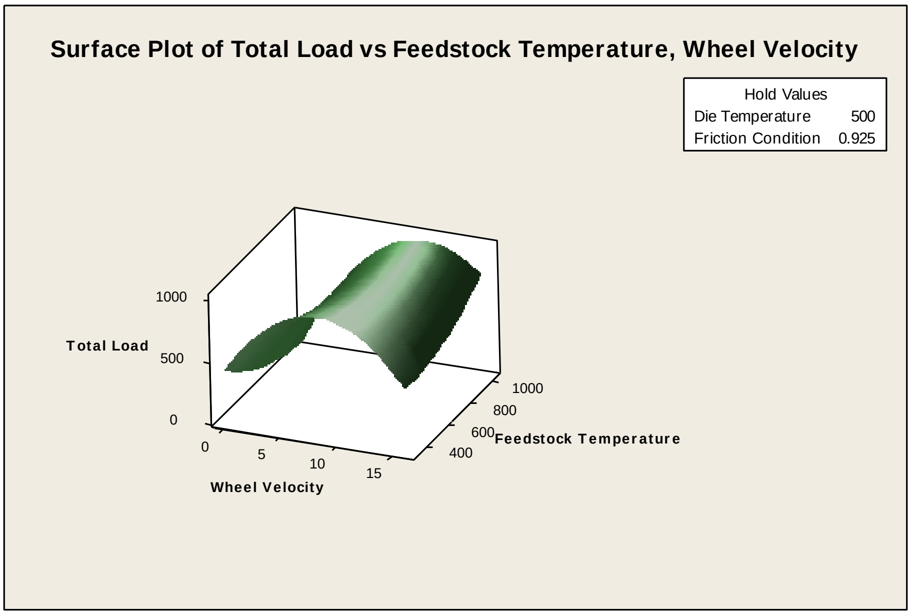

FIGURE 4. 17: SURFACE PLOT OF TOTAL LOAD VS WV AND FT

Figure 4.18 also shows a 3D surface plot of total load at the different input parameters of driving wheel speed and dies temperature at holding values of 675℃ feedstock temperature and 0.925 friction factor.

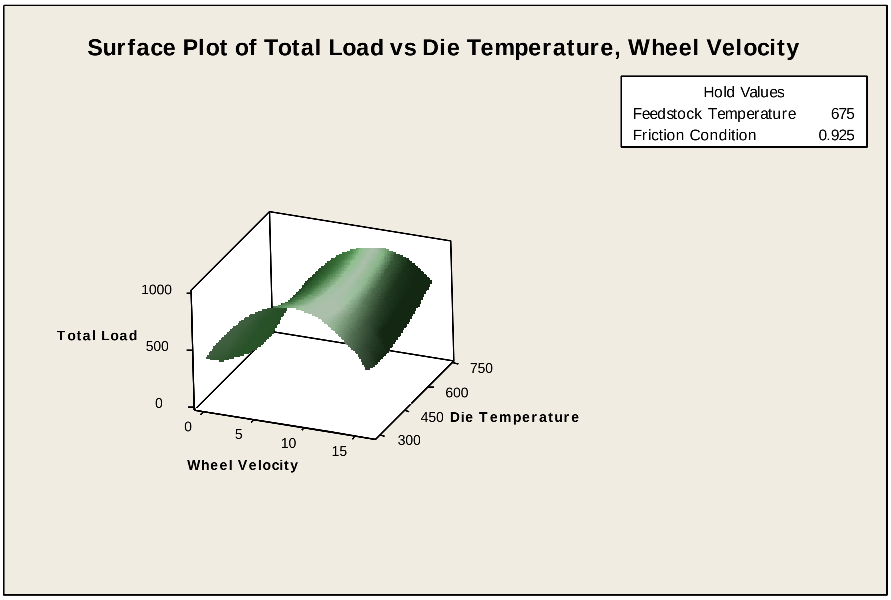

FIGURE 4. 18: SURFACE PLOT OF TOTAL LOAD VS WV AND DT

Figure 4.19 shows a 3D surface plot for total load verses wheel speed and friction factor. The plot shows the maxima points. Therefore, the left side of the plot is the minima at 675℃ of feedstock temperature and 500℃ of die temperature.

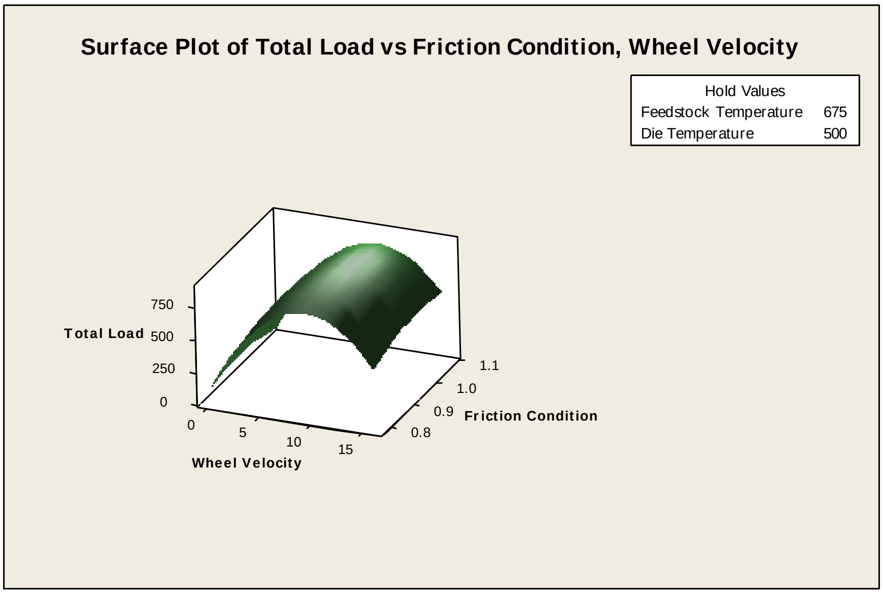

FIGURE 4. 19: SURFACE PLOT OF TOTAL LOAD VS WV AND FF

Figure 4.20 shows a 3D surface plot for total load verses feedstock temperature and die temperature. The plot looks a bowl in shape; therefore, it gives the minima total power requirement in the middle of the input parameters.

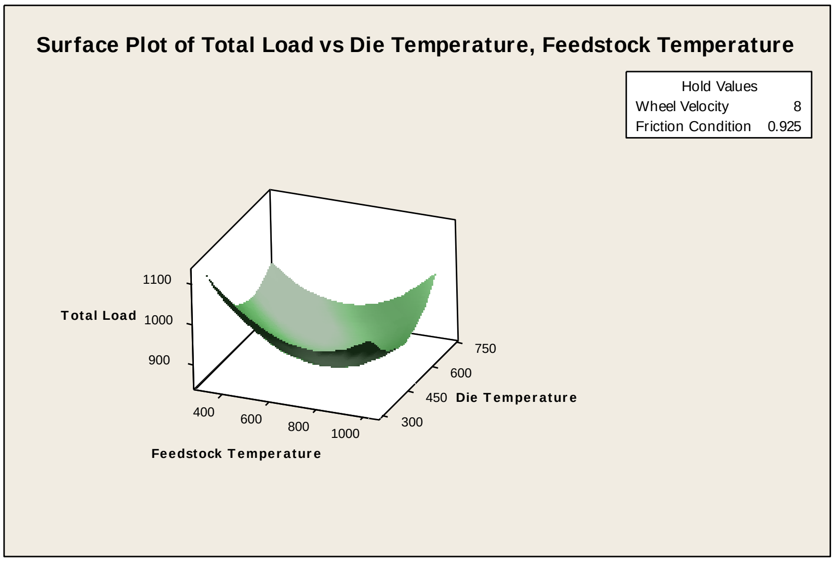

FIGURE 4. 20: SURFACE PLOT OF TOTAL LOAD VS DT AND FT

Figure 4.21 shows a 3D surface plot of total load verses feedstock temperature and friction factor. The surface plot looks a saddle in shape; therefore, the minima total load is in the lower and higher feedstock temperature and in the either side of friction factor.

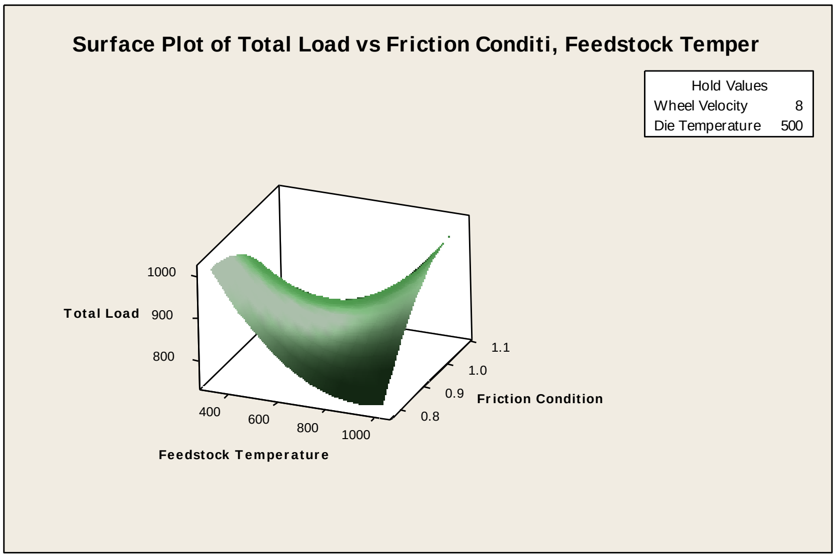

FIGURE 4. 21: SURFACE PLOT OF TOTAL LOAD VS FF AND FT

It is observed from Fig. 4.22 that load of 247.2961kN was required if the wheel velocity, feedstock temperature, die temperature, and frictional factor were 1 revolutions per minute (RPM), 678.53 C, 506.77°C and 1.0174 respectively. The optimum value of load (247.2961kN) was obtained with composite desirability of 0.82683using RSM.

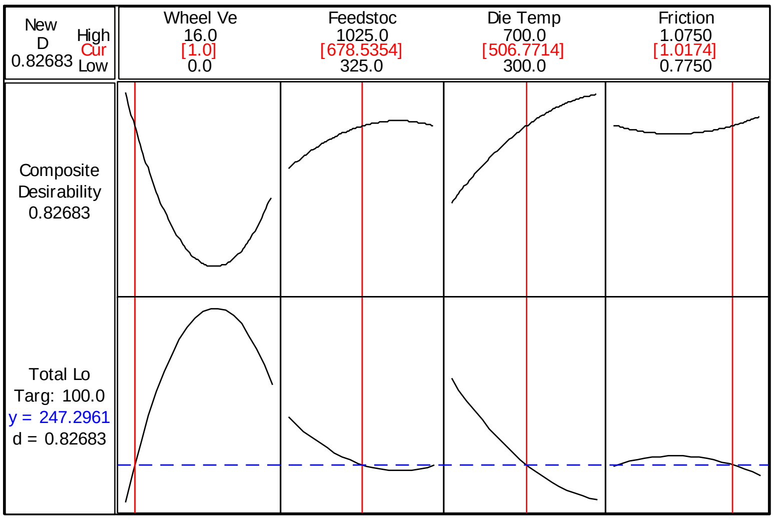

FIGURE 4. 22: OPTIMIZATION OF TOTAL LOAD USING WV, FT, DT AND FF

4.3.2.2. Modeling and optimization of effective stress of a C101 alloy through RSM

A total of 31 numerical simulations have been carried out as per the experiments generated using CCRD method. Table 3.22 shows the input process parameters and their respective levels. During the computational analysis of C101 metal using DEFORM-3D, the effective stress of the material considered encompasses in all the phases. Those phases are before the entry of the feed metal into grooved portion of extrusion wheel, during, and after the CE extrusion of the raw material the final deformation through die exit has been considered. All the designed experiments were performed through DEFORM-3D. The effects of the input variables on effective stress were considered and the corresponding effective stress values were tabulated in Table 4.5. The variables i.e., wheel velocity, frictional condition, and feedstock temperature and die temperature at three levels and extrudate diameter of 6mm produced out of 12.5mm in diameter copper feedstock metal were taken for the computational analysis.

Figure 4.23 shows the effective stress distribution on the feedstock material during and after the CE processes. It is observed the effective stress induced in the feedstock during the extrusion process increases initially as the feedstock material moves in to the grooved portion of the wheel and it became maximum when the material was in collision with the abutment and decreases and became around zero when the extrusion was taken place. The main reason is the process itself had a work softening effect immediately after the feedstock left the abutment zone.

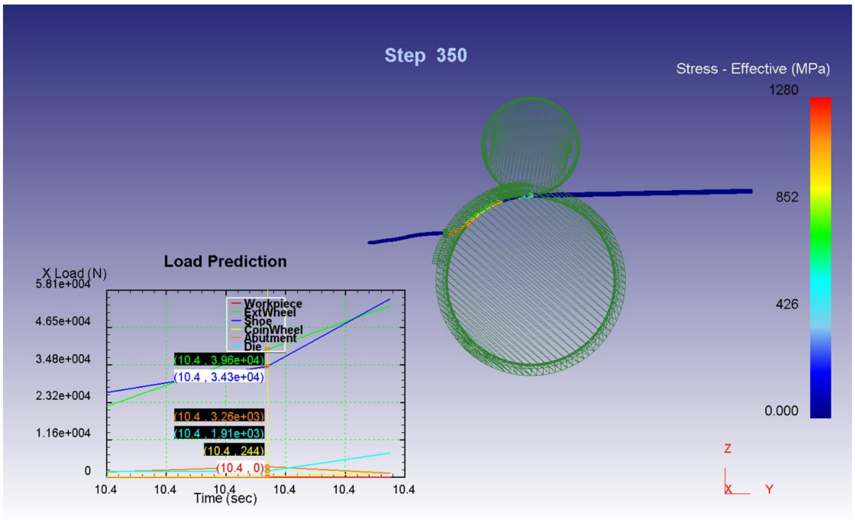

FIGURE 4. 23: EFFECTIVE STRESS DISTRIBUTION OF C101 CU ALLOY

A regression model developed to obtain a mathematical expression for an effective stress induced in the C101 alloy feed stock material during the CE process at various process parameters. Significance test of C101 performed using the data presented in Table 4.8. If the p values in Table 4.8 for the input variables in the model are < 0.05 (i.e., greater than 95% confidence level) for the linear and quadratic effect of wheel velocity and extrudate diameter are taken to develop the regression model. The values of R^2, as well as adjusted R^2, are 94.69% and 90.05% respectively. The results imply that the multivariate model delivers a comprehensive relationship between the input and response parameters.

Table 4. 8: Estimated regression coefficients of effective stress for C101

Term	Coef	SE Coef	T	P
Constant	1451.57	34.52	42.045	0.000
Wheel Velocity	182.32	18.65	9.779	0.000
Feedstock Temperature	8.42	18.65	-0.451	0.658
Die Temperature	-11.42	18.65	-0.612	0.549
Friction Condition	10.17	18.65	0.545	0.593
Wheel Velocity*Wheel Velocity	-213.08	17.08 -	12.474	0.000
Feedstock Temperature*Feedstock Temperature	26.06	17.08	1.525	0.147
Die Temperature*Die Temperature	46.18	17.08	2.704	0.016
Friction Condition* Friction Condition	29.81	17.08	1.745	0.100
Wheel Velocity*Feedstock Temperature	13.69	22.84	0.599	0.557
Wheel Velocity*Die Temperature	-1.06	22.84	-0.047	0.963
Wheel Velocity*Friction Condition	18.06	22.84	0.791	0.441
Feedstock Temperature*Die Temperature	22.19	22.84	0.972	0.346
Feedstock Temperature*Friction Condition	3.81	22.84	0.167	0.869
Die Temperature*Friction Condition	-35.94	22.84	-1.574	0.135

The mathematical expression (equation) model developed using Table 4.8 to determine an optimal effective stress induced in a C101 extrudate is indicated in equation 4.22. Therefore the model is found to be statistically highly significant and adequate. The actual mathematical model expression for the effective stress is:

$$Y = 1451.57 + 182.32x_1 - 213x_1^{\,2} + 46.18x_2^2 \quad \textbf{.....} \ (4.22)$$

It was observed from Table 4.8 and Eq. 4.22 that *F*-value (Fishers test value) for of wheel velocity (linear effect), and that of quadratic effect of wheel velocity and feedstock temperature only had a significant influence on the effective stress induced in the material whereas the rest parameters not having much effect on it. The developed regression model for effective stress was found to be statistically significant as per R^2 values. The statistical significance can also be validated from F-value from Table 4.9.

The plot of residuals for dependent parameter i.e., effective stress is shown in Fig. 4.24. It can be seen from the plot that all residuals are uniformly and normally located along the straight line and hence the plot satisfies the condition of model adequacy. It can also be observed from the Fig. 4.24 that all the data are very close to the straight-line. The data which fall away from the straight-line are said to be significant effects. The outliers are always discarded from the rest of the data.

Table 4. 9: Analysis of variance for effective stress to extrude C101 alloy

Source	DOF	SS	MSS	F	P
Regression	14	2381631	170117	20.39	0.000
Linear	4	805127	201282	24.12	0.000
Wheel Velocity	1	797818	797818	95.62	0.000
Feedstock Temperature	1	1700	1700	0.20	0.658
Die Temperature	1	3128	3128	0.37	0.549
Friction Condition	1	2481	2481	0.30	0.593
Square	4	1539495	384874	46.13	0.000
Wheel Velocity*Wheel Velocity	1	1450319	1298339	155.61	0.000
Feedstock Temperature*Feedstock Temp.	1	10264	19416	2.33	0.147
Die Temperature*Die Temperature	1	53507	60989	7.31	0.016
Friction Condition*Friction Condition	1	25406	25406	3.05	0.100
Interaction	6	37009	6168	0.74	0.626
Wheel Velocity*Feedstock Temperature	1	2998	2998	0.36	0.557
Wheel Velocity*Die Temperature	1	18	18	0.00	0.963
Wheel Velocity*Friction Condition	1	5220	5220	0.63	0.441
Feedstock Temperature*Die Temperature	1	7877	7877	0.94	0.346
Feedstock Temperature*Friction Condition	1	233	233	0.03	0.869
Die Temperature*Friction Condition	1	20664	20664	2.48	0.135
Residual Error	16	133494	8343		
Lack-of-fit	10	133415	13342	1010.54	0.000
Pure Error	6	79	13		
Total	30	2515125			

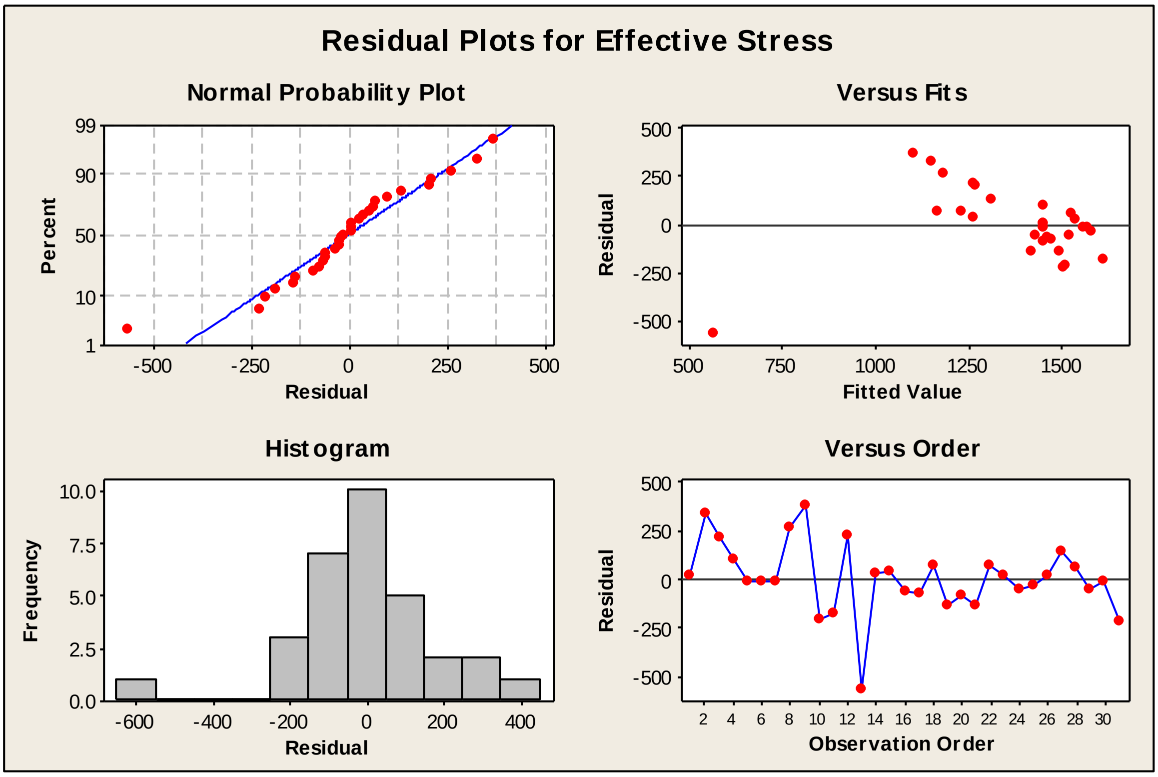

FIGURE 4. 24: RESIDUAL PLOTS FOR EFFECTIVE STRESS

Figure 4.25 to Fig. 4.30 show the parametric combination effects of input process variables on effective stress induced in the material during the entire CE extrusion processing of C101 alloy. Figure 4.31 to Fig. 4.37 show the surface plot and the optimization plot for the interaction effects of input process variables on effective stress. During the process the stress rises to a higher level; however, it was also possible to consider from the Fig. 4.23 that the stress was relived once the extrudates left the die opening.

It can be observed from Fig. 4.25 that the effect of driving wheel speed and feedstock temperature on effective stress induced in the material due to the CE extrusion parameters on a C101 metal. Effective stress is highest in dark green zone and is lowest in dark blue zone. So, it can be concluded from the figure that it is less than 400N/mm^2 if wheel RPM is very low and feedstock temperature is just above 450°C at holding values of friction condition is 0.925, and die temperature is 500°C.

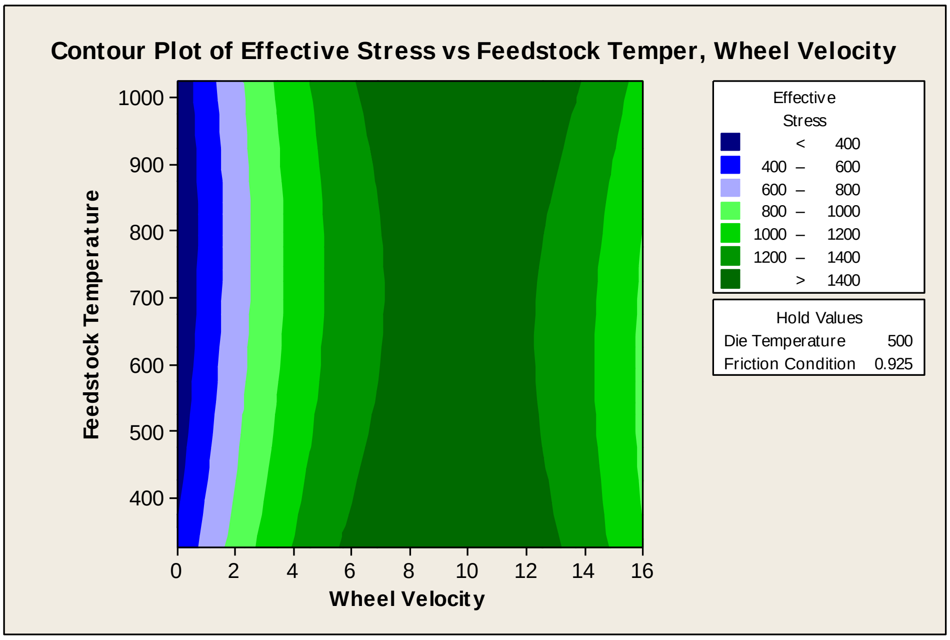

FIGURE 4. 25: EFFECT OF WV AND FT ON EFFECTIVE STRESS

The effect of wheel velocity and die temperature on effective stress has been observed in Fig. 4.26. The effective stress induced in C101 alloy is highest in dark green zone and is lowest in dark blue zone. So, it is concluded from the Fig. 4.26 that the least effective stress which is lower than 400N/mm^2 if both the wheel velocity is between 7-12rpm and die temperature is ether below 350°C or above 680°C by taking holding values of feedstock temperature at 675°C and friction condition 0.925.

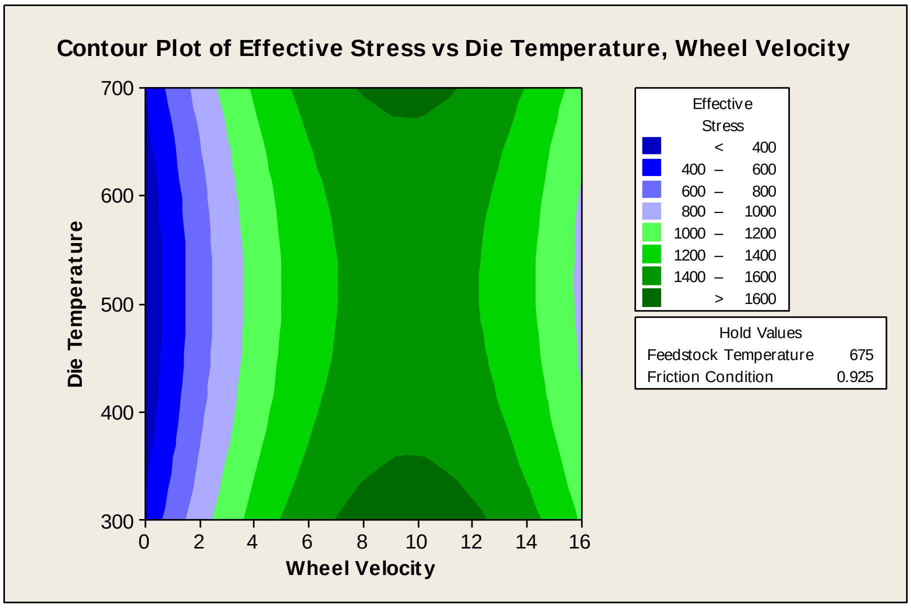

FIGURE 4. 26: EFFECT OF WV AND DT ON EFFECTIVE STRESS

It can be perceived from Fig. 4.27 on the effect of wheel velocity and friction factor on effective stress. The effective stress induced in the alloy due to the entire CE extrusion process was highest in dark green zone and lowest in dark blue zone. So, it was decided from the Fig.4.27 that the least effective stress which was lower than 400N/mm^2 was induced if the wheel velocity was very low and friction factor also above 0.75 taking holding values of feedstock temperature at 675°C and die temperature at 500°C during the process.

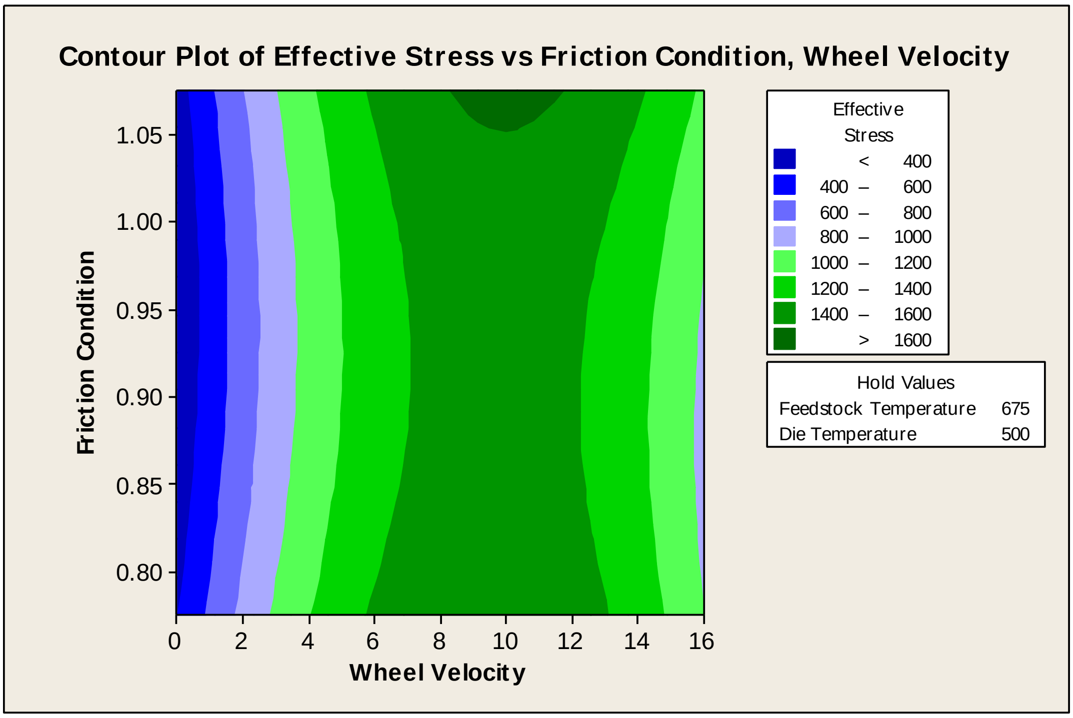

FIGURE 4. 27: EFFECT OF WV AND FF ON EFFECTIVE STRESS

It can also be perceived from Fig. 4.28 on the effect of feedstock temperature and die temperature on effective stress. Effective stress induced in the C101 was highest in dark green zone and lowest in light green zone. So, it was quantified that the least effective stress induced during the process that was lower than 1500N/mm^2 induced in the extrudates if both the feedstock temperature and die temperature were either both simultaneously in the middle level feedstock temperature (in the range of 450-950°C) and die temperature (in the range of 400-630°C) at holding values of wheel velocity at 8rpm and friction condition 0.925.

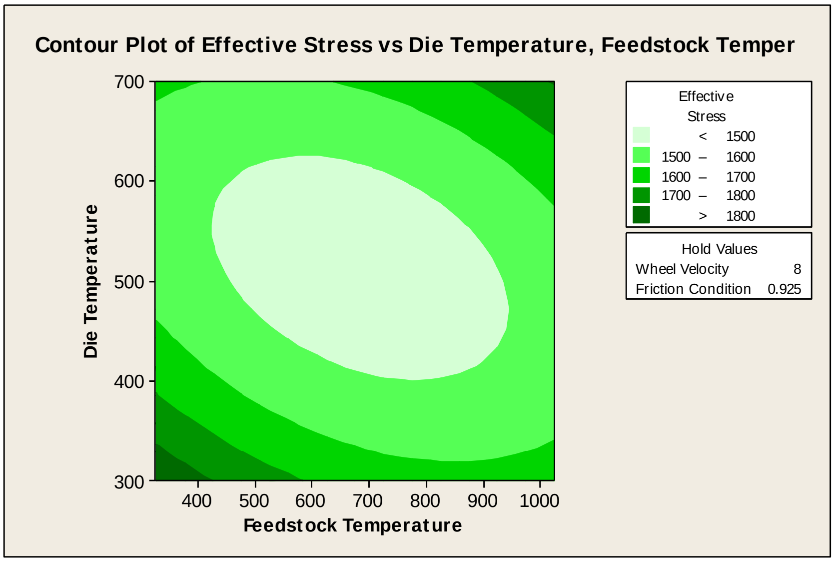

FIGURE 4. 28: EFFECT OF DT AND FT ON EFFECTIVE STRESS

It was observed from Fig. 4.29 effective stress was influenced by the effect of feedstock temperature and friction factor. The effective stress induced in the metal was highest in dark green zone and lowest in dark blue zone. So, it was decided that the least effective stress induced during the process which was lower than 1450N/mm^2 induced in the material due to the CE extrusion if the feedstock temperature was in the middle (in the range of 670-730°C) and friction factor was also in the middle in between 0.90 and 0.925 at holding values of wheel velocity and die temperature at 8rpm and 500°C respectively.

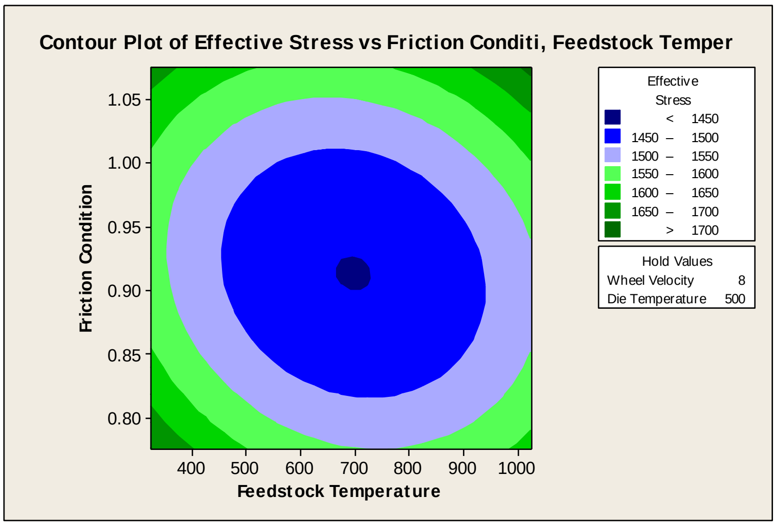

FIGURE 4. 29: EFFECT OF FF AND FT ON EFFECTIVE STRESS

It was notified from the Fig. 4.30 that effective stress was influenced by the effect of die temperature and friction factor. It was highest in dark green zone and lowest in light green one. It was less than 1500N/mm^2 if the die temperature was in-between 380 and 630°C and friction factor was also in-between 0.8 and 1.0 at holding values of wheel velocity at 8rpm and feedstock temperature at 675°C.

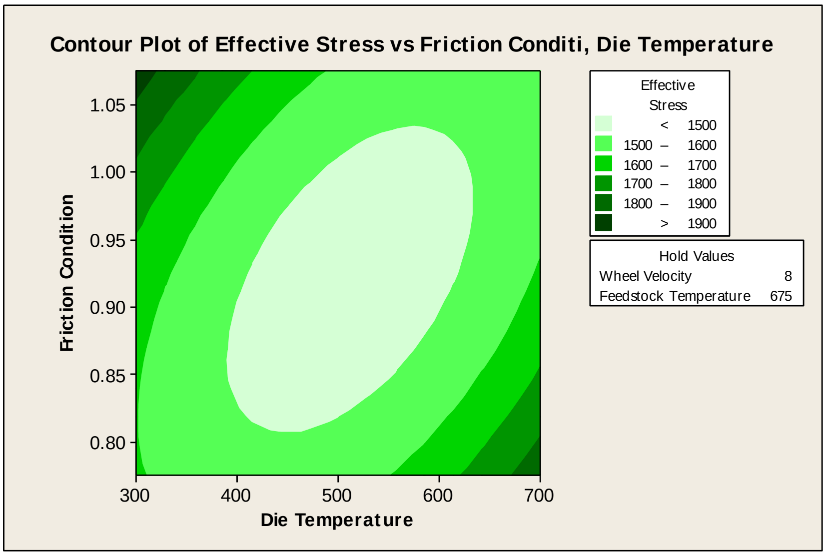

FIGURE 4. 30: EFFECT OF DT AND FF ON EFFECTIVE STRESS

Figure 4.31 shows a 3D surface plot of an effective stress for input parameters. Least effective stress induced in the material at lower wheel RPM and at any feed temperature.

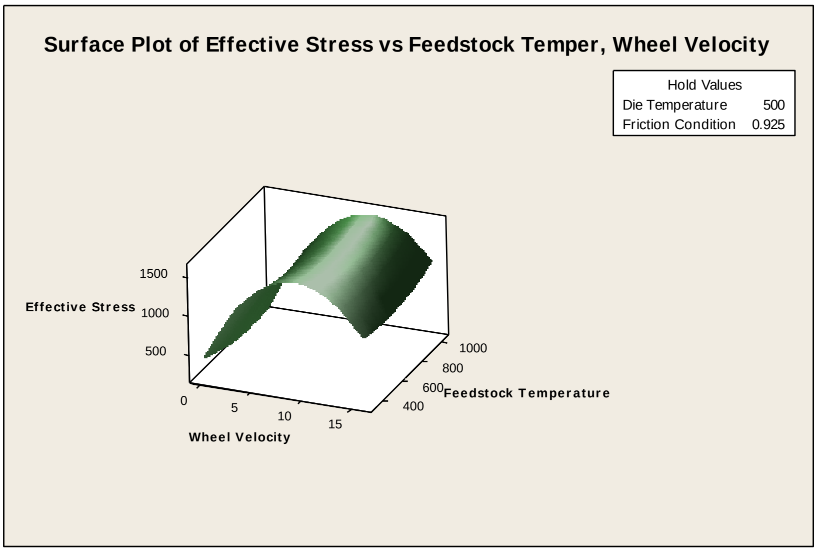

FIGURE 4. 31: SURFACE PLOT OF EFFECTIVE STRESS VS WV AND FT

Figure 4.32 shows a 3D surface plot of effective stress response for input parameters. Least effective stress induced in the feed at lower wheel RPM and at any die temperature.

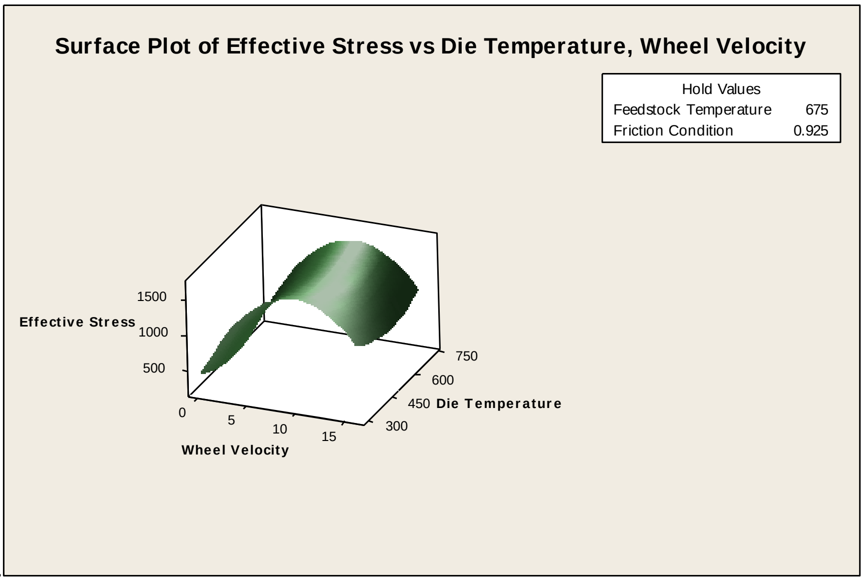

FIGURE.4. 32: SURFACE PLOT OF EFFECTIVE STRESS VS WV AND DT

Figure 4.33 shows a 3D surface plot for effective stress for wheel speed and friction factor. To the left side of the plot, lower stress induced in the feedstock during process.

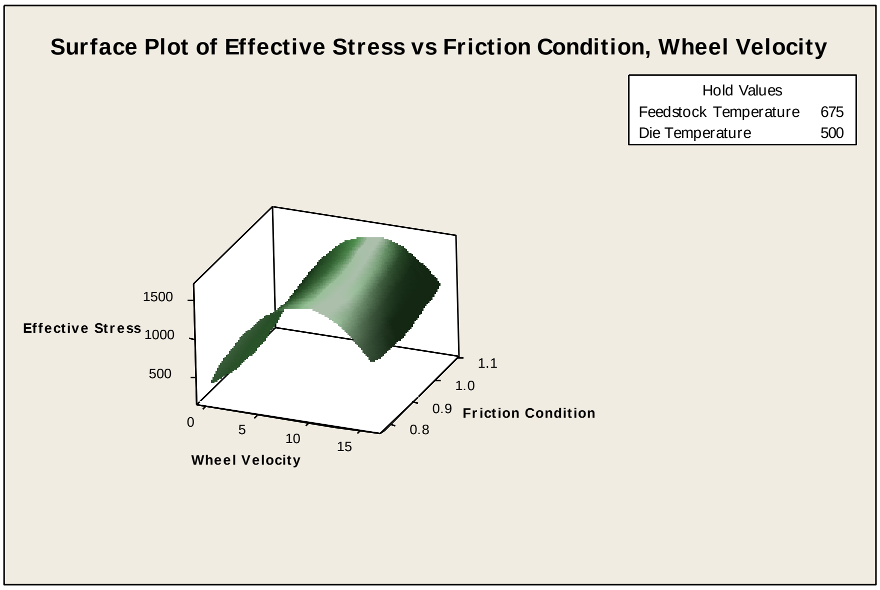

FIGURE 4. 33: SURFACE PLOT OF EFFECTIVE STRESS VS WV AND FF

Figure 4.34 shows a bowl shape 3D surface plot for effective stress verses feedstock temperature and die temperature. So, it was minima around and in the middle of the inputs.

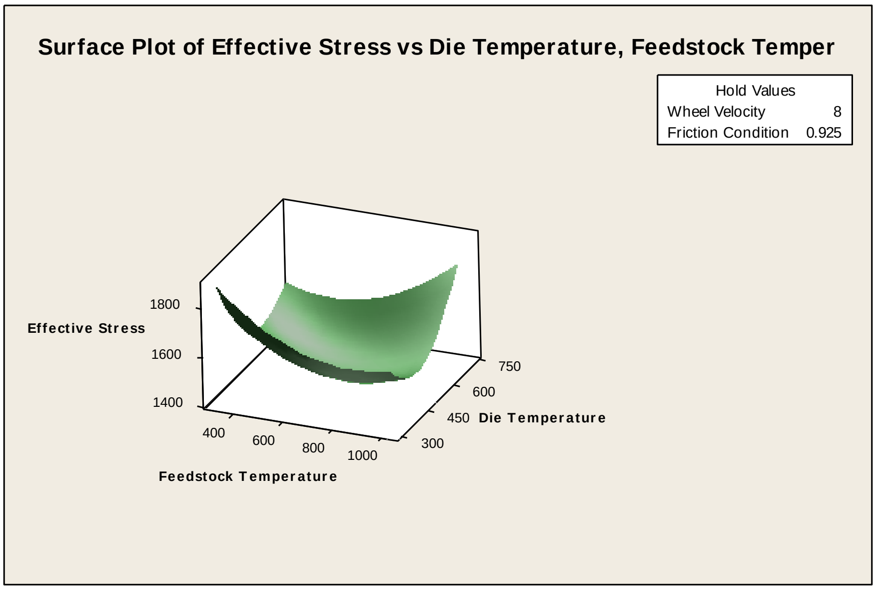

FIGURE. 4. 34: SURFACE PLOT OF EFFECTIVE STRESS VS FT AND DT

Figure 4.35 shows a one-side stretched (flattened) bowl shape 3D surface plot for effective stress verses die temperature and friction factor. Therefore, effective stress was minima in the middle and towards lower die temperature and higher friction factor.

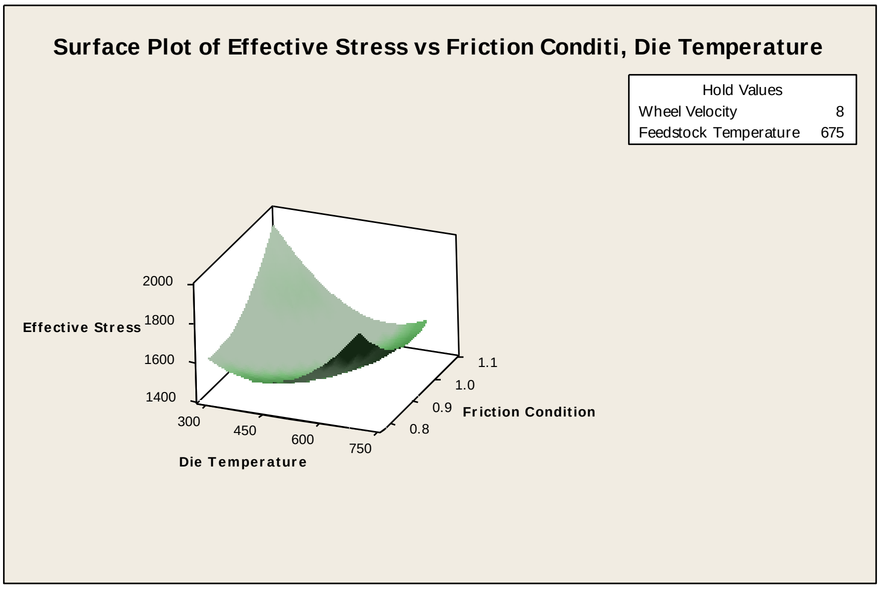

FIGURE 4. 35: SURFACE PLOT OF EFFECTIVE STRESS VS DT AND FF

It is observed from Fig. 4.36 that minimum effective stress of 799.9678N/mm^2 was induced in the feedstock during the process due to the CE process parameters when the wheel velocity, feedstock temperature, die temperature and frictional factor were 1.4545 revolutions per minute (RPM), 400℃, 400℃, and 0.9356, respectively. The optimum value of effective stress 799.9678 was induced with composite desirability of 0.99996 using RSM. Upon comparing the strength of H13 tool steel with effective stress developed in the process, the tool life could be improved. The yield and tensile strengths of hardened condition H13 tool steel were in the range of 1290–1570 and 1500–1960 MPa respectively. It was observed that all feed stock materials leaves the die exit with or towards zero effective stress induced upon leaving the die exit. Such a case is common in the CE extrusion process as the process itself perform process (work) relieving effect by itself as far as the parameters are properly controlled see Fig. 4.23.

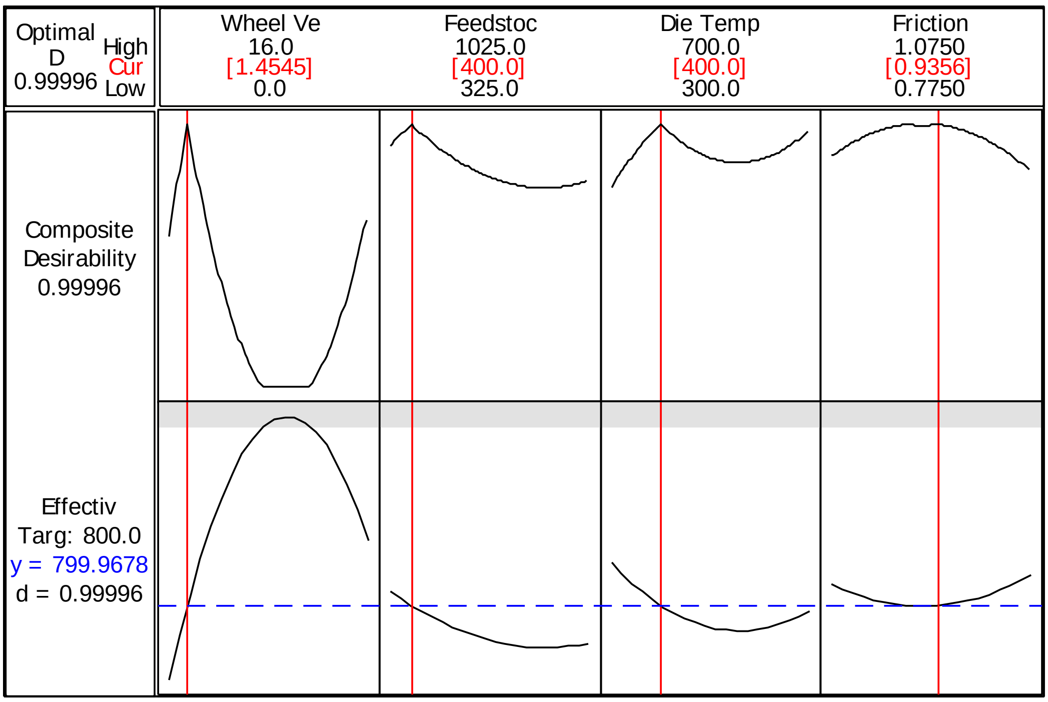

FIGURE 4. 36: OPTIMIZATION OF EFFECTIVE STRESS DUE TO WV, FT, DT AND FF

4.3.2.3. Modeling and optimization of damage through RSM for C101 feed metal

Modeling and optimization were carried out to investigate the extent of damage the feed metal experienced due to the CE process as a result of the CE process parameters. The independent variables such as extrusion wheel velocity, feedstock temperature, friction factor, and tool temperature were taken for experimental investigation. The variables at three levels were also taken into consideration and also shown in Table 3.22. The numerical experiments were performed through DEFORM-3D simulation tool from a 12.5mm in diameter C101 feedstock material into 6mm extrudate is shown in Fig. 4.37. Therefore, 31 numerical simulations, generated using CCRD method, performed as per the experimental plan. The damage the feedstock material experienced at various working conditions summarized in Table 4.5. The table indicates the computational results of the response the feedstock experienced during CE extrusion upon manufacturing an extrudate of a C101 alloy.

From Fig.4.37, we can also observe the damage C101 feedstock experienced during the computational analysis using DEFORM-3D. The damage of the feed metal considered encompassed all the three phases. They were before entry into grooved portion of extrusion wheel, during and after the CE extrusion of the raw material passed through die exit. The feedstock experience damage during the extrusion process increases initially as the feedstock material passed through the grooved portion of the wheel and was maximum when the material was entered into extrusion shoe and in collision with the abutment and finally decreased and goes to nil were observed upon leaving the die exit; Therefore, the extrudate experienced almost no noticeable damage when and after it left the die exit for all tests.

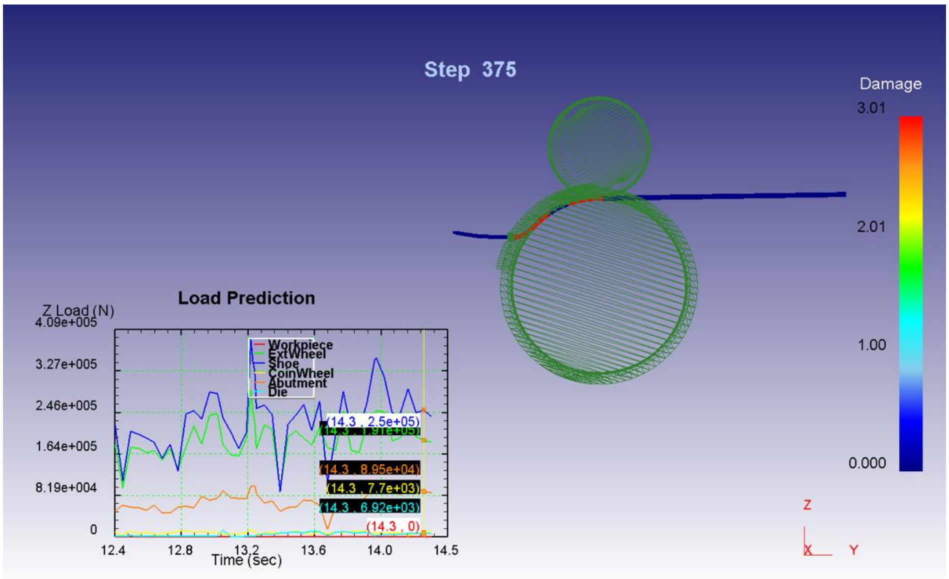

FIGURE 4. 37: DAMAGE DISTRIBUTION OF A 12.5MM C101 FEEDSTOCK

The RSM was used for modeling of process and optimization of damage characteristic on the feedstock. Therefore, based on the P-value, the parameter significance was evaluated.

If -value of any treatment fell below 0.05, then the treatment or effect had significant influence on the dependent variable i.e., damage. The significance of factors affecting dependent parameter is seen in Table 4.10.

Table 4. 10: Estimated regression coefficients for damage test results for C101

Term	Coef	SE Coef	T	P
Constant	122.303	0.04714	2594.290	0.000
Wheel Velocity	2.671	0.02546	104.896	0.000
Feedstock Temperature	-1.232	0.02546	-48.393	0.000
Die Temperature	2.397	0.02546	94.150	0.000
Friction Condition	4.180	0.02546	164.194	0.000
Wheel Velocity*Wheel Velocity	-29.160	0.02332	-1250.171	0.000
Feedstock Temperature*Feedstock Temperature	-30.000	0.02332	-1286.168	0.000
Die Temperature*Die Temperature	-27.258	0.02332	-1168.643	0.000
Friction Condition*Friction Condition	-22.193	0.02332	-951.491	0.000
Wheel Velocity*Feedstock Temperature	-0.394	0.03118	-12.647	0.000
Wheel Velocity*Die Temperature	1.156	0.03118	37.060	0.000
Wheel Velocity*Friction Condition	-4.317	0.03118	-138.440	0.000
Feedstock Temperature*Die Temperature	2.312	0.03118	74.141	0.000
Feedstock Temperature*Friction Condition	2.259	0.03118	72.457	0.000
Die Temperature*Friction Condition	-1.773	0.03118	-56.863	0.000

The actual mathematical model developed based on the data value of the coefficients shown in Table 4.10 is shown in the Eq. 4.23. In the expression, all the main, quadratic, and interaction effects of the Conform extrusion input processes parameters were taken into consideration. The value of correlation coefficient (R^2) and adjusted R^2 was found to be 100% and 100%, respectively, which indicated that the data were well correlated with the regression mathematical model developed. ANOVA for damage is also shown in Table 4.11.

The mathematical model expression for damage

$$Y = 122.303 + 2.671x_1 - 1.222x_2 + 2.397x_3 + 4.180x_4 - 29.16x_1^2 - 30x_2^2 - 27.258x_3^2 - 22.193x_4^2$$
$$-0.394x_1x_2 + 1.156x_1x_3 - 4.317x_1x_4 + 2.312x_2x_3 + 2.259x_2x_4 - 1.773x_3x_4$$

……………………………………………………………………………………… (4.23)

It was observed from Table 4.1 that *F*-value (Fishers test value) for linear and quadratic and interaction effects of the variables on damage were very high which signified that the developed mathematical model was significant statistically.

Table 4.11: Analysis of Variance of damage during C101 alloy extrusion

Source	DoF	SS	MSS	F	P
Regression	14	66408.6	4743.5	304903.44	0.000
Linear	4	764.9	191.2	12292.24	0.000
Wheel Velocity	1	171.2	171.2	11003.08	0.000
Feedstock Temperature	1	36.4	36.4	2341.84	0.000
Die Temperature	1	137.9	137.9	8864.28	0.000
Friction Condition	1	419.4	419.4	26959.77	0.000
Square	4	65104.2	16276.0	1046199.92	0.000
Wheel Velocity *Wheel Velocity	1	14486.6	24314.9	1562926.39	0.000
Feedstock Temperature *Feedstock Temp.	1	18604.3	25735.3	1654228.68	0.000
Die Temperature*Die Temperature	1	17928.7	21247.0	1365725.68	0.000
Friction Condition *Friction Condition	1	14084.6	14084.6	905335.19	0.000
Interaction	6	539.5	89.9	5779.91	0.000
Wheel Velocity*Feedstock Temperature	1	2.5	2.5	159.96	0.000
Wheel Velocity*Die Temperature	1	21.4	21.4	1373.47	0.000
Wheel Velocity*Friction Condition	1	298.2	298.2	19165.71	0.000
Feedstock Temperature *Die Temperature	1	85.5	85.5	5496.86	0.000
Feedstock Temperature *Friction Condition	1	81.7	81.7	5250.04	0.000
Die Temperature *Friction Condition	1	50.3	50.3	3233.44	0.000
Residual Error	16	0.2	0.0		
Lack-of-fit	10	0.2	0.0	*	*
Pure Error	6	0.0	0.0		
Total	30	66408.9			

From Fig.4.38 to Fig. 4.43 show the parametric combination effects of CE input process variables on damage C101 alloy undergone during the entire CE extrusion processing. From Fig. 4.44, to Fig. 4.49 show the surface plot and the optimization plot for parametric combination of input process variables contributing to damage.

It was observed from Fig. 4.38 that wheel speed and feedstock temperature had effect on damage. The damage experienced during the CE extrusion processing of C101 alloy was highest in dark green zone and lowest in light, bright, and Kelly green zone. So, based on the figure, the least damage which was less than or equal to zero was induced at each corners and over wider kelly green zones (especially when feedstock temperature (FT) was very low and wheel velocity (WV) was also very low; FT was very low and WV was very high; FT was very high and WV was very low, FT was very high and WV was also very high at holding values of die temperature 500°C and friction factor 0.925.

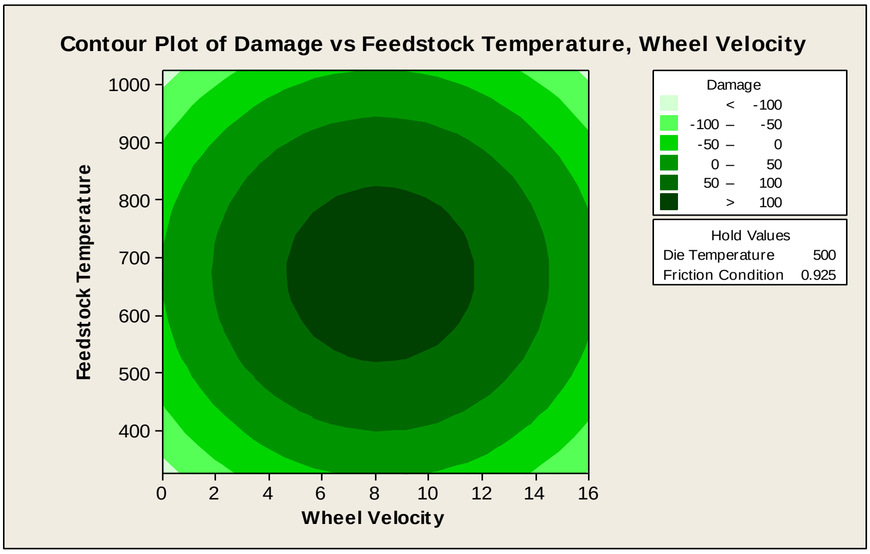

FIGURE 4. 38: EFFECT OF WV AND FT ON DAMAGE

The effect of wheel velocity and die temperature on damage can be perceived from Fig. 4.39. Based on the figure, the feedstock experienced highest damage in dark green zone and it was lowest in light, bright, and Kelly green zones. So, the least damage which less than or equal to zero 0 was developed at each corners and over wider light green and green zones (especially at four different corners or conditions such as when die temperature (DT) was very low and wheel velocity (WV) was also very low; DT was very low and WV was very high; and DT was very high and WV was very low, DT was very high and WV was also very high at holding values of feedstock temperature (FT) 675°C and friction factor (FF) 0.925.

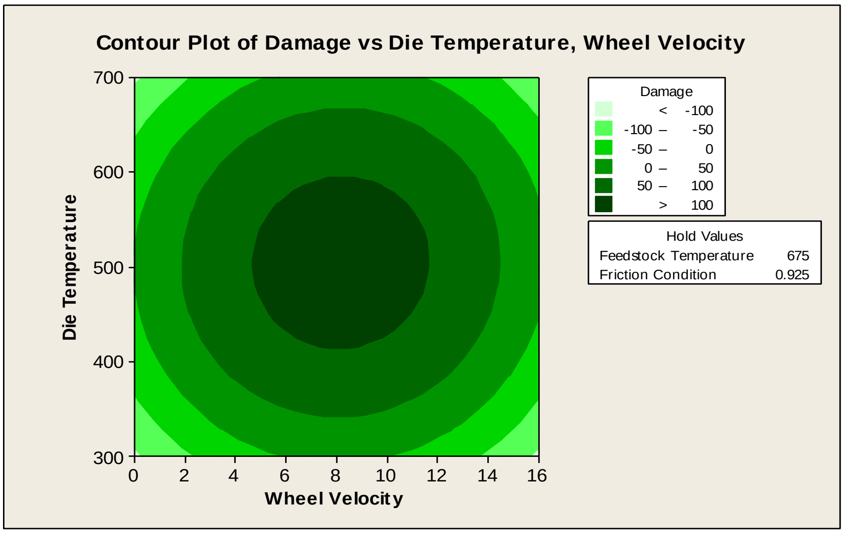

FIGURE 4. 39: EFFECT OF WV AND DT ON DAMAGE

It is observed the influence of extrusion wheel velocity and friction factor on feedstock damage from Fig. 4.40. Based on Fig. 4.40, the material experienced certain damages during the CE extrusion process. It reached to the highest in dark green zone and the lowest in light green and green zones. So, it can be concluded that the least damage was induced in the feed metal around each corners when WV was very low and FF was also very low taking holding values of feedstock temperature 675°C and die temperature 500°C.

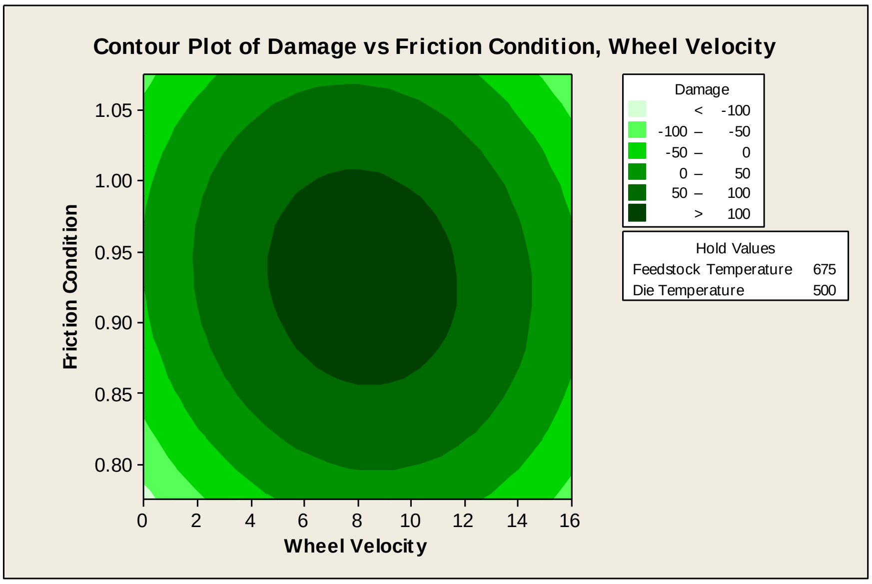

FIGURE 4. 40: EFFECT OF WV AND FF ON DAMAGE

It was observed the effect of die temperature and feedstock temperature on damage from Fig. 4.41. Based on the figure, the feed metal experienced highest damage in dark green zone and lowest in light green and green zones. So, it can be concluded that the least damage was induced at each corners and outside of the two inner regions (at two different zones or conditions such as when FT was very high and DT was also very low or FT was very low and DT was very high taking holding values of wheel velocity 8rpm and friction factor 0.925 for all the above cases.

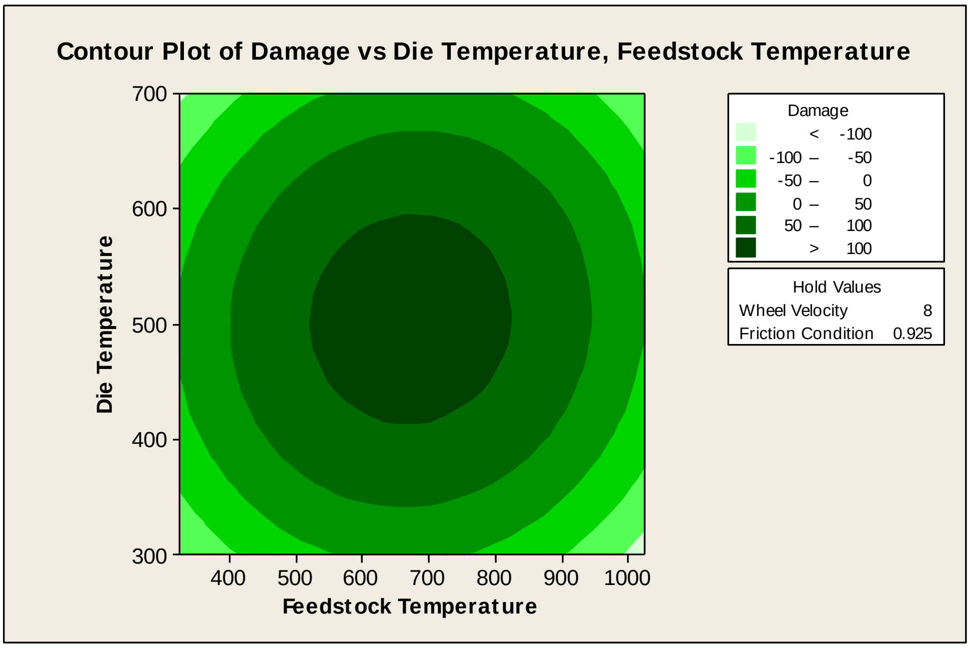

FIGURE 4. 41: EFFECT OF DT AND FT ON DAMAGE

It was also be perceived the effect of feedstock temperature and friction factor on damage from the Fig. 4.42. Based on the figure, the damage material experienced was highest in dark green zone and lowest in light green and green zones. So, it was possible tp conclude that the least damage was induced in at each corners (at four different zones or conditions such as when FT was very low and FF was also very low; FT was very low and FF was very high; FT was very high and FF was very low, and FT was very high and FF was also very high at holding values of wheel velocity 8rpm and die temperature 500°C.

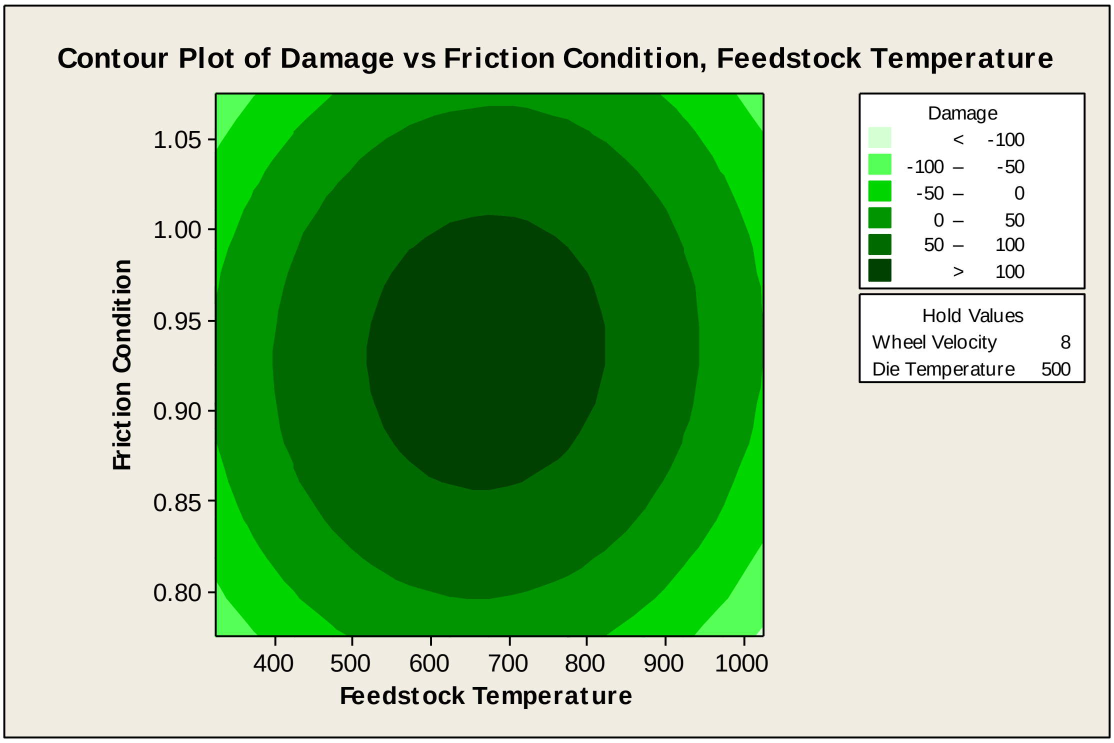

FIGURE 4. 42: EFFECT OF FF AND FT ON DAMAGE

It could also be perceived from Fig. 4.43 that damage the feed experienced was affected by feedstock temperature and die temperature. Based on the figure, highest damage during the CE extrusion was experienced in dark green zone and lowest one in light green one. So, it could be concluded that the least damage was induced in at each corners (in the four different zones or conditions such as when FT was very low and DT was also very low; FT was very low and DT was very high; FT was very high and DT was very low, FT was very high and DT was also very high taking holding values of wheel velocity 8rpm and friction factor 0.925.In any region where zero or less damage observed was always favored to prefer.

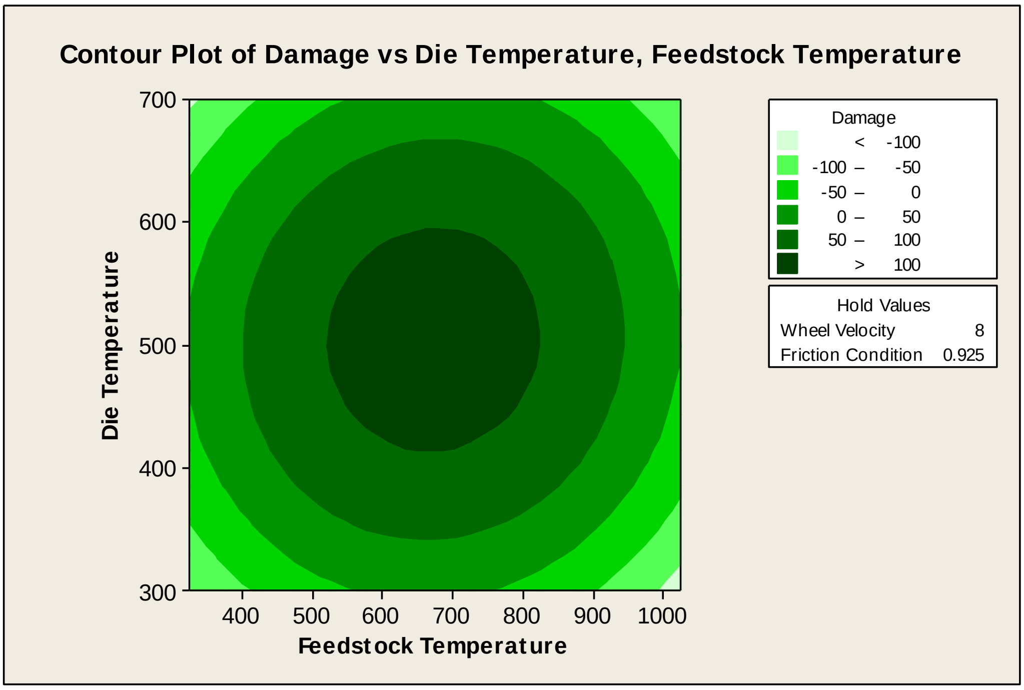

FIGURE 4. 43: EFFECT OF DT AND FT ON DAMAGE

Figure 4.44 shows a doom shape 3D surface plot of damage response for driving wheel velocity and FT variables. So, the damage was least at each corner of the plot.

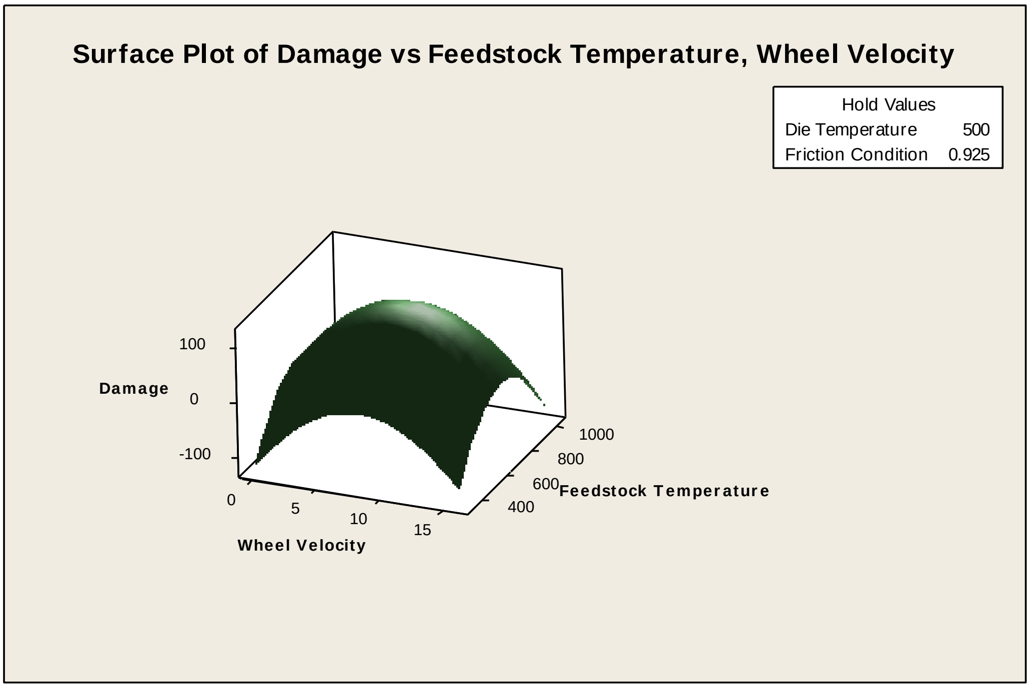

FIGURE 4. 44: SURFACE PLOT OF DAMAGE VERSUS WV AND FT

Figure 4.45 also shows a doom shaped 3D surface plot of damage response for WV and DT variables. So, damage was minimum at each corner of the plot. Least damage the feedstock experienced when the variables set at their extreme levels simultaneously.

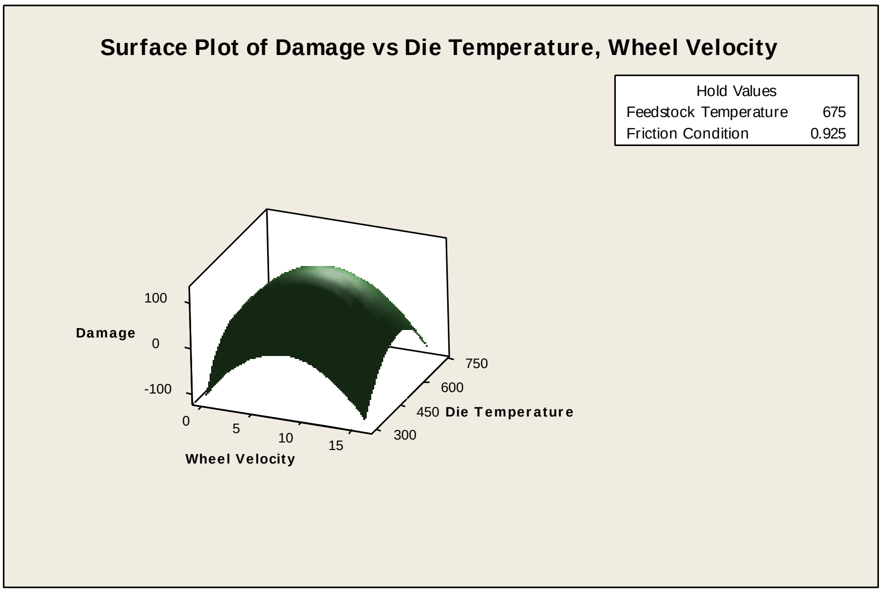

FIGURE 4. 45: SURFACE PLOT OF DAMAGE VERSUS WV AND DT

Similarly Fig. 4.46 also shows a doom shape 3D surface plot of damage response for wheel velocity and friction factor variables. So, the damage was least at least input parameters taking holding values of FT at 675°C and DT 500°C

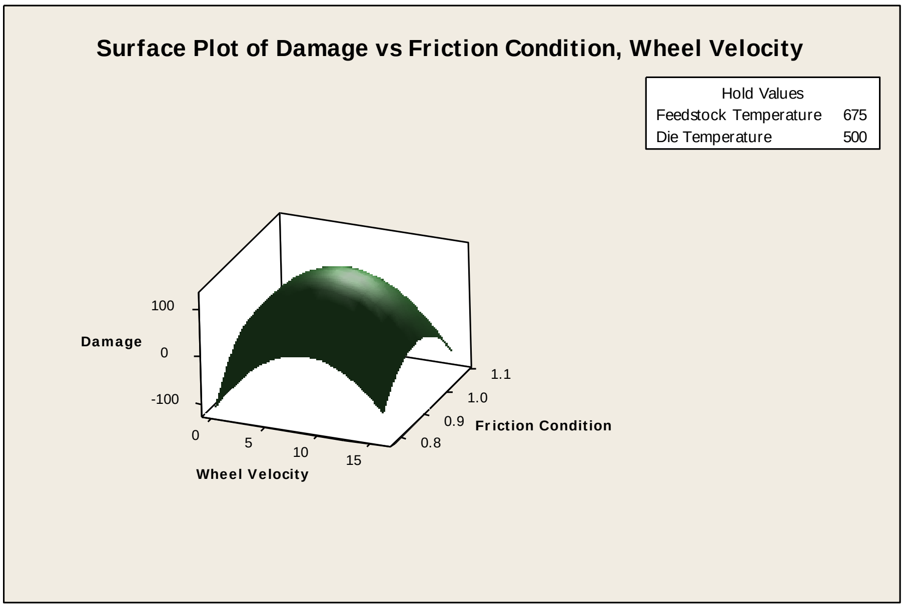

FIGURE 4. 46: SURFACE PLOT OF DAMAGE VERSUS WV AND FF

Figure 4.47 also shows a doom shaped 3D surface plot of damage response for wheel velocity and friction factor variables. So, least damage was observed at each corner of the plot.

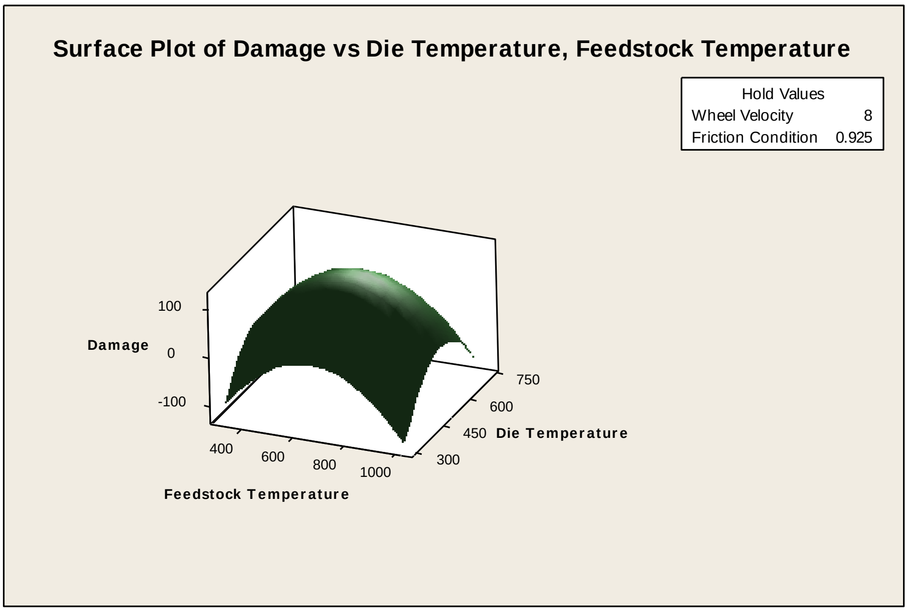

FIGURE 4. 47: SURFACE PLOT OF DAMAGE VERSUS FT AND DT

Similarly Fig. 4.48 also shows a doom shape 3D surface plot of damage response for wheel velocity and friction factor variables. So, damage was least at high FT and low FF.

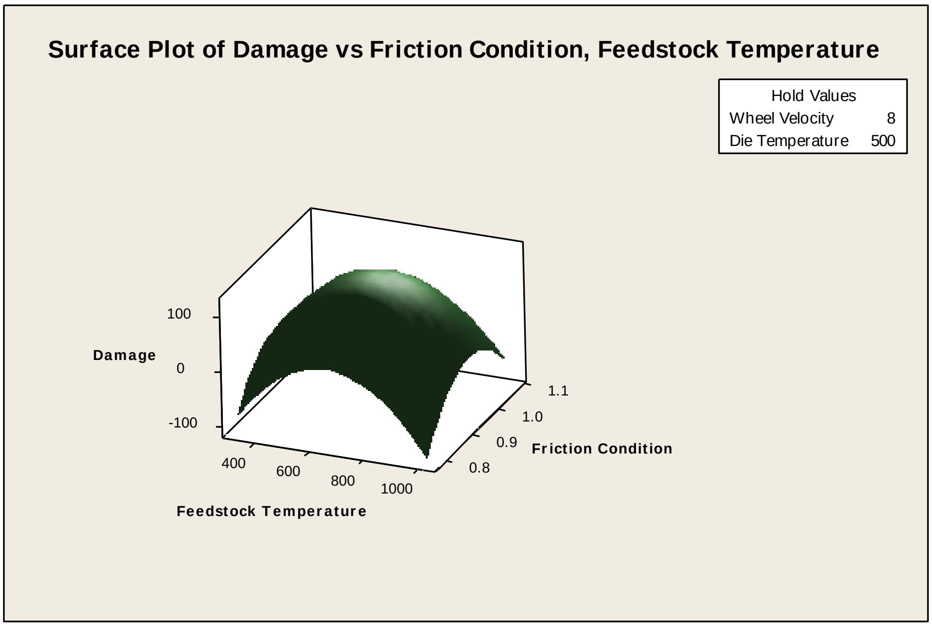

FIGURE 4. 48: SURFACE PLOT OF DAMAGE VERSUS FT AND FF

It is observed from Fig. 4.49 that the feedstock and extrudate experiences minimum damage of 0.9859 during the process if the wheel velocity, the feedstock temperature, the die temperature and frictional factor were 11.63 revolutions per minute (RPM), 400°C, 400°C, and 0.9.86, respectively. The optimum value of damage (0.9859) was obtained with composite desirability of 1.0 using RSM.

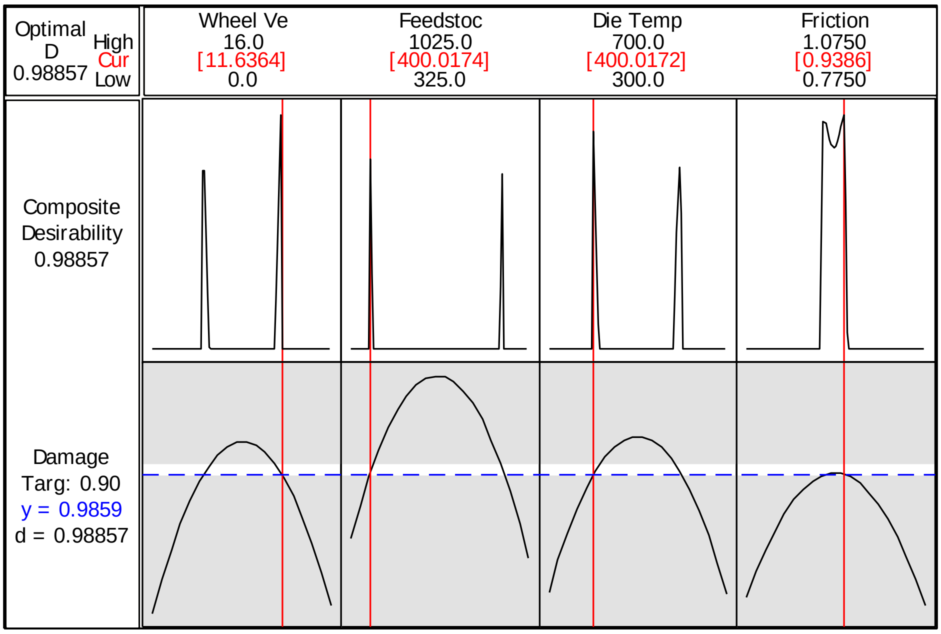

FIGURE 4. 49: OPTIMIZATION OF DAMAGE DUE TO WV, FT, DT AND FF

4.3.3. Modelling and optimization of Conform processing of C18150 alloy

The details of independent process variables with their respective levels and the experimental plan for C18150 were shown in Table 3.16 and Table 3.17 respectively. Simulation pre-process conditions were performed as per Table 3.8. The summary of tetrahedral mesh elements is shown in Table 3.9. Based on Table 3.17, 27 experimental plans were generated using Box Behnken Design method. Using the plans, all numerical simulations were carried out performed numerically through DEFORM-3D software. C18150 alloy with 12.5mm in diameter feedstock material was taken to manufacture an extrudate diameter of 8mm for computational analysis. The four input variables such as wheel speed, feedstock temperature, die temperature and friction factor of the RCE process were investigated for their effect on responses such as extrusion load, effective stress, and damage.

4.3.3.1. Modeling of total load requirement for C18150 alloy

From Fig. 4.50 to Fig. 4.52 show the total load distribution on each CE tooling including feedstock material in the x, y, and *z*-direction respectively. During investigation, the driving wheel was assumed as a rigid punch and a frictionless side plate (Kim, Y. H., et al., 2000). The figures show that the load needed for extrusion rises originally as the feedstock material moves through grooved part of the wheel, peaks whenever the feed material was about to be extruded in the die chamber and finally reduces once the extrusion was taken place.

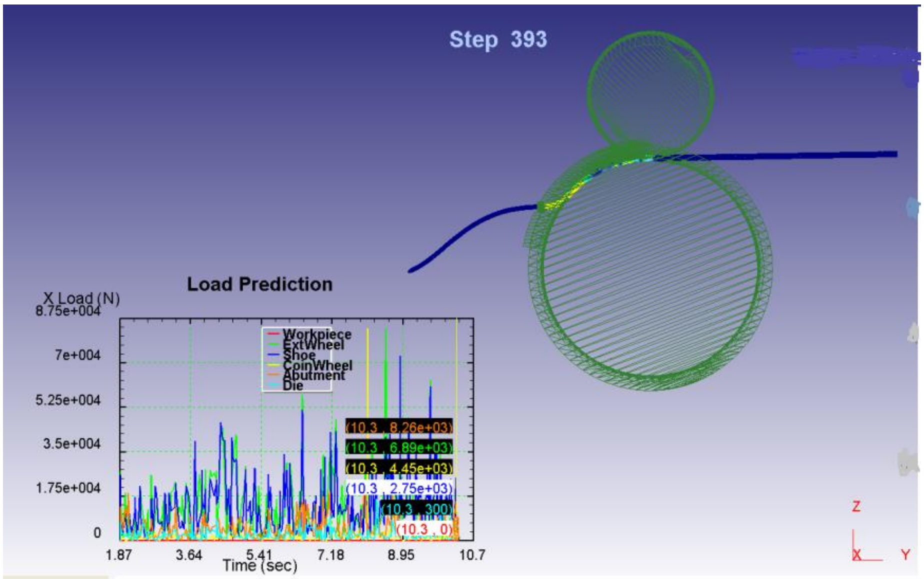

FIGURE 4. 50: *X*-LOAD DISTRIBUTION ON A C18150 FEEDSTOCK ALLOY

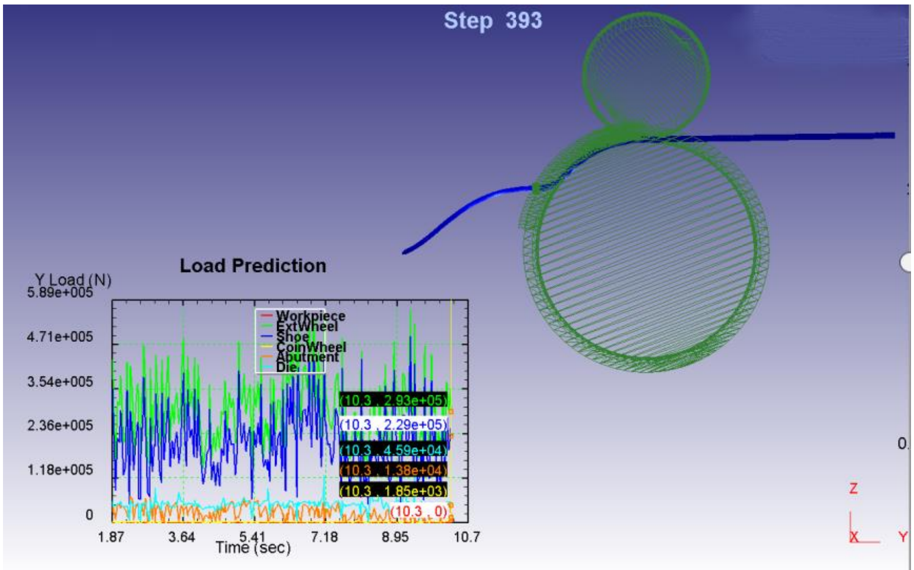

FIGURE 4. 51: *Y*-LOAD DISTRIBUTION ON A C18150 FEEDSTOCK ALLOY

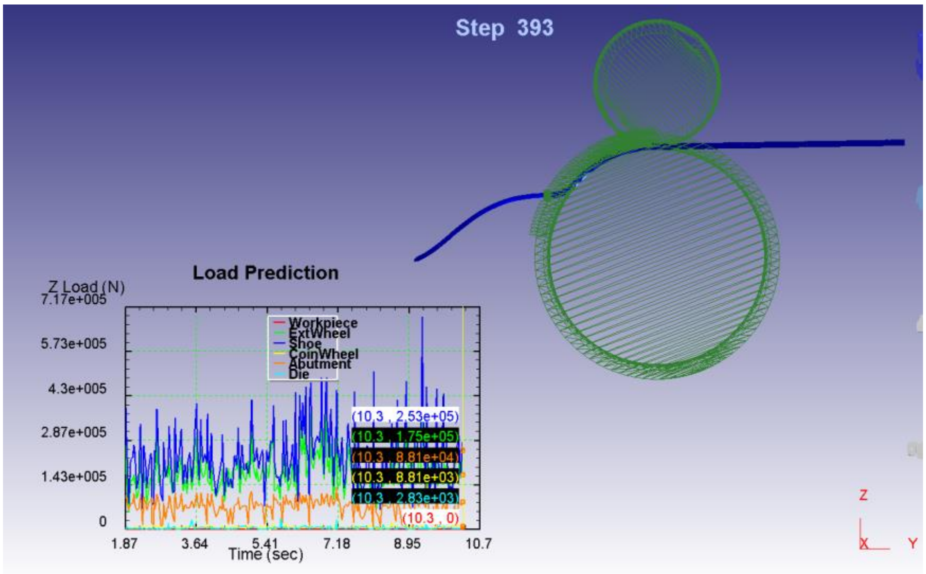

FIGURE 4. 52: *Z*-LOAD DISTRIBUTION ON A C18150 FEEDSTOCK ALLOY

Table 4. 12: Deform-3D simulation analysis results of C18150 alloy for five factors

Exp. Trail	x_1	x_2	x_3	x_4	Total load	Effective stress	Damage
1	4	600	500	0.95	799	1356	38.8
2	8	600	500	0.90	728	1391	6.6
3	12	600	600	0.90	766	1416	20.0
5	8	600	400	0.85	832	1413	32.5
5	8	500	500	0.95	929	1424	19.9
6	12	600	500	0.85	771	1398	9.0
7	12	600	400	0.90	786	1321	19.0
8	8	600	500	0.90	758	1369	6.6
9	8	700	600	0.90	802	1451	42.0
10	8	700	400	0.90	593	1401	20.0
11	4	500	500	0.90	696	1406	-3.0
12	12	500	500	0.90	713	1431	20.0
13	12	600	500	0.95	657	1479	15.0
14	4	600	400	0.90	687	1354	13.0
15	8	600	400	0.95	771	1398	8.0
16	12	700	500	0.90	742	1384	0.7
17	8	500	500	0.85	692	1448	6.9
18	8	600	600	0.85	707	1406	-0.1
19	4	700	500	0.90	744	1353	30.0
20	4	600	600	0.90	726	1424	40.0
21	8	600	600	0.95	629	1414	69.0
22	8	600	500	0.90	773	1439	6.6
23	8	700	500	0.95	749	1409	41.0
24	8	700	500	0.85	771	1398	9.0
25	8	500	600	0.90	605	1498	22.5
26	4	600	500	0.85	832	1355	2.0
27	8	500	400	0.90	680	1432	16.5

Note: The product diameter taken for computational simulation is 8mm.

Legends x_1: wheel velocity; x_2: feedstock temperature; x_3: die temperature, and x_4: friction factor.

The values of the process inputs and extrusion force needed during the CE extrusion of the feed alloy from its entry into grooved portion of extrusion wheel up to the final exit through extrusion die are tabulated in Table 4.12. The input variables taken for the investigation were driving wheel speed, feed temperature, and die temperature and friction factor.

Table 4.12 shows how the CE input variables have an impact on the outcome parameters such as the total load. The total load requirement analyzed to work within compliance with the research setup at numerous different working conditions such as wheel velocities, friction factors, and feedstock temperatures and die temperatures taking at a product diameter of 8mm. The table also shows the computational results of the total load requirement during manufacturing of an extrudate of a C18150 alloy. The general regression mathematical model adopted for the total load necessary to extrude a C18150 alloy was expressed in Eq. 3.60. Based on the general regression mathematical model, the actual mathematical model expression was developed for total load. The model equation could be constructed utilizing the P-values indicated in Table 4.13.

Table 4. 13: Estimated regression coefficients for total load for C18150

Terms	**Coefficients**	**Standard error coefficient**	**t-value**	**P-value**
Constant	8490.71	194.673	43.615	0.000
Wheel Velocity	73.75	2.885	25.567	0.000
Feedstock Temperature	-8.22	0.124	-66.128	0.000
Die Temperature	-23.80	0.121	-196.154	0.000
Friction Factor	-310.00	372.869	-0.831	0.422
Wheel Velocity*Wheel Velocity	-2.31	0.031	-73.808	0.000
Feedstock Temperature*Feedstock Temperature	-0.00	0.000	-35.159	0.000
Die Temperature*Die Temperature	0.00	0.000	2.743	0.018
Friction Factor * Friction Factor	-8000.00	200.520	-39.896	0.000
Wheel Velocity*Feedstock Temperature	0.01	0.001	9.933	0.000
Wheel Velocity*Die Temperature	0.15	0.001	104.085	0.000
Wheel Velocity*Friction Factor	-126.25	2.894	-43.621	0.000
Feedstock Temperature*Die Temperature	0.00	0.000	64.783	0.000
Feedstock Temperature*Friction Factor	9.25	0.116	79.900	0.000
Die Temperature*Friction Factor	22.55	0.116	194.782	0.000

Table 4.13 demonstrates that the effects of CE input variables on extrusion load. The input variables had significant influences, since their p-values were less than 0.05. Other factors which did not affect the extrusion load model because their p-values were significantly larger than the lower one. The load needed during the process was also influenced by all independent parameters if the die and feedstock temperature levels were

raised, the material's shear resistance decreases, lowering the load demand. The actual mathematical model was developed based on utilizing the data amount occurring in the coefficients revealed in Table 4.13 and also shown in Eq.4.24. Table 4.14 shows F-test result for the model test.

Table 4. 14: Analysis of Variance for total load to extrude C18150 alloy

Source	**DOF**	**SSS**	**AMS**	F	P
Regression	14	138933	9923.8	7404.25	0.000
Linear	4	47200	15307.1	11420.83	0.000
Wheel Velocity	1	9577	876.1	653.66	0.000
Feedstock Temperature	1	56	5860.9	4372.91	0.000
Die Temperature	1	936	51569.1	38476.41	0.000
Friction Condition	1	36631	0.9	0.69	0.422
Square	4	9498	2374.5	1771.68	0.000
Wheel Velocity*Wheel Velocity	1	5900	7301.3	5447.63	0.000
Feedstock Temperature *Feedstock Temperature	1	1076	1656.7	1236.12	0.000
Die Temperature*Die Temperature	1	388	10.1	7.52	0.018
Friction Condition*Friction Condition	1	2133	2133.3	1591.71	0.000
Interaction	6	82234	13705.7	10226.02	0.000
Wheel Velocity*Feedstock Temperature	1	132	132.3	98.67	0.000
Wheel Velocity*Die Temperature	1	14520	14520.3	10833.76	0.000
Wheel Velocity*Friction Condition	1	2550	2550.3	1902.78	0.000
Feedstock Temperature*Die Temperature	1	5625	5625.0	4196.89	0.000
Feedstock Temperature*Friction Condition	1	8556	8556.3	6383.94	0.000
Die Temperature*Friction Condition	1	50850	50850.2	37940.08	0.000
Residual Error	12	16	1.3		
Lack-of-fit	10	16	1.6	*	*
Pure Error	2	0	0.0		
Total	26	138949			

Based on the expression stated in section 3.3, the actual mathematical expression developed for total load in Eq.4.24. In the expression, all the main, quadratic, and interaction effects of the CONFORM extrusion input processes parameters were taken into considerations using the p-value of the parameters shown in Table 4.13. It was observed from Table 4.14 that *F*-value for all combinations of factors were very high which signified that the developed mathematical model was significant statistically based on the analysis of variance Table 4.14.The actual model equation is written as follows:

The developed mathematical model expression for the total load

$$Y = 8490.71 + 73.75x_1 - 8.22x_2 - 23.80x_3 - 2.31x_1^2 - 8000x_4^2 + 0.01x_1x_2 + 0.15x_1x_3 - 126.25x_1x_4 + 9.25x_2x_4 + 22.55x_3x_4$$

………………………………………………………………………………………. (4.24)

Figure 4.53 shows a residual graph for dependent parameter i.e., extrusion force. It is evident that those residuals are normally distributed anywhere along a straight line and thus satisfy the circumstance of model fit. In Fig. 4.53, all the data are very close to the straight-line. Main influences are defined as data that deviates from the straight line. Outliers have always been excluded from the entire data.

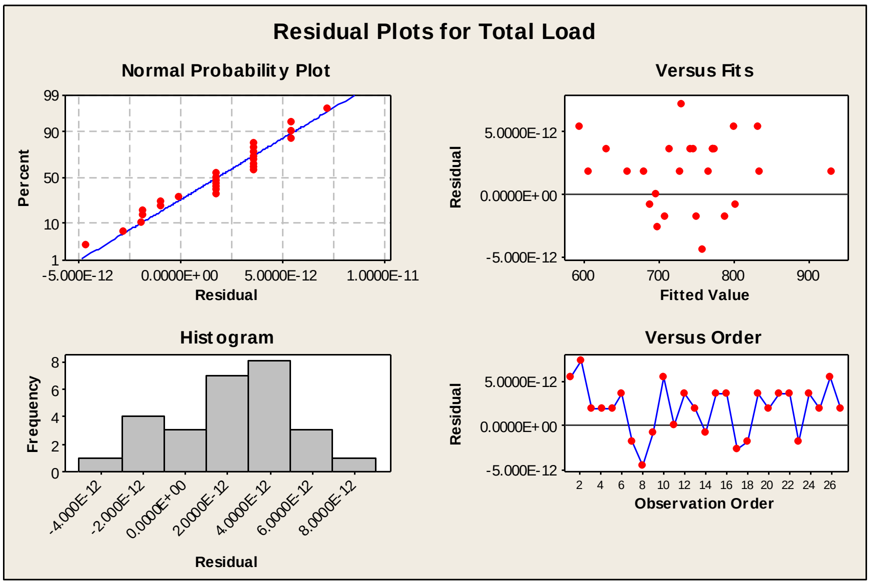

FIGURE 4. 53: TOTAL LOAD OF RESIDUAL PLOTS FOR C18150

Figure 4.54 to 4.59 show the parametric combination effects of CE extrusion input process variables on the total load needed to process a C18150 feedstock material.

The effect of wheel speed and feedstock temperature on total load was observed from Fig. 4.54. The load needed to extrude the material was highest in dark green zone and lowest in light green zone. As a result, Fig. 4.54 indicated that that less than 700kN load required for extrusion if wheel speed set extremely low and feedstock temperature set either very low around 500°C or very high above 640°C taking holding values of friction factor 0.9 and die temperature 500°C.

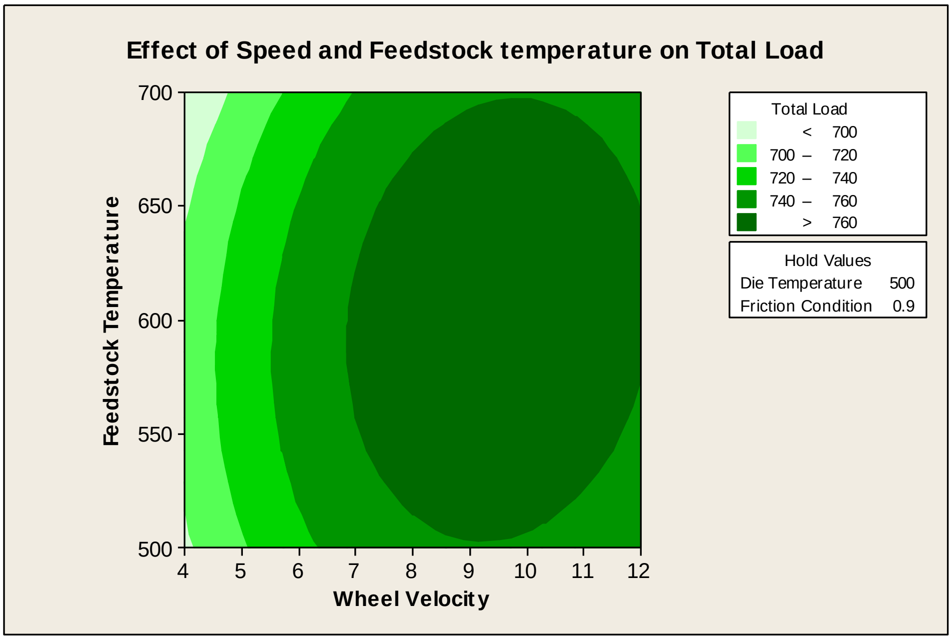

FIGURE 4. 54: CE LOAD RESPONSE AGAINST DRIVING WV AND FT

It was also observed the effect of die temperature and friction factor on total load from Fig. 4.55. A load required for extrusion of the alloy was maximum in dark green zone and minimum in dark blue zone. As a result, we could say that less than 600kN extrusion load was required if the die temperature was set very high above 540°C and friction factor set below 0.865, holding values of wheel velocity at 8rpm and feedstock temperature at 600°C.

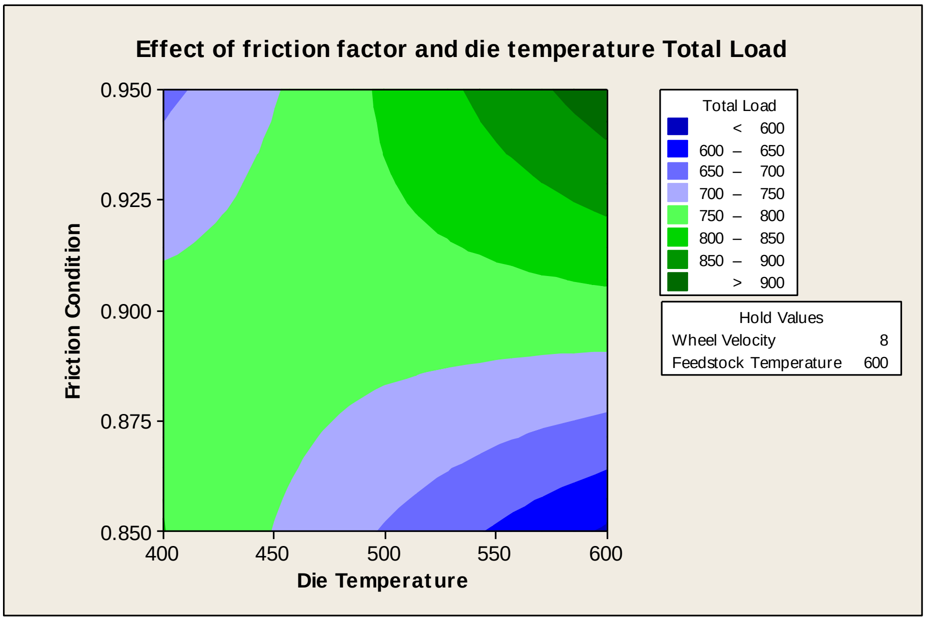

FIGURE 4. 55: EFFECT OF DT AND FF ON THE CE LOAD

It can also be perceived the effect of feedstock temperature and friction factor on total load from the Fig. 4.56. The load needed for extrusion of the alloy was highest in dark green zone and lowest in light green zone. As a result, one concluded that the least load required for the process was lower than 650kN if the feedstock temperature was very high above 680°C and friction factor was very low below 0.865, holding wheel velocity at 8rpm and die temperature at 500°C.

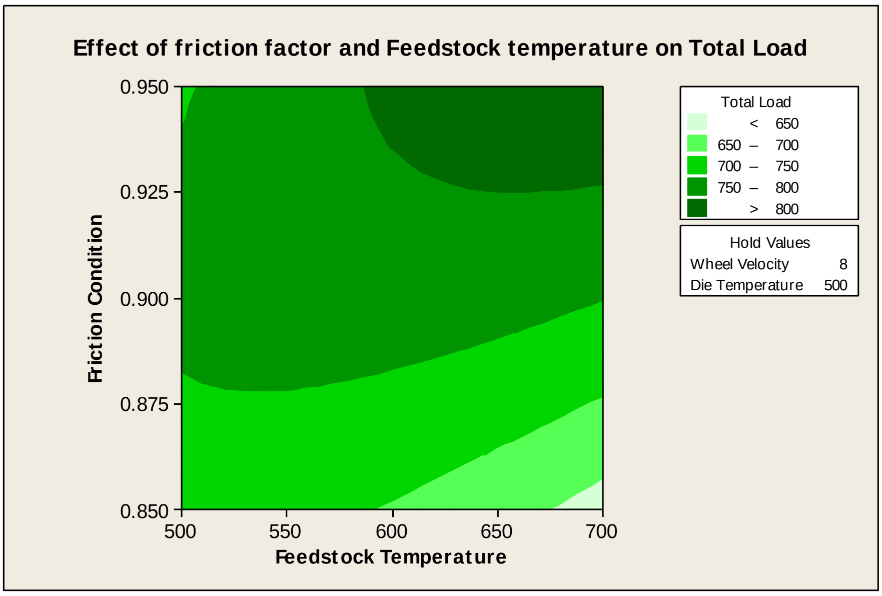

FIGURE 4. 56: EFFECT OF FF AND FT ON EXTRUSION LOAD

It can also be perceived on the effect of feedstock temperature and die temperature on total load from the Fig. 4.57. The load required for CE extrusion of C18150 alloy was greatest in dark green zone and lowest in dark blue zone. Therefore, it was reasonable to conclude that smaller than 720kN load could be applied for the CE extrusion of the alloy if the temperature in the feedstock was above 680°C and the temperature of the die was around and just below 425°C, holding wheel velocity at 8rpm and friction factor 0.9.

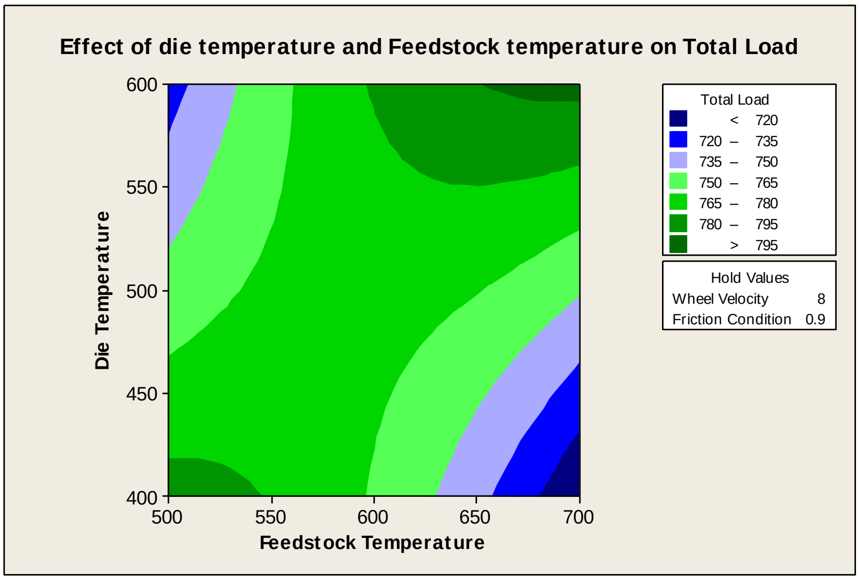

FIGURE 4. 57: EFFECT OF DT AND FT ON TOTAL LOAD

It can also be perceived the effect of wheel velocity and friction factor on total load from Fig. 4.58. The load was greatest in dark green zone and lowest in light green zone. Therefore, we could say that the least load than 650kN load applied for CE extrusion if both parameters such as wheel velocity and friction factor were very low level taking holding values of feedstock temperature at 600°C and die temperature at 500°C.

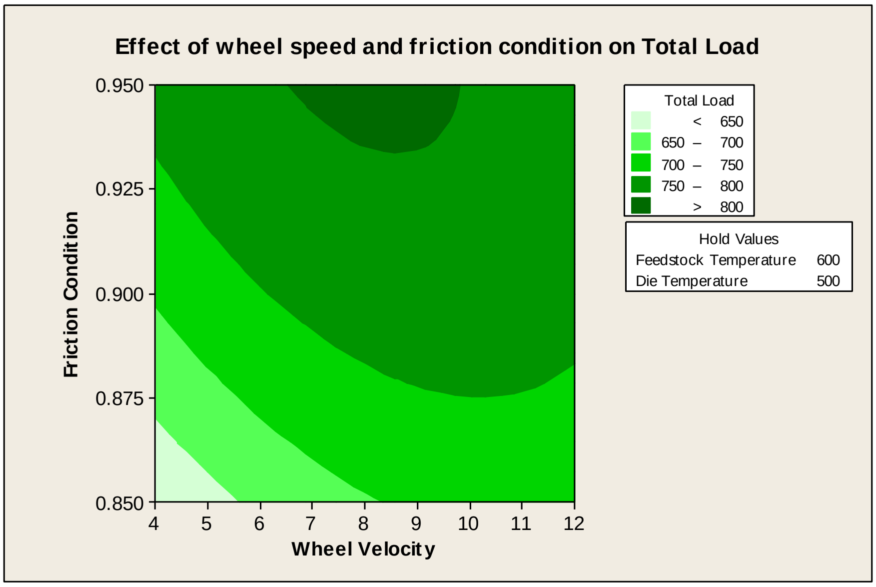

FIGURE 4. 58: EFFECT OF WV AND FF ON TOTAL LOAD

The influence of the wheel velocity and friction condition factor on extrusion load is apparent from Fig. 4.59. The load was greatest in dark green zone and least in dark blue zone. As a result, the least load required if the wheel velocity was very low and die temperature was enormously high around 600°C with holding values of feedstock temperature at 600°C and friction factor 0.9.

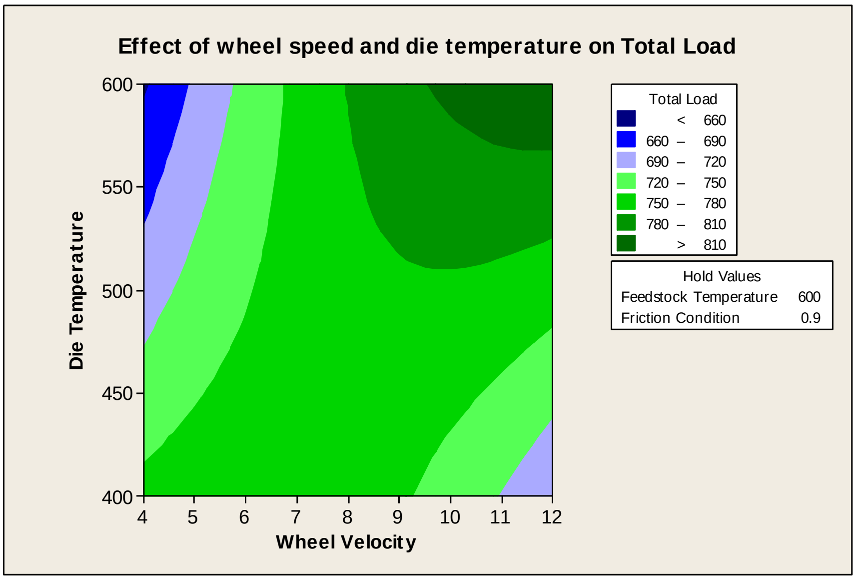

FIGURE 4. 59: EFFECT OF WV AND DT ON DEFORMATION LOAD

Figure 4.60 shows a doom shape 3D surface plot of extrusion load response for wheel velocity and feedstock temperature variables. So, it was minimum if the input variables set at their low levels simultaneously.

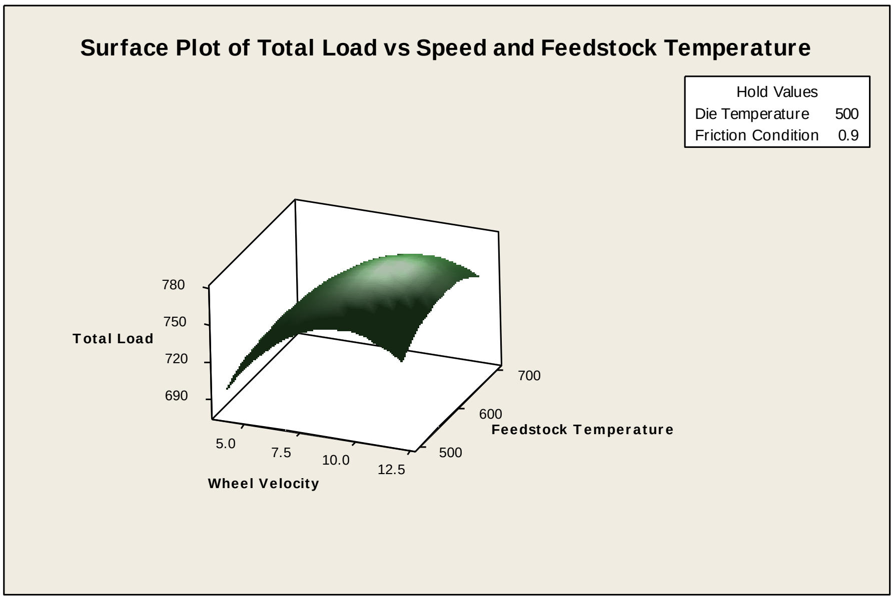

FIGURE 4. 60: SURFACE PLOT OF TOTAL LOAD VS WV AND FT

Figure 4.61 shows a flatted saddle shaped extrusion load 3D surface plot for wheel velocity and die temperature variables. So, the load was minimum, if the input variables set at wheel velocity low and die temperature was high; or wheel velocity at high and die temperature is low at holding values of FT of 600℃ and FF of 0.9.

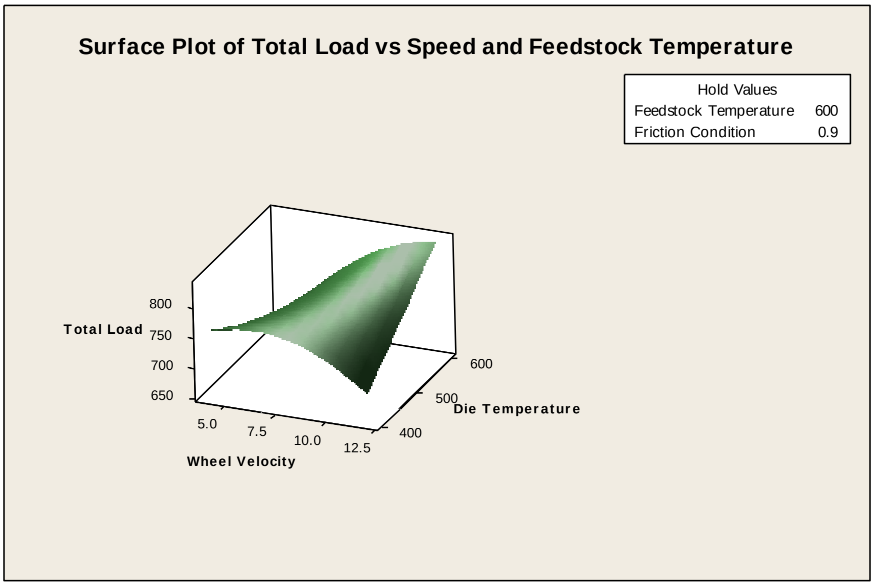

FIGURE 4. 61: SURFACE PLOT OF EXTRUSION LOAD VS WV AND DT

Figure 4.62 shows a flattened and offset doom looked 3D surface plot of load for wheel velocity and friction factor variables. So, the load was minimum, if the input variables set at their low levels simultaneously at holding values of FT of 600℃ and DT of 500℃.

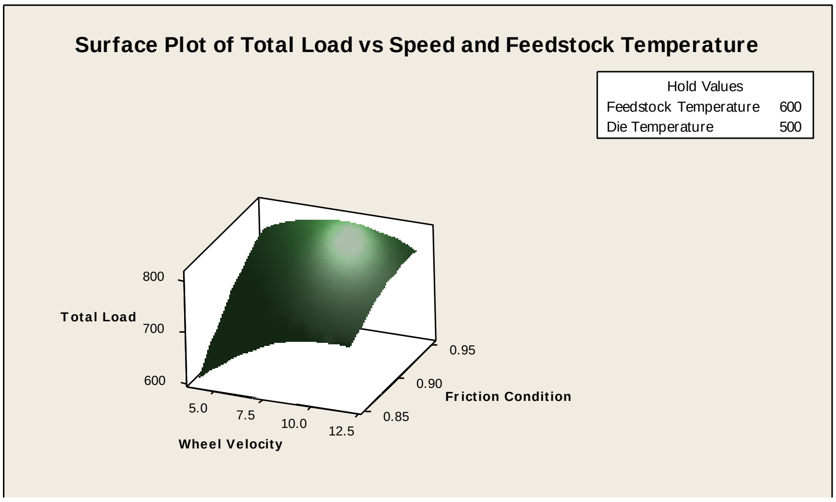

FIGURE 4. 62: SURFACE PLOT OCCURS IN EXTRUSION LOAD VS WV AND FF

Figure 4.63 shows a partially domed 3D surface plot of extrusion load for friction factor and feedstock temperature. So, the load is minima if the feed stock temperature is set at high and friction factor is low at holding values of 8RPM for WS and 500℃ for DT.

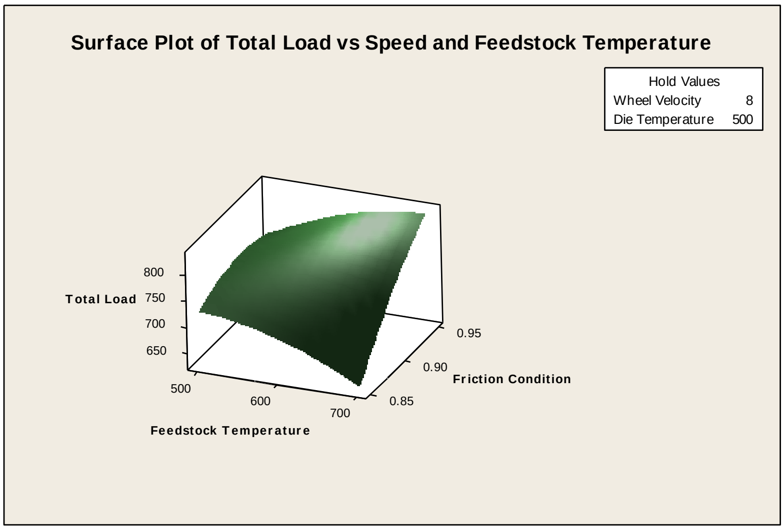

FIGURE 4. 63: SURFACE PLOT OF CE LOAD VS FF AND FT

Figure 4.64 shows a partially saddle 3D surface plot of extrusion load for feedstock temperature and die temperature. So, the load was minimum, if the former set at high and the latter was low at holding values of 8RPM for WV and 0.9 for FF.

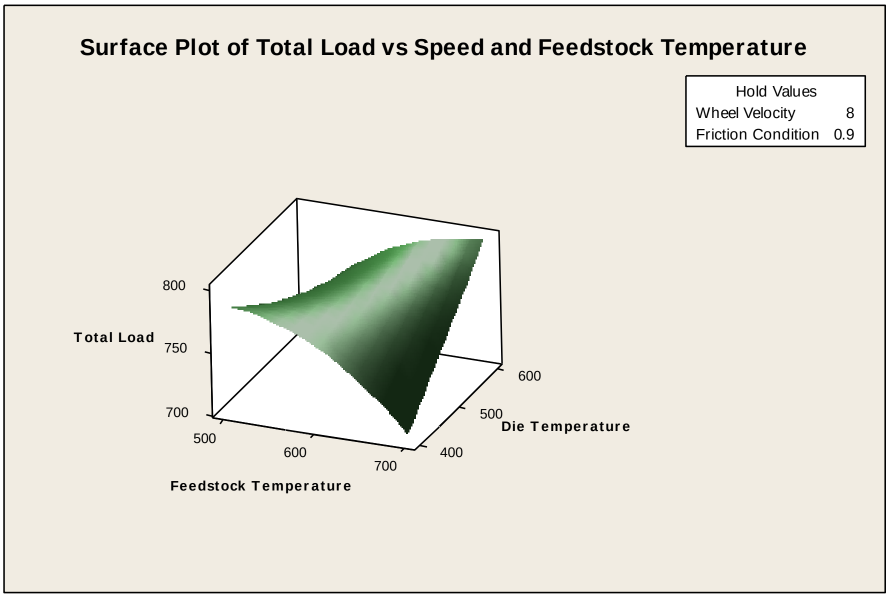

FIGURE 4. 64: SURFACE GRAPH OF CE LOAD VS DT AND FT

It is observed from Fig. 4.65 that an optimized load of 408.17kN was required if the wheel velocity, feed metal temperature, die temperature, and frictional factor were 4RPM, 700°C, 600°C and 0.85 respectively. The optimum value of load (408.17kN) was obtained with composite desirability of 1.0 using RSM.

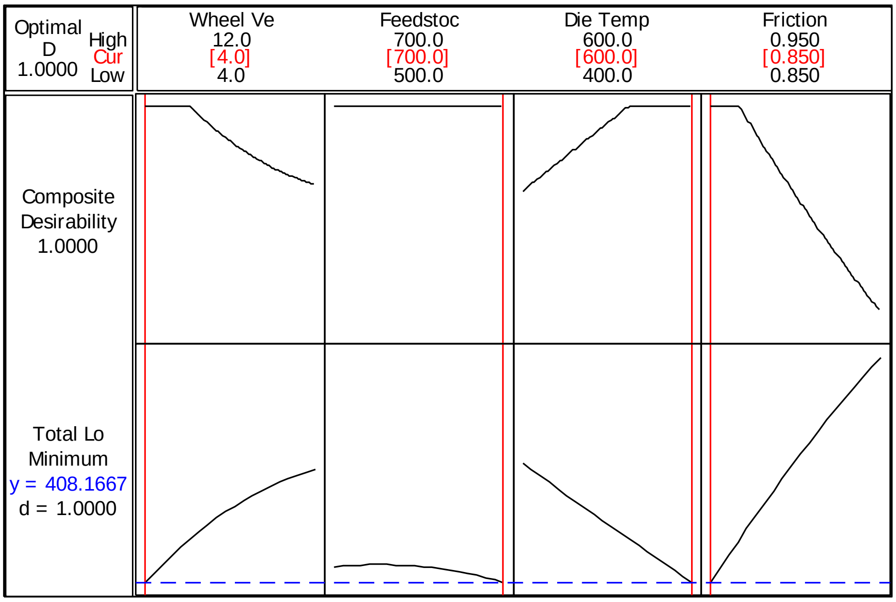

FIGURE 4. 65: OPTIMIZATION OF EXTRUSION LOAD VIA THE EFFECTS OF WV, FF, DT AND FT

I. Numerical data optimization through ANN model for C18150

In this analysis case of ANN Feed Forward Neural Network (FFNN) configuration was used. A predictive model with four input variables of the CE process i.e., wheel velocity, frictional factor, feedstock temperature and die temperature having significant impact on the output response of the CE process such as CE load required was built using Multi-Layer Perception (MLP). Every input including output was normalized in a domain of (0.1–0.9) for assurance of regular attention within the process of training. There were no general rules for selection of neuron in hidden layer; the best way was to apply trial and error method. The MATLAB program was used to perform ANN-based modeling studies.in this investigation, topology 4-12-1 was selected. Therefore the network consisted of four input nodes representing the input process variables of the CE process, twelve neurons for the hidden layer and one output node for the output response process parameters of the CE process at the end of training process.

The algorithm was exploited as the training data and utilized for testing the efficiency of the neural network. The number of neurons in hidden layer chosen in a range of 10–18 by cross-validating for the lowest values of root-mean-square error (MSE) and standard error of prediction (SEP). During the supervised training process, the associated learning error rate (mean-squared error) was minimized by increasing the number of training epochs (cycles).

However, an optimal number of training epochs needed to be determined in order to avoid any possible overtraining of the network. Figure 4.66 shows the training and test epoch cycles versus the calculated mean squared error of the supervised training and the comparison of input benchmark data and corresponding ANN predictions for the training process. It can be observed from Fig. 4.66 that a total number of 218 epochs became the optimum number of training cycles for the ANN structure and the corresponding MSE (relative error between the network output and target value) was found to be 1.31e^{-16}.

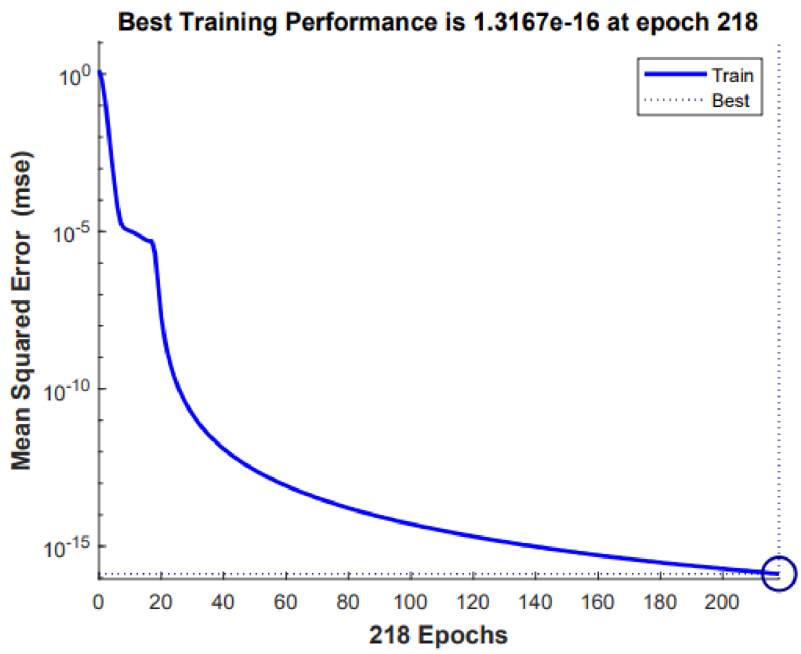

FIGURE 4. 66: TRAINING EPOCH CYCLES VERSUS CALCULATED MEAN SQUARE ERROR OF THE SUPERVISED TRAINING FOR THE DESIGNED ANN

The convergence of Mean-Squared Error during supervised training process was found to be 1.31e^{-16} at 218 epochs. Figure 4.67 showed the coefficient of correlation between the experimental and predicted data using ANN. The data were very closely spaced and distributed normally along the straight line which signified that experimental and predicted data were highly correlated.

Further, the fitness of the neural network prediction was analyzed by calculating the coefficient of R^2 using the experimental and predicted data. The R^2 (entire data including training and testing data) was found to be 0.99996 indicating that the used network was significant and the obtained data was also more accurate. This was further confirmed from Fig. 4.67 which showed that the predictions were concentrated near the diagonal line on the graph without much scattering.

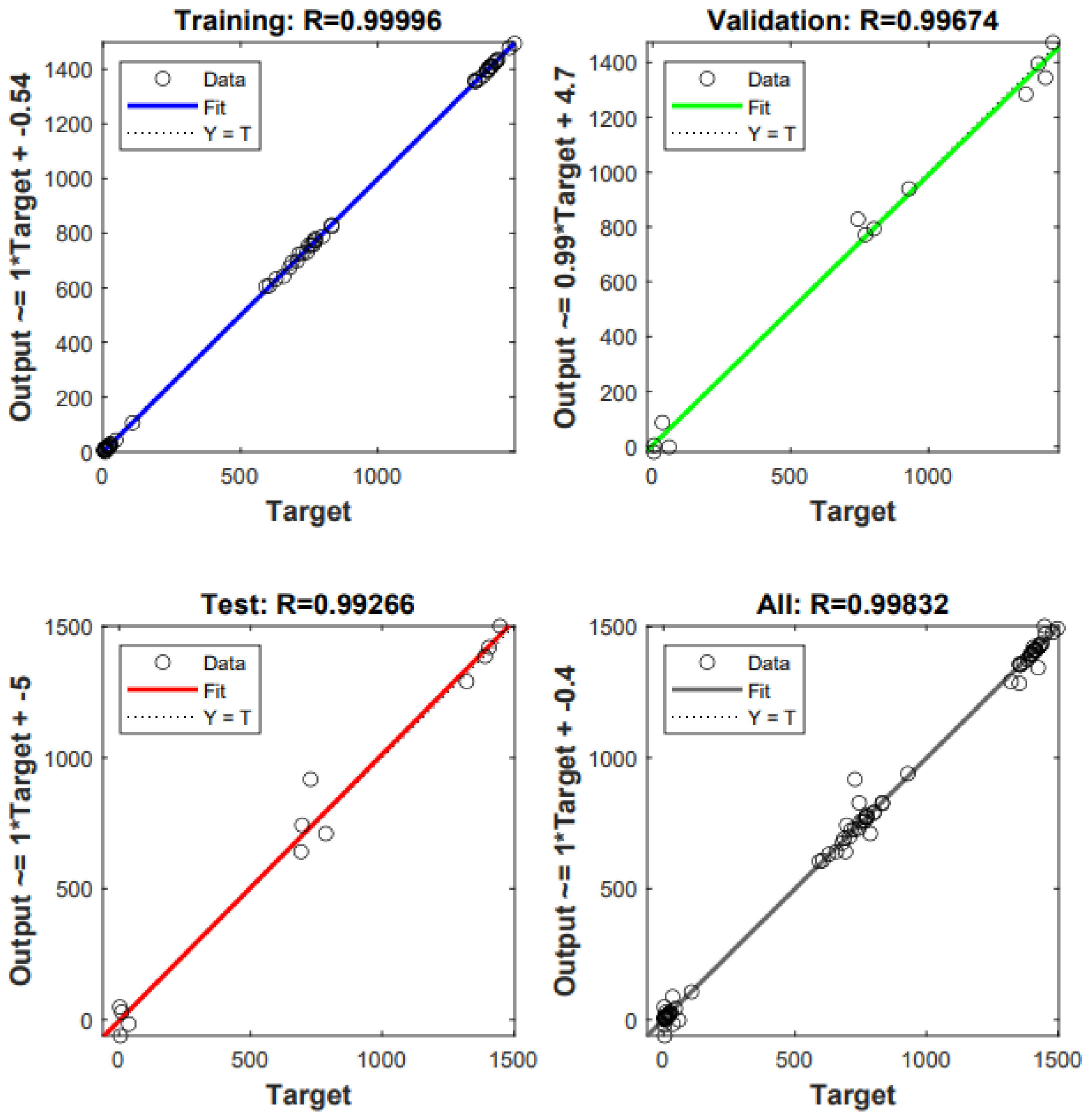

FIGURE 4. 67: CORRELATION CHART FOR EXPERIMENTAL AND PREDICTED LOAD REQUIRED FOR CE

II. GA-based optimization using ANN model

To facilitate a solution for an optimization problem done by regression technique, GA created an initial population of randomly generated individuals called chromosomes, generally represented as strings of binary digits. At each step, the GA selected the individuals at random, from current population, to be parents and used them to produce the offspring for the next generation. Crossover operator combined two parents to form children for upcoming generations. However, mutation rules were concerned with introducing new diversities among individual parents producing children. Point mutations were the most commonly occurring mutations, used to avoid any convergence to local maxima. This iterative process continued until a satisfactory solution according to the need of fitness function was achieved. The MATLAB was used to perform GA-based modeling studies.

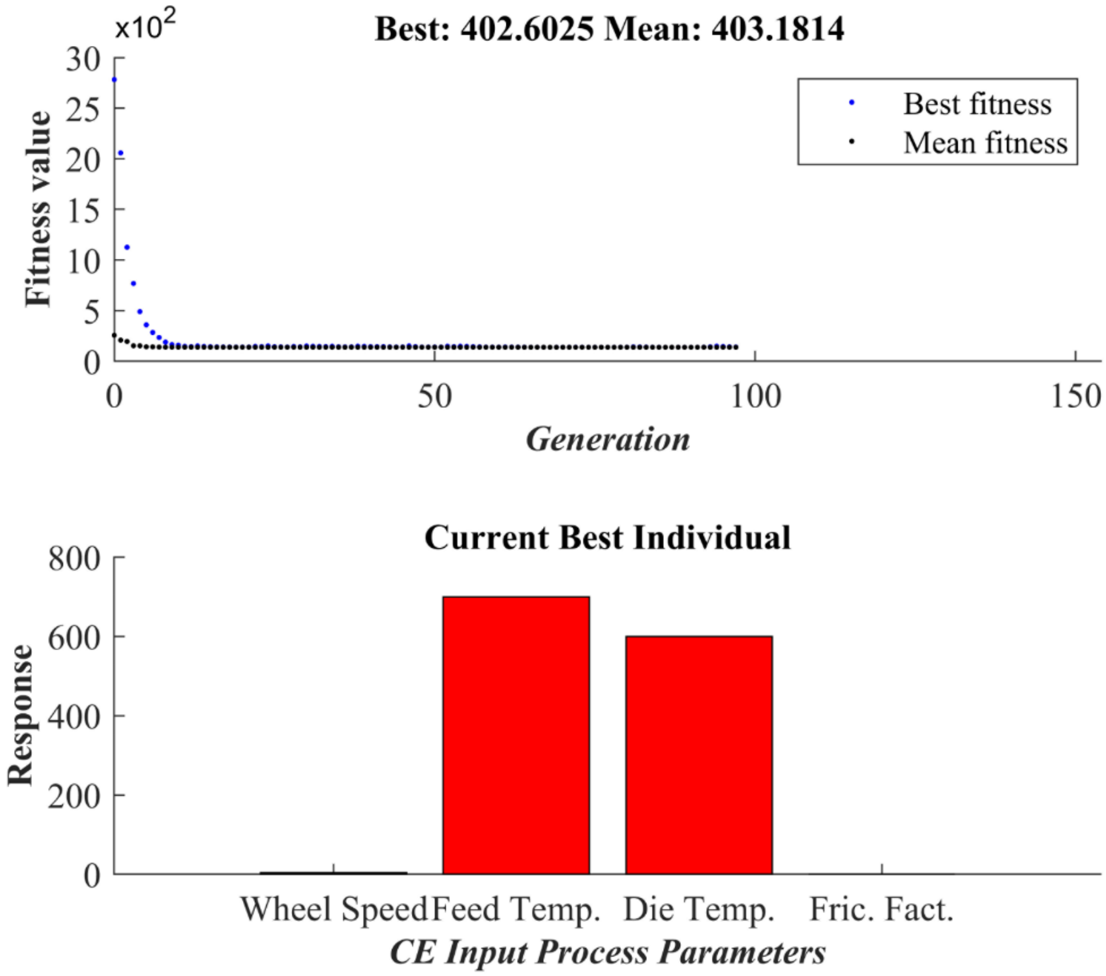

FIGURE 4. 68: BEST AND MEAN OPTIMAL TOTAL CE LOAD GENERATED BY GA WITH THEIR MODEL GENERATED PREDICTED VALUES

To facilitate an optimum solution, GA was employed on the newly generated population (data sets) of independent variables. The ANN based models were executed as the fitness functions by GA for minimum load required in CE process. All the five parameters of the model were represented in terms of chromosomes for GA-based optimization technique with the following constraints:

4 ≤ Wheel velocity ≤ 12; Product diameter =8mm; 0.85 ≤ Friction factor *≤ 0.95;*

500 ≤ Feedstock temperature ≤ 700; 400 ≤ Die temperature ≤ 600.

The GA parameters in the MATLAB software for the optimization of load required in CE of C18150 feedstock were set as follows: double vector; original population size: 100; cross over probability: 0.8; elite count: 20; crossover function: @crossover single point; migration direction: forward; selection function: @selection Roulette; mutation function: @mutation Gaussian; total generations: 100. Best fitness plot Fig.4.68 showing the progressive performance (for load required) of GA over generations till the achievement of optimum solution (upper plot). Variables (in lower plot) showing the level of wheel velocity, product diameter, friction factor, feedstock temperature and die temperature. Figure 4.68 below showed five random trials generated by GA with their model generated predicted values.

It can be observed from the plot that the convergence occurred at the value of 402.6425kN. The optimized values of independent process parameters for minimum value of load of extrusion obtained were 3.9RPM as wheel velocity, 8mm as product diameter, and 0.85 as friction factor, 700℃ as feedstock temperature and 600℃ as die temperature. The validation of the optimal solutions was carried out by independent experiments using the same conditions. The numerical validation of the ANN-GA results was carried out by carrying out numerical experiment at the optimum value of input process variables. The extrusion load corresponding to these optimum process variables was found to be 402.64kN obtained through GA using ANN which is very close to the value of 408.17kN through RSM. This finding may be very important in design and fabrication of the complete machine setup.

4.3.3.2. Numerical investigation and optimization of effective stress of a C181500 alloy through RSM

Based on Table 3.17, A total of 27 numerical simulations were performed as per the experimental plan generated using the Box-Behnken Design method for C18150 alloy.

Simulation pre-process conditions were performed as per Table 3.8. The summary of tetrahedral mesh elements is shown in Table 3.9. The details of independent process variables and experimental plan for C18150 are shown in Table 3.16 and Table 3.17 respectively. From these variables such as wheel speed, feedstock temperature, die temperature and friction factor of the RCE process were investigated for their effect on dependent variable effective stress. All the designed experiments were performed numerically through DEFORM-3D software. The feedstock and extrudate diameters used for the investigation were 12.5mm and 8mm respectively.

The input process factors and its respective response effective stress is found in Table 4.12. Effective stress induced in the material during the process was investigated according to the experimental setup at numerous different working conditions during a computational analysis of the alloy using DEFORM-3D, the effective stress of the material considered encompassed three stages. They were 'before the entry into the extrusion wheel’s recessed part, during and after the Conform extrusion of the raw material through die departure. The effects of the input variables on effective stress were investigated and their response values also tabulated in Table 4.12. The table shows a computational result of the effective stress induced in the feed metal upon CEP extruded at various input process parameters taking 12.5 mm feedstock to manufacture an 8 mm extrudate of the alloy.

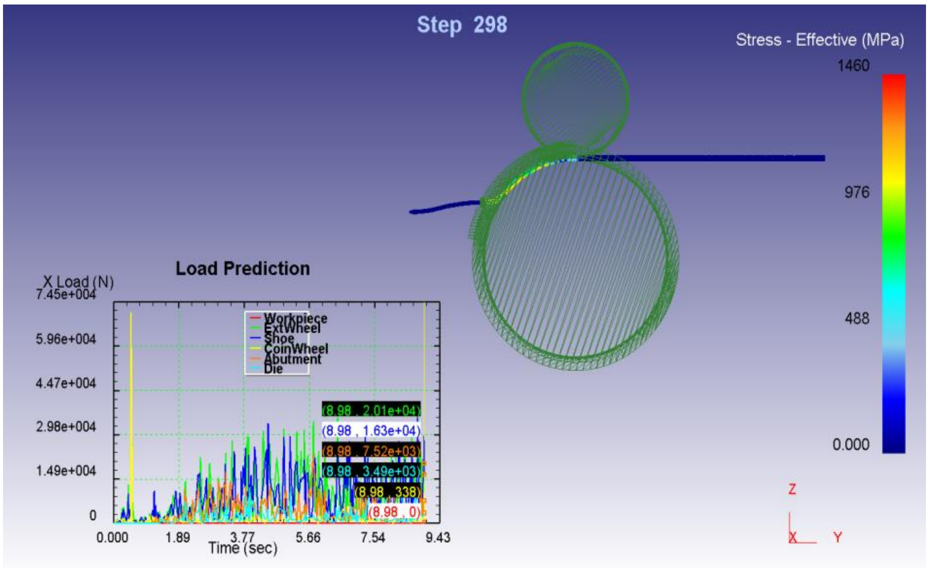

FIGURE 4. 69: EFFECTIVE STRESS DISTRIBUTION OF Cu-Cr-Zr ALLOY FEEDSTOCK DURING CE PROCESS

Figure 4.69 displays an effective stress induced within the feedstock material due to the CE processes before, during and after the CE process even on the extrudate. It could be observed as of Fig. 4.69 that the stress induced in a feedstock during the process raised primarily when the feedstock entered into the grooved segment of both the wheels and reached an to a maximum level whenever the material was in the direction changing zones such as in the secondary deformation zone and where in collision with the abutment and significantly reduced to normal or stress free state once the product left the extrusion die.

The RSM was utilized to model process factors quantity and optimization of output characteristics i.e., the Effective Stress induced in the raw material and the extrudate. As a result, if P-value of whatever treatment < 0.05, the treatment has a considerable impact on the dependent variable, Effective Stress. Table 4.15 shows vital factors influencing dependent factors. An actual mathematical model for effective stress prediction during the process was developed Eq. 4.25 based on the data shown in Table 4.15. In the expression, all the main, quadratic, and interaction effects of the CONFORM extrusion input processes parameters have been taken into consideration. The coefficient of correlation (R^2) and adjusted R^2 values are 91.49% and 89.03%, respectively, indicating that the data are very well strongly associated with the produced regression mathematical model.

Table 4. 15: Estimated regression coefficients for effective stress for C18150

Term	Coef	SE Coef	T	P
Constant	11621.2	105.795	109.847	0.000
Wheel Velocity	- 67.2	1.568	-42.886	0.000
Feedstock Temperature	0.6	0.068	8.818	0.000
Die Temperature	-1.4	0.066	-20.474	0.000
Friction factor	-21486.7	202.635	-106.036	0.000
Wheel Velocity*Wheel Velocity	1.7	0.017	99.108	0.000
Feedstock Temperature*Feedstock Temperature	-0.0	0.000	-64.695	0.000
Die Temperature*Die Temperature	-0.0	0.000	-43.589	0.000
Friction factor*Friction factor	8400.0	108.972	77.084	0.000
Wheel Velocity*Feedstock Temperature	-0.0	0.001	-0.795	0.442
Wheel Velocity*Die Temperature	-0.1	0.001	-161.328	0.000
Wheel Velocity*Friction factor	112.5	1.573	71.525	0.000
Feedstock Temperature*Die Temperature	-0.0	0.000	-95.366	0.000
Feedstock Temperature*Friction factor	3.5	0.063	55.630	0.000
Die Temperature*Friction factor	6.0	0.063	95.366	0.000

The F-value for the linear and quadratic impacts velocity of wheel, temperature of feedstock, temperature of die, factors of friction, the interaction outcome feedstock temperature, and die temperature seems to be indeed very considerable effect. Table 4.16 indicates that the established mathematical model was statistically significant.

Table 4. 16: Variance analysis for effective stress of C18150 alloy

Obs.	Std Order	Effective Stresses	Fit	SE Fit	Residual	Standard Residuals	F-value	P-value
1	16	1356.000	1355.833	0.481	0.167	0.41	7393.07	0.000
2	15	1391.000	1390.667	0.481	0.333	0.82	3566.56	0.000
3	11	1416.000	1416.333	0.481	-0.333	-0.82	1839.20	0.000
4	24	1413.000	1413.125	0.481	-0.125	-0.31	77.76	0.000
5	8	1424.000	1423.542	0.481	0.458	1.13	419.20	0.000
6	27	1398.000	1398.000	0.363	0.000	0.00	11243.65	0.000
7	13	1321.000	1321.167	0.481	-0.167	-0.41	7905.42	0.000
8	17	1369.000	1368.792	0.481	0.208	0.51	9822.32	0.000
9	5	1451.000	1450.708	0.481	0.292	0.72	4185.47	0.000
10	6	1401.000	1400.208	0.481	0.792	1.95	1900.00	0.000
11	1	1406.000	1405.708	0.481	0.292	0.72	5941.89	0.000
12	10	1431.000	1430.667	0.481	0.333	0.82	8737.89	0.000
13	19	1479.000	1479.792	0.481	-0.792	-1.95	0.63	0.442
14	7	1354.000	1354.042	0.481	-0.042	-0.10	26026.74	0.000
15	26	1398.000	1398.000	0.363	0.000	0.00	5115.79	0.000
16	2	1384.000	1383.875	0.481	0.125	0.31	9094.74	0.000
17	18	1448.000	1447.958	0.481	0.042	0.10	3094.74	0.000
18	14	1406.000	1406.333	0.481	-0.333	-0.82	9094.74	0.000
19	23	1353.000	1352.958	0.481	0.042	0.10		
20	21	1424.000	1424.625	0.481	-0.625	-1.54	*	*
21	22	1414.000	1414.792	0.481	-0.792	-1.95		
22	12	1439.000	1439.000	0.481	0.000	0.00		
23	4	1409.000	1408.542	0.481	0.458	1.13		
24	25	1398.000	1398.000	0.363	0.000	0.00		
25	9	1498.000	1498.000	0.481	0.000	0.00		
26	20	1355.000	1355.958	0.481	-0.958	-2.36 R		
27	3	1432.000	1431.375	0.481	0.625	1.54		

R denotes an observation with a large standardized residual.

Therefore, the developed mathematical model expression for the effective stress is

$$Y = 11621.2 - 67.2x_1 + 0.6x_2 - 1.4x_3 - 21486.7x_4 + 1.7x_1^2 + 8400x_4^2 -$$
$$-0.1x_1x_3 - 112.5x_1x_4 + 3.5x_2x_4 + 6.0x_3x_4 \qquad \text{……….. (4.25)}$$

Figure 4.70 depicts the residuals graph for effective stress. The graph demonstrates that all residuals are homogeneously and nearly normally distributed all along straight line, satisfying the circumstance of model fit. The figure also shows that all of the data points are indeed very close to the straight line. Significant effects are defined as data that deviates from the straight line. Outliers are almost always eliminated first from rest of the data information.

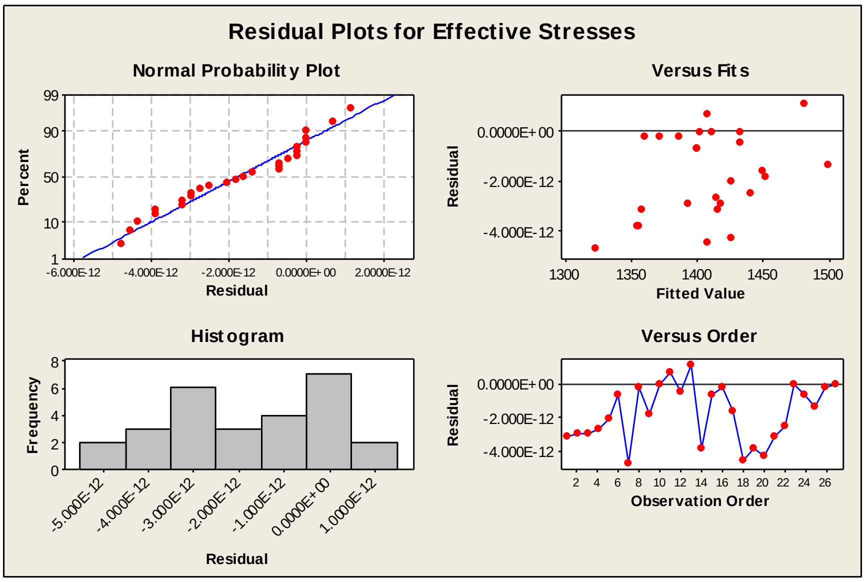

FIGURE 4. 70: RESIDUAL PLOTS FOR EFFECTIVE STRESS

From Fig. 4.71 to 4.76, the parametric combination effects of input variables on effective stress induced in the material during the entire CE extrusion processing of C18150 alloy are shown; however, from Fig. 4.77 to 4.83 surface plots and graph of optimization were displayed.

It is illustrated in Fig. 4.71 that feedstock temperature and speed of the driving wheel had an influence on effective stress induced in the material. The stress induced in the alloy was largest in the dark green zone and least the dark blue zone. As a result, it is reasonable to determine that less than 1370N/mm^2 effective stress was induced in the feed metal if the wheel speed was in-between 7.5 and 10rpm and feedstock temperature was lower than 520^{o}C at holding values of friction factor 0.9 and the die temperature 500^{o}C.

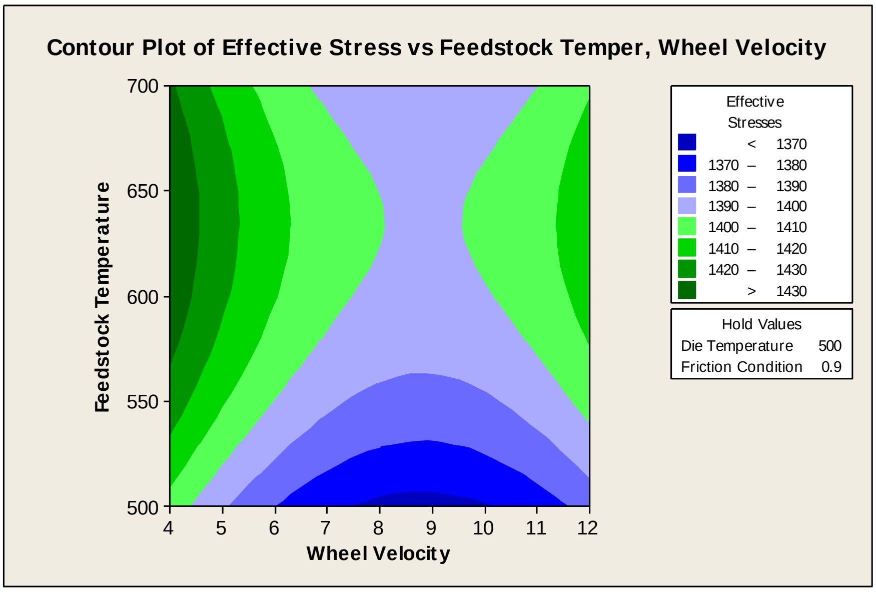

FIGURE 4. 71: EFFECT OF WV AND FT ON EFFECTIVE STRESS

An effect of effective stress occurred due to die temperature and friction factor is observed in Fig. 4.72. The stress in the dark green zone was the greatest and the least in the light green zone. As a result, it was possible to deduce using the figure that 1360N/mm^2 effective stress induced if the die temperature was very low less than 420^{o}C, the friction factor was very high at holding amounts occurred into velocity of wheel at 8rpm and the temperature of feedstock at 600^{o}C.

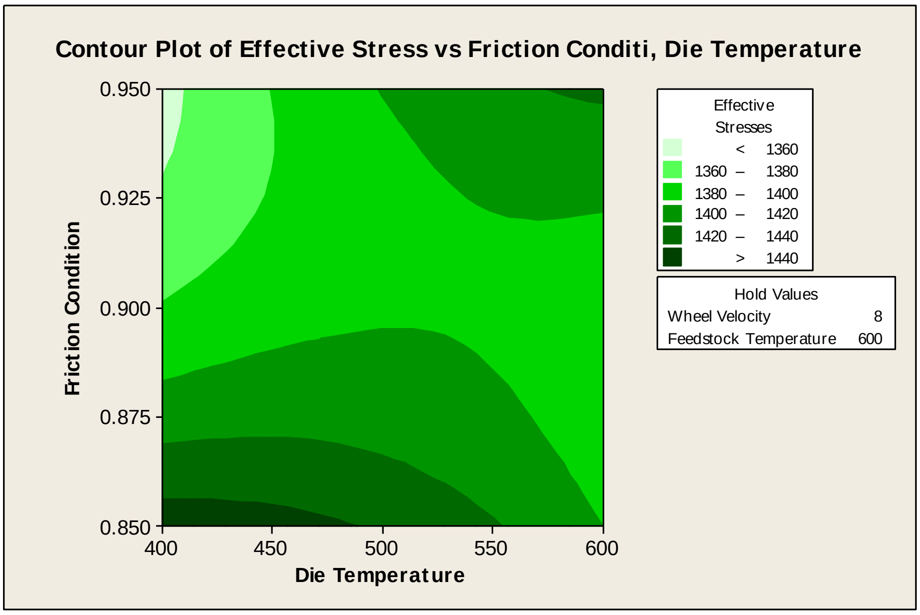

FIGURE 4. 72: EFFECT OF DT AND FF ON EFFECTIVE STRESS

The effect of feedstock temperature and friction factor on effective stress was observed in Fig. 4.73. It could also be perceived from the figure that the stress was maximum in the dark green zone and least in the light green zone. As a result, it was reasonable to infer from the figure that the least effective stress induced in CE process, if the feedstock temperature was lower than 520^{o}C and the friction factor was very high above 0.910 at holding amounts velocity of wheel at 8rpm and temperature of die tat 500^{o}C.

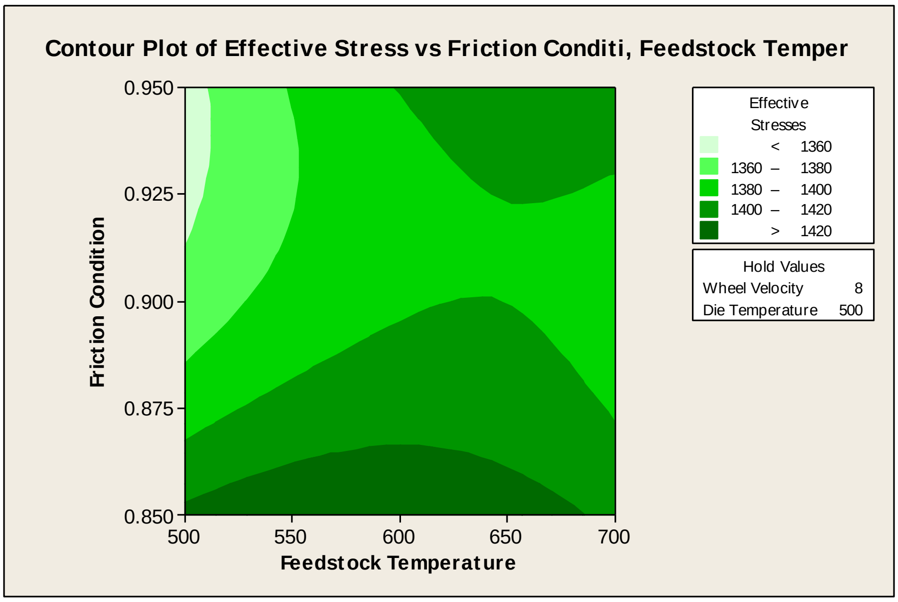

FIGURE 4. 73: EFFECT OF FF AND FT ON EFFECTIVE STRESS

It can also be perceived the effect of feedstock and die temperatures on effective stress induced in Fig. 4.74. The stress in the C18150 alloy was the greatest in the dark green zone; however, least in the light green zone As a result, it was possible to deduce that lower than 1335N/mm^2 effective stress was induced if both the feedstock and die temperature were very low levels with holding velocity of the wheel at 8rpm and friction factor at 0.9.

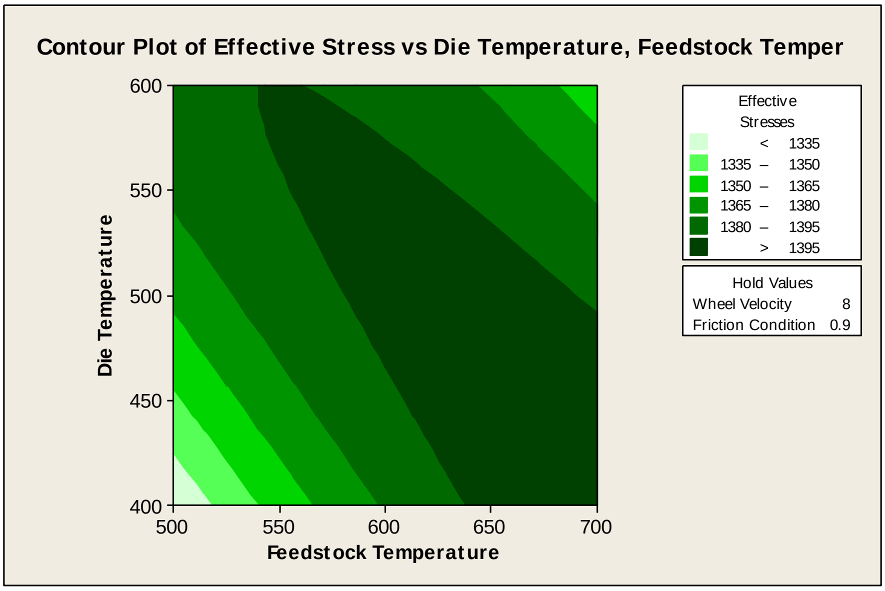

FIGURE 4. 74: EFFECT OF DT AND FT ON EFFECTIVE STRESS

The effect of wheel velocity and friction factor on effective stress can also be perceived from Fig. 4.75. The stress induced in the alloy due to the entire CEP extrusion was largest in the dark green zone; however, it was the least the light green zone. As a result, it is possible to deduce which the least effective stress induced in the alloy which was lower than 1400N/mm^2 if the wheel velocity was in-between 6 and 10.5 rpm and friction factors were just above 0.887 taking holding values of feedstock temperature at 600^{o}C and die temperature at 500^{o}C.

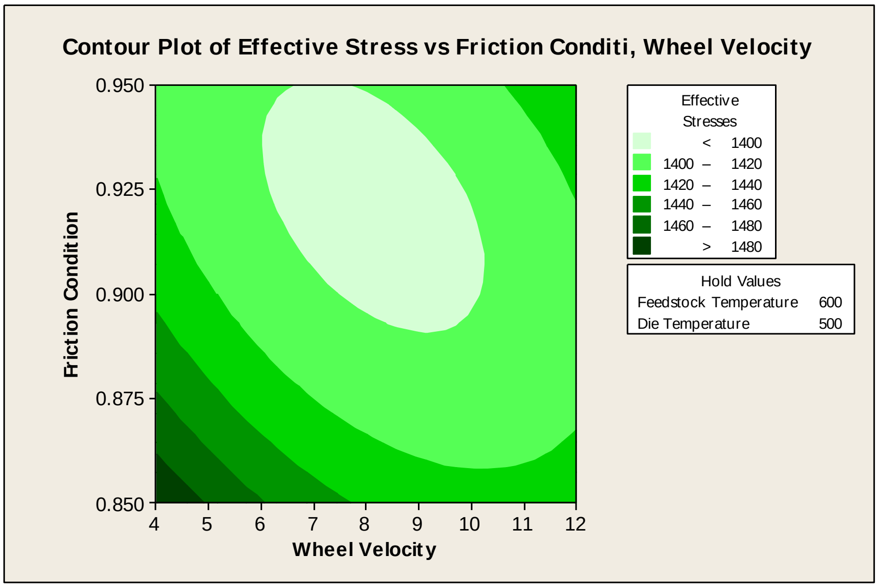

FIGURE 4. 75: EFFECT OF WV AND FF ON EFFECTIVE STRESS

The influence of wheel speed and temperature of die on effective stress can be observed in Fig. 4.76. The effective stress was greatest in dark green zone and least inside the light green zone. So, it was possible to conclude from the figure that the least effective stress induced if both the wheel velocity and die temperature were very high by taking holding values of feedstock temperature at 600^{o}C and. friction factor at 0.9.

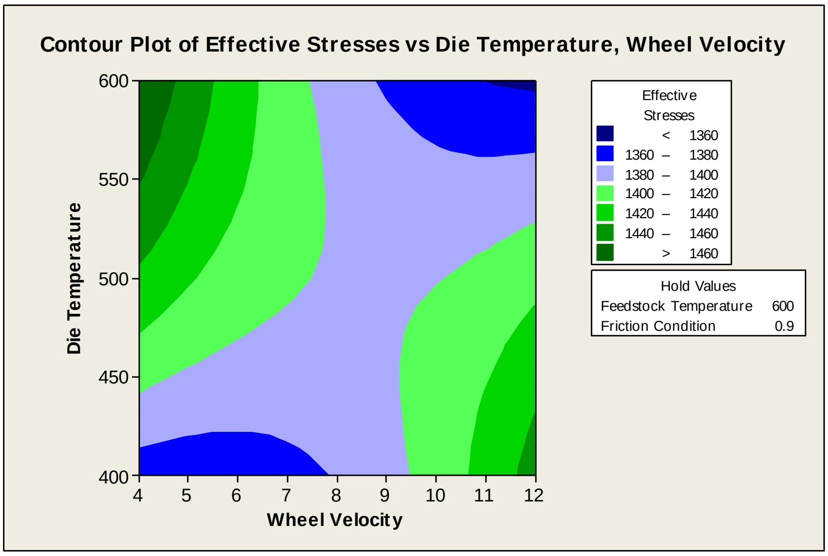

FIGURE 4. 76: EFFECT OF WV AND DT ON EFFECTIVE STRESS

Figure 4.77 shows a saddle shaped effective stress 3D surface plot for wheel speed and feedstock temperature. Lowest stress was induced when FT was well below 530^{o}C and WV between 8 and 11RPM at holding values of 500 ^{o}C FT and 0.9FF.

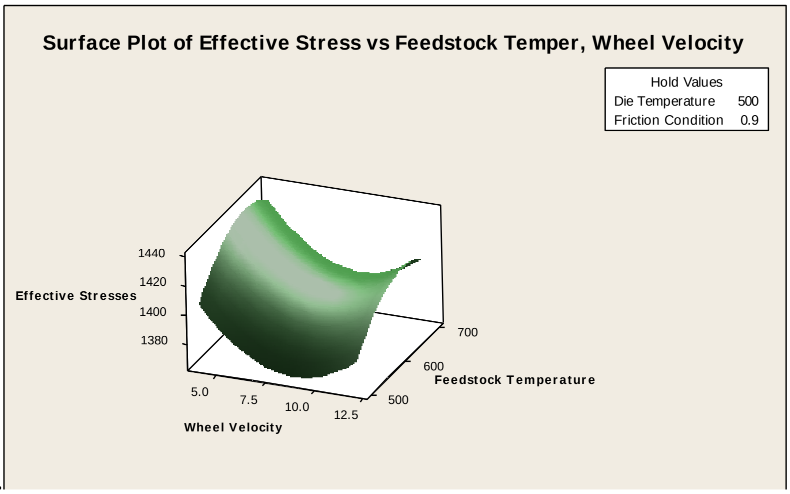

FIGURE 4. 77: SURFACE GRAPH GENERATED FOR EFFECTIVE STRESS VS WV AND FT

Figure 4.78 shows a 3D surface plot of effective stress for friction factor and die temperature. It became lowest, if the former variable was very high and the latter one was very low.

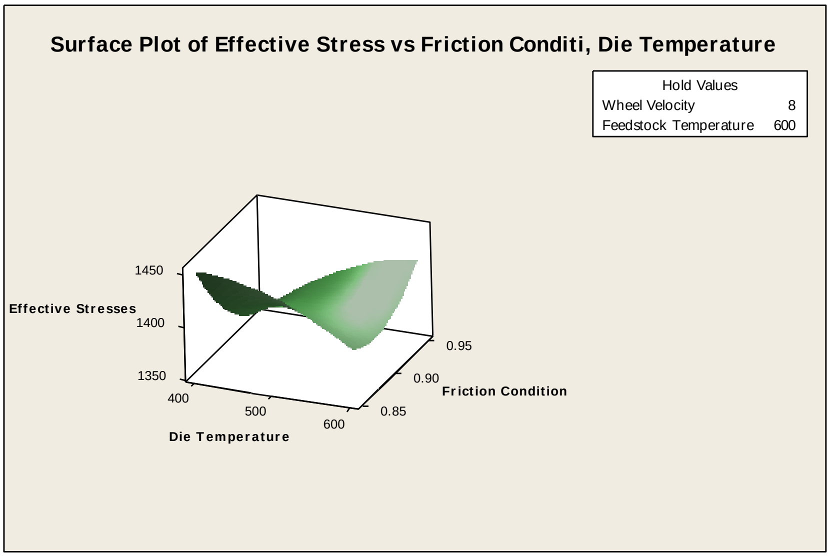

FIGURE 4. 78: SURFACE GRAPH GENERATED FOR EFFECTIVE STRESS VS DT AND FF

Figure 4.79 shows a flattened and twisted saddle shaped 3D surface plot for effective stress for friction factor and feedstock temperature. It became lowest, if the friction factor was very high and feedstock temperature was very low simultaneously.

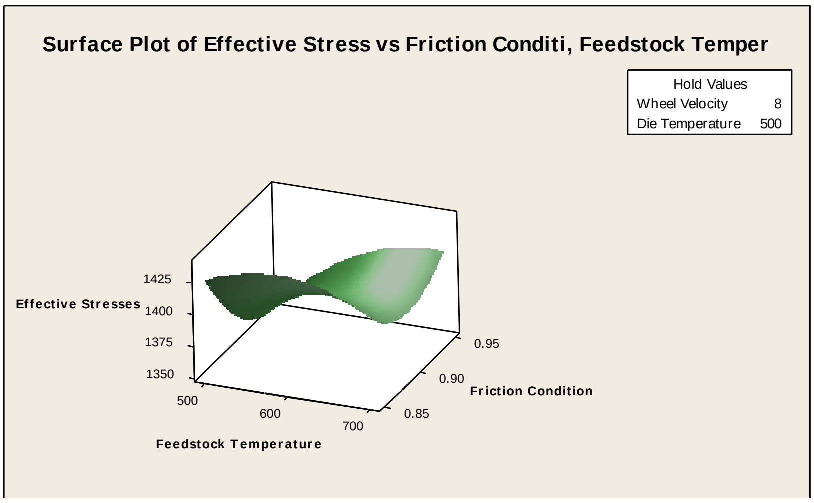

FIGURE 4. 79: SURFACE GRAPH GENERATED FOR EFFECTIVE STRESS VS FT AND FF

Figure 4.80 shows effective stress surface plot for die temperature and feedstock temperature. It became lowest, if both the CE input parameters were very low levels.

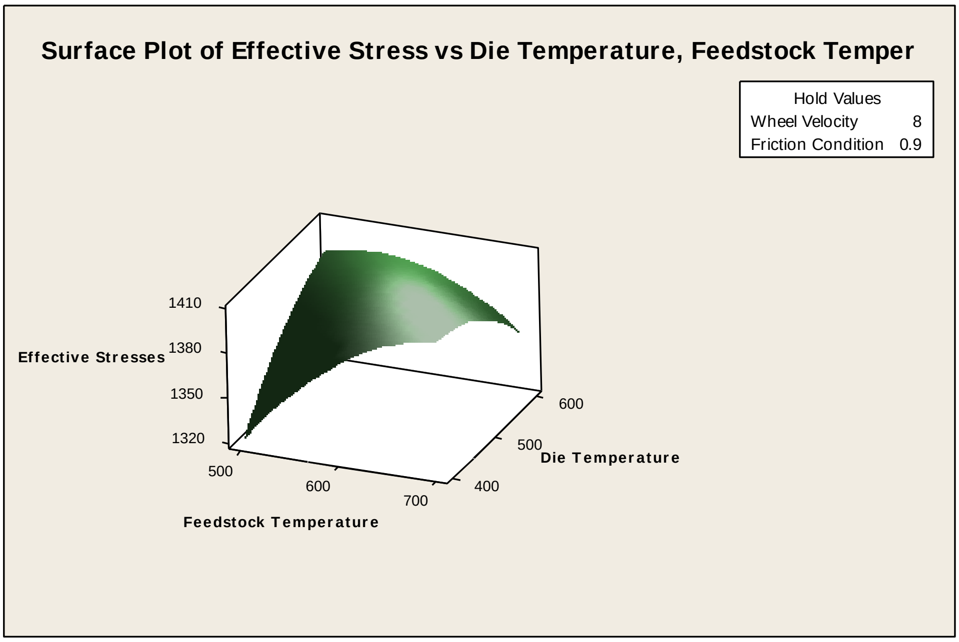

FIGURE 4. 80: SURFACE GRAPH OF EFFECTIVE STRESS GENERATED AGAINST FT AND DT

Figure 4.81 shows a bowl shaped effective stress 3D surface plot for wheel velocity and friction factor. It became lowest, if both the input parameters were in the middle.

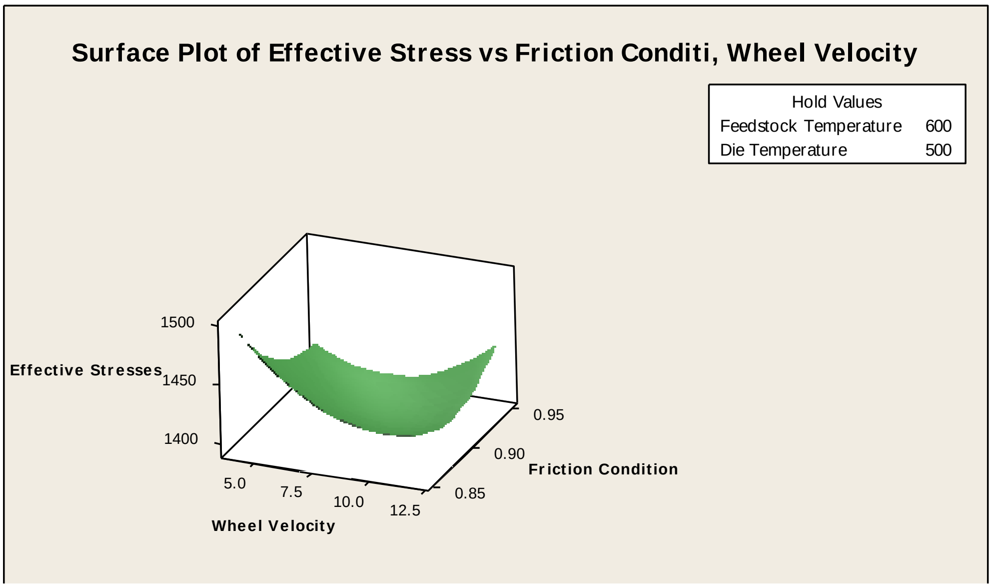

FIGURE 4. 81: SURFACE GRAPH EFFECTIVE STRESS DUE TO WV AND FF

Figure 4.82 shows a saddle shaped effective stress surface plot for wheel velocity and die temperature. It became lowest, if both the input parameters were either in the lowest or highest levels simultaneously.

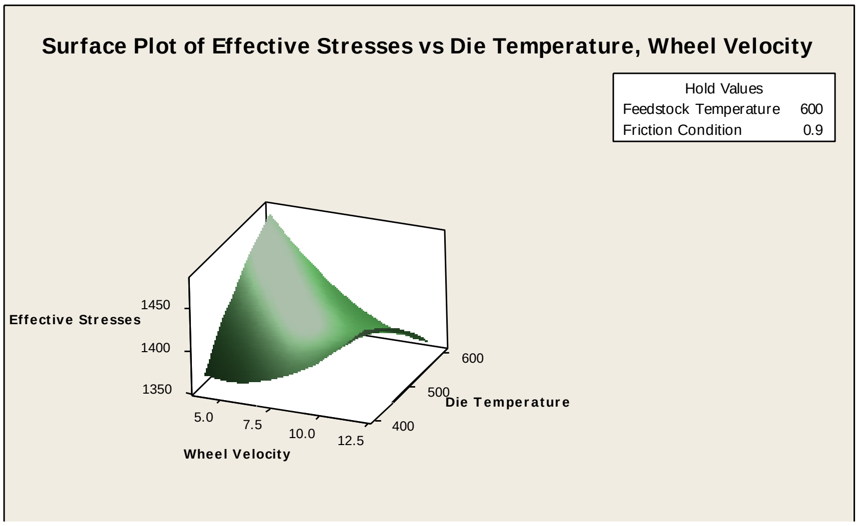

FIGURE 4. 82: EFFECTIVE STRESS SURFACE GRAPH OCCURRED BETWEEN WS AND DT

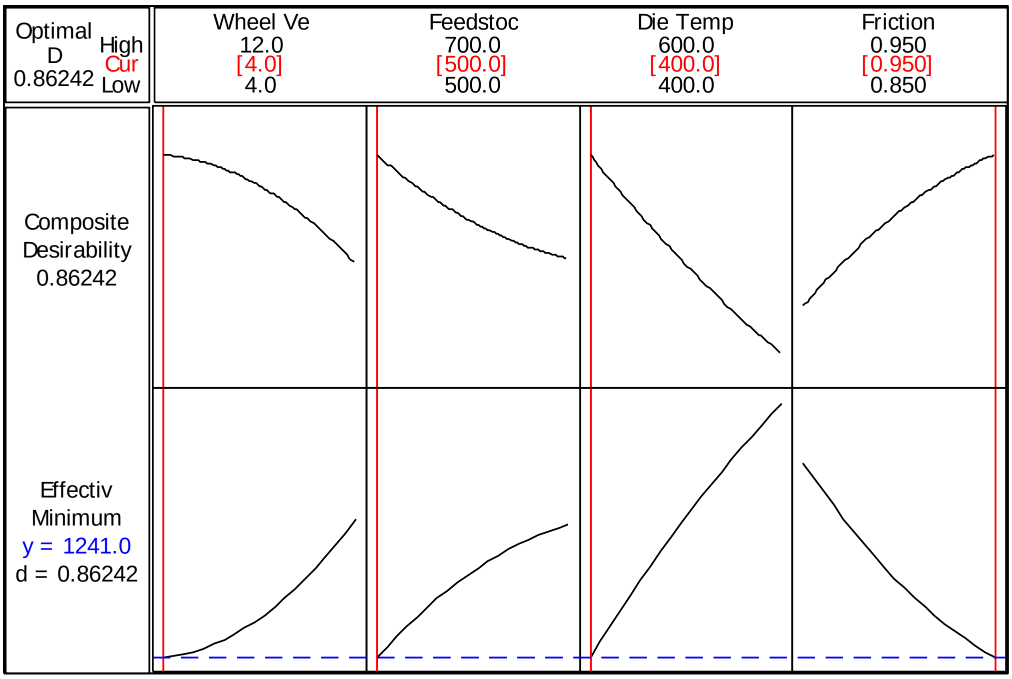

FIGURE 4. 83: OPTIMIZATION OF EFFECTIVE STRESS EFFECT VIA WV, FT, DT, AND FF

It can be seen in Fig. 4.83 that although the minimum effective stress of 1241.0kN/mm^2 induced in the alloy due to the continuous forming process if the wheel velocity, feedstock temperature, die temperature, and frictional factor situations were 4 revolutions per minute (RPM), 500^{o}C, 400^{o}C, and 0.95, respectively. Through RSM, the optimum value of effective stress of 1241.0kN/mm^2 was obtained with a composite desirability/worthiness of 0.86242.

4.4. Experimental Investigation and Validation

Several experiments were performed using the commercial continuous extrusion setup of TBJ350 shown in Fig. 3.5 and with the specifications at Table 3.18; Experimentations were taken place for Aluminum AA1100, Copper C101 and Copper-Chromium-Zirconium C18150. Moreover validations of experimental results of power requirement with analytical and computational ones were made for each material.

4.4.1. Experimental plans

Experimentations were carried out based on the best optimal input process parameter obtained through RSM, ANN-GA results for each material under investigation for optimal extrusion load. The power calculated by taking AC motor power factor = 0.8.

4.4.1.1. Aluminum (Al 1100) alloy experimentation

Several experiments were performed for various process parameters with the optimal load. Extrusion of the alloy was carried out and power consumption also summarized, from the commercial continuous extrusion setup TBJ350, in Table 4.17.

Table 4. 17: Results of experimental load for aluminum alloy

Sample No.	Product diameter (mm)	Extrusion Ratio	RPM	I	V	Total Power (kW)
1	6	2.5	4	43.08	439.2	15.13
			6	42.24	437.5	14.78
			8	40.13	438.6	14.08
			10	38.63	438.5	13.55
2	7	1.84	4	41.53	439.6	14.6
			6	39.5	440	13.9
			8	38.11	438.7	13.37
			10	37.3	440	13.13
3	8	1.41	4	40	440	14.08
			6	39.06	439.3	13.72
			8	37.03	439.6	13.02
			10	36.48	440	12.84

*Where, **I**: Current in Amperes,   **V**: Voltage in Volts*

Validation of the experimental results of power requirements to extrude the aluminum feedstock made with computational and theoretical ones are in Table 4.18.

Table 4. 18: Validation for aluminum alloy for power requirement

Parameters	Theoretical (kW)	Computational (kW)	Experimental (kW)	% Error
Extrudate diameter=6mm, RPM of Extrusion wheel=8, Extrusion ratio=2.5	15.6	15.53	14.08	8.77
Extrudate diameter=7mm, RPM Extrusion wheel=8, Extrusion ratio=1.84	14.85	14.79	13.37	9.60
Extrudate diameter=8mm, RPM Extrusion wheel=8, Extrusion ratio=1.41	14.05	13.9	13.02	6.33

The error percentage between the simulation and experimentation comparison was indicated in the Table 4.18. Among three extrudates of AA1100 alloy, more percentage error was found for 7mm (9.6%) extrudate and followed by the 6mm (8.77%) and 8mm (6.33%) respectively.

4.4.1.2. Experimental investigation for Copper (C101) feedstock

The experiments were done for the copper feedstock with the optimized process parameters using the commercial setup. Table 4.19 and 4.20 showed the experimentation results and validation of the results obtained for the C101 feedstock material.

Table 4. 19: Results of experiments for Copper feedstock on setup

S. No.	Product diameter (mm)	Extrusion Ratio	RPM	Voltage (Volts)	Current (Ampere)	Power*=V*I (kW)
1	6	4.34	4	439.3	133.9	47.06
			6	439.67	133.6	46.99
			8	439	132.7	45.60
			10	439	132.3	46.46
2	7	3.18	4	438.98	130.1	45.69
			6	440	128	45.05
			8	439.3	126.2	44.35
			10	438.94	125.3	44

**AC motor power factor = 0.8*

Validation of the experimental results of power requirements to extrude the C101 copper alloy made with computational and theoretical ones are presented in Table 4.20.

Table 4. 20: Validation of power requirements for copper feedstock

Parameters	Analytical (kW)	Simulation (kW)	Experimental (kW)	% Error
Extrudate diameter=6mm, RPM Extrusion wheel=8, Extrusion ratio=4.34	49.89	47.96	45.60	5
Extrudate diameter=7mm, RPM Extrusion wheel=8, Extrusion ratio=3.18	48.21	46.16	44.35	3.98

The error percentage between the simulation and experimentation comparison were indicated in the Table 4.20. Among three extrudates of C101 alloy, more percentage error is found for 6mm (5%) extrudate and followed by the 7mm (3.96%) respectively.

4.4.1.3. Copper-Chromium-Zirconium (C18150) feedstock alloy experimentation

Several experiments on Copper-Chromium-Zirconium (C18150) alloy were performed using the optimal process parameters setup for the process response extrusion load. Power consumptions during the CE extrusion Copper-Chromium-Zirconium alloy using the commercial continuous extrusion setup TBJ350were summarized in Table 4.21. Table 4.21 and Table 4.22 show that the experimentation results and validation of the results obtained for the Copper-Chromium-Zirconium feedstock material.

Table 4. 21: Results of experiments for C18150 feedstock

Product diameter (mm)	Extrusion wheel (RPM)	Extrusion ratio	V	A	Experimental Power (kW)
6	8	4.34	-	-	-
8	8	2.44	440	192	70.4
10	8	1.56	440	192	67.58

** Feedstock Diameter=12.5mm*

Validation of the experimental results of power requirements to extrude the C18150 alloy made with computational and analytical values are presented in Table 4.22.

The error percentage between the simulation and experimentation comparison were indicated in the Table 4.22. Among the two extrudates of C18150 alloy, more percentage error was found for 10mm (5.65%) extrudate and followed by the 8mm (4.76%) respectively.

Table 4. 22: Validation of power requirement for C18150 feedstock

Parameters	Analytical (kW)	Simulation (kW)	Experimental (kW)	% Error
Product diameter=6mm, RPM Extrusion wheel=8, Extrusion ratio=4.34	78.8	77.2	–	–
Product diameter=8 mm, RPM Extrusion wheel=8, Extrusion ratio=2.44	76.03	73.92	70.4 (440 V, 192 A)	4.76
Extrudate diameter=10 mm, RPM Extrusion wheel=8, Extrusion ratio=1.56	73.66	71.63	67.58 (440 V, 192 A)	5.65

4.5. Microstructure Analysis

The microstructure of all the feed stock and extrudates of AA1100, C101 and C18150 are presented in detail in this sub-section. The analyses were carried out according to the procedures stated in Section 3.8.

4.5.1. Microstructure analysis of AA1000 alloy

The microstructure of aluminum feedstock and extrudates of AA1100 grade materials were observed (based on Section 3.8.1) at different magnifications such as 50×, 100× and 200×. The microstructure was captured for 6mm, 7mm and 8mm diameter extradites at 6RPM, 8 RPM and 10 RPM along with feed stock materials of 9.5mm diameter. It was observed that there were changes in grain size after deformation, the elongations in grains were observed. The average grain size of the extruded product was found to be 80 to 200μm under wheel speed of 6 to 10RPM. However under the wheel speed of 8RPM, very fine, uniform grains structure and better grain structure homogeneity observed. The further increase in wheel speed slightly increased the grain size. Figure 4.84, to Fig. 4.91 shows the microstructures of aluminum samples at various wheel velocities and extrusion ratio.

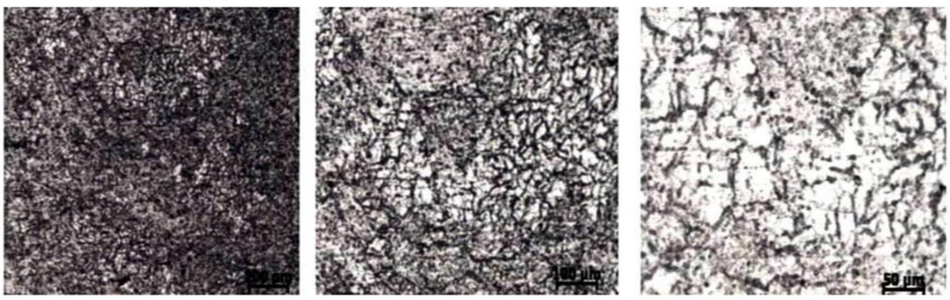

(a) (c) (b)

FIGURE 4. 84: a–c MICROGRAPHS OF 6MM AA1100 EXTRUDATED AT 6RPM WITH 200×, 100×, AND 50× MAGNIFICATIONS RESPECTIVELY

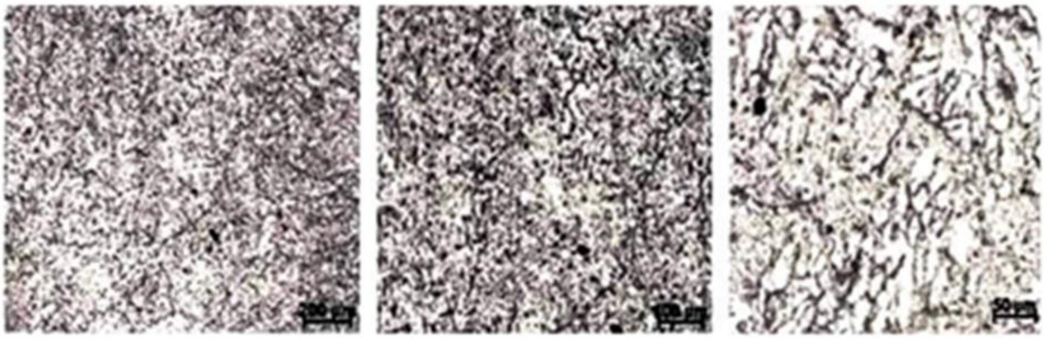

(a) (b) (c)

FIGURE 4. 85: a–c MICROGRAPHS OF 7MM AA1100 EXTRUDATED AT 6RPM WITH 200×, 100×, AND 50× MAGNIFICATIONS RESPECTIVELY

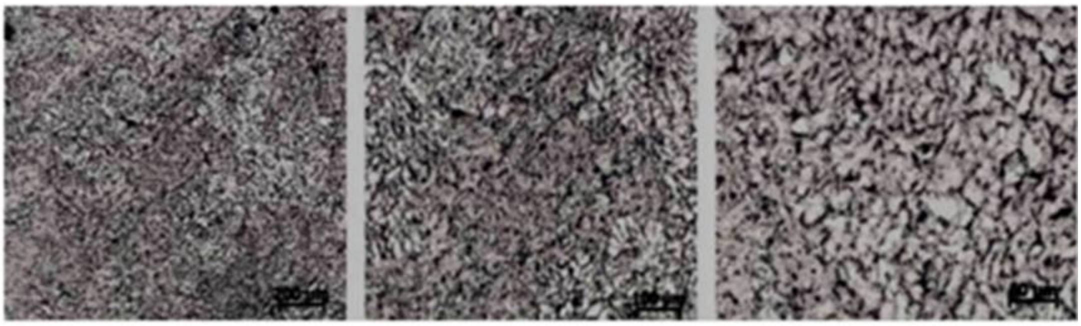

(a) (b) (c)

FIGURE 4. 86: a–c MICROGRAPHS OF ALUMINUM AT 8MM, 6RPM AT 200×, 100×, AND 50× MAGNIFICATIONS RESPECTIVELY

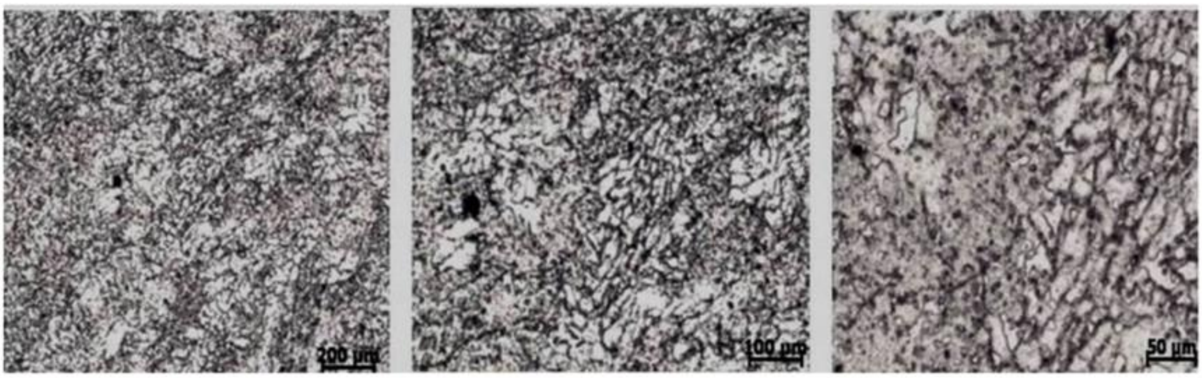

(a) (b) (c)

FIGURE 4. 87: a–c MICROGRAPHS OF ALUMINUM AT 6MM, 8 RPM AT 200×, 100×, AND 50× MAGNIFICATIONS RESPECTIVELY

(a) (b) (c)

FIGURE 4. 88: a–c MICROGRAPHS OF ALUMINUM AT 7MM, 8 RPM AT 200×, 100×, AND 50× MAGNIFICATIONS RESPECTIVELY

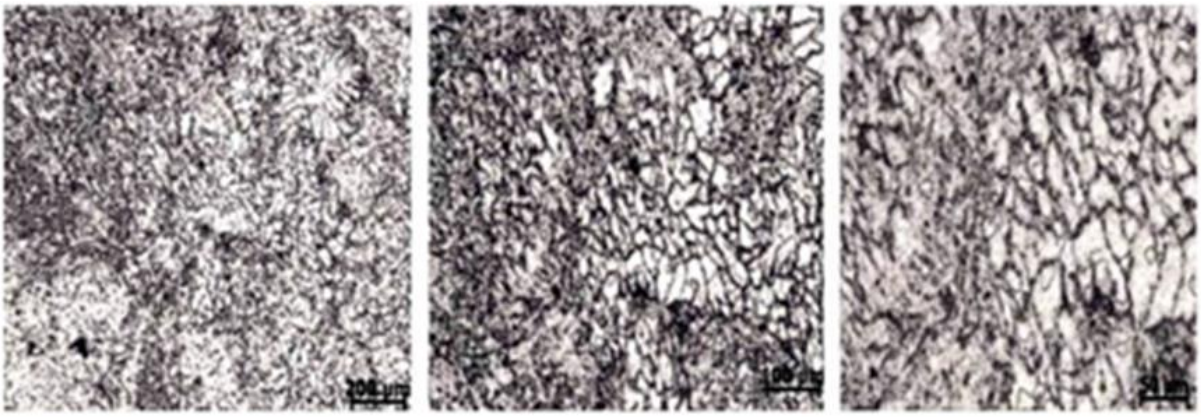

(a) (b) (c)

FIGURE 4. 89: a–c MICROGRAPHS OF ALUMINUM AT 8MM, 8 RPM AT 200×, 100×, AND 50× MAGNIFICATIONS RESPECTIVELY

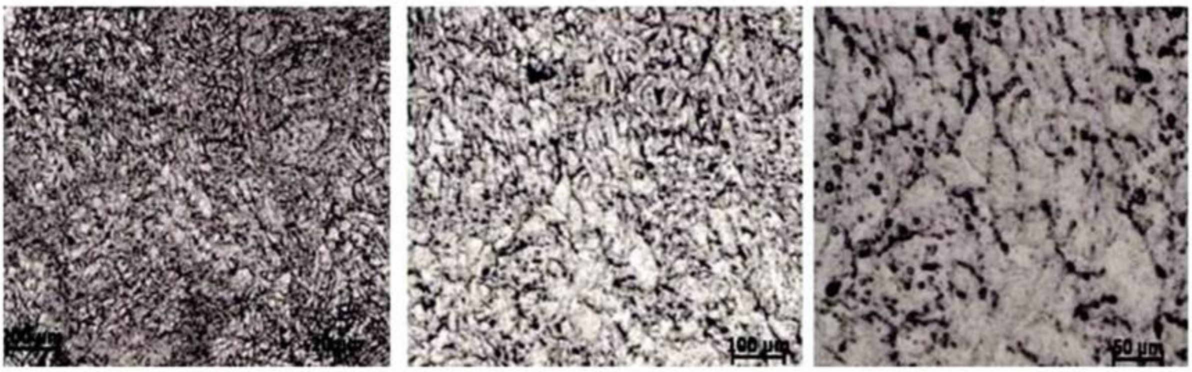

(a) (b) (c)

FIGURE 4. 90: a–c MICROGRAPHS OF ALUMINUM OF 8MM AT 10 RPM AT 200×, 100×, AND 50× MAGNIFICATIONS RESPECTIVELY

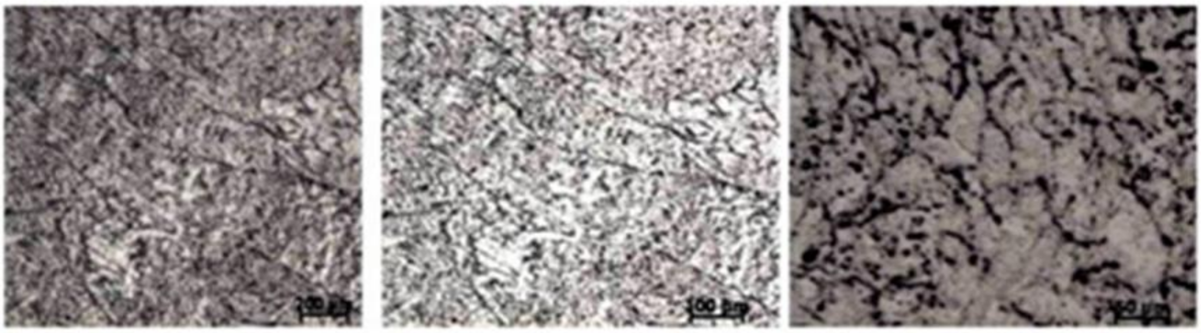

(a) (b) (c)

FIGURE 4. 91: a–c MICROGRAPHS OF ALUMINUM FEEDSTOCK AT 200×, 100×, AND 200× MAGNIFICATIONS RESPECTIVELY

4.5.2. Microstructure analysis of C101 metal

The microstructure samples of the C101 alloy at various Conform extrusion wheel speed and extrudate diameters are shown from Fig. 4.92 to Fig.4.100. The average grain size of ranging from 80μm to 200μm was obtained when the extrusion wheel speed from 6 to 8RPM. It was also observed that larger and inhomogeneous grain structures were obtained under Conform wheel speed of 6 and 8RPM. Fine and uniform grain structures were obtained when the wheel speed at 10RPM. A further increase in the driving wheel speed to 12RPM and slight increment in the grain size were detected.

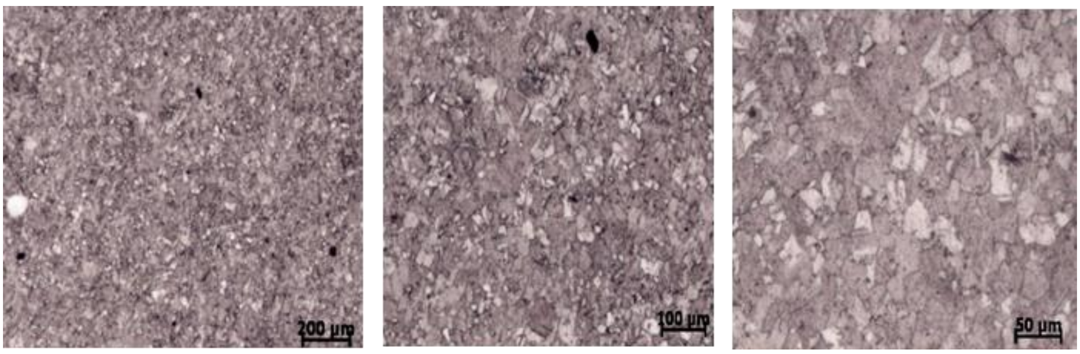

(a) (b) (c)

FIGURE 4. 92: a-c MICROSTRUCTURES OF EXTRUDATE WITH 6MM IN DIAMETER AT 4 RPM WITH MAGNIFICATIONS AT 200×, 100× AND 50× RESPECTIVELY

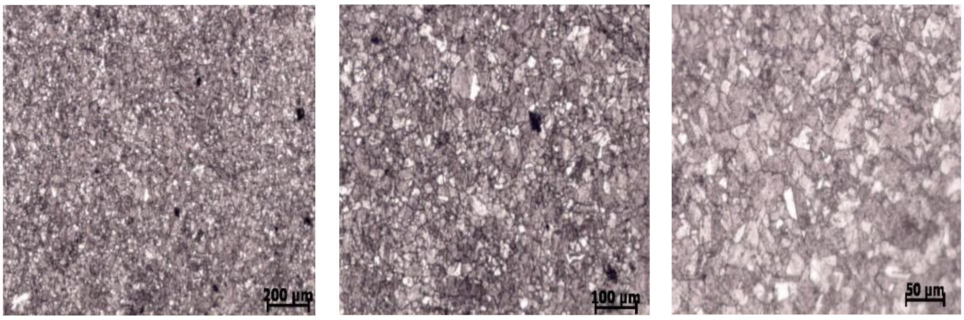

(a) **(b)** **(c)**

FIGURE 4. 93: a-c MICROSTRUCTURES OF EXTRUDATE WITH 6MM IN DIAMETER AT 6 RPM AT MAGNIFICATIONS OF 200×, 100×, AND 50× RESPECTIVELY

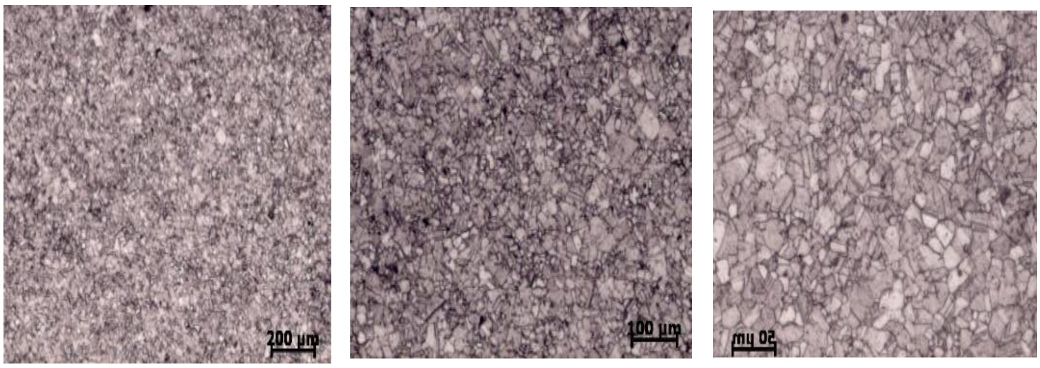

(a) **(b)** **(c)**

FIGURE 4. 94: a-c MICROSTRUCTURES OF EXTRUDATE WITH 6MM IN DIAMETER AT 8RPM AT MAGNIFICATIONS OF 200×, 100× AND 50× RESPECTIVELY

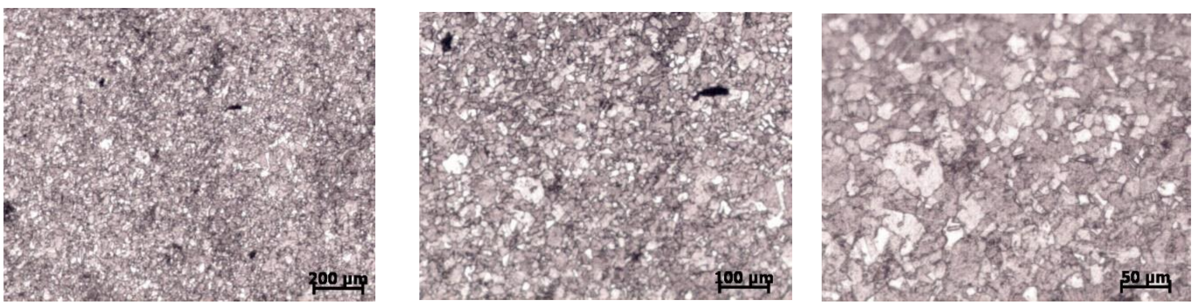

(a) **(b)** **(c)**

FIGURE 4. 95: a-c MICROSTRUCTURES OF EXTRUDATE WITH 6MM IN DIAMETER AT 10RPM AT MAGNIFICATIONS OF 200×, 100× AND 50× RESPECTIVELY

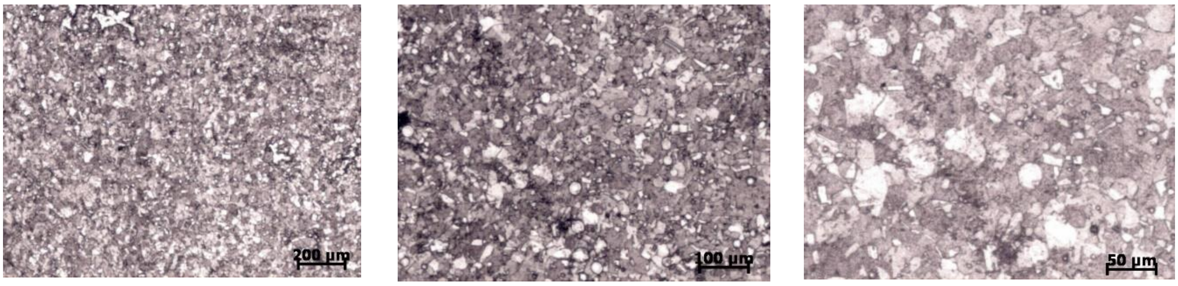

(a) **(b)** **(c)**

FIGURE 4. 96: a-c MICROSTRUCTURES OF EXTRUDATE WITH 7MM IN DIAMETER AT 4RPM AT MAGNIFED AT 200×, 100× AND 50× RESPECTIVELY

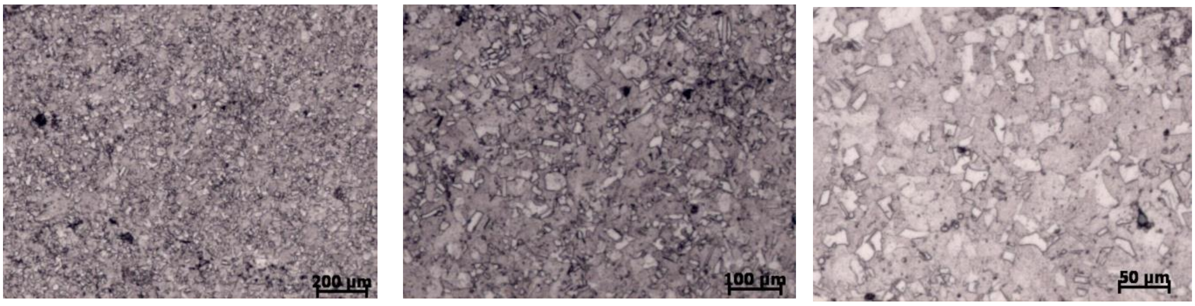

(a) **(b)** **(c)**

FIGURE 4. 97: a-c MICROSTRUCTURES OF C101 COPPER SAMPLE OF EXTRUDATE WITH 7MM IN DIAMETER AT 6 RPM AT MAGNIFIED OF 200×, 100× AND 50× RESPECTIVELY

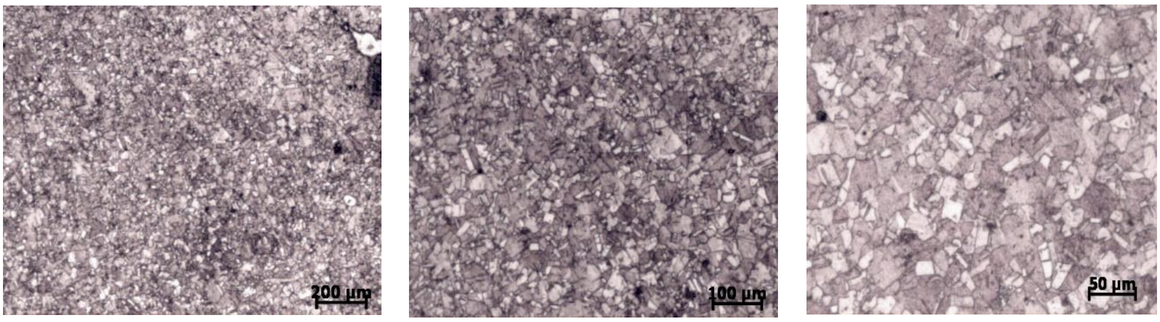

(a) **(b)** **(c)**

FIGURE 4. 98: a-c MICROSTRUCTURE OF EXTRUDATE OF 7MM IN DIAMETER SIZE AT 8RPM MAGNIFIED AT 200×, 100× AND 50× RESPECTIVELY

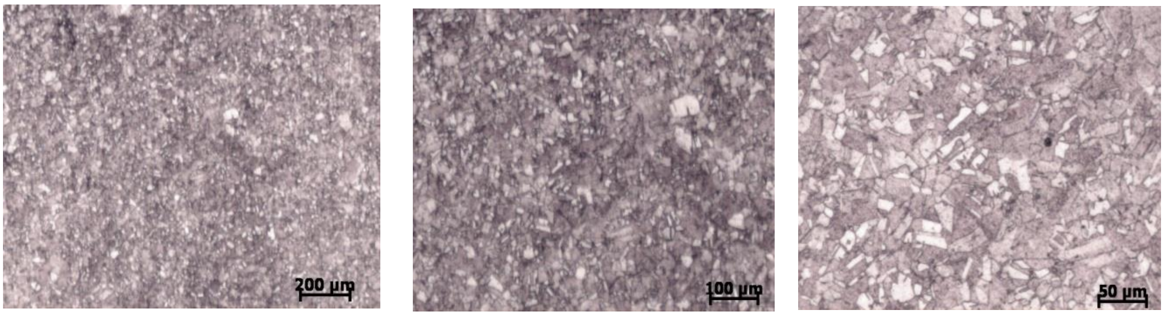

(a) (b) (c)

FIGURE 4. 99: a-c MICROSTRUCTURES OF EXTRUDATE WITH 7MM IN DIAMETER SIZE AT 10RPM AT MAGNIFICATIONS OF 200×, 100× AND 50× RESPECTIVELY

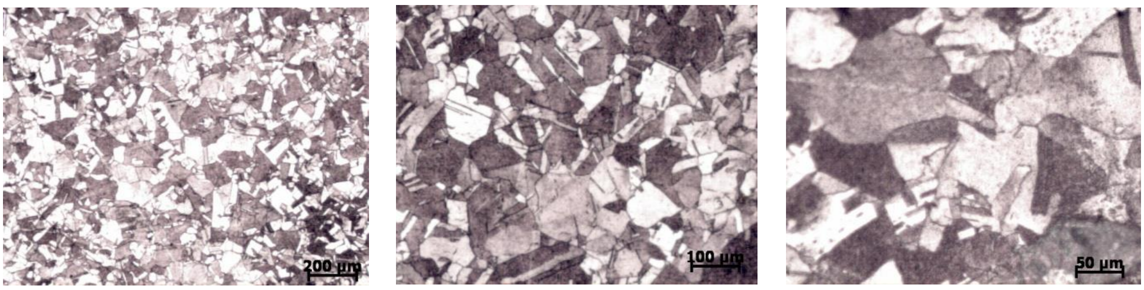

(a) (b) (c)

FIGURE 4. 100: a-c MICROSTRUCTURES OF C101 FEEDSTOCK AT 200×, 100× AND 50× RESPECTIVELY

4.5.3. Microstructure analysis of C18150 Cu-Cr-Zr alloy

The microstructure analyses of the feedstock C18150 alloy grade of 12.5mm diameter and two extrudates of 10mm and 8mm diameter were performed based on procedures in Section 3.8. The microstructures of the test samples manufactured at different combination of CE input parameters are shown from Fig. 4.101 to Fig.103. The microstructure images were taken at 100×, 200× and 400× magnifications. Since the C18150 samples had alloying elements of Zr and Cr, the distributions of these alloys were noted in the homogenous manner as shown in the Fig. 4.103 of 8 mm diameter of the extrudate.

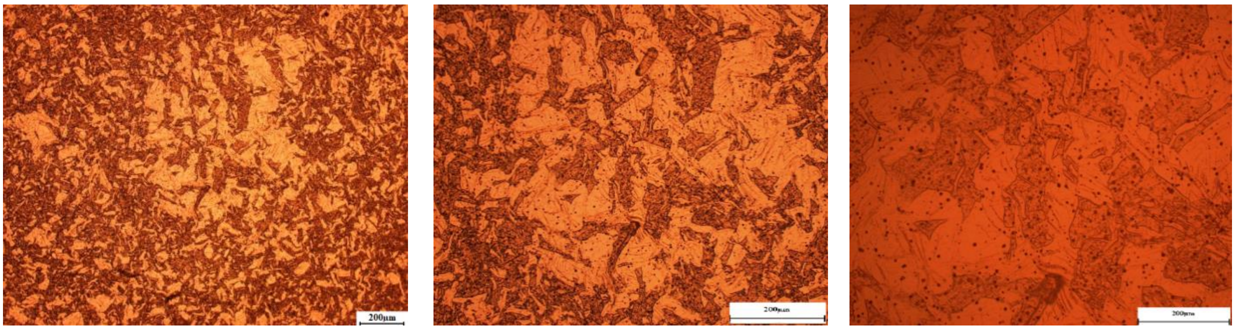

At 100× **At 200×** **At 400×**

FIGURE 4. 101: MICROSTRUCTURE OF FEED METAL WITH 12.5MM IN DIA. C18150 ROD AT MAGNIFICATIONS OF 100×, 200×, AND 400× RESPECTIVELY

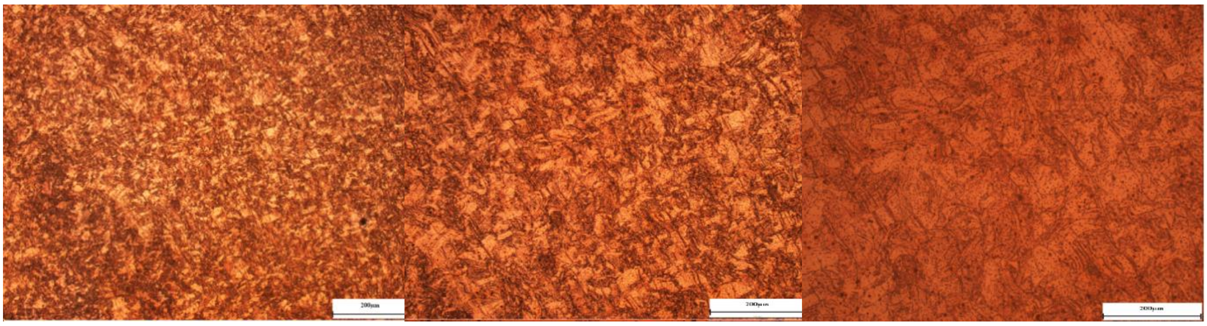

At 100× **At 200×** **At 400×**

FIGURE 4. 102: MICROSTRUCTURE IMAGES OF 10MM DIA. OF C18150

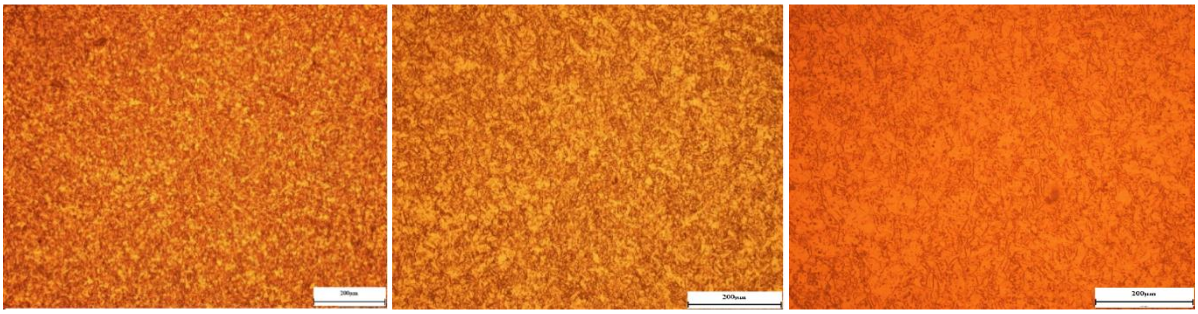

At 100× **At 200×** **At 400×**

FIGURE 4. 103: MICROSTRUCTURE IMAGES OF 8MM DIA. OF C18150

The fine precipitates distributed within the ultra-fine grain matrix significantly improved strain hardening, as a consequence improvements in tensile strength, hardness, and wear resistance of the alloy without notably sacrificing the percentage of elongation to failure due to the combined effect of grain refinement and precipitation. Moreover, a clear grain structures with better uniformity with respect to the feedstock material were also observed in the case of the 8mm and 10mm diameters rods in all magnifications shown in Fig. 4.102 and 4.103. Cr and Zr distribution were relatively uniform as per observations in the Cu matrix of 8mm extrudates seen in Fig. 4.103.

4.6. Mechanical Testing

4.6.1. Mechanical testing of AA1100

Samples of AA1100 were mechanically tested to explore the effects the CE process factors on the material properties such as yield strength and elongation percentages. The tensile tests were carried out as per the experimental design plan taking different conform extrusion driving wheel speeds and extrudate diameters.

4.6.1.1. Yield strength of AA1100 testing

The effect of the wheel speed on 0.2% yield strength of extruded product is shown in Fig. 4.104. It can be noticed that if the wheel speed increases, the yield strength of product increases and it will be maximum at a certain value of wheel speed and decreases the yield strength thereafter if wheel speed is increased further.

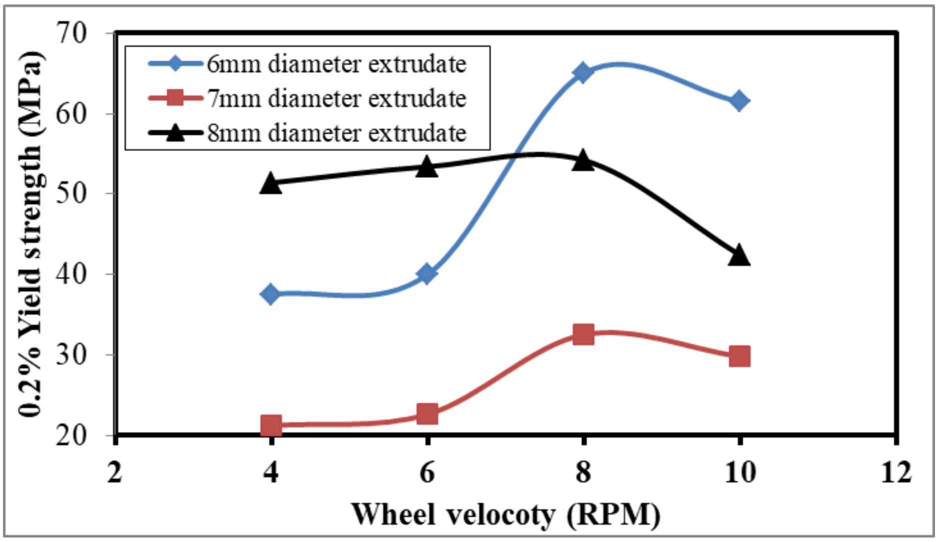

FIGURE 4. 104: VARIATION OF 0.2% YS WITH EXTRUSION WV AND PD

The effect of extrusion ratio on yield strength is shown in Fig. 4.105. As the extrusion ratio increases, the yield strength value of the extruded product samples decreased initially, became minimum at a given extrusion ratio at a given speed, and increased thereafter.

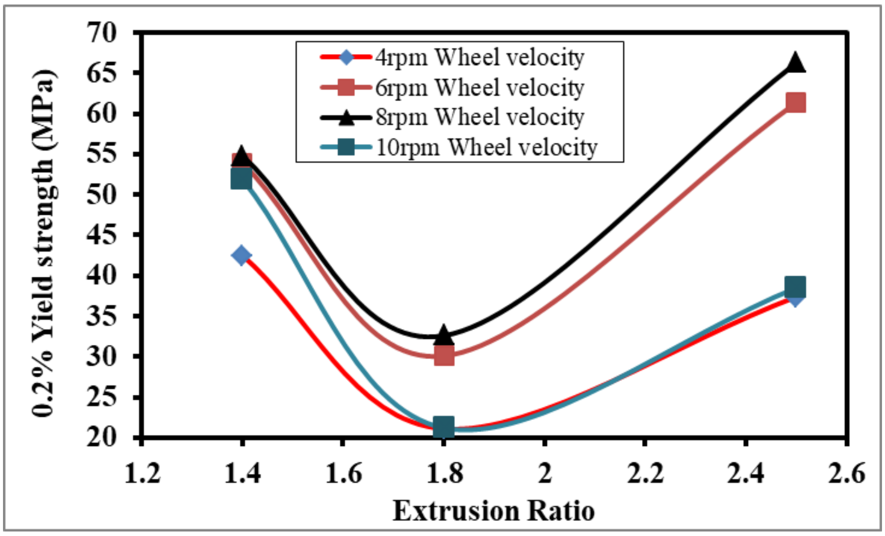

FIGURE 4. 105: VARIATION OF 0.2% YS WITH EXTRUSION RATIO

Using RSM it is also possible to optimize and obtain best combination of CE process factors to generate maximum yield strength. Based on Fig. 4.106, maximum value of yield strength 70.93MPa was obtained if the values of wheel speed and product diameter were 8.6364RPM and 9mm respectively. The optimum value of yield strength (70.93MPa) was obtained with composite desirability of 0.8585.

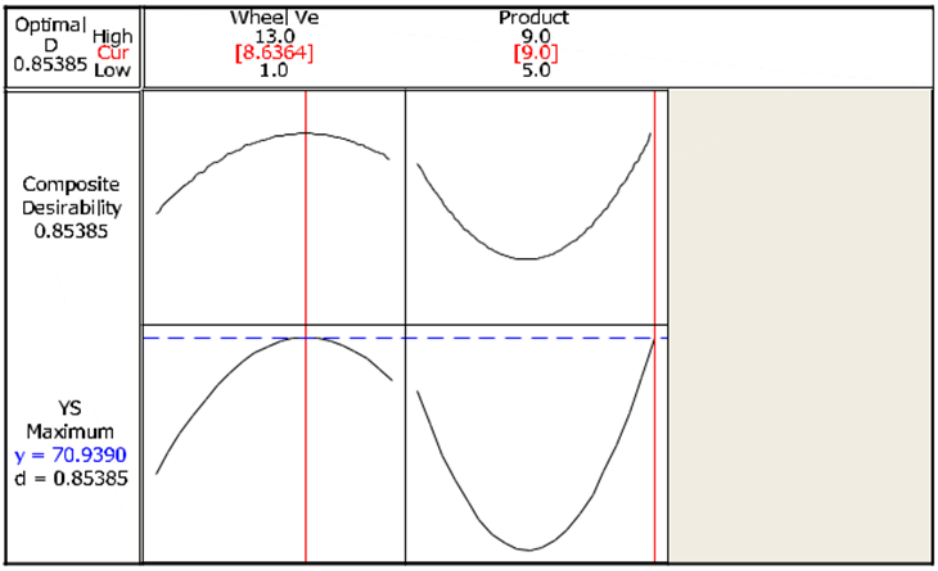

FIGURE 4. 106: OPTIMIZED VALUE OF YS IN TERMS OF WV AND PD

4.6.1.2. Percentage of elongation optimization

In case of % elongation, similar method was followed like yield strength case. Important observation after the optimization is represented in Fig. 4.107. It was possible to infer from Fig. 4.107 that the best optimal value of 45.8% was achieved at wheel speed of 8rpm and 6mm diameter of product.

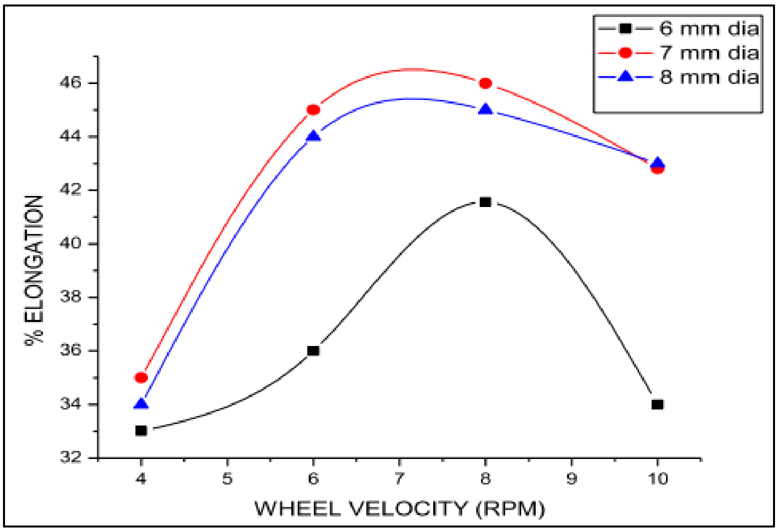

FIGURE 4. 107: VARIATION OF % ELONGATION WITH EXTRUSION WV

Figure 4.108 shows the variation of percentage elongation with the wheel velocity for the aluminum alloy. It can be analyzed that percentage elongation increases with the increase in the value of the driving wheel speed and reaches maximum at a given value of wheel speed for each value of extrusion ratio and decreases thereafter.

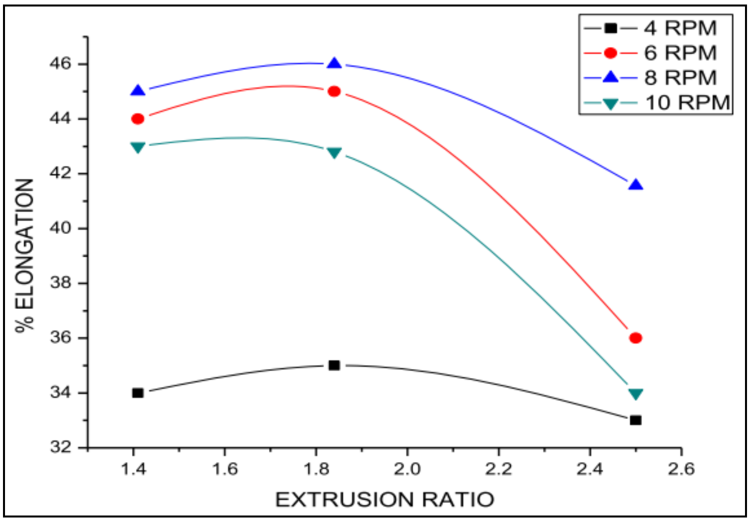

FIGURE 4. 108: VARIATION OF % ELONGATION WITH EXTRUSION RATIO

Figure 4.108 also indicates the variation of percentage elongation with extrusion ratio for aluminum alloy. It can be analyzed that percentage elongation increases with increase in the value of extrusion ratio and becomes maximum at a given value of extrusion ratio for each value of wheel speed and de-creases thereafter. It was noted that percentage elongation increased with increased in the value of extrusion ratio and became maximum at a given value of extrusion ratio for each value of wheel speed and decreased thereafter.

4.6.1.3. Hardness analysis on Aluminum alloy AA1100 samples

Finally, from Fig. 4.109, the hardness test results of AA1100 Aluminum alloy samples were observed. From the graph, the highest Vickers hardness number of 33.4VHN for 6mm extrudates manufactured at 8RPM followed by 8mm extrudate at 8RPM but the least hardness was obtained for a product of 6mm manufactured at 4RPM. This hardness results seems to have some liner correlations with yield strength values of the extrudates especially manufactured at 8RPM.

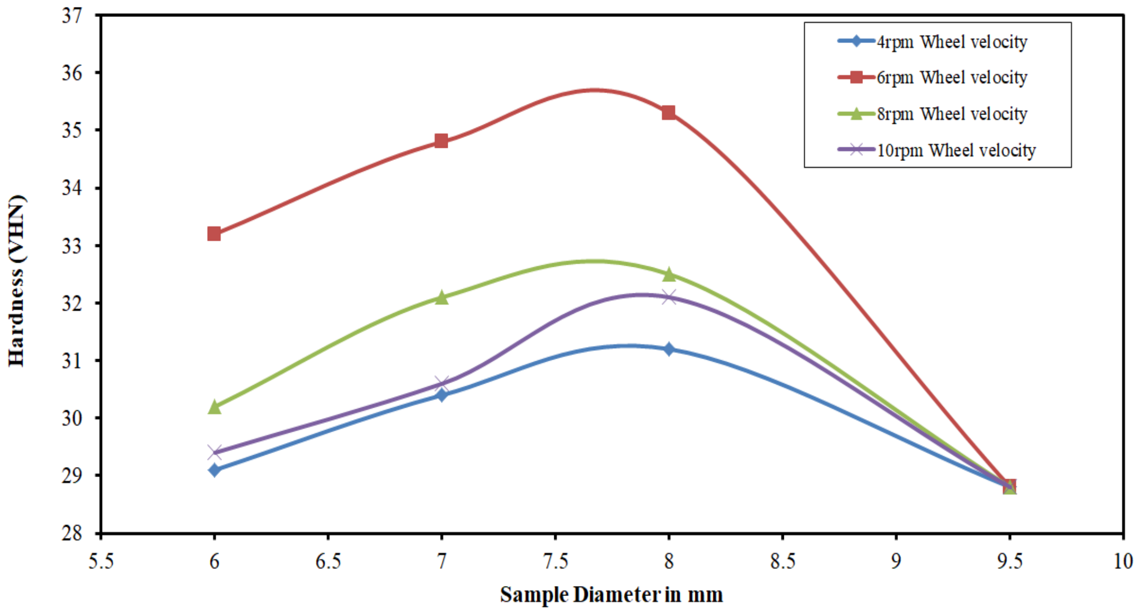

FIGURE 4. 109: HARDNESS TEST RESULTS OF ALUMINUM SAMPLES

4.6.2. Mechanical testing and optimization for C101

The effect of CE input process parameters on extrusion load, effective stress, damage analysis, effective strain, ultimate tensile strength (UTS), and hardness of C101 were investigated. The responses were modeling and optimized. The detail of UTS modeling and optimization is discussed in this section.

4.6.2.1. Ultimate tensile strength

The tensile tests were performed based on the experimental design at various driving wheel speeds and extrudate diameters. The experimental plan was done based on the CCRD. The experimental results of ultimate tensile strength tests with respect to extrusion wheel velocity and feedstock to extrudate ratio are shown in Fig. 4.110.

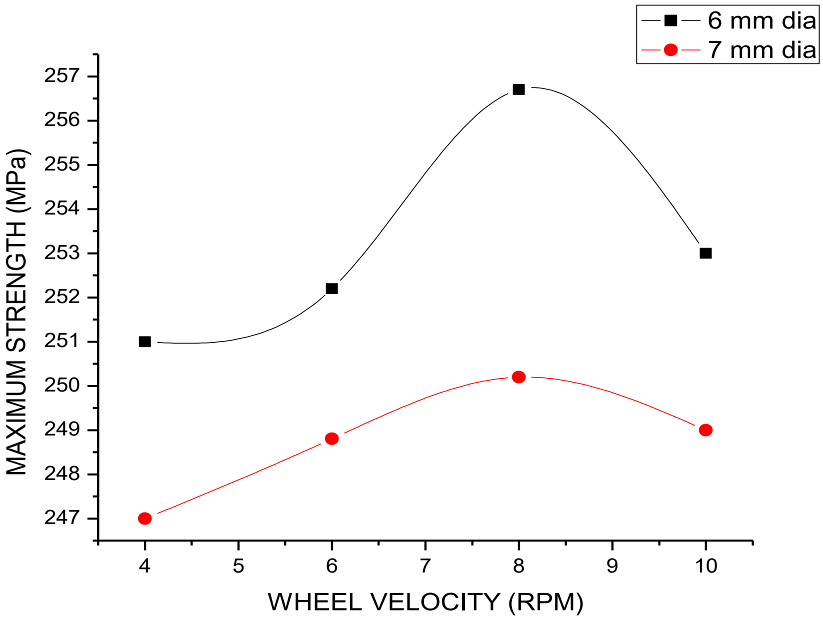

FIGURE 4. 110: VARIATION OF UTS WITH WV FOR C101 EXTRUDATE

The tensile tests were performed based on the experimental design at various driving wheel speeds and extrudate diameters. The experimental plan and results of ultimate tensile strength tests are shown in Table 4.26. The experimental plan was done based on the CCRD to obtain maximum UTS.

The significance test of UTS results was done using the quadratic model. The model developed to estimate optimized UTS is given in Table 4.27. R^2 and adjusted R^2 values were 99.51 % and 99.26%. The regression multivariate analysis model (expression) delivers a comprehensive relationship between independent and dependent parameters. The associated p-value of each factor of the model which is <0.05 (i.e., $\alpha=0.05$ or 95% confidence) for quadratic as well as the linear effect of the driving wheel rpm and extrudate diameter indicates that there were significant effects of the independent parameters on UTS.

Table 4. 23: Experimental plan and results for UTS using CCRD

Experiment No.	Extrusion Wheel RPM		Extrudate diameter (mm)		UTS (MPa)
	Coded	Actual	Coded	Actual	
1	-2	1	0	7	248
2	1	10	1	8	246
3	-1	4	1	8	248
4	0	7	0	7	240
5	0	7	-2	5	244
6	0	7	0	7	250
7	2	13	0	7	248
8	-1	4	-1	6	249
9	0	7	0	7	248
10	1	10	-1	6	249
11	0	7	2	9	248
12	0	7	0	7	249
13	0	7	0	7	246

Table 4. 24: Significance test of UTS

Term	Coefficient	*t*	*P*
Constant	248.069	2599.934	0.000
Extrusion Wheel Velocity(X_1)	0.750	11.306	0.000
Extrudate diameter(X_2)	-2.250	-33.919	0.000
Wheel Velocity *Wheel Velocity(X_1^2)	-0.121	-2.574	0.000
Product diameter* Product diameter(X_2^2)	-0.871	-18.138	0.000

Using the P-values and the coefficient results presented in Table 4.27, a mathematical model is derived and shown in Eq. 4.26 as follows,

$$UTS\ (\sigma) = 248.069+0.750X_1 -2.250X_2 -0.121X_1^2 - 0.871X_2^2 \quad \cdots\cdots\cdots \quad (4.26)$$

Table 4. 25: The ANOVA test result for UTS

Source	DF	Sum of Squares	Mean Sum of squares	*F*-value	*P*-value
Regression	4	85.2699	21.3175	403.73	0.000
Linear	2	66.5000	33.7500	639.18	0.000
Square	2	16.7699	8.8849	168.27	0.000
Residual error	8	0.4224	0.0528		
Lack of fit	4	0.4224	0.1056		
Pure error	4	0.0000	0.0000		
Total	12	85.6923			

Table 4.28 depicts ANOVA test executed to validate the statistical significance of the mathematical model developed for UTS. The standard F values at a 95% confidence level for the quadratic effect as well as the linear effect of the extrusion wheel velocity and extrudate diameter were very high. Hence the model was found to be statistically significant as well as adequate.

Figure 4.111 illustrates the residuals of normal probability for UTS. It was easily realized from the plot that the residual values were along a straight line and distributed normally. Therefore, the model was adequate.

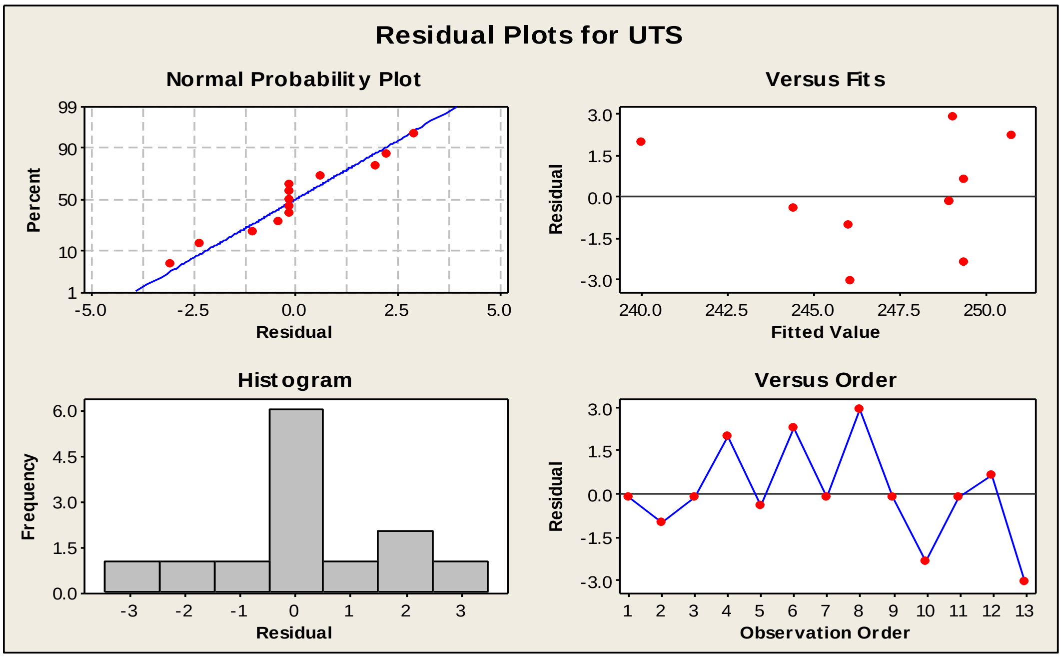

FIGURE 4. 111: RESIDUAL PLOTS FOR UTS

The effect of the driving wheel speed (RPM) and extrudate diameter on the UTS of the extrudates is shown in Fig. 4.112 and Fig. 4.113. It can be inferred from the figures that the contour plot and the surface plot that as the wheel RPM increases and extrudate diameter decreases, thus the extrudate strength (ultimate tensile) increases and reaches to a maximum. Further increase in the rate of driving wheel RPM and extrusion ratio leads to a decrease in the value of UTS.

By correlating various continuous extrusion input process variables that can affect the UTS of the extrudates, the second-order response surface equations developed. The optimal values of the extrusion wheel RPM and extrusion ratio were determined.

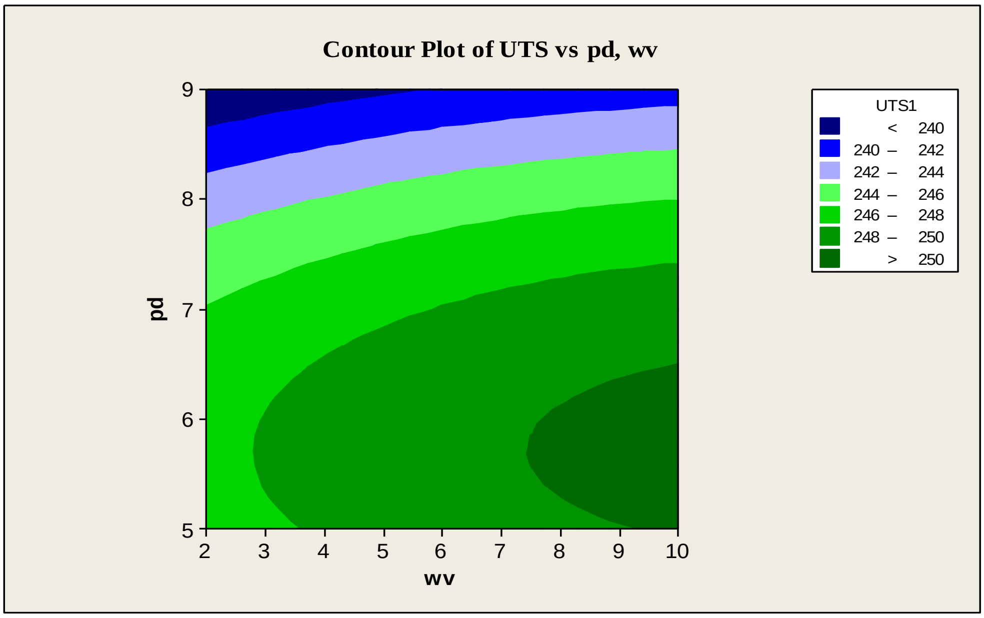

FIGURE 4. 112: CONTOUR PLOT OF UTS VERSUS WV AND PD

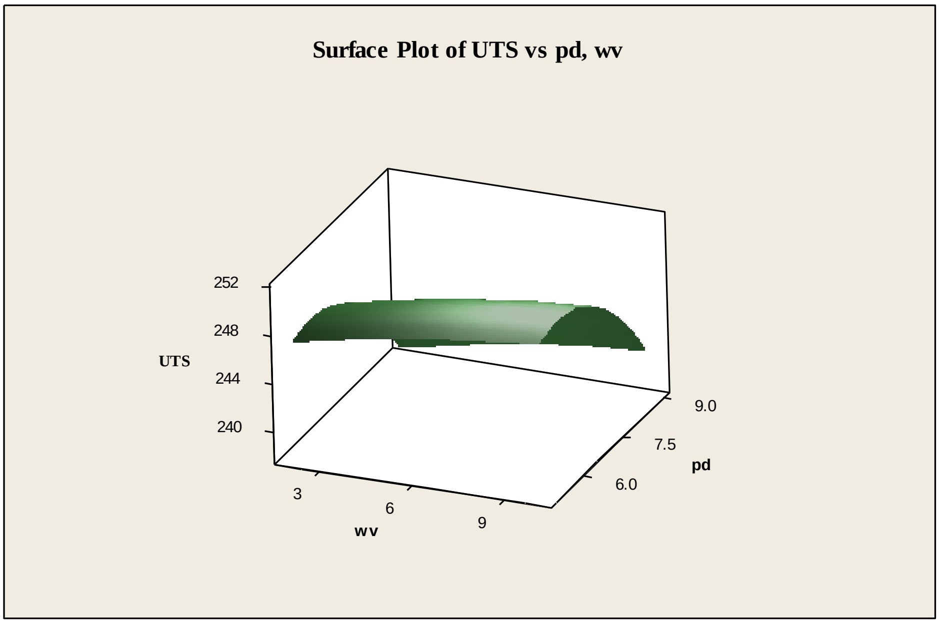

FIGURE 4. 113: SURFACE PLOT OF C101 UTS AGAINST WV AND PD

The optimal rates of the independent process variables such as driving wheel rpm and extrudate diameter are 10RPM and 5.72mm respectively. For C101 feedstock metal, through an optimum parametric combination of the continuous extrusion process input variables as high as 250.5MPa UTS can be achieved. The result is shown in Fig.4.114.

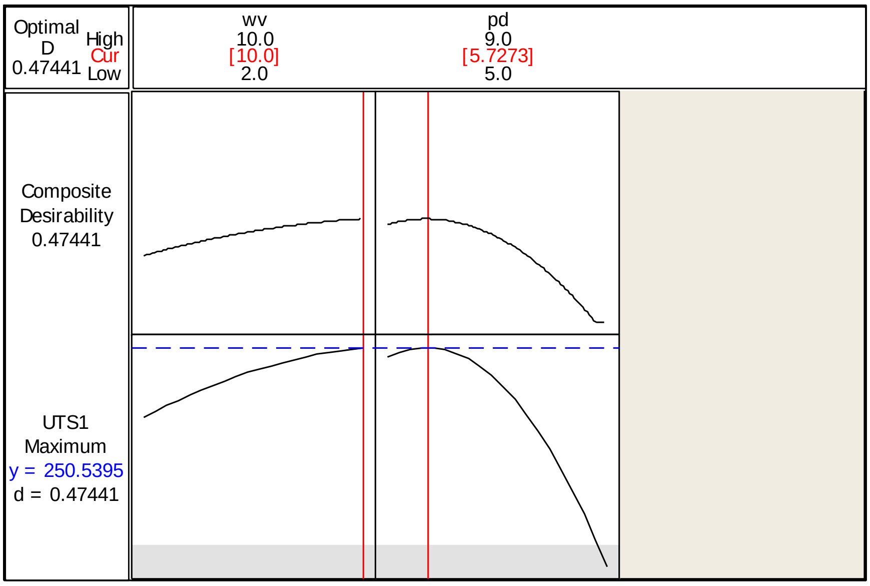

FIGURE 4. 114: OPTIMIZATION OF UTS VERSUS DRIVING WV AND PD

4.6.2.2. Percentages of elongation optimization

The percentages of elongation variation with the extrusion driving velocity for C101 alloy are shown in Fig. 4.115. As the extrusion speed increases the percentage elongation of the extrudates initially increases but a further increase in driving speed the percentages of elongation decrease. Significant improvements were observed in percentage of elongation from 28.2% of feedstock material to that of 59.23% of a product with 6mm manufactured at 8RPM.

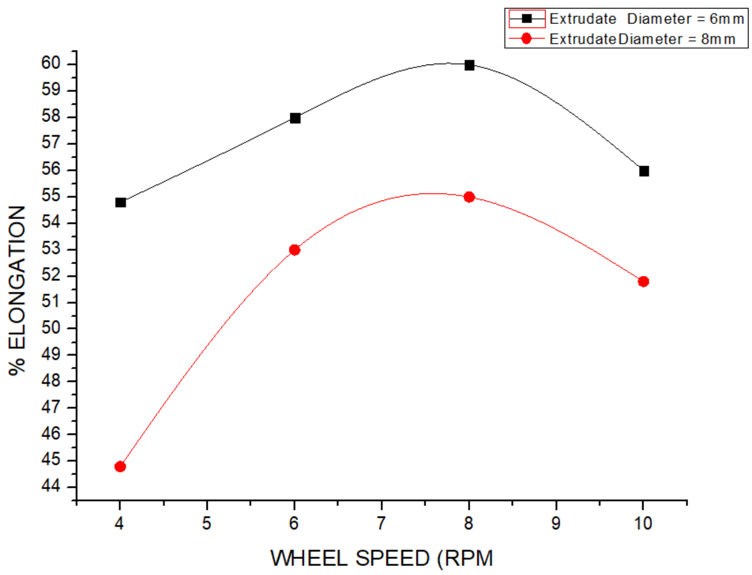

FIGURE 4. 115: VARIATION OF PERCENTAGE OF ELONGATION WITH PD

4.6.2.3. Hardness testing of C101

In the similar manner, the hardness testing was performed. The variation of hardness with the driving wheel rpm for C101 alloy is shown in Fig. 4.116. Based on the figure, as the driving wheel RPM increased, the extrudate sample hardness also increased and reached at a maximum point further increases driving wheel rpm and decreased hardness for both test samples.

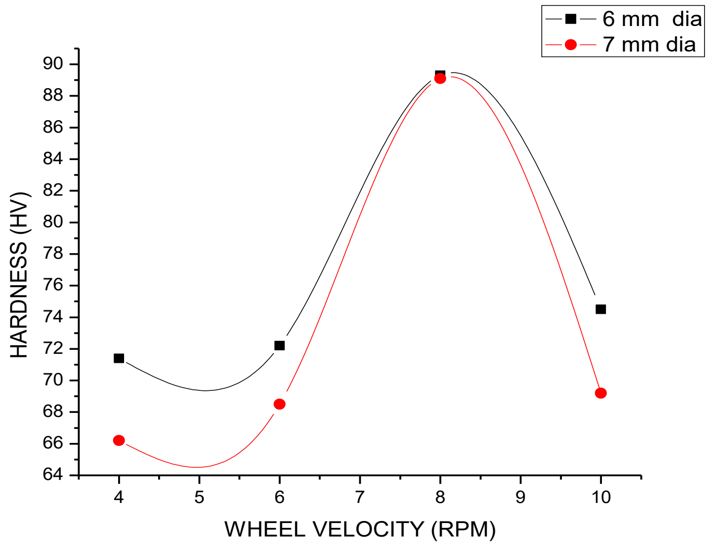

FIGURE 4. 116: HARDNESS VARIATION WITH WV

The optimization plots revealed that hardness greater than 90HV was achieved when the driving wheel rpm and extrudate diameter lay in the range of 4 to10RPM and 5 to 8mm.

4.6.3. Copper-Chromium-Zirconium (C18150) testing

Extrudates were manufactured taking the input parameters obtained through RSM, ANN-GA, except the extrudate diameters, at 8RPM as wheel speed, 0.85 as friction factors, 700°C as feedstock temperature and 600°C as die temperature. The extrudates experienced no post-process treatment and artificial-aging except system providing quenching. Varies mechanical testing were performed on C18150 feedstock and extrudates with 8 and 10mm diameters. Details of testing and results are discussed below in this subsection. In summary, the extrusion ratio does have a significant influence on the hardness of the Cu-Cr-Zr alloys.

4.6.3.1. C18150 hardness test

The hardness testing was carried out using the Vickers's hardness testing machine as per ASTM E384 .The hardness tests were performed to figure out the effect of the CE input processes parameters on the mechanical performance of the Cu-Cr-Zr alloy. The applied load and dwell time for hardness testing of 8mm, 10mm and 12.5mm diameter of C18150 samples were set according to the ASTM standard for all test samples and the testing were carried out based on the procedure stated in Section 3.11. Hardness values were recorded from center to near peripheral surface. Based on figure 4.117, the highest hardness value (VHN) was reported in the 8mm extrudate diameter and followed by 10mm and 12.5mm ones. Among all tests, the maximum hardness was found at a peak value which was 146.7±5 VHN near the outer surface of 8mm product diameter. Therefore the hardness of the C18150 alloy increases with the increase of extrusion ratio.

4.6.3.2. Tensile testing on Copper-Chromium-Zirconium (C18150)

The tensile testing of C18150 rods with 12.5mm, 10mm, and 8mm in diameter were carried out on the MCS/UTM 20T testing machine. One set specimen was made as per the ASTM- E8M in which the outer surfaces of the sample were machined to standard test sizes and another set were As-conform extruded. Replications of the tensile tests were done twice and their average test results were recorded.

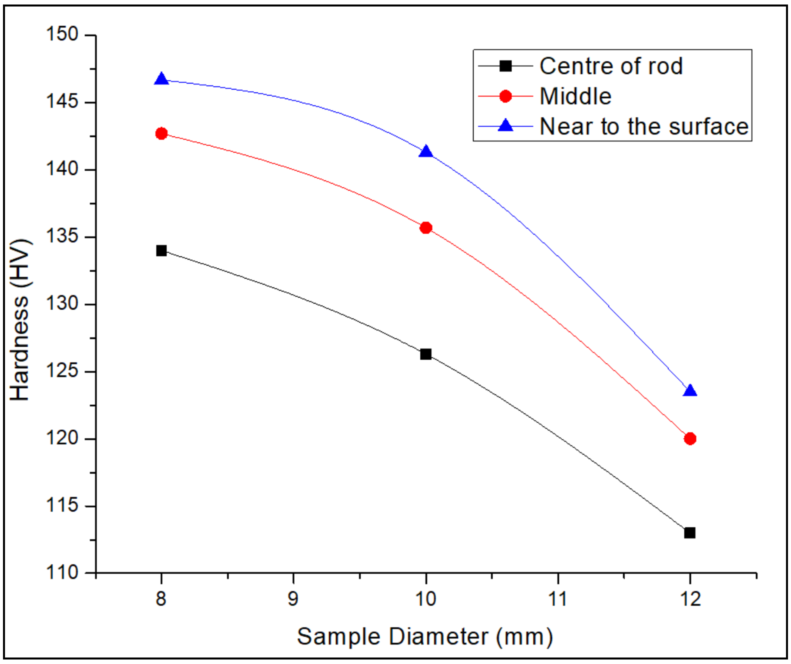

FIGURE 4. 117: HARDNESS VALUES OF C18150 TEST SAMPLES

From Fig. 4.118 and 4.119, it is possible to come in to conclusion that, the strength of As-extrude samples of 8mm in diameter had better UTS which was 542.6±4MPa and yield strength (YS) value of 509.2±6MPa than the As-machined samples with518.2±6MPa UTS value and 498.5±4MPa YS respectively . The UTS value of the feedstock was improved with 15.37 percent in yield strength and 14.66 percent for the ultimate tensile strength percent for As-machined samples. However the ultimate tensile strength of the feedstock was improved with 17.8 percent in UTS value and 20.06 percent for that of the As-extrudate samples. The overall improvements in tensile behavior were seen for both 8mm diameter extrudate sample and followed by 10mm extrudates with respect to 12.5mm diameter feed stock test rods. The feedstock had UTS and YS values of 452.03 and 432.01 MPa respectively. Therefore optimized CE process parameters have significant influence on the mechanical properties of the extrudates.

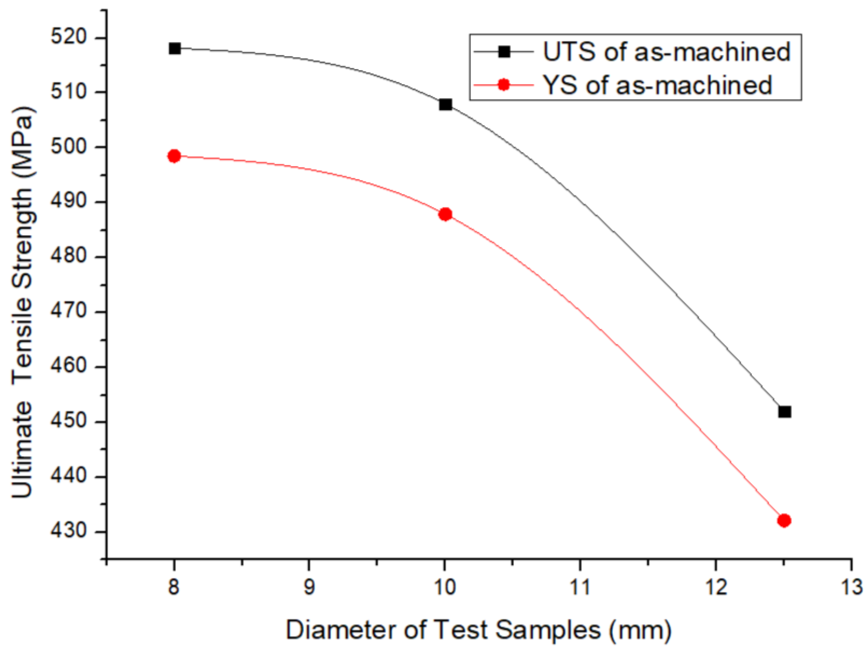

FIGURE 4. 118: COMPARISON OF THE UTS AND YS OF AS-SURFACE MACHINED TEST SAMPLES

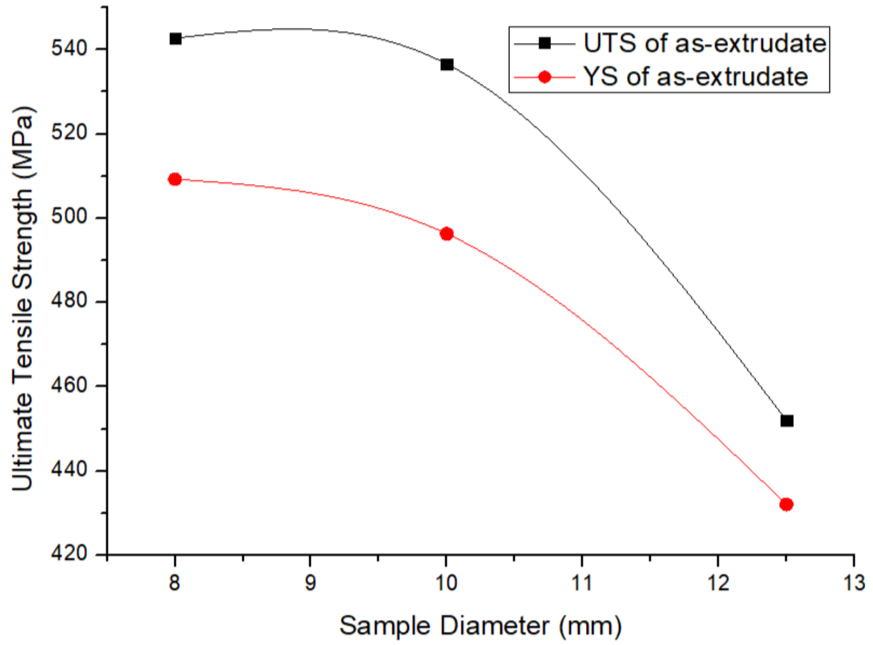

FIGURE 4. 119: COMPARISON OF THE UTS AND YS VALUES OF AS-EXTRUDED C18150 ALLOY

In the case of test samples of As-conform extruded ones, the maximum total elongation was seen for 8mm diameter as 21.8% and 19.86% maximum total elongation was observed for 8mm of As-machined sample shown in Fig 4.120. Therefore the outer layer had good contribution to percentage of elongation. Moreover the optimal process parameter improves the percentage of elongation of the feedstock by 57.97% for 8mm diameter As-conform extruded sample. Such unusual mechanical behavior improvement may be caused by the unique nanostructures generated through SPD processing and evenly distribution of Zirconium element in the copper matrix, through the process. The combination of ultrafine grain size and high-density dislocation pile-ups around the periphery may be the main causes for enhanced mechanical properties. This finding is also coinciding with the microstructure and hardness values.

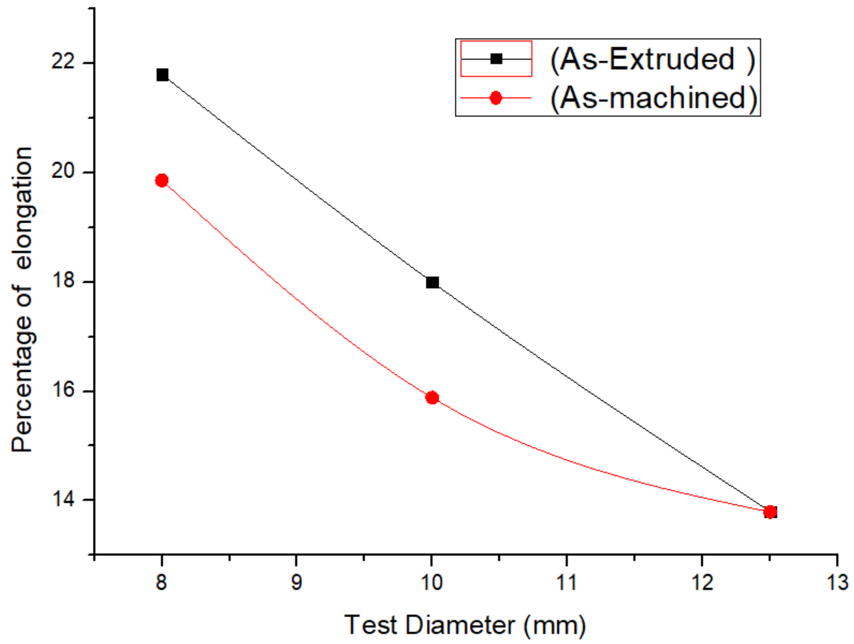

FIGURE 4. 120: PERCENTAGE OF ELONGATION FOR AS-MACHINED AND AS-EXTRUDED C18150 TEST SAMPLES

4.7. Wear Test

The wear tests were performed to investigate the effects of Conform input process parameters on the wear resistance properties of extrudates. AA1100 and C101 samples were tested using Micro Pin on Disc TRIBOMETER (TR-20Micro) machine. The sliding wear behaviors of AA1100 samples were studied as a function of extrusion wheel speeds of 6, 8, and 10RPM using a pin-on-disk test system. However, the sliding wear behavior of C101 copper metal samples was studied as a function of extrudate diameters (6, 7, and 8mm) using a pin-on-disk test system.

4.7.1. Wear characteristics of AA1100

Aluminum sliding wear test were performed based on test conditions in Table 3.19 using test samples shown in Fig.3.17. The samples were sliding over AISI 1045 carbon steel disc in un-lubricated sliding conditions. The samples were tested with the conditions of normal load of 10N, a sliding velocity of 0.5m/s, and sliding distances of 500m. The weights of the samples were measured pre and post-test. Table 4.29 shows the summery of the test and wear characteristics of extrudates and feedstock test samples. The mass loss is shown in Fig. 4.121. Regarding the sliding wear behaviors of AA1100, the specific wear rate increased with decreasing RPM up to 40 wt. % after which a drop in wear rate was observed. No correlation existed between the hardness and sliding wear of these alloys. A study of wear mechanisms shows that oxidative wear is the primary material removal mechanism at low contact pressures. Rajabi *et al.* (2019) *expresses* the phenomena of dry-wear as poughing, plastic deformation, and adhesion are the rate-controlling mechanisms at high contact pressures/forces.

Table 4. 26: Wear test results of AA1100

Extrudate	**Initial weight [gm]**	**Final weight [gm]**	**Mass loss Δm [gm] [10^{-3}]**	**CoF**	**SD**
Feedstock	0.9217(b)	0.9154	6.3	0.86	0.13
8mm at 8rpm	0.9167(n)	0.9118	4.9	0.701	0.11
7mm at 8rpm	0.8671(r)	0.8620	5.1	0.70	0.10

Wear test results of AA1100 extrudates are presented in Fig 4. 121 based on Table 4.30. From the Fig. 4.121 extrudates with 8mm diameter manufactured at 8RPM worn out least and the feed material worn-out most. This result had some correlation with hardness values. Therefore CE process improves feedstock wear resistance characteristics.

Using the formulas (Appendix-III) and data shown in Table 3. 19, to determine wear characteristics such as wear rate and specific wear characteristics and the specific wear characteristics of AA1100 developed graphically in Fig. 4.122 to explore the Conform input process parameters on the specific wear rate of AA1100 extrudates manufactured at different product diameters. Based on the graph the product with 8mm had least specific wear rate. All the extrudates were manufactured with a wheel speed of 8RPM.

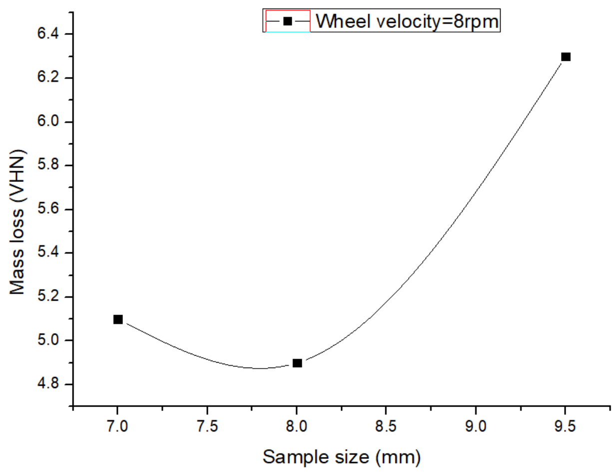

FIGURE 4. 121: WEAR TEST (MASS LOSS) RESULTS OF AA1100

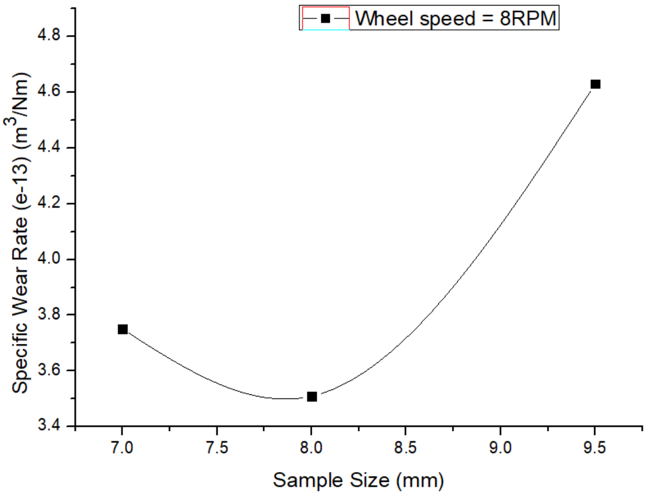

FIGURE 4. 122: SPECIFIC WEAR CHARACTERISTICS OF AA1100

Table 4. 27: Tabulated wear characteristics of AA1100

Specimen	**Frictional force (N)**	**(Δm) [gm]** e**10**$^{-3}$	**Wear resistance (gm^{-1})**	**Wear rate(Q)** (kg/m) [x10^{-6}]	**Wear rate(Q)** (kg/min) [x10^{-4}]	**Specific wear rate** (m^3/Nm), [x10^{-14}]
Feedstock	8.6	6.3	158.73	377.92	12.6	4.6323
8mm at 8rpm	7.01	4.9	204.08	293.94	9.8	3.6029
7mm at 8rpm	7.0	5.1	196.07	305.93	10.2	3.75

4.7.2. Wear characteristics of C101 test samples

Test samples were slide over AISI 1045 carbon steel disc in un-lubricated sliding conditions. The wear characteristics of the feedstock and extrudates of C101 samples were tested based on the conditions and samples stated in Table 3.19 and Fig. 3.19 respectively. The sliding wears behavior of the C101 feedstock and extrudate copper samples manufactured at the extrusion wheel speed of 8RPM for extrudates of 6 and 7mm in diameter. Using the procedure stated in Section 3.11, sliding wear tests were conducted on C101 test samples.

The testing conditions were at a relatively light load of 20N, a sliding velocity of 0.5m/s, and sliding distances of 500m. The weights of the samples were measured before and after the test. Wear test results of C101 are summarized in Table 4. 31. The table shows the weight loss, coefficient of friction, and the specific wear characteristics of C101 test samples.

Table 4. 28: Wear test results of C101 Copper

Sample detail	**Initial weight [mg]**	**Final weight [mg]**	**Mass loss $(\Delta m)e^{-3}$ [mg]**	**Coefficient of friction (CoF)**	**Standard Deviation (SD)**
Feed stock	2.8412(b)	2.8369	4.3	0.63	0.13
(6mm*8rpm)	2.9942 (r)	2.9913	2.9	0.91	0.18
(7mm*8rpm)	2.9408	2.9374	3.4	0.79	0.16

Legend b: blue (feedstock); r: red, (6mm extrudate, at 8rpm) and n: no-color (7mm extrudate at 8rpm)

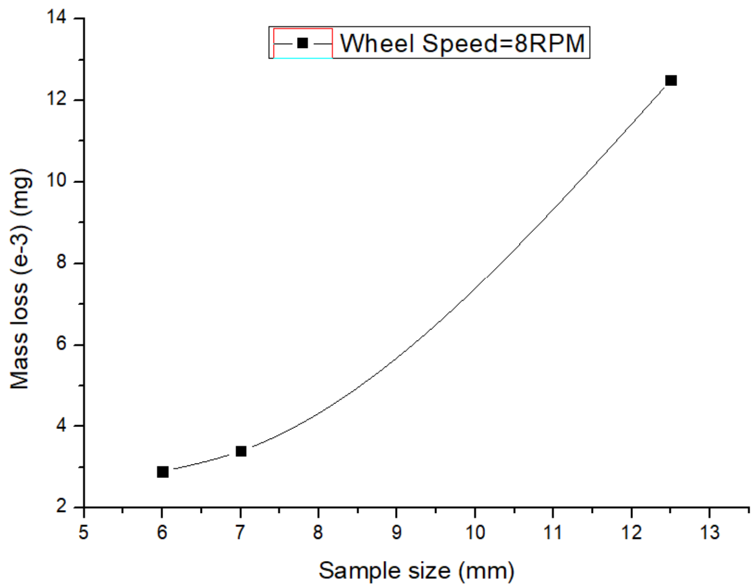

FIGURE 4. 123: WEAR TEST RESULTS OF C101 COPPER

Based on Table 4.26, Figure 4.123 is developed. From the graph it can be concluded that products with 6mm diameter had highest wear resistance compared to 7mm extrudates and feed metal.

Parameters such as frictional force, mass loss, wear resistance, wear rate and coefficient of wear rate (specific wear rate) were determined and shown in Table 4.32 with the data obtained from experiment in presented in Table 4.31 and Table 3.19 and the empirical formulas in (Appendix III). Specific wear rate has also been plotted in Fig. 4.124. Based on the test result the sample with high extrusion ratio had higher wear rate. Zinov'ev *et al.* (2019) investigated M1 feedstock during the CE process; based on his investigation as the feedstock stay longer in the extrusion die-chamber the feed metal decreases its hardness due to thermo-mechanical action or work softening effect.

Table 4. 29: Tabulated wear parameters of C101 Copper

Specimen	**Frictional force (N)**	**Δm) [gm] e10^{-3}**	**Wear resistance (gm^{-1})**	**Wear rate(Q)** (Kg/m) [x10^{-6}]	**Wear rate(Q)** (Kg/min) [x10^{-4}]	**Specific wear rate** (m^3/Nm), [x10^{-14}]
feedstock	12.6	4.3	232.55	8.6	2.5795	4.8206
6mm,8rpm	18.2	2.9	344.82	5.8	1.7397	3.2511
7mm,8rpm	15.8	3.4	294.11	6.8	2.0396	3.8117

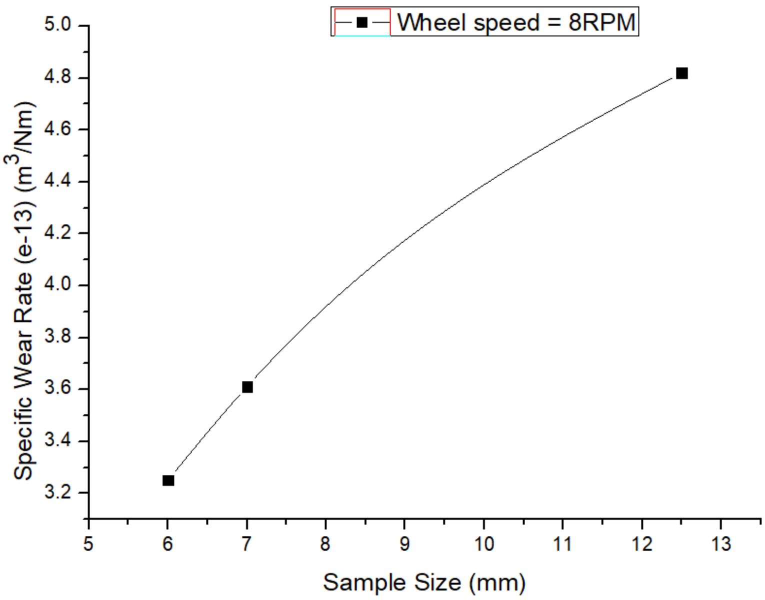

FIGURE 4. 124: SPECIFIC WEAR RATE OF C101

4.7.3. Copper-Chromium-Zirconium (C18150) wear test

Wear test was conducted as mentioned in the section 3.11 in Table 3.20 and using Fig.3.21. Wear test results of C18150 alloy were noted in terms of mass loss at different loading conditions and test sample diameters. The wear test values at 8RPM at various loading conditions and diameters (extrudates and feed) are shown in Fig. 4.125 and 4.126 respectively. Based on the figures, sample with 8mm in diameter extruded at 8RPM experienced with least mass losses.

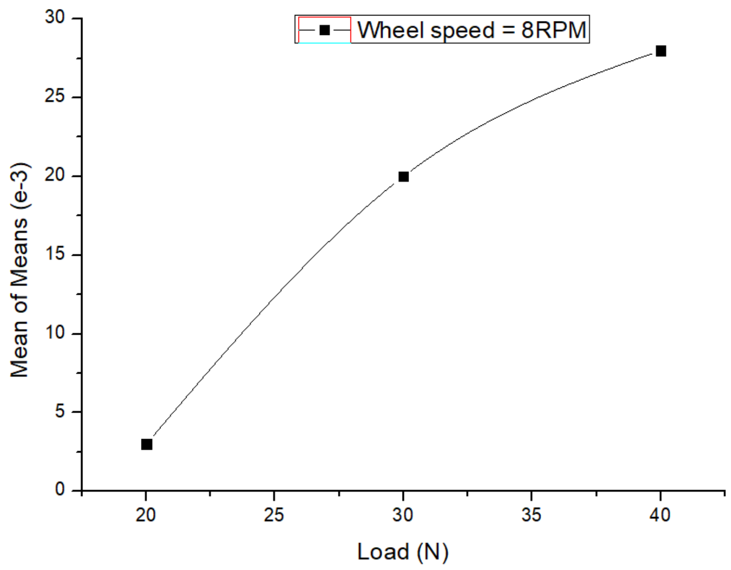

FIGURE 4. 125: WEAR TEST RESULTS OF C18150 DUE TO LOAD

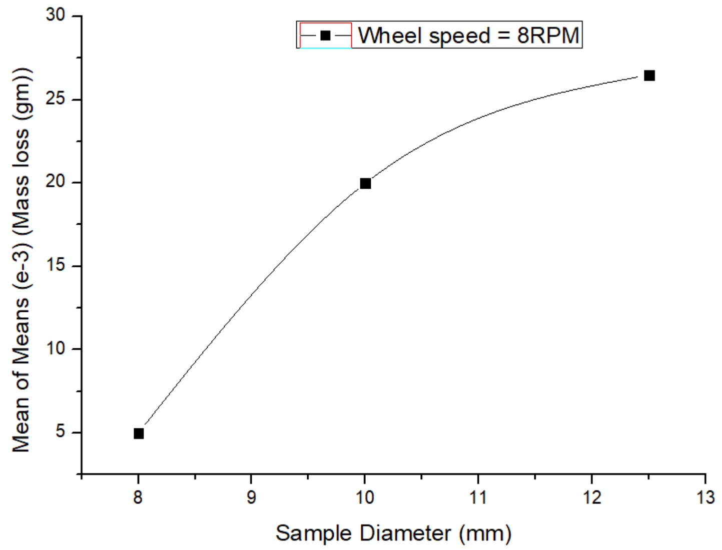

FIGURE 4. 126: MASS LOSS OF C18150 TEST SAMPLES

Experimental results showed that the load and the speed affect wear rate of the alloy. The results showed that the wear rate (weight lose) increased with increasing load and also increased with increasing sliding distance. The overall, it is clear from micro-structures, hardness tests, tensile tests, and wear tests 8mm diameter showed the best performance compared to 10 and 12.5mm diameters test samples. The Cu–Cr–Zr alloy wear behavior was found to be strongly related to its strength and hardness. The wear results also indicate that the wear behavior of the alloy in all processing conditions is consistent with the

Archard approach (Purcek, G., 2014). As per Conform extrusion process phenomenon, severe plastic deformation takes place while reducing or extrusion of any material to smaller dimension through the CE process. Due to this severe plastic deformation, improvement in mechanical properties is seen from test results. Similar findings have also been reported in the existing literatures.

Therefore taking all the findings into consideration, it is possible to conclude that mechanical, microstructural and tribological properties of feedstock materials are influenced by process variables of CE. Even with optimized CE extrusion power, extrudates enhances their tested properties.

CONCLUSIONS AND RECOMMENDATIONS

I. Conclusion

The investigated work dealt with the deformation behaviors of non-ferrous alloys in CE process. The various approaches such as analytical, computational, and experimental methods were used to explore the effects of the input process parameters of CE process such as *extrusion wheel speed, feed metal temperature, die temperature, friction factors and extrusion ratio* on the properties of feedstock materials and extrudates of Aluminum (AA1100), Copper (C101) and Copper-Chromium-Zirconium (C18150). From the results obtained, the following conclusions made:

Conclusions on feedstock and extrudates of Aluminum alloy (AA1100)

- The estimation of extrusion load necessary to extrude 9.5mm feedstock of AA1100 through UBM is carried. It is found that the extrusion load of 15.6kW, 14.85kW and 14.05kW for the extrusion of 9.5mm feedstock rod to 6mm, 7mm and 8mm respectively at 8rpm as extrusion wheel velocity.
- The extrusion power for the deformation of 9.5mm AA1100 is also carried out using the data of computational method. It is found that for the deformation of 9.5mm feed rod to 6mm extrudate extrusion load of 15.53kW is estimated which is in close agreement with the theoretical result. The optimized value of input process variables for the minimum total load required for extrusion of Aluminum alloy (AA1100) has been found to be 13RPM as wheel speed, 5mm as product diameter, 0.95 as friction condition, 650°C as feedstock temperature and 550°C as die temperature using ANN-GA technique and optimum value of load achieved is 136.4kN. The numerical result verified experimentally in good agreement.
- The experimental investigation of deformation behavior for 9.5mm feedstock materials has been carried out on TBJ300 commercial setup. It is found that the extrusion power of 14.08, 13.37 and 13.02kW are obtained for CE of 9.5mm feedstock to 6mm, 7mm and 8mm extrudates respectively at 8rpm wheel velocity. The close agreements of numerical and experimental results are achieved.
- The optimized value of input process variables of wheel speed and diameter of product are found to be 8.63RPM and 9mm as diameter of product respectively for yield strength 70.939MPa. The optimized value of input process variables, i.e., the wheel speed and diameter of product, is found to be 7.06RPM and 7.18mm

diameter of product respectively for maximum percentage elongation of 46.44. The percentage improvement in yield strength was 46.44%. Significant improvements were also observed in percentage of elongation of 59.23% of a product with 6mm manufactured at 8RPM.The average grain size of the extruded product is found to be 80 to 200µm under wheel speed of 4 to 10RPM. As the wheel speed increases from 4RPM to 8 RPM, the grains become refined and uniform. The further increase in wheel speed to 10 RPM slightly increased the grain size. The optimized value of input process variables, i.e., the wheel speed and diameter of product, is found to be 6.36 RPM and 7.53mm diameter of product respectively for maximum hardness value of 35.34 VHN which is 24% improvement to that of feedstock. The least mass loss and specific wear rate values 4.9×10^{-3}gm and 3.6029×10^{-14}m3/Nm are observed for the wear sample extruded with input process variables of 10RPM and 8mm diameter of product.

Conclusions on feedstock and extrudates of Copper Alloy (C 101)

- The estimation of total extrusion power through upper bound method is carried out for 12.5mm C101 feedstock material. It is found that the extrusion load of 49.89kW and 48.21kW for the continuous extrusion of 12.5mm feedstock rod to 6mm and 7mm respectively at 8rpm as wheel velocity.
- The extrusion power for the deformation of 12.5mm C101 is also carried out using data from computational analysis. It is found that for the CE deformation of 12.5mm feedstock rod to 6mm and 7mm extrudates extrusion load of 47.96 kW and 46.16kW was estimated which is in close agreement with the theoretical result.
- The experimental investigation of deformation behavior for 12.5mm feedstock is carried out on a TBJ350 commercial setup. It is found that the extrusion power of 45.60 and 44.35kW is estimated for CE of 12.5mm feedstock to 6mm and 7mm diameter extruded at 8RPM wheel velocity. The close agreements of experimental and numerical results are achieved with percentage of error between computational and experimental 5% and 3.98% for 6mm and 7mm extrudates respectively.
- The optimized value of input process variables for the minimum total force required for extrusion of Copper alloy (C101) has found to be 1RPM as wheel speed, 6mm as product diameter, 1.01 as friction condition, 678.53°C as feedstock temperature and 506.77°C as die temperature using RSM technique and an optimum value of load which is 247.23kN has been obtained. The numerical result

is verified experimentally total extrusion load of the system and in good agreement. This data is helpful for the complete machine setup designers.

- Effective stress and damage had been intensively investigated on C101 feedstock during the process. The minimum effective stress of 799.97N/mm^2 induced in the feedstock during the process if the wheel velocity, feedstock temperature, die temperature and frictional factor are 1.45 RPM, 400℃, 400℃, and 0.94 respectively. The optimum value of effective stress 799.97N/mm^2 has been obtained with composite desirability of 0.99996 using RSM. This stress value is much less than that of H13 tool steel. Therefore tool life will be improved significantly if the feedstock material processed with these parametric combinations. Additionally, the amount of damage on the extrudate during the process has become less than 0.9859 if the wheel velocity, feedstock temperature, die temperature and frictional factor are 11.63RPM, 400℃, 400℃, and 0.938 respectively The optimum value of damage (0.9859) has been obtained with composite desirability of 1.0 using RSM. Additionally, almost zero damage on the extrudate even before it leaves the extrusion die is observed on all the extrudates.

- The optimized value of input process variables of wheel speed and diameter of product are found to be 10RPM and 5.7273mm as diameter of product respectively for ultimate strength of 250.5393Mpa which is 20.77% improvements to that of feedstock. Optimal value of percentage elongation of 45.8% was found at input process variables of the 8RPM driving wheel speed and 6mm extrudate diameter.
- The microstructure samples of the C101 alloy at various Conform extrusion wheel speed and extrudate diameters. The average grain size of ranging from 80µm to 200µm (similar with aluminium) was obtained when the extrusion wheel speed from 6 to 8RPM. It is also observed that larger and inhomogeneous grain structures are obtained under Conform wheel speed of 6 and 8RPM. Fine and uniform grain structures are obtained when the wheel speed at 6RPM. A further increase in the driving wheel speed to 10RPM and slight increment in the grain size has been detected.

- The maximum hardness value of 89VHN is obtained for the input process variables, i.e., the wheel speed and diameter of product of 8RPM and 6mm diameter of product respectively. Therefore optimal percentage of improvement in hardness which was 41.12% was achieved for the above extrudate. The least mass loss and specific wear rate values $2.9x10^{-3}$gm and $3.2511x10^{-14}m^3/Nm$ were also observed for the wear sample extruded with input process variables of 8RPM and 6mm diameter of product.

Conclusions on C18150 alloy feedstock and extrudates

- The estimation of total extrusion power through upper bound method was carried out for 12.5mm C18150 feedstock material. It was found that the extrusion load of 78.8kW, 76.03kW and 73.66kW for the continuous extrusion of 12.5mm feedstock rod to 6mm, 8mm and 10mm respectively at 8rpm as wheel velocity.
- The extrusion power for the deformation of 12.5mm C18150 was also carried out using data from computational analysis. It was found that for the CE deformation of 12.5mm feedstock rod to 6mm, 8mm and 10mm extrudates, extrusion load of 77.2 kW, 73.92kW and 71.63kW was estimated which is in close agreement with the theoretical result.
- The experimental investigation of deformation behavior for 12.5mm feedstock materials was carried out on TBJ350 commercial setup. It was found that the extrusion powers of 70.4kW and 67.58kW were estimated for CE of 12.5mm C18150 feedstock to 8mm and 10mm extrudate diameters with an extrusion wheel velocity of 8RPM. The close agreements of numerical and experimental results are achieved.
- The optimized value of input process variables for the minimum total load required for extrusion of C18150 alloy had been found to be 3.99RPM as wheel speed, 8mm as product diameter, 0.85 as friction factor, 700℃ as feedstock temperature and 600℃ as die temperature using ANN-GA technique and optimum value of load achieved was 402.64kN. The result achieved with ANN was better than RSM. The optimal result with RSM 408.16kN with the desirability of 1.00.
- Effective stress and damage had been intensively investigated on C18150 feedstock during the process. The minimum effective stress of $1241N/mm^2$ induced in the feedstock during the process if the wheel velocity, feedstock temperature, die temperature and frictional factor were 4RPM, 500℃, 400℃, and 0.95, respectively. The optimum value of effective stress 799.97 had been obtained with composite desirability of 0.99996 using RSM. This stress value was much less than

that of H13 tool steel. Therefore tool life would be improved significantly if the feedstock material processed with these parametric combinations. Additionally, the amount of damage on the extrudate during the process had become less than 1. Almost zero damage on the extrudate even before it leaves the extrusion die was observed on all the extrudates.

- The UTS values as-Extrude samples and as-machined samples of 8mm compared and found 542.6±4Mpa and 518.2±6MPa respectively. UTS values of 542.6±4MPa were registered as the highest among the entire test samples. The YS of as-extrude samples and that of as-machined samples were 509.2±6MPa and 498.5±4MPa YS respectively. The UTS value of the feedstock was improved with 10.2% in yield strength and 14.66% for the ultimate tensile strength percent for as-machined samples respectively. However, the ultimate tensile strength of the feedstock was improved with 12.6% in UTS value and 19.9% as-extrudate samples. The overall improved tensile behavior was seen for the 8mm diameter extrudate sample and followed by 10mm and 12.5mm diameter rods respectively. Therefore CE can improve the mechanical properties of the extrudates. Concerning yield strength of as-extrude samples and as-machined samples significant differences also observed in-between. Therefore the outer layer removals did have contributions on the material yield strength loss for as-machined samples. Whenever CE C18150 products are required for any engineering application getting the right CE extrudates are much better rather than machining to the required size.
- Optimal value of input process variables, i.e., the wheel speed and diameter of product, is found to be 8RPM and 8mm diameter of product respectively for maximum percentage elongation of 21.82% and 19.86% are obtained for samples of as conform extruded ones and as-machined samples respectively. Therefore the optimal CE process parameter improves the percentage of elongation of the feedstock by 57.97% for 8mm diameter As-conform extruded sample of 8mm extruded at 8RPM.
- The maximum hardness value of 146.7VHN was obtained for the input process variables, i.e. 8mm diameter of product. The percentage improvement in hardness becomes 9.48% for 8mm extrudate. The least mass loss and specific wear rate values $3.3x10^{-3}$gm for 20N was also observed for the same sample.

- The microstructure samples of the C18150 alloy at various Conform extrusion wheel speed and extrudate diameters. The average grain size of ranging from 80µm to 200µm was obtained when the extrusion wheel speed from 8 RPM to 10RPM. It is also observed that larger and inhomogeneous grain structures obtained under Conform wheel speed of 10 RPM. Relatively fine and uniform grain structures were obtained when the wheel speed at 8RPM.

- Therefore, the extrudate grain size had been refined therefore its hardness, mechanical (UTS yield strength and percentage of elongation) and technological properties were also improved. The exploration of mechanical, metallurgical and tribological behavior carried out to ascertain the strength and quality of product obtained at optimum value of input process variables of CE process.

II. Recommendations (Future Scope)

1. Determination of extrusion load and power through existential theory and uniqueness theorem

2. Reductive extrusion process can be extended to Expanded Continuous Extrusion process with enhanced numerical simulation for non-ferrous alloys.
3. Powder continuous forming can be explored with the present materials and methodologies

4. Development of Cu-Cr-Zr alloy dynamic material model (DMM), its processing map and its application for controlling micro-structures and properties.

5. Development of a more complex theoretical analysis in order to define the relationship between the feedstock, friction conditions, tool temperatures, feed metal temperatures and peripheral and surface temperature of Conform extrusion tooling temperature. It can be the scope of future investigation. However, the variation of CE input process parameters such as extrusion driving speed, friction factors and product diameter on feed stock temperature have been investigated during computational analysis suing a finite element analysis tool-Deform 3D for comparative purposes.

6. Thermal dissipation analysis: development of evolution equations of CE process.

REFERENCES

Abdel-Aziem, W., Hamada, A., Makino, T., & Hassan, M. (2020). Microstructural evolution during extrusion of equal channel angular-pressed AA1070 alloy in micro/mesoscale. *Materials Science and Technology*, *36*(11), 1169-1177.

Abib, K., Azzeddine, H., Tirsatine, K., Baudin, T., Helbert, A. L., Brisset, F., & Bradai, D. (2016). Thermal stability of Cu-Cr-Zr alloy processed by equal-channel angular pressing. *Materials Characterization*, *118*, 527-534.

Abib, K., Larbi, F. H., Rabahi, L., Alili, B., & Bradai, D. (2015). DSC analysis of commercial Cu–Cr–Zr alloy processed by equal channel angular pressing. *Transactions of Nonferrous Metals Society of China*, *25*(3), 838-843

Aksenov, D. A., Asfandiyarov, R. N., Raab, G. I., Fakhretdinova, E. I., & Shishkunova, M. A. (2021). Influence of the Chromium Content in Low-Alloyed Cu–Cr Alloys on the Structural Changes, Phase Transformations and Properties in Equal-Channel Angular Pressing. *Metals*, *11*(11), 1795.

Asfandiyarov, R. N., Raab, G. I., & Aksenov, D. A. (2018, December). Modeling of a combined process for the production of contact wires for high-speed railways. In *IOP Conference Series: Materials Science and Engineering* (Vol. 461, No. 1, p. 012002). IOP Publishing.

ASTM, B. (2005). B221–Standard Specifications for Aluminum and Aluminum-Alloy Extruded Bars. Rods, Wire, Profiles, and Tubes.

Avitzur, B., & Van Tyne, C. J. (1982). Ring forming: an upper bound approach. Part 1: flow pattern and calculation of power.

Azzeddine, H., Bradai, D., Baudin, T., & Langdon, T. G. (2022). Texture evolution in high-pressure torsion processing. *Progress in Materials Science*, *125*, 100886.

Bagherpour, E., Reihanian, M., Pardis, N., Ebrahimi, R., & Langdon, T. (2018). Ten years of severe plastic deformation (SPD) in Iran, part I: Equal-channel angular pressing (ECAP). *Iranian Journal of Materials Forming*, *5*(1), 71-113.

Barcellona, A., Cannizzaro, L., and Riccobono, R. (2000). The Continuous Extrusion Process CONFORM: a full 3D Thermal and Mechanical Analysis. In Proceedings of the 33rd International MATADOR Conference (pp. 353-358). Springer, London.

Baş, D., & Boyacı, I. H. (2007). Modeling and optimization I: Usability of response surface methodology. Journal of food engineering, 78(3), 836-845.

Basri, M., Rahman, R. N. Z. R. A., Ebrahimpour, A., Salleh, A. B., Gunawan, E. R., & Rahman, M. B. A. (2007). Comparison of estimation capabilities of response surface methodology (RSM) with artificial neural network (ANN) in lipase-catalyzed synthesis of palm-based wax ester. BMC biotechnology, 7(1), 1-14.

Bazan, D. A., Gorokhov, Y. V., & Hetchikov, A. V. (2022). Measures for elimination of large crystal rim in the wall of the pipe obtained by continuous extrusion.

Belyaev, S. V., Gubanov, I. Y., Gorokhov, Y. V., Lesiv, E. M., Kosovich, A. A., Gubanova, M. I., ... & Goreyavchev, E. A. (2022). Analysis of the shoe length for continuous pressing equipment with a horizontal rotation axis of impeller. The International Journal of Advanced Manufacturing Technology, 118(3), 1295-1303.

Bhaduri, A. (2018). Mechanical properties and working of metals and alloys (Vol. 264, p. 119). Singapore: Springer.

Bhaduri, A. (2018a). Fundamentals of mechanical working. In Mechanical Properties and Working of Metals and Alloys (pp. 413-463). Springer, Singapore.

Borodin, E. N., Morozova, A., Bratov, V., Belyakov, A., & Jivkov, A. P. (2019). Experimental and numerical analyses of microstructure evolution of Cu-Cr-Zr alloys during severe plastic deformation. *Materials Characterization*, *156*, 109849.

Bourezg, Y. I., Abib, K., Azzeddine, H., & Bradai, D. (2020). Kinetics of Cr clustering in a Cu-Cr-Zr alloy processed by equal-channel angular pressing: A DSC study. *Thermochimica Acta*, *686*, 178550.

Bridgman, P. W. (2013). Studies in large plastic flow and fracture. In Studies in Large Plastic Flow and Fracture. Harvard University Press. Bridgman, P. W. (2013). Studies in large plastic flow and fracture. In Studies in Large Plastic Flow and Fracture. Harvard University Press.

Cao, F. R., Shi, Z. Y., and Wen, J. L. (1999). Upper-bound approach analysis of driving power of wheel for CASTEX. Transactions of Nonferrous Metals Society of China, 9(1), 99-104.

Cao, F. R., Wen, J. L., Hua, D. I. N. G., Wang, Z. D., Li, Y. L., Guan, R. G., *and* Hui, H. O. U. (2013). Force analysis and experimental study of pure aluminum and Al–5%

Ti–1% B alloy continuous expansion extrusion forming process. Transactions of Nonferrous Metals Society of China, 23(1), 201-207.

Cao, F. R., Wen, J. L., Hua, D. I. N. G., Wang, Z. D., Yu, C. P., & Fei, X. I. A. (2014). Extrusion force analysis of aluminum pipe fabricated by CASTEX using expansion combination die. *Transactions of Nonferrous Metals Society of China*, *24*(11), 3621-3631.

Chakraborty, J., Oellers, T., Raghavan, R., Ludwig, A., & Dehm, G. (2022). Microstructure and residual stress evolution in nanocrystalline Cu-Zr thin films. *Journal of Alloys and Compounds*, *896*, 162799.

Chan, C. H., Yusoff, R., & Ngoh, G. C. (2017). An energy-based approach to scale up microwave-assisted extraction of plant bioactives. In Ingredients extraction by physicochemical methods in food (pp. 561-597). Academic Press.

Chembarisova, R. G., Alexandrov, I. V., & Yamileva, A. M. (2019). The influence of structural factors on strength and electric conductivity of bulk nanostructured copper alloys. *Technical Physics*, *64*(2), 162-170.

Chembarisova, R. G., Sarkeeva, E. A., Alexandrov, I. V., & Wei, W. (2020). Analysis of the effect of equal-channel angular pressing on the strength and electrical conductivity of low-alloyed alloys of the Cu-Cr-Zr system. In *Journal of Physics: Conference Series* (Vol. 1431, No. 1, p. 012065). IOP Publishing

Chen, X., Yun, X., Zhao, Y., and Fan, Z. X. (2010). Effect of the porthole structure on extending forming of copper during continuous extrusion. Journal of Plasticity Engineering, 17(2), 68-72.

Chen, Y., Lu, W., Yin, J., Zhong, Y., Shao, G., Zhang, J., & Li, X. (2019). Effect of extrusion ratio on the microstructure and property of the Al–Zn–Mg–Cu alloy prepared by spray conform. *Materials Research Express*, *6*(10), 106536.

Chenna Krishna, S., Karthick, N. K., Sudarshan Rao, G., Jha, A. K., Pant, B., & Cherian, R. M. (2018). High strength, utilizable ductility and electrical conductivity in cold rolled sheets of Cu-Cr-Zr-Ti alloy. *Journal of Materials Engineering and Performance*, *27*(2), 787-793.

Cho, J. R., & Jeong, H. S. (2001). Parametric investigation on the curling phenomenon in CONFORM process by three-dimensional finite element analysis. Journal of Materials Processing Technology, 110(1), 53-60.

Cho, J. R., and Jeong, H. S. (2000). Parametric investigation on the surface defect occurrence in CONFORM process by the finite element method. Journal of Materials Processing Technology, 104(3), 236-243.

Cho, J. R., and Jeong, H. S. (2003). CONFORM process: surface separation, curling and process characteristics to the wheel diameter. Journal of Materials Processing Technology, 136(1-3), 217-226.

Dalan, F. C., de Lima Andreani, G. F., Travessa, D. N., Faizov, I. A., Faizova, S., & Cardoso, K. R. (2022). Effect of ECAP processing on distribution of second phase particles, hardness and electrical conductivity of Cu−0.81 Cr− 0.07 Zr alloy. *Transactions of Nonferrous Metals Society of China*, *32*(1), 217-232.

Darvell, B. W. (1990). Uniaxial compression tests and the validity of indirect tensile strength. Journal of Materials Science, 25(2), 757-780.

Davis, J. R. (1993). Asm Specialty Handbook: Aluminum & Aluminum Alloys. ASM international.

Davis, J. R. ASM Specialty Handbook: Copper and Copper Alloys. ASM International: Materials Park, OH,(2001) 3-9.

Edalati, K., Bachmaier, A., Beloshenko, V. A., Beygelzimer, Y., Blank, V. D., Botta, W. J., and Zhu, X. (2022). Nanomaterials by severe plastic deformation: review of historical developments and recent advances. Materials Research Letters, 10(4), 163-256.

Edalati, K., Hashiguchi, Y., Pereira, P. H. R., Horita, Z., & Langdon, T. G. (2018). Effect of temperature rise on microstructural evolution during high-pressure torsion. *Materials Science and Engineering: A*, *714*, 167-171.

Estrin, Y., & Vinogradov, A. (2013). Extreme grain refinement by severe plastic deformation: A wealth of challenging science. *Acta materialia*, *61*(3), 782-817.

Etherington, C. (1974). CONFORM—a new concept for the continuous extrusion forming of metals.

Fang, G., Zhou, J., and Duszczyk, J., 2009, "FEM Simulation of Aluminum Extrusion through Two-Hole Multi-Step Pocket Dies", Journal of Materials Processing Technology, 209(4) pp. 1891- 1900.

Faraji, G., and Torabzadeh, H. (2019). An overview on the continuous severe plastic deformation methods. Materials transactions, 60(7), 1316-1330.

Farokhpey, A., & Parsa, M. H. (2022). Analyzing the accumulative roll bonding deformation zone behavior by FEM, upper bound, and experimental methods. Journal of Manufacturing Processes, 81, 328-345.

Fu, Q., Li, B., Gao, M., Fu, Y., Yu, R., Wang, C., & Guan, R. (2022). Quantitative mechanisms behind the high strength and electrical conductivity of Cu-Te alloy manufactured by continuous extrusion. *Journal of Materials Science & Technology*, *121*, 9-18.

Giuliano, G. (Ed.). (2011). Superplastic forming of advanced metallic materials: Methods and applications. Elsevier.

Green D. (1972). : Continuous Extrusion of Wire sections, J. Inst. Metals, Vol. 100296-300.

Gronostajski, Z., Pater, Z., Madej, L., Gontarz, A., Lisiecki, L., Łukaszek-Sołek, A., and Ziółkiewicz, S. (2019). Recent development trends in metal forming. Archives of Civil and Mechanical Engineering, 19(3), 898-941.

Guo, T., Tai, X., Wei, S., Wang, J., Jia, Z., & Ding, Y. (2020a). Microstructure and Properties of Bulk Ultrafine-Grained Cu1. 5Cr0. 1Si Alloy through ECAP by Route C and Aging Treatment. *Crystals*, *10*(3), 207.

Guo, T., Wang, J., Wu, Y., Tai, X., Jia, Z., & Ding, Y. (2020). Fabricate of High-Strength and High-Conductivity Cu–Cr–Si Alloys through ECAP-Bc and Aging Heat Treatment. Materials, 13(7), 1603.

Haghighat, H., & Amjadian, P. (2013). A generalized upper bound solution for extrusion of bi-metallic rectangular cross-section bars through dies of any shape. Journal of Theoretical and Applied Mechanics, 51(1), 105-116.

Halmos, G. T. (2005). Roll forming handbook. CRC Press.

Hanrahan, G., & Lu, K. (2006). Application of factorial and response surface methodology in modern experimental design and optimization. Critical Reviews in Analytical Chemistry, 36(3-4), 141-151.

Harding, R. A., Homer, C., and Baudelet, B. (1980). Recrystallization of 70/30 brass during induction heating. Journal of Materials Science, 15(7), 1804-1813.

HE WX, W. E., CHEN, H., YU, Y., & LIU, J. (2007). Effects of deformation on microstructures and properties of submicron crystalline Cu-5% Cr alloy (J). *Trans Nonferrous Met Soc China*, *17*(2), 384-388.

He, Y. L., Gao, F., Song, B. Y., Fu, R., Wu, G. M., Li, J., and Jiang, L. (2012). Grain refinement of magnesium alloys by CONFORM: a continuous severe plastic deformation route. In Materials Science Forum (Vol. 706, pp. 1781-1786). Trans Tech Publications Ltd.

He, Y., Gao, F., Song, B., Li, J., Fu, R., & Wu, G. (2010). Production of very fine grained Mg–3% Al–1% Zn alloy by continuous extrusion forming (Conform). Advanced Engineering Materials, 12(9), 843-847.

Hernández-Escobar, D., Rahman, Z. U., Yilmazer, H., Kawasaki, M., & Boehlert, C. J. (2019). Microstructural evolution and intermetallic formation in Zn-Mg hybrids processed by high-pressure torsion. *Philosophical Magazine*, *99*(5), 557-584.

Heyduk, F., Ziółkiewicz, S., Bochniak, W., & Korbel, A. (2015). Manufacturing rods for production of spot welding electrodes using the KOBO extrusion method. *Metal Forming/Obróbka Plastyczna Metali*, *26*(4).

Higginson, R. L., & Sellars, C. M. (2003). Worked examples in quantitative metallography (Vol. 788). CRC Press.

Hill, R. O. D. N. E. Y. (1963). A general method of analysis for metal-working processes. Journal of the Mechanics and Physics of Solids, 11(5), 305-326.

Hosford, W. F., & Caddell, R. M. (2011). Metal forming: mechanics and metallurgy. Cambridge university press.

Hu, C., Wang, J., Lin, L., Weng, J., Outeiro, J., & Zhuang, K. (2022). Characterization of material flow mechanism for chamfered tools utilizing coupled slip-line-slab method. Journal of Materials Processing Technology, 300, 117424.

Hu, J., Kulagin, R., Ivanisenko, Y., Baretzky, B., and Zhang, H. (2020). Finite element modeling of Conform-HPTE process for a continuous severe plastic deformation path. Journal of Manufacturing Processes, 55, 373-380.

Hu, J., Teng, J., Ji, X., Fu, D., Zhang, W., & Zhang, H. (2017). Enhanced mechanical properties of an Al-Mg-Si alloy by repetitive continuous extrusion forming process and subsequent aging treatment. *Materials Science and Engineering: A*, *695*, 35-44.

Hu, J., Zhang, W., Fu, D., Teng, J., & Zhang, H. (2019). Improvement of the mechanical properties of Al–Mg–Si alloys with nano-scale precipitates after repetitive continuous extrusion forming and T8 tempering. *Journal of Materials Research and Technology*, *8*(6), 5950-5960.

Hu, P. H., Song, H. W., Wang, S. W., Chen, Y., & Zhang, S. H. (2021). Mechanisms of primary phase refinement and toughness improvement of Cu–2 wt% Ag–0.15 wt% La alloy through continuous extrusion forming. *Materials Science and Engineering: A*, *819*, 141521.

Huang, A. H., Wang, Y. F., Wang, M. S., Song, L. Y., Li, Y. S., Gao, L., ... & Zhu, Y. T. (2019). Optimizing the strength, ductility and electrical conductivity of a Cu-Cr-Zr alloy by rotary swaging and aging treatment. *Materials Science and Engineering: A*, *746*, 211-216.

Hwang, Y. M., & Hwang, T. F. (2002). An investigation into the plastic deformation behavior within a conical die during composite rod extrusion. Journal of Materials Processing Technology, 121(2-3), 226-233.

Ito, Y., & Horita, Z. (2009). Microstructural evolution in pure aluminum processed by high-pressure torsion. *Materials Science and Engineering: A*, *503*(1-2), 32-36.

Jagota, V., & Sharma, R. K. (2020). Wear volume prediction of AISI H13 die steel using response surface methodology and artificial neural network. Journal of Mechanical Engineering and Sciences, 14(2), 6789-6800.

Jalilova, D. A., Alikulov, A. K., Khasanov, O. A., & Abidov, A. I. (2022). Review of Modern Methods for Improving Complex Properties of Cu-Cr Alloy. *Web of Scientist: International Scientific Research Journal*, *3*(1), 890-900.

Jaseem, I., Immanuel, R. J., Rao, P. N., Khan, F., Sahoo, B. N., Panigrahi, S. K., & Kamaraj, M. (2018). Synergetic effect of cryorolling and postroll aging on simultaneous increase in wear resistance and mechanical properties of an Al–Cu alloy. *Journal of Tribology*, *140*(6), 061607.

Jeong, H. T., & Kim, W. J. (2021). Microstructure tailoring of Al0. 5CoCrFeMnNi to achieve high strength and high uniform strain using severe plastic deformation and an annealing treatment. Journal of Materials Science & Technology, 71, 228-240.

Ji, X., Zhang, H., Luo, S., Jiang, F., and Fu, D. (2016). Microstructures and properties of Al–Mg–SI alloy overhead conductor by horizontal continuous casting and continuous extrusion forming process. Materials Science and Engineering: A, 649, 128-134.

Jiang, K., Gan, B., Li, J., Dou, Q., & Suo, T. (2021). Towards strength-ductility synergy in a Cr-Co-Ni solid solution alloy via nano-twins. Materials Science and Engineering: A, 816, 141298.

Kao, Y. T. (2014). Effect of Severe Plastic Deformation and Subsequent Heat Treatment on Hardness and Electrical Conductivity of Oxygen-Free High Conductivity (OFHC) Copper, Commercial Pure Copper, and Copper Chromium Alloy (Doctoral dissertation).

Kapoor, G., Kvackaj, T., Heczel, A., Bidulská, J., Kočiško, R., Fogarassy, Z., & Gubicza, J. (2020). The Influence of Severe Plastic Deformation and Subsequent Annealing on the Microstructure and Hardness of a Cu–Cr–Zr Alloy. *Materials*, *13*(10), 2241.

Karamış, M. B., and Nair, F., 2008, "Effects of Reinforcement Particle Size in MMCs on Extrusion Die Wear", Wear, 265(11-12) pp. 1741-1750.

Katajarinne, T., Manninen, T., & Ramsay, P. (2006). Numerical simulation of flash formation in continuous rotary extrusion of copper. Journal of materials processing technology, 177(1-3), 604-607.

Katajarinne, T., Manninen, T., and Ramsay, P. (2006). Numerical simulation of flash formation in continuous rotary extrusion of copper. Journal of materials processing technology, 177(1-3), 604-607.

Khawaja, K., Althoefer, K., Clode, M. P., and Seneviratne, L. D. (2004, April). Gap sensing benefits in Conform/spl trade/extrusion machinery. In IEEE International

Conference on Robotics and Automation, 2004. Proceedings. ICRA'04. 2004 (Vol. 1, pp. 529-534). IEEE.

Khawaja, K., Seneviratne, L., and Clode, M. P. (2005). Benefits of wheel-tool gap sensing in Conform/spl trade/extrusion machinery. IEEE/ASME Transactions on Mechatronics, 10(4), 428-436.

Khomskaya, I. V., Kheifets, A. E., Zel'dovich, V. I. I., Korshunov, L. G., Frolova, N. Y. Y. Y., & Abdullina, D. N. (2018). The formation of friction-induced nanocrystalline structure in submicrocrystalline Cu-Cr-Zr alloy processed by DCAP. *Letters on Materials*, *8*(4), 410-414.

Khomskaya, I. V., Zel'dovich, V. I. I., Frolova, N. Y. Y. Y., Abdullina, D. N., & Kheifets, A. E. (2019). Investigation of Cu5Zr particles precipitation in Cu-Zr and Cu-Cr-Zr alloys subjected to quenching and high strain rate deformation. *Letters on Materials*, *9*(4), 400-404.

Kim, Y. H., Cho, J. R., Jeong, H., Kim, K. S., and Yoon, S. S. (1998). A study on optimal design for CONFORM process. Journal of Materials Processing Technology, 80, 671-675.

Kim, Y. H., Cho, J. R., Kim, K. S., Jeong, H. S., & Yoon, S. S. (2000). A study of the application of upper bound method to the CONFORM process. Journal of Materials Processing Technology, 97(1-3), 153-157.

Kim, Y. H., Cho, J. R., Kim, K. S., Jeong, H. S., & Yoon, S. S. (2000). A study of the application of upper bound method to the CONFORM process. Journal of Materials Processing Technology, 97(1-3), 153-157.

Koshmin, A. N., Zinoviev, A. V., Chasnikov, A. Y., & Grachev, G. N. (2021). Investigation of the Stress-Strain State and Microstructure Transformation of Electrotechnical Copper Buses in the Deformation Zone during Continuous Extrusion. *Russian Journal of Non-Ferrous Metals*, *62*(2), 179-189.

Koshmin, A., Zinoviev, A., Chasnikov, A., & Grachev, G. (2020). INFLUENCE OF PROCESS PARAMETERS ON THE PROPERTIES OF CONTINUOUSLY EXTRUDED COPPER BUSES. In Magnitogorsk Rolling Practice 2020 (pp. 88-89).

Kubina, T., Kövér, M., Dlouhý, J., & Nacházel, J. (2015). Link between technological parameters and material properties of EN 6082 Processed by ECAP-CONFORM and precipitation hardening. Int. J. Mater. Mech. Eng, 4, 36-43.

Kumari, S., Rai, A. K., Sinha, D. K., and Francis, R. C. (2015). Deformation behavior and characterization of copper alloy in extrusion process. International Journal of Mechanical Engineering and Technology, 6(7), 72-78.

Kuramoto, S., & Furuta, T. (2019). Severe Plastic Deformation to Achieve High Strength and High Ductility in Fe–Ni Based Alloys with Lattice Softening. *Materials transactions*, *60*(7), 1116-1122.

Langdon, T. G., Figueiredo, R. B., Kumar, P., & Kawasaki, M. (2018, December). Exploring the Paradox of Strength and Ductility. In *2018-Sustainable Industrial Processing Summit* (Vol. 5, pp. 43-46). Flogen Star Outreach.

Lengyel, B., & Kamyab-Tehrani, S. (1977). Investigations into continuous extrusion. In Proceedings of the Seventeenth International Machine Tool Design and Research Conference: held in Birmingham 20th–24th September, 1976 (pp. 423-428). Macmillan Education UK.

Li, B., Li, C. H., Yao, X. J., *and* Song, B. Y. (2011). Effects of continuous extrusion on microstructure evolution and property characteristics of brass alloy. In Advanced Materials Research (Vol. 189, pp. 2921-2924). Trans Tech Publications Ltd

Li, B., Lin, Z., Peng, C., Wang, X., & Zhang, J. (2017). Characteristics of microstructure evolution of two-phase H62 brass alloy during continuous extrusion. Procedia Engineering, 207, 1123-1128.

Li, B., Wei, Q., Pei, J. Y., and Zhao, Y. (2014). Flow characteristics of brass rod during continuous extrusion. Procedia Engineering, 81, 647-651.

Li, B., Yao, X., Yun, X., and Song, B. (2013, May). Effect of die shape on H62 brass forming for continuous extrusion based on numerical simulation research. In AIP Conference Proceedings (Vol. 1532, No. 1, pp. 918-923). American Institute of Physics.

Li, R., Guo, E., Chen, Z., Kang, H., Wang, W., Zou, C., & Wang, T. (2019). Optimization of the balance between high strength and high electrical conductivity in

CuCrZr alloys through two-step cryorolling and aging. *Journal of Alloys and Compounds*, *771*, 1044-1051.

Liang, D., Mi, X., Peng, L., Xie, H., Huang, G., & Yang, Z. (2020). Relationship between microstructure and properties of Cu–Cr–Ag alloy. *Materials*, *13*(3), 732.

Liao, W., Liu, X., & Yang, Y. (2020). Relationship and mechanism between double cold rolling-aging process, microstructure and properties of Cu–Ni–Si alloy prepared by two-phase zone continuous casting. *Materials Science and Engineering: A*, *797*, 140148.

Lin, G. Y., Tan, X., Feng, D., Wang, J. L., and Lei, Y. X. (2019). Effects of conform continuous extrusion and heat treatment on the microstructure and mechanical properties of Al–13Si–7.5 Cu–1Mg alloy. International Journal of Minerals, Metallurgy, and Materials, 26(8), 1013-1019.

Liu, G., Zhou, J., and Duszczyk, J. (2007). Finite element simulation of magnesium extrusion to manufacture a cross-shaped profile.

Liu, Y., Li, Z., Jiang, Y., Zhang, Y., Zhou, Z., & Lei, Q. (2017). The microstructure evolution and properties of a Cu–Cr–Ag alloy during thermal-mechanical treatment. *Journal of Materials Research*, *32*(7), 1324-1332.

Liu, Y., Yin, F., Yu, H., Feng, J., Ji, P., Zhang, J. & Wang, Q. (2022). Microstructural evolution, damping and tensile mechanical properties of multilayer Zn–22Al alloy fabricated by accumulative roll bonding (ARB). *Materials Science and Engineering: A*, *840*, 142911.

Lu, J., Saluja, N., Riviere, A. L., & Zhou, Y. (1998). Computer modeling of the continuous forming extrusion process of AA6061 alloy. Journal of Materials Processing Technology, 79(1-3), 200-212.

Lu, L. P., Yun, X. B., Yang, J. Y., & Song, B. Y. (2010). Study on deforming behavior of copper-magnesium alloy wire in extending continuous-extrusion process. Hot Working Technology, 39, 92-95.

Lu, R., Zheng, S., Teng, J., Hu, J., Fu, D., Chen, J., & Zhang, H. (2021). Microstructure, mechanical properties and deformation characteristics of Al-Mg-Si alloys processed by a continuous expansion extrusion approach. *Journal of Materials Science & Technology*, *80*, 150-162.

Ma, M., Li, Z., Qiu, W., Xiao, Z., Zhao, Z., Jiang, Y., & Huang, H. (2020). Development of homogeneity in a Cu-Mg-Ca alloy processed by equal channel angular pressing. *Journal of Alloys and Compounds*, *820*, 153112.

Manninen, T., Katajarinne, T., & Ramsay, P. (2006). Analysis of flash formation in continuous rotary extrusion of copper. Journal of Materials Processing Technology, 177(1-3), 600-603.

Mao, Q., Liu, Y., & Zhao, Y. (2022). A review on mechanical properties and microstructure of ultrafine grained metals and alloys processed by rotary swaging. *Journal of Alloys and Compounds*, *896*, 163122.

Mao, Q., Wang, L., Nie, J., & Zhao, Y. (2022). Enhancing strength and electrical conductivity of Cu–Cr composite wire by two-stage rotary swaging and aging treatments. Composites Part B: Engineering, 231, 109567.

Meng, A., Chen, X., Nie, J., Gu, L., Mao, Q., & Zhao, Y. (2021). Microstructure evolution and mechanical properties of commercial pure titanium subjected to rotary swaging. *Journal of Alloys and Compounds*, *859*, 158222.

Mertová, K., Palán, J., Duchek, M., Studecký, T., Džugan, J., & Poláková, I. (2020). Continuous production of pure titanium with ultrafine to nanocrystalline microstructure. Materials, 13(2), 336.

Mingdian, L., & Baoyun, S. (1993). Study of the velocity field and the stress field in the CONFORM, Advanced Technology of Plasticity. In Proceedings of the Fourth International Conference on Technology of Plasticity, Beijing (pp. 668-673).

Mitka, M., Gawlik, M., Bigaj, M., Szymanski, W., and Misiolek, W. Z. (2018). Continuous rotary extrusion of AZ81 magnesium alloy. Procedia Manufacturing, 15, 257-263.

Molaei, S. H., Shahbaz, M., & Ebrahimi, R. (2014). The relationship between constant friction factor and coefficient of friction in metal forming using finite element analysis. Iranian Journal of Materials Forming, 1(2), 14-22.

Monteiro, W. A. (Ed.). (2014). Light metal alloys applications. BoD–Books on Demand.

Morozova, A., Mishnev, R., Belyakov, A., & Kaibyshev, R. (2018). Microstructure and properties of fine grained Cu-Cr-Zr alloys after termo-mechanical treatments. *Reviews on Advanced Materials Science*, *54*(1), 56-92.

Mosleh, A. O., Mikhaylovskaya, A. V., Kotov, A. D., & Portnoy, V. K. (2018). Arrhenius-type constitutive equation model of superplastic deformation behaviour of different titanium based alloys. In Defect and Diffusion Forum (Vol. 385, pp. 45-52). Trans Tech Publications Ltd.

Mungole, T. (2018). *Deformation Mechanisms in Multilayer Materials at Small Length Scales*. Washington State University.

Murashkin, M., Medvedev, A., Kazykhanov, V., Krokhin, A., Raab, G., Enikeev, N., & Valiev, R. Z. (2015). Enhanced mechanical properties and electrical conductivity in ultrafine-grained Al 6101 alloy processed via ECAP-conform. Metals, 5(4), 2148-2164.

Myshkin, N. K., Petrokovets, M. I., & Kovalev, A. V. (2005). Tribology of polymers: Adhesion, friction, wear, and mass-transfer. Tribology International, 38(11-12), 910-921.

Niu, X., Shen, L., Chen, C., Zhou, J., & Chen, L. (2019). An Arrhenius-type constitutive model to predict the deformation behavior of Sn0. 3Ag0. 7Cu under different temperature. Journal of Materials Science: Materials in Electronics, 30(15), 14611-14620.

Nouri, M., Semnani, H. M., Emadoddin, E., & Kim, H. S. (2018). Investigation of direct extrusion channel effects on twist extrusion using experimental and finite element analysis. *Measurement*, *127*, 115-123.

Olszówka-Myalska, A., Wrześniowski, P., Ostachowski, P., Godzierz, M., & Kuc, D. (2022). Effect of Magnesium Powder Application on the Microstructure and Properties of Rods Extruded by the Forward-Backward Rotating Die Extrusion Method. *Materials*, *15*(12), 4094.

Ostachowski, P., Bochniak, W., Łagoda, M., & Ziółkiewicz, S. (2019). Strength properties and structure of CuCrZr alloy subjected to low-temperature KOBO extrusion and heat treatment. *The International Journal of Advanced Manufacturing Technology*, *105*(12), 5023-5044.

Özbeyaz, K., Kaya, H., & Kentli, A. (2022). Novel SPD method: twisted variable channel angular extrusion. *Metals and Materials International*, *28*(5), 1290-1305.

Pan, H., Zhong, Y., Zhang, Z., & Pan, C. (2019). Characteristics, Industrial Application, and Prospects of Continuous Extrusion Technology.

Pardoe, J. A. (1984). CONFORM continuous extrusion process–its contribution to energy conservation. Metals technology, 11(1), 358-365.

Park, N., Song, Y., Jung, S. H., Song, J., Lee, J., Lee, H., ... & Bae, G. (2021). Numerical and Experimental Investigation on the Surface Defect Generation during the Hot Extrusion of Al6063 Alloy. Materials, 14(22), 6768.

Pavia, D. L., Lampman, G. M., Kriz, G. S., & Vyvyan, J. A. (2014). Introduction to spectroscopy. Cengage learning.

Peng, D. S., Yao, B. Q., & Zuo, T. Y. (1992). The experimental simulation of deformation behavior of metals in the conform process. Journal of materials processing technology, 31(1-2), 85-92.

Peng, D. S., Yao, B. Q., and Zuo, T. Y. (1992). The experimental simulation of deformation behavior of metals in the conform process. Journal of materials processing technology, 31(1-2), 85-92.

Peris, R. G. (2007). Effects of extrusion conditions on" Die Pick-Up" formed during extrusion of aluminium alloy AA6060 (Doctoral dissertation, Auckland University of Technology).

Prasad, Y. V. R. K., Rao, K. P., & Sasidhar, S. (Eds.). (2015). Hot working guide: a compendium of processing maps. ASM international.

Purcek, G., Yanar, H. A. R. U. N., Demirtas, M. U. H. A. M. M. E. T., Shangina, D. V., Bochvar, N. R., & Dobatkin, S. V. (2020). Microstructural, mechanical and tribological properties of ultrafine-grained Cu–Cr–Zr alloy processed by high pressure torsion. *Journal of Alloys and Compounds*, *816*, 152675.

Purcek, G., Yanar, H. A. R. U. N., Saray, O., Karaman, I., and Maier, H. J. (2014). Effect of precipitation on mechanical and wear properties of ultrafine-grained Cu–Cr–Zr alloy. Wear, 311(1-2), 149-158.

Purcek, G., Yanar, H. A. R. U. N., Shangina, D. V., Demirtas, M. U. H. A. M. M. E. T., Bochvar, N. R., & Dobatkin, S. V. (2018). Influence of high pressure torsion-induced grain refinement and subsequent aging on tribological properties of Cu-Cr-Zr alloy. *Journal of Alloys and Compounds*, *742*, 325-333.

Qi, Y., Kosinova, A., Lakin, E., Popov Jr, V. V., Rabkin, E., & Lapovok, R. (2019). Effect of SPD Processing on the Strength and Conductivity of AA6061 Alloy. *Advanced Engineering Materials*, *21*(8), 1801370.

Rahim, S. N. A., Lajis, M. A., and Ariffin, S. (2016). Effect of extrusion speed and temperature on hot extrusion process of 6061 aluminum alloy chip. ARPN J. Eng. Appl. Sci, 11(4), 2272-2277.

Rajabi, M., Miresmaeili, R., & Aliofkhazraei, M. (2019). Hardness and wear behavior of surface mechanical attrition treated titanium. Materials Research Express, 6(6), 065003.

Rajendran, N. (2021). Metal Flow Optimization Within the Deformation Zone in Continuous Rotary Extrusion (Cre) of AZ91 Magnesium Alloy (Doctoral dissertation, Lehigh University).

Rajendran, N., Valberg, H., and Misiolek, W. Z. (2017, October). The FEM simulation of continuous rotary extrusion (CRE) of aluminum alloy AA3003. In AIP Conference Proceedings (Vol. 1896, No. 1, p. 050004). AIP Publishing LLC.

Ravisankar, B., Sivaprasad, K., Babu, N. R., Raab, G. I., & Valiev, R. Z. (2019, November). High strength and high conductive copper-based alloy produced by SPD for contact wires for high speed railway lines-A short review. In *IOP Conference Series: Materials Science and Engineering* (Vol. 672, No. 1, p. 012055). IOP Publishing.

Segal, V. (2018). modes and processes of severe plastic deformation (SPD). *Materials*, *11*(7), 1175.

Shan, L., Yang, L., & Wang, Y. (2022). Improving the high temperature mechanical performance of Cu–Cr alloy induced by residual nano-sized Cr precipitates. *Materials Science and Engineering: A*, *845*, 143250.

Shangina, D. V., Bochvar, N. R., Morozova, A. I., Belyakov, A. N., Kaibyshev, R. O., & Dobatkin, S. V. (2017). Effect of chromium and zirconium content on structure, strength and electrical conductivity of Cu-Cr-Zr alloys after high pressure torsion. *Materials Letters*, *199*, 46-49.

Shangina, D., Maksimenkova, Y., Bochvar, N., Serebryany, V., Raab, G., Vinogradov, A., & Dobatkin, S. (2016). Influence of alloying with hafnium on the microstructure, texture, and properties of Cu–Cr alloy after equal channel angular pressing. *Journal of Materials Science*, *51*(11), 5493-5501.

Sheik Hassan, M., Sharma, S., & Kumar, B. (2017). A Review of Severe Plastic Deformation. *Int. Refereed J. Eng. Sci*, *6,* 66-85.

Shen, Y. F., Guan, R. G., Zhao, Z. Y., and Misra, R. D. K. (2015). Ultrafine-grained Al–0.2 Sc–0.1 Zr alloy: The mechanistic contribution of nano-sized precipitates on grain refinement during the novel process of accumulative continuous extrusion. Acta Materialia, 100, 247-255.

Shen, Z., Lin, Z., Shi, P., Zhu, J., Zheng, T., Ding, B., ... & Zhong, Y. (2022). Enhanced electrical, mechanical and tribological properties of Cu-Cr-Zr alloys by continuous extrusion forming and subsequent aging treatment. *Journal of Materials Science & Technology*, *110*, 187-197.

Shen, Z., Lin, Z., Shi, P., Zhu, J., Zheng, T., Ding, B., ... & Zhong, Y. (2022). Enhanced electrical, mechanical and tribological properties of Cu-Cr-Zr alloys by continuous extrusion forming and subsequent aging treatment. *Journal of Materials Science & Technology*, *110*, 187-197.

Sheng, B. I., Yun, X. B., Pei, J. Y., Ying, Z. H. A. O., Yan, Z. Y., and Zhang, X. (2017). Microstructure evolution of Al–Sr master alloy during continuous extrusion. Transactions of Nonferrous Metals Society of China, 27(2), 305-311.

Sheppard, T. (1981). Temperature and speed effects in hot extrusion of aluminium alloys. Metals technology, 8(1), 130-141.

Sidelnikov, S. B., Dovzhenko, N. N., Konstantinov, I. L., Galiev, R. I., Kiselev, A. L., & Samchuk, A. P. (2015). Experience of using and application prospects of rolling-extruding process for obtaining semi-finished products from aluminum alloys.

Silberschmidt, V. V. (Ed.). (2020). Mechanics of materials in modern manufacturing methods and processing techniques. Elsevier.

Silva, J. D., Santos, P. A., Unfer, R. K., Verran, G. O., & Plaine, A. H. (2021). Upper-Bound Analysis for Equal Channel Angular Pressing (ECAP) with an Intersecting Channel Angle of 120°. Materials Research, 24.

Sinha, D. K., Kumar, S., and Kumar, A. (2012). Virtual design and fabrication of a continuous extrusion setup with process analysis. Int. J. Eng. Res. Technol, 1, 1-7.

Sinha, D. K., Kumar, S., Kumar, A., and Yadav, A. (2018, August). Mathematical modelling to predict mechanical properties of Copper () feedstock in continuous extrusion. In IOP Conference Series: Materials Science and Engineering (Vol. 404, No. 1, p. 012052). IOP Publishing.

Smythe 2020, S. A., Thomas, B. M., *and* Jackson, M. (2020). Recycling of titanium alloy powders and swarf through continuous extrusion (Conformtm) into affordable wire for additive manufacturing. Metals, 10(6), 843.

Snopiński, P., Woźniak, A., & Pagáč, M. (2021). Microstructural Evolution, Hardness, and Strengthening Mechanisms in SLM AlSi10Mg Alloy Subjected to Equal-Channel Angular Pressing (ECAP). *Materials*, *14*(24), 7598.

Song, L., Yuan, Y., & Yin, Z. (2013). Microstructural evolution in Cu-Mg alloy processed by conform.

Sousa, T. G., de Brito Moura, I. A., Garcia Filho, F. D. C., Monteiro, S. N., & Brandao, L. P. (2020). Combining severe plastic deformation and precipitation to enhance mechanical strength and electrical conductivity of Cu–0.65 Cr–0.08 Zr alloy. *Journal of Materials Research and Technology*, *9*(3), 5953-5961.

Struers, V. V. C. L., & Yang, D. (2019). ASM Releases Updated Handbook on Materials Characterization.

Su, N., Guan, R., Wang, X., Wang, Y., Jiang, W., and Liu, H. (2016). Grain refinement in an AlEr alloy during accumulative continuous extrusion forming. Journal of Alloys and Compounds, 680, 283-290.

Sun, X., Jie, J., Wang, T., & Li, T. (2021). Effect of two-step cryorolling and aging on mechanical and electrical properties of a Cu–Cr–Ni–Si alloy for lead frames applications. *Materials Science and Engineering: A, 809*, 140521.

Suresh, M., Sharma, A., More, A. M., Kalsar, R., Bisht, A., Nayan, N., & Suwas, S. (2019). Effect of equal channel angular pressing (ECAP) on the evolution of texture, microstructure and mechanical properties in the Al-Cu-Li alloy AA2195. *Journal of Alloys and Compounds*, *785*, 972-983.

Takata, N., Ohtake, Y., Kita, K., & Kitagawa, K. (2009). Increasing the ductility of ultrafine-grained copper alloy by introducing. *Book name Scripta Materialia*, *60*, 590-593.

Tirosh, J., Grossman, G., and Gordon, G. (1979). Theoretical and experimental study of the CONFORM metal forming process.

Tressia d, G., de Almeida, L., and Moreira, V. C. (2017). Influence of the Tool Geometry in the Mechanical Properties of Copper Wire Manufactured by the Conform Process, Anais do Seminário de Laminação e Conformação, vol. 54, num. 1, 1-9.

Tressia, G., Moreira, V. C., de Almeida, L., and Aniceto, P. D. J. (2018). Influence Of The Extrusion Speed On The Microstructural Homogeneity Of The Continuous Forming Process/Influência Da Velocidade De Extrusão Na Homogeneidade Microestrutural Do Processo De Conformação Contínua. Tecnologia em Metalurgia, Materiais e Mineração, 15(2), 182.

Valberg, H. S. (2010). Applied metal forming: including FEM analysis. Cambridge University Press.

Valberg, H., Rajendran, N., & Misiolek, W. (2018). The Mechanics of the Continuous Rotary Extrusion Process Investigated by FEM analysis. In Proceedings of the Eighth International Conference On Advances in Mechanical, Aeronautical and Production Techniques-MAPT (pp. 1-7).

Valiev, R. (2004). Nano-structuring of metals by severe plastic deformation for advanced properties. Nature materials, 3(8), 511-516.

Valiev, R. Z., Alexandrov, I. V., Zhu, Y. T., & Lowe, T. C. (2002). Paradox of strength and ductility in metals processed by severe plastic deformation. Journal of Materials research, 17(1), 5-8.

Valiev, R. Z., Estrin, Y., Horita, Z., Langdon, T. G., Zechetbauer, M. J., and Zhu, Y. T. (2006). Producing bulk ultrafine-grained materials by severe plastic deformation. Jom, 58(4), 33-39.

Valiev, R. Z., Straumal, B., and Langdon, T. G. (2022). Using Severe Plastic Deformation to Produce Nanostructured Materials with Superior Properties. Annual Review of Materials Research, 52.

Venkatesh, C., & Venkatesan, R. (2015). Optimization of process parameters of hot extrusion of SiC/Al 6061 composite using Taguchi's technique and upper bound technique. Materials and Manufacturing Processes, 30(1), 85-92.

Vinogradov, A., Patlan, V., Suzuki, Y., Kitagawa, K., & Kopylov, V. I. (2002). Structure and properties of ultra-fine grain Cu–Cr–Zr alloy produced by equal-channel angular pressing. *Acta materialia*, *50*(7), 1639-1651.

Wagiman, A., Mustapa, M. S., Asmawi, R., Shamsudin, S., Lajis, M. A., and Mutoh, Y. (2020). A review on direct hot extrusion technique in recycling of aluminium chips. The International Journal of Advanced Manufacturing Technology, 106(1), 641-653.

Wang, Y. D., Liu, M., Yu, B. H., Wu, L. H., Xue, P., Ni, D. R., & Ma, Z. Y. (2021). Enhanced combination of mechanical properties and electrical conductivity of a hard state Cu-Cr-Zr alloy via one-step friction stir processing. Journal of Materials Processing Technology, 288, 116880.

Wang, Y., Fu, R., Li, Y., & Zhao, L. (2019). A high strength and high electrical conductivity Cu-Cr-Zr alloy fabricated by cryogenic friction stir processing and subsequent annealing treatment. *Materials Science and Engineering: A*, *755*, 166-169.

Wood, P. K. (1990). The mechanics of the conform continuous extrusion process (Doctoral dissertation, Aston University).

Wu, C. W., & Hsu, R. Q. (2000). A universal velocity field for the extrusion of non-axisymmetric rods with non-uniform velocity distribution in the extrusion direction. Journal of Materials Processing Technology, 97(1-3), 180-185.

Wu, P. Y., Xie, S. S., Li, H. Q., Ming, Y., Huang, G. J., and Cheng, L. (2007). Effect of extrusion wheel angular velocity on continuous extrusion forming process of copper concave bus bar. Transactions of Nonferrous Metals Society of China, 17(2), 280-286.

Wu, X., Zhang, J., Wang, R., Zafar, Z., Liu, X., Liu, Y., & Sun, L. (2022). Achieving high strength and high conductivity synergy through hierarchical precipitation stimulated structural heterogeneities in a Cu-Ag-Zr alloy. Materials & Design, 110777.

Xie, M., Huang, W., Chen, H., Gong, L., Xie, W., Wang, H., & Yang, B. (2021). Microstructural evolution and strengthening mechanisms in cold-rolled Cu–Ag alloys. *Journal of Alloys and Compounds*, *851*, 156893.

Xu, C., Schroeder, S., Berbon, P. B., and Langdon, T. G. (2010). Principles of ECAP–Conform as a continuous process for achieving grain refinement: Application to an aluminum alloy. Acta Materialia, 58(4), 1379-1386.

Xu, G. L., Peng, L. J., Huang, G. J., Xie, H. F., Yang, Z., Feng, X., ... & Mi, X. J. (2021). Microstructural evolution and properties of a Cu–Cr–Ag alloy during continuous manufacturing process. *Rare Metals*, *40*(8), 2213-2220.

XU, M., & DAI Na-Na, Z. Y. (2012). Calculation of pressure and power required by continuous extrusion of copper bus bar by slab method. *China Mechanical Engineering*, *23*(21), 2630.

Yadav, R. R., Dewang, Y., and Raghuvanshi, J. (2018). A study on metal extrusion process. International Journal of LNCT, 2(6), 124-230.

Yang, B., Wang, Y., Gao, M., Wang, C., & Guan, R. (2022). Microstructural evolution and strengthening mechanism of Al–Mg alloys with fine grains processed by accumulative continuous extrusion forming. Journal of Materials Science & Technology.

Yang, H., Ma, Z., Lei, C., Meng, L., Fang, Y., Liu, J., & Wang, H. (2020). High strength and high conductivity Cu alloys: A review. *Science China Technological Sciences*, *63*(12), 2505-2517.

Ying, Z. H. A. O., Pei, J. Y., Guo, L. L., and Yun, X. B. (2021). Effects of extrusion speed of continuous extrusion with double billets on welding performance of 6063 Al alloy. Transactions of Nonferrous Metals Society of China, 31(6), 1561-1571.

Ying, Z. H. A. O., SONG, B. Y., YUN, X. B., PEI, J. Y., JIA, C. B., and YAN, Z. Y. (2012). Effect of process parameters on sheath forming of continuous extrusion sheathing of aluminum. Transactions of Nonferrous Metals Society of China, 22(12), 3073-3080.

Yousif, A. D., Enab, T. A., Galal, A. M., and El-Gayyar, M. S. (2016), Effect of Die Material and Hardness on the Productivity of Copper Strips via Hot Continuous

Extrusion Process, IPASJ International Journal of Mechanical Engineering (IIJME), Volume 4, Issue 8., pp.22-27.

Yu. N. Raikov, Treatment of Copper, High School Textbook (in Russian), OAO Inst. Tsvet. Met., Moscow (2006).

Yuan, D., Wang, J., Chen, H., Xie, W., Wang, H., & Yang, B. (2018). Mechanical properties and microstructural evolution of a Cu–Cr–Ag alloy during thermomechanical treatment. *Materials Science and Technology*, *34*(12), 1433-1440.

Yuan, Y., Li, Z., Xiao, Z., Zhao, Z., & Yang, Z. (2017). Microstructure evolution and properties of Cu-Cr alloy during continuous extrusion process. *Journal of Alloys and Compounds*, *703*, 454-460

Yun, X. B., Wei, Y. O. U., Ying, Z. H. A. O., Bing, L. I., and Fan, Z. X. (2013). Continuous extrusion and rolling forming velocity of copper strip. Transactions of Nonferrous Metals Society of China, 23(4), 1108-1113.

Yun, X. B., Yao, M. L., Wu, Y., and Song, B. Y. (2011). Numerical simulation of continuous extrusion extending forming under the large expansion ratio for copper strip. In Applied Mechanics and Materials (Vol. 80, pp. 91-95). Trans Tech Publications Ltd.

Yun, X., Wan, F., Bi, S., and Li, B. (2017). Effect of billet preheating temperature on continuous extrusion forming of Al-Sr alloy. Procedia engineering, 207, 395-400.

Yun, X., Zhou, M., Tian, T., and Zhao, Y. (2015). Continuous extrusion and rolling forming technology of copper strip manufacture. In MATEC Web of Conferences (Vol. 21, p. 03004). EDP Sciences.

Yun, X., Zhou, M., Tian, T., and Zhao, Y. (2016). Continuous extrusion and rolling forming of copper strips. Manufacturing Review, 3, 7.

Zemko, M., Hodek, J., Kraus, L., and Dlouhy, J. (2013). FEM Modelling of Continuous Extrusion of High-Strength Metals Using Commercial Conform™ Machine. Advanced Science Letters, 19(3), 701-704.

Zeng, Z., Stanford, N., Davies, C. H. J., Nie, J. F., and Birbilis, N. (2019). Magnesium extrusion alloys: a review of developments and prospects. International Materials Reviews, 64(1), 27-62.

Zhang, H., Jiang, F., Shang, X., & Li, L. (2013). Flow stress and microstructural evolution of the horizontal continuous casting Al–0.96 Mn–0.38 Si–0.18 Fe alloy during hot compression. Materials Science and Engineering: A, 571, 25-32.

Zhang, H., Yan, Q., and Li, L. (2008). Microstructures and tensile properties of AZ31 magnesium alloy by continuous extrusion forming process. Materials Science and Engineering: A, 486(1-2), 295-299.

Zhang, P. C., Shi, J. F., Yu, Y. S., Sun, J. C., & Li, T. J. (2020). Effect of cryorolling on microstructure and property of high strength and high conductivity Cu− 0.5 wt.% Cr alloy. Transactions of Nonferrous Metals Society of China, 30(9), 2472-2479.

Zhang, S., Li, R., Kang, H., Chen, Z., Wang, W., Zou, C., & Wang, T. (2017). A high strength and high electrical conductivity Cu-Cr-Zr alloy fabricated by cryorolling and intermediate aging treatment. Materials Science and Engineering: A, 680, 108-114.

Zhang, X. Y., Zhang, H., Kong, X. X., and Fu, D. F. (2015). Microstructure and properties of Al–0.70 Fe–0.24 Cu alloy conductor prepared by horizontal continuous casting and subsequent continuous extrusion forming. Transactions of Nonferrous Metals Society of China, 25(6), 1763-1769.

Zhang, X., Huang, L. K., Zhang, B., Chen, Y. Z., & Liu, F. (2020). Microstructural evolution and strengthening mechanism of an Al–Si–Mg alloy processed by high-pressure torsion with different heat treatments. Materials Science and Engineering: A, 794, 139932.

Zhao, N., & Ban, C. (2022). Developing a High-Strength Al–Mg–Si Alloy with Improved Electrical Conductivity by a Novel ECAP Route. Metals and Materials International, 1-16.

Zhao, Y., Song, B. Y., Pei, J. Y., & Yun, X. B. (2011). Study on metal flow in continuous extrusion cladding of cable aluminum sheath using FEM analysis. In Advanced Materials Research (Vol. 189, pp. 1934-1940). Trans Tech Publications Ltd.

Zhao, Y., Song, B., Pei, J., Jia, C., Li, B., & Linlin, G. (2013). Effect of deformation speed on the microstructure and mechanical properties of AA6063 during continuous extrusion process. Journal of Materials Processing Technology, 213(11), 1855-1863.

Zhao, Y., Song, B., Yan, Z., Zhang, X., and Pei, J. (2016). Microstructure and mechanical properties of extrusion welds in continuous extrusion of AA6063 aluminium alloy with double billets. Journal of Materials Processing Technology, 235, 149-157.

Zinov'ev, A. V., Koshmin, A. N., & Chasnikov, A. Y. (2019). Effect of continuous extrusion parameters on alloy M1 round section bar microstructure and mechanical property formation. Metallurgist, 63(3), 422-428.

LIST OF PUBLICATIONS

JOURNALS (Papers Published)

1. Desta, T., Sinha, D. K., Ramulu, P. J., & Tufa, H. B. (2021). Microstructural and mechanical studies of feedstock material in continuous extrusion process. *International Journal of Mechanical and Materials Engineering*, *16*(1), 1-14.

2. Desta, T., Sinha, D. K., Ramulu, P. J., & Singh, R. S. (2021). Numerical modeling and optimization of process parameters in continuous extrusion process through response surface methodology, artificial neural network & genetic algorithm. *International Journal of Modeling, Simulation, and Scientific Computing*, *12*(06), 2150060.

PAPERS UNDER REVIEW

Under Review

3. Desta, T., Sinha, D. K., Ramulu, P. J, "*Mechanical Behaviour and Wear Characteristics of a Conform Extruded C18150 (Cu-Zr-Cr) alloy Rods*"

4. Desta, T., Sinha, D. K., Ramulu, P. J., "*Optimization of Deformation Behavior during Continuous Forming Extrusion of C18150 Copper Alloy Through Response Surface Methodology*"

5. Desta, T., Sinha, D. K., Ramulu, P. J., "*Mechanical and Metallurgical investigation of feedstock material in Continuous Extrusion Process of Copper Alloy"*

BOOK CHAPTER (Accepted and Under-printing)

Tariku Desta, Devendra Kumar Sinha, Perumalla Janaki Ramulu, Birhane Assefa Gemeda, and Ram Sewak Singh, *"Modeling and Optimization of Deformation Load in Warm Continuous Extrusion Process",* Optimization of Advanced Manufacturing Processes, ISBN: 9781774916025, January-2024.

APPENDIX

APPENDIX-I: Some of the Basic Formulas Applied

i. ***Some of the basic formulas used during the analysis.***

Given working condition

W_d = *Wheel Diameter = 350mm*
w_v = *Wheel Velocity*
pd = Product diameter
Ft = Feedstock temperature
Dt = Die temperature
μ *=Friction factor*

- **Power** required to extrude with the above working conditions

$$P = Fv \text{ .... } \mathbf{(1)}$$

Where P = *Power required*
F= Resultant force
v = Tangential velocity

- **The Resultant force** can be determined using the component forces

$$F = \sqrt{(F_x)^2 + (F_y)^2 + (F_z)^2} \text{ .... } (2)$$

Where F_x *Force along x-axis*
F_y*= Force along y-axis*
F_z*= Force along z-axis*

- **Tangential velocity** can be determined using

$$V = \frac{\pi DN}{60} \text{ .... } (3)$$

Where V = Tangential velocity
N = Extrusion Wheel speed (RPM)
D = Extrusion Wheel Diameter = 350mm

ii. Total power consumption during experimentation

Note: The power factor for the three phases is 0.8

Voltage	Current	Power factor	Total power consumed
V	I	0.8	**0.8 V x I**

APPENDIX-II: Internal Power of Dissipation

The internal power dissipation in the extrusion die chamber can be calculated with Fig 3.2. Using Fig 3.2 the extrusion die chamber zone can be further subdivide into five (5) sub-regions taking the velocity discontinuity lines as a boundary.

$$w_i = \frac{2}{\sqrt{3}}\sigma_0 \int_v \sqrt{\frac{1}{2}\dot{\varepsilon}_{ij}\,\dot{\varepsilon}_{ji}}\,dv \quad \text{(for secondary deformation zone) ……………….. (4)}$$

$$\therefore w_{II} = \frac{2\sigma_0}{\sqrt{3}} b \int_{r_f}^{r_o} \int_{\psi_{i(r)}}^{\psi(r)} \sqrt{\frac{1}{2}\dot{\varepsilon}_{rr}^{\,2} + \frac{1}{2}\dot{\varepsilon}_{\theta\theta}^{\,2} + \dot{\varepsilon}_{r\theta}^{\,2}}\, r\,d\theta\,dr \text{ ………………………….…….. (5)}$$

Where σ_S: the mean flow states of feedstock material

$$\sigma_s = \frac{1}{\varepsilon}\int \sigma\, d\varepsilon \text{ ……………………………………………………………… (6)}$$

$$\varepsilon = \ln\frac{t_o}{t_f} \text{ ………………………………………..…………….…...…….. (7)}$$

Shear power loss

$$w_s = \frac{\sigma_0}{\sqrt{3}} \int_{S_c} |\Delta v|\, ds \text{ …………………………………………………………..…. (8)}$$

The shear power losses along the velocity discontinuity surfaces S_1 and S_2 are given below.

$$w_{s1} = \frac{\sigma_s}{\sqrt{3}} V_o r_o b \int_0^{\alpha} \left(1 + r_o \left.\frac{\Delta\psi}{\Delta r}\right|_{r=r_o} \cot\alpha\right) \sin\theta\, d\theta \text{ ………………………….……… (9)}$$

Frictional power losses

The generalized expressions for the frictional power losses for the surface with a constant friction factor (m).

$$w_f = m\frac{\sigma_o}{\sqrt{3}}\int_{S_f}|\Delta v|\,ds \ldots\ldots\ldots\ldots\ldots\ldots\ldots\ldots\ldots\ldots\ldots \text{(10)}$$

For the die surface S_5

$$dS_5 = \sqrt{1+(r\frac{\Delta\psi}{\Delta r})^2}\,dr \ldots\ldots\ldots\ldots\ldots\ldots\ldots\ldots\ldots\ldots\ldots \text{(11)}$$

$$|\Delta V| = |U_r \cos\eta + U_\theta \,\mathrm{n}\,\eta|_\theta = \psi \ldots\ldots\ldots\ldots\ldots\ldots\ldots\ldots\ldots\ldots \text{(12)}$$

Where is the local angle of die surfaces with respect to the local radial velocity component

$$\cos\eta = \frac{1}{\sqrt{1+(r\frac{\Delta\psi}{\Delta r})^2}}, \sin\eta = \frac{r\frac{\Delta\psi}{\Delta r}}{\sqrt{1+(r\frac{\Delta\psi}{\Delta r})^2}} \ldots\ldots\ldots\ldots\ldots\ldots\ldots\ldots \text{(13)}$$

The frictional power losses along the die surfaces are calculated as

$$w_f = \frac{\sigma_s}{\sqrt{3}} m V_o r_o \int_{r_f}^{r_o} \frac{\sin\alpha}{r\tan\psi}\left[1+(r\frac{\Delta\psi}{\Delta r})^2\right] \ldots\ldots\ldots\ldots\ldots\ldots\ldots\ldots\ldots \text{(14)}$$

Where m; friction factor between feedstock and die surface.

The frictional power losses along the container surface is given by

$$w_{f4} = \frac{\sigma_s}{\sqrt{3}} m V_o b\left[L - x\right] \ldots\ldots\ldots\ldots\ldots\ldots\ldots\ldots\ldots\ldots\ldots \text{(15)}$$

Where x---displacement of the punch

Lo----initial contact length of feedstock material

k= strength coefficient

n= strain hardening exponent

- **Work Primary deformation zone**

$$W_1 = \frac{\sigma_0}{\sqrt{3}} \int_S |V| ds$$

$$W_1 = \frac{\sigma_0}{\sqrt{3}} bV_o \int_o^{L_1} dl \qquad \ldots\ldots\ldots\ldots\ldots\ldots\ldots\ldots\ldots\ldots(16)$$

- **Work in the secondary deformation zone**

$$W_2 = \frac{\sigma_0}{\sqrt{3}} \int_S |V| ds$$

$$W_2 = \frac{\sigma_0}{\sqrt{3}} bV_o \int_o^{L2} dl \qquad \ldots\ldots\ldots\ldots\ldots\ldots\ldots\ldots\ldots\ldots(17)$$

- **Abutment feedstock collision zone**

Load at the abutment (Fa) can be calculated

$$F_{f1} = \frac{2}{3}\left(\frac{d_3}{2} + L_{(2b-2c)}\right)(SA+W)\tau_{m(2b-3)} \qquad \ldots\ldots\ldots\ldots\ldots (18)$$

Where Ff1: the dead zone friction effect

$$F_{f2} = L_a \tau_{m(2b-2c)} SA \qquad \ldots\ldots\ldots\ldots\ldots\ldots\ldots\ldots (19)$$

Where F_{f2}*: the friction effect over the abutment tool landed region.*

d3: diameter in the secondary deformation zone

L(2b-2c) : length along the abutment region

- **The total deformation work** (both external and internal) on the abutment tool can be denoted in the expression.

$$F_a = F_{f1} + F_{f2} + W_T A_a \qquad \ldots\ldots\ldots\ldots\ldots\ldots\ldots\ldots\ldots (20)$$

Where, F_a*: Force of the Abutment tool ,* $W_T A_a$*: external deformation work on the abutment tool*

APPENDIX-III: Wear Characteristics Calculation Formulas

It is useful in evaluating and contrasting wear rate characteristics of those materials tested under different testing conditions. Therefore, the experimental results of the wear test were further analyzed to assess the wear rate and wear coefficient, the cumulative loss in mass (or volume) per sliding distance (or sliding time) determined using the linear equation as follows.

i. Sliding distance and sliding speed

Therefore elapsed time can be calculated using the above formula.

$$t = \frac{S}{v} \quad \ldots\ldots\ldots\ldots\ldots\ldots\ldots\ldots\ldots\ldots(21)$$

$$= \frac{500m}{0.5m/s} = \underline{16.67 \text{ min}}$$

Therefore each experiment had taken 16.67 min

Where:- S: the sliding distance (S=v.t): the total experimental distance taken for experimentation by test sample which is 500m ; v: the mean value for the slide rate; t: the running time.

ii. Friction force and wear coefficients

Friction force was calculated. Measured calculation of the friction coefficient multiplied by the normal load exerted on the pin by the testing machine's dead weight.

Frictional force (f_f)

$$\mu = \frac{f_f}{F_n} \quad \ldots\ldots\ldots\ldots\ldots\ldots\ldots\ldots\ldots\ldots (22)$$

Therefore $\boldsymbol{f_f = F_n * \mu =}$

Where f_f = frictional force (N), μ = coefficient of friction ,F_n = applied normal load (N)

iii. Wear amount (Mass loss, volume loss, length loss)

Wear amount can be calculated by taking different parameters depending on the available data types. The most common types are mass loss wear amount, linear dimensional change wear amount, and volume loss wear amount. In this investigation mass loss (direct) technique had been selected by measuring the weights of the samples before and after the test. Volume loss was also determined indirectly using empirical formulas.

Wear amount = mass loss (kg)

$$\Delta \mathbf{m} = \mathbf{m_1} - \mathbf{m_2}$$

Where: - Δm = mass loss or the difference in mass of a sample before and after the wear test (kg or g); m_1 = mass of wear test specimen before wear test ; m_2 = mass of wear test specimen after wear test;

$$\Delta \mathbf{l} = \mathbf{l_1} - \mathbf{l_2}$$

Where: - Δl = length loss or linear dimensional change before and after the test (m or mm or cm) o

$$\Delta \mathbf{V} = \mathbf{V_1} - \mathbf{V_2}$$

ΔV = volume loss (m^3) before and after the test ; **V_1:** volume of wear test specimen before wear test; **V_2 :**volume of wear test specimen after wear test

iv. **Wear resistance**

Wear resistance is an inverse of the wear amount.

$$w_R = \frac{1}{\Delta m} = \frac{1}{\Delta l} = \frac{1}{\Delta V} \quad \ldots (23)$$

Where w_R ; Wear resistance = [m^{-1}, m^{-3}, kg^{-1}]

v. **Wear rate**

It is a wear amount that is the amount of loss in mass or length, volume, per sliding distance, or per elapsed time for the sliding distance. It is independent of the load applied.

A most commonly applied equation to calculate the wear rate:

$$w_r = \frac{\Delta m}{S} = \frac{\Delta l}{S} = \frac{\Delta V}{S} \quad \ldots (24)$$

$$w_r = \frac{\Delta m}{t} = \frac{\Delta l}{t} = \frac{\Delta V}{t} \quad \ldots (25)$$

*Where w_r **:** Wear rate [m/m, m^3/m, m/s, m^3/s, and kg/s]; t: Time elapsed to complete the sliding distance*

vi. **Wear coefficient,** or **specific wear rate** (also sometimes called wear factor)

Contrary to wear rate, specific wear rate depends on the applied load that causes wear; it is volume loss per unit meter per unit load. Its unit is (m3/Nm). It is the wear rate per normal force. Since the wear properties of a metal, alloy, or engineering materials can be described with better accuracy through specific wear rate techniques.

This technique can be taken as a precision indication of the wear characteristics of the sliding bodies under different testing conditions normal loads, sliding speeds, and sliding distance or elapsed time. It is also a tool to describe a specific property. After the investigation of dry friction sliding wear tests, the mass loss and coefficient of frictional calculated.

The wear coefficient values related to the cumulative mass (or volume) loss per sliding distance (or time) can be determined with the linear equation as follows using equation (10).

$$k = \frac{\Delta m}{\rho * F_n * S} = \frac{\Delta V}{F_n * S} \quad \text{.......................................} \quad (26)$$

Therefore $V = k.F_n.S$ .... (27)

$$k = \frac{w_r}{F_n} \quad \text{..} \quad (28)$$

Where K = Specific wear rate or wear coefficient, (m^3/Nm), (mm^3/Nm); = density of the specimen (g/cm^3); F_n = applied normal load (N); S = Sliding distance (m);
V = Cumulative lost volume of samples: C101, Al1100 and C18150sample

APPENDIX-IV: Temperature Determination at Each Stage of Plastic Deformation

When a metal is deformed especially in plastic form, the majority of the internal deformation work reveals itself as heat form. In general, the feedstock temperature of in the deformation zone depends on certain conditions such as the tooling chamber and feedstock initial temperature, plastic deformation related heat generation, friction caused heat generation especially between feedstock and tooling such as the interface feedstock and extrusion wheel or extrusion container or die chamber and, heat transfer cases between the deforming feed metal and the toolings and the surroundings expressed in in Eq.29 as follows.

$$\delta T_i = \frac{\beta_1 w_t}{\rho_f C_f J} \quad \text{...} (29)$$

Where *δT : the change in temperature due to plastic deformation;β_1: the fraction of deformation work converted into heat; Wt: work done in the deformation zone; ρ: the density of the feed metal; C_f: specific heat capacity of the feed metal; J: the mechanical equivalent of heat*

For a heavily deformed metal, between 90 and 99 % of the work done is changed into heat (Prasad *et al.* 2015; Myshkin *et al.* 2005). Therefore significant amount of heat generated due to the plastic deformation per unit volume. In other words, the feedstock temperature increases because of plastic deformation caused by the work done, the density and specific heat capacity of the feed metal. The constant β_1 is the fraction of deformation work which is converted into heat. The value β_1= 95 % has been assumed.

The intention is to determine the temperature at each stage of plastic deformation corresponding to a change in strain, in order to predict a temperature profile in the feed metal across the deformation zone. To do this, it is necessary to determine the constitutive equation for stress state at each stage of deformation. It is then possible to determine the plastic work done at each stage of deformation. Clearly, an iterative solution to the upper bound equation will be required, since the temperature is determined from the upper bound equation for work done and the constitutive equation requires knowledge of temperature. The temperature increase in the primary extrusion chamber arises due to friction resistance at the stationary tooling segment, and moving feed metal interface. The expressions given below for the temperature increase due to friction is detailed below (Green, D., 1972) as follows,

$$\delta T_{(2a-2b)} = \frac{\tau_{m(2a-2b)} \dot{V}_1 A_a \delta t}{\rho_f C_f V_f J}$$ …………………..…………..………. (30)

Where:- $\tau_{m(2a-2b)}$ *: shear stress in the secondary deformation zone between regions 2a and 2b;* $\dot{V}_1$*: feed stock entry speed (m/s);* A_a*: feed metal cross sectional area;* V_f *: flash removal rate by scrapper*

Where $$\tau_{m(2a-2b)} = \frac{(\sigma_{(2a)} + \sigma_{m(2b-3)})}{2\sqrt{3}}$$ *: the mean stress in (30) shear using the von Mises yield criterion and m = 1 detailed under section.*

The expression in Eq. 30 was modified in order to determine the temperature increase in the feed metal in the primary extrusion chamber as follows in Eq.31.

$$\delta T_{(2a-2b)} = \frac{\beta_2 \tau_{m(2a-2b)} L_{(2a-2c)}}{\rho_f C_f d_2 J}$$ …………….…. (31)

Where:- β_2*:the fraction of deformation work in the secondary deformation zone;* $L_{(2a-2C)}$*: secondary deformation zone between 2a to 2c in the Figure 4.;*

It is noted, that part of the heat generated through friction is transferred to the feed metal and the remaining portion to the tooling (in particular the tooling segment) in the primary extrusion chamber. The development of a simple mathematical expression which describes the heat lost to the container and die for a discrete billet in a conventional extrusion chamber has not been forthcoming. However, It had been presented in a simplified model, which is as follows.

When a metallic feedstock material is initiated to be extruded, the temperature of the feed stock metal (or billet) becomes higher than that of the extrusion container, as a result heat flows away from the deformation zone of the feedstock (taking that the chamber temperature is at the same temperature of the feedstock initial temperature). The heat balance is complicated by the forward motion of the feed metal and by the fact that the chamber progressively heats up as extrusion process continues.

The heat balance considered based on many assumptions. Temperature of the extrudate product, the emergent from the die orifice, expressed as a function of the temperature generated through plastic deformation (i.e. the maximum temperature developed in the deforming feed metal before heat conduction takes place. The emergent (or final) temperature of the feedstock corresponding to plastic deformation in the Conform extrusion-die chamber (i. e. stages 3 to 5), decided by considering the heat lost to the extrusion chamber and die assembly in a short period of time. The heat balance is described as follows,

$$\theta_f = \theta_i + \theta_c + \theta_d \quad \text{.......................................} \quad (32)$$

Where: - θ_f: the heat balance between extrudate and extrusion di-chamber assembly; θ_i: the initial heat of the container; θ_c: the heat lost rate to the extrusion die chamber; θ_d: the heat lost rate to die face in the traditional extrusion container.

The extrudate temperature estimated,

$$T_f = \left[\frac{T_i}{\left(1 + \frac{\dot{\theta}_C \, k}{\rho_f{}^2 C_f{}^2 V^2 A_i} + \frac{\dot{\theta}_d}{\rho_f C_f V} \right)} \right] \quad \text{......................} \quad (33)$$

Where T_f: the final temperature due to plastic deformation; T_i: the initial feedstock temperature; $\dot{\theta}_c$: the rate of heat lost to the container; $\dot{\theta}_d$: the rate of heat lost to die face in the conventional extrusion chamber.

The rate of heat loss to the continuous forming extrusion die is presented as follows.

$$\dot{\theta}_d = At^c \text{ ……………………………………………………….(34)}$$

Where: - A, B: constants (Details of constant values are provided in ASTM standard book)

The rate of heat lost to the continuous extrusion chamber during the process was estimated using analytical model. It was determined using Eq. 34

$$\dot{\theta}_c = (A + \frac{Bd_i}{d_d})t^c \text{ ………………………………..………….. (35)}$$

Where: -di and df diameters of initial(feedstock) and final (die)

It is well-known, that the exit temperature of the continuous forming extrudate is supposed uniform all over the cross-sectional area. Actually, the above mathematical expressions detailed above adopt that the extrudate temperature at any step is constant throughout any cross-section in the deformation zone.

The expression for β_2 subsequently derived from the interpretation of experimental data as follows.

$$\beta_2 = A(\frac{d_i}{SA})^c \text{ ……………………………….…………..... (35)}$$

Finally, the temperature distribution in the primary and die chambers i.e. stages 2a to 2b, 2b to 3 and 3 to 5 in Figure 3.1 and Figure 4.2, determined by the summation of the final temperatures pertaining to each stage in the deformation zone.